UNIVERSITY OF OKLAHOMA

GRADUATE COLLEGE

INTEGRATED CHARACTERIZATION OF TIGHT SILICICLASTIC RESERVOIRS: EXAMPLES FROM THE CRETACEOUS BURRO CANYON FORMATION, COLORADO, AND MISSISSIPPIAN MERAMEC STRATA, OKLAHOMA

A DISSERTATION

SUBMITTED TO THE GRADUATE FACULTY

in partial fulfillment of the requirements for the

Degree of

DOCTOR OF PHILOSOPHY

By

JERSON JESID JAVIER TELLEZ RODRIGUEZ
Norman, Oklahoma
2021

INTEGRATED CHARACTERIZATION OF TIGHT SILICICLASTIC RESERVOIRS: EXAMPLES FROM THE CRETACEOUS BURRO CANYON FORMATION, COLORADO, AND MISSISSIPPIAN MERAMEC STRATA, OKLAHOMA

A THESIS APPROVED FOR THE
SCHOOL OF GEOSCIENCES

BY THE COMMITTEE CONSISTING OF

Dr. Matthew Pranter, Chair

Dr. Heather Bedle

Dr. John Pigott

Dr. Deepak Devegowda

Dr. Rex Cole

Acknowledgments

I want first to thank life. I have been fortunate enough to have the love of my entire family, alive and healthy after several years outside my country as a first-generation graduate and immigrant. My parents Sixto Tellez and Mery Rodriguez, my siblings Sebastian, Valentina, Andres, Jenny, and my nieces, Paula, Alison, and Luna are the reason to keep me going every day. I love them. I want to thank my committee members: Dr. Matthew Pranter, Dr. Rex Cole, Dr. Heather Bedle, Dr. Deepak Devegowda, and Dr. John Pigott, for their support and encouragement. I am very thankful for my supervisor Dr. Matthew Pranter, who patiently gave me numerous opportunities to grow professionally as a teacher and geoscientist. I am highly grateful for his support and advice to tackle professional and personal challenges during my doctoral journey. To the School of geosciences and the administrative staff, Rebecca, Ginger, Ashley, and Leah, thank you so much for helping me whenever I needed support to solve any issue. I acknowledge COLCIENCIAS and the Agencia Nacional de Hidrocarburos grant for their support.

I would like to thank all the people I met during my master's and doctoral journey after almost seven years at the University of Oklahoma. Each of you supported me in some form to finish this journey. It will be easy to miss a name, so I won’t mention them. I hope they know my immense appreciation. Finally, but not less important, I want to thank a couple of people that changed the course of my life for good, Dr. Roger Slatt. I know you are looking at here from the sky, my forever angel (#SLATT_GRAD); and the most wonderful woman, my beautiful, charismatic, charming, and resilient, Kare. I would not have finished this journey without your love and support. You are my north and drive.

Table of contents

List of tables

List of figures

Abstract

Integration of multiscale data sources for reservoir characterization becomes problematic and challenging due to the collected information variable resolution. Core and well data provide high vertical resolution to evaluate stratigraphic variability but fails to assess lateral variability and connectivity. In contrast, outcrop exposures and seismic data are used to extract dimensional statistical measurements and three-dimensional spatial distribution of reservoirs, respectively. It is time-consuming to characterize large outcrops, and rock exposures are often discontinuous. Seismic data offers great horizontal coverage with a low resolution, making it hard to evaluate small lateral variability and spatial distribution of reservoirs. This research explores workflows using new emerging techniques and methods for reservoir characterization such as petrophysics, seismic interpretation, and stratigraphic analysis to effectively address the intrinsic uncertainty in predicting large- and small-scale heterogeneity caused by lateral and vertical facies changes and their petrophysical properties. This detailed characterization reduces the risk associated with exploring and developing potential reservoirs for fluid storage or hydrocarbon production. The applied techniques detailed in this study are used to collect and integrate multiple data sources for reservoir characterization of unconventional reservoirs, mainly fluvial tight sandstones and mixed siliciclastic-calcareous deep marine platform deposits. I present three case studies using workflows that include new techniques for reservoir characterization at different scales. The research starts using UAS (drones) for three-dimensional outcrop reconstruction models for 50 miles of rock exposure combined with fieldwork to define the sequence stratigraphy and architecture of a fluvial reservoir. Then, I present a workflow to integrate information that includes thin-sections, core description, petrophysical data, well logs, and seismic data through machine learning techniques to define the sequence stratigraphic variability and structural

configuration of a mixed siliciclastic system. The last case study shows a workflow to predict, map, and analyze the mechanical stratigraphy of the Meramecian STACK play in Oklahoma and its impact on hydrocarbon production. The illustrated workflows allowed collecting and integrating data from diverse sources to build robust geological models and better constrain reservoir models to reduce uncertainty in reservoir prediction and volumetric estimation.

Introduction

The worldwide demand for energy production and the increasing demand for geological storage of CO_2 require multidisciplinary reservoir characterization. An optimal subsurface characterization allows for the efficient exploitation of hydrocarbon reservoirs. It helps assess new and old depleted reservoir capacity to store CO_2, natural gas or other fluids relevant as natural resources.

A detailed reservoir characterization requires significant amounts of data to build robust, well constrained, geological models. The most common data sources are obtained from well logs and core samples and derived data from various measurements and observations (i.e., porosity, permeability, X-ray diffraction, thin-sections, stress-strain, X-ray fluorescence, ultraviolet light, lithofacies descriptions, etc.). Previous studies have collected two-dimensional data from outcrop exposures that contain information about the geological record of fluvial (Pranter 2007; Pranter 2009; Cole and Cumella, 2005) and ancient deep-water systems (Pranter et al., 2005; Slatt and Pyles, 2008; Tellez, 2015). These studies use statistical measurements to constrain the modeling of geological elements in the surface when well data is scarce or the environment of deposition is complex and highly heterogeneous (Pranter et al., 2007, Colombera et al., 2012). Lastly, the most common three-dimensional source of data for subsurface characterization are seismic surveys. They provide high volumetric coverage but are expensive data with a limited vertical resolution to evaluate small-scale heterogeneity and variability. Seismic data provide excellent horizontal coverage for large-scale studies and depositional environment definition. Because multiple data sources exhibit variable scales and resolution, the integration of datasets is not trivial.

This dissertation explores workflows to integrate multiple data sources to characterize tight siliciclastic reservoirs and analyze stratigraphic and lateral geological variability. The research focuses on examples from the Piceance Basin of Colorado and Anadarko Basin of Oklahoma. The document is organized into different chapters independent among themselves but connected by integrating data methodologies used to address different research questions.

The first chapter of this dissertation is presented as it was published in the journal *Interpretation* (Tellez et al., 2020). It explores the geological characterization of outcrops related to the Cretaceous Burro Canyon Formation. Fluvial deposits like the ones that comprise the Burro Canyon Formation are evaluated vertically using stratigraphic columns that provide a means to evaluate stacking patterns and infer stratigraphic variability to estimate changes in net-to-gross ratio and petrophysical properties. Laterally, rock exposures of fluvial deposits are discontinuous and show high lateral heterogeneity. The statistical information collected from the outcrop regarding fluvial architecture and reservoir dimensions is essential to reduce subsurface characterization uncertainty. The use of UAS (Unmanned Aerial Systems) and stratigraphic columns to build three-dimensional outcrop reconstructions allowed me to collect statistical measurements of width and thickness from sandstone bodies composed of bar sets within a fluvial system. The generated reconstructions along 50 miles of outcrop allowed me to define a regional sequence stratigraphic framework that explains the evolutionary stages of the fluvial system.

In the second chapter, I use methods and workflows to define the stratigraphy and structure of a mixed siliciclastic-carbonate platform of the Meramec strata in central Oklahoma. The stratigraphic characterization integrates data from thin-section and core descriptions to estimate lithofacies and evaluate the sequence stratigraphic framework. To classify lithologies in

non-cored wells, I use a supervised machine learning technique (ANN) to establish the stratigraphic variability of lithologies and refine the stratigraphic framework. To evaluate and map the lateral variability of lithologies and petrophysical properties, I use a combination of well logs and seismic data to perform a supervised Bayesian approach that, combined with a geostatistical analysis, helps me to generate a seismic-constrained reservoir model to represent the lateral and horizontal variability of the Meramec unconventional reservoir.

The third chapter is presented as it was published in the journal *Interpretation* (Tellez et al., 2021). It explores the use of dynamic velocity data acquired from core plugs and the application of supervised machine learning techniques (ANN) to estimate geomechanical properties. The chapter content shows a methodology that combines mineralogical information inverted from an X-ray diffraction analysis from stratigraphic interpretation, ANN-derived geomechanical well logs, and seismic inversion attributes to evaluate the mechanical stratigraphy of the Meramec and its effect in hydrocarbon production.

The last chapter encompasses an executive summary of my findings with the most important conclusions about the stratigraphy and structure of the Burro Canyon and Meramec tight reservoirs. I also provide insights into the benefits of using integrated workflows for regional and small-scale reservoir characterization studies.

.

References

Cole, R. D., and S. P. Cumella, 2005, Sand body architecture in the lower Williams Fork Formation (Upper Cretaceous), Coal Canyon, Colorado, with comparison to the Piceance Basin subsurface: The Mountain Geologist, 42, 85–107.

Colombera, L., Felleti, f., Mountney, N.P., and McCaffrey, w.d., 2012, a database approach for constraining stochastic simulations of the sedimentary heterogeneity of fluvial reservoirs: American Association of Petroleum Geologists, Bulletin, v. 96, p. 2143–2166.

Pranter, M.J., Z.A.Reza, and P.Weimer, 2005, Deepwater Reservoir Modeling Using Sequence Stratigraphic and Geomorphic Constraints, SPE 95952

Pranter, M. J., A. I. Ellison, R. D. Cole, and P. E. Patterson, 2007, Analysis and modeling of intermediate-scale reservoir heterogeneity based on a fluvial point-bar outcrop analog, Williams Fork Formation, Piceance Basin, Colorado: American Association of Petroleum Geologists Bulletin, 91, 1025–1051, doi: 10.1306/ 02010706102.

Pranter, M. J., R. D. Cole, H. Panjaitan, and N. K. Sommer, 2009, Sandstone-body dimensions in a lower coastal plain depositional setting: Lower Williams Fork Formation, Coal Canyon, Piceance Basin, Colorado, USA: American Association of Petroleum Geologists Bulletin, 93, 1379–1401, doi: 10.1306/06240908173.

Pyles, D.R., and Slatt, R.M., 2008, Integrating outcrop and subsurface data to define regional and reservoir-scale patterns in the Lewis Shale and Fox Hills Sandstone of the Great Divide and Washakie Basins, Wyoming: AAPG Rocky Mountain Section Meeting, abstracts

Tellez, J. J., 2015. Seismic Sequence Stratigraphy and Architectural Elements for Cenozoic Strata at the Rankin Platform Sub-Basin, North Carnarvon Basin, Australia. Master thesis. The University of Oklahoma, pp. 108

Tellez, J. J., M. J. Pranter, and R. Cole, 2020, Fluvial sequence stratigraphy and architecture of the Burro Canyon Formation, southwestern Piceance Basin, Colorado, Interpretation vol:8 iss: 4

Tellez, J., M. J. Pranter, C. Sondergeld, Rai, C., Fu, J., Han, H., and C. McLain, 2021, Mechanical stratigraphy of Mississippian strata using machine learning and seismic-based reservoir characterization and modeling, Anadarko Basin, Oklahoma. Interpretation vol:9, iss:2, 1-62.

Chapter 1: Fluvial architecture and sequence stratigraphy of the Burro Canyon Formation, southwestern Piceance Basin, Colorado.

Jerson Tellez[1], Matthew Pranter[1], Rex Cole[2]

[1]School of Geosciences, The University of Oklahoma, 100 East Boyd Street, RM 710, Norman, Oklahoma, 73019, USA

[2] Department of Physical and Environmental Sciences, Colorado Mesa University, Grand Junction, Colorado, 81501, USA

Preface

The characterization of fluvial systems architecture based on outcrop studies is challenging and vital to define its horizontal and vertical variability. In this chapter, I characterized tight fluvial sandstones exploited for gas production in the Piceance Basin, CO. I used a combination of fieldwork and 3D outcrop models derived from Unmanned Aerial Vehicles (drones) to characterize qualitatively and quantitatively extensive deposits of the Burro Canyon Formation in the Piceance, Basin. Colorado.

This manuscript appears in Interpretation, Vol. 8, No. 4 (November 2020); p. T1037–T1055 http://dx.doi.org/10.1190/INT-2019-0215.1.
Tellez, J. J., *M. J. Pranter, and R. Cole, 2020, Fluvial sequence stratigraphy and architecture of the Burro Canyon Formation, southwestern Piceance Basin, Colorado, Interpretation vol:8, iss:4*

This chapter was presented by invitation in an AAPG workshop
Tellez, J. J., *M. J. Pranter, 2016, Application of UAV-Based Photogrammetry for Outcrop Characterization of Fluvial Deposits of the Burro Canyon Formation, Piceance Basin, GTW, New Opportunities with Drones: New Needs, FAA Rule Changes, New Technologies, Houston, TX, Dec 2016*

This chapter was presented by invitation in 7TH International Symposium on Hydrocarbon Accumulation Mechanism and Petroleum Resources Evaluation
Tellez, J. J., *M. J. Pranter, and R. Cole, 2017, Application of UAV-Based Photogrammetry for Outcrop Characterization of Fluvial Deposits of the Burro Canyon Formation, Piceance Basin, Colorado, 7TH International Symposium on Hydrocarbon Accumulation Mechanism and Petroleum Resources Evaluation, Beijing, China, Oct 2017*

Abstract

The Lower Cretaceous Burro Canyon Formation in the southwestern Piceance Basin, Colorado, is composed of deposits that represent a braided fluvial system with high net to gross that transitions stratigraphically upward into a low net-to-gross, low sinuosity, meandering fluvial system. The fluvial deposits are composed of multiple upward fining, conglomeratic-to-sandstone successions forming bars and bar sets that exhibit inclined heterolithic strata that we have interpreted to have formed by oblique and downstream accretion. We used well exposed outcrops, detailed measured sections, and unmanned aerial system-based imagery to describe the fluvial architecture of the Late Cretaceous formation using a hierarchical approach. We described the Burro Canyon Formation as comprising sandstone-rich amalgamated channel complexes (ACC) overlain by non- to semi amalgamated channel complexes. The lower interval of the formation is composed of ACC that contain channel-fill elements with cross-stratification and numerous truncated contacts. These stacked channel-fill elements exhibit an apparent width range of 137–1300 ft (40–420 m) and a thickness range of 5–60 ft (1.5–18 m).

The upper interval of the Burro Canyon Formation comprises mudstone-prone intervals of the non amalgamated channel complex with isolated channel-fill elements interbedded with floodplain mudstones that represent a period of relatively high base level. Associate channel fill elements range in apparent width from 200 to 1000 ft (60 to 300 m) and thickness from 20 to 30 ft (6 to 18 m). The characteristics and spatial distribution of architectural elements of the Burro Canyon Formation correspond to one depositional sequence. The erosional basal surface of the formation, as well as lateral changes in thickness and net to gross, suggest that the Burro Canyon Formation within this study area was deposited as an incised valley fill. Fluvial deposits of the

Burro Canyon Formation serve as outcrop analogs for subsurface interpretations in similar reservoirs.

Introduction

The study of fluvial systems is challenging for geoscientists due to the high lateral variability of lithologies, lack of preservation of sequences, and other local and regional processes that affect the geologic record in alluvial deposits (Holbrook, 1996; Holbrook et al. 2006; Miall, 2006; Durkin et al., 2017). Local studies of fluvial systems offer great detail about the vertical configuration of lithofacies and the sedimentologic characteristics of the fluvial systems. However, large-scale studies are needed (Miall, 1996; Labourdette and Jones, 2007; Pranter et al., 2009, 2014) to better define the fluvial architecture and stratigraphic evolution of the system through time as a response of base-level, tectonic, and climate changes. The understanding of the alluvial architecture in fluvial depositional systems helps to model and predict the occurrence of architectural elements and lithologies in the subsurface where often the information is limited to 1D data, making it harder to predict the oil and gas reservoir rocks in the subsurface.

Previous studies have mapped and analyzed outcrops in terms of their continuity, and fluvial architecture using unmanned aerial systems (UAS) (Banes et al., 2017; Bliscaux et al., 2018). However, the lithological relationship between local and regional scales is not yet well understood and more studies of fluvial sequence stratigraphy, architectural element dimensions, and changes in fluvial architecture are needed to documented and understand their heterogeneity and variability. We explore the use of UAS to integrate observations of local outcrops in a large

study area to characterize the stratigraphic evolution and fluvial architecture of the Early Cretaceous Burro Canyon Formation in western Colorado.

The Burro Canyon Formation was first defined by Stokes and Phoenix (1948) in southeast Utah and southwest Colorado to describe the nonmarine lower Cretaceous interval characterized by non carbonaceous deposits described in its type section in Montrose, County, Colorado. Stokes (1952) also describes the Cedar Mountain Formation in central and northeast Utah as being the lateral equivalent of the Burro Canyon Formation and highlights the problems associated with differentiating the Burro Canyon from the Cedar Mountain formations in the Colorado Plateau. Young (1960, 1970, 1973) interprets and divides the Dakota Group into two formations, the Naturita and the Cedar Mountain (Burro Canyon Formation equivalent) Formations, and describes the Burro Canyon Formation in the Colorado Plateau using data from 150 measured sections in western Colorado and eastern Utah.

During the late 1980s, studies in Utah and western Colorado concluded that sea-level variations and lowering of base-level during the Late Cretaceous produced incised streams that were filled by alluvial deposits of the Burro Canyon Formation (Aubrey, 1986, 1989; Aubrey and Skipp, 1992). The interpretation of sea-level changes is consistent with the unconformities interpreted in several studies of the Early Cretaceous strata in the region (Stokes, 1952; Young, 1960, 1970, 1973). Kirkland et al. (1999) divide the Cedar Mountain Formation using paleontological and biostratigraphic information into five members and recognize significant vertebrate fossils to define the age of the Cedar Mountain Formation as Early Cretaceous.

More recent studies by Cole and Moore (2012) use well log information combined with 11 measured sections, 9 cores, and petrographic information to define lithofacies and interpret the Burro Canyon depositional environment in the southwestern Piceance Basin, Colorado. They interpret the Burro Canyon Formation as braided fluvial channels that flowed from southwest to northeast and defined two principal unconformities, K1 and K2, which underlie and overlie the Burro Canyon Formation, respectively.

The definition of the sequence stratigraphic framework for the Burro Canyon Formation was first presented by Owen et al. (2005). Their work summarizes the sequence stratigraphy for the Burro Canyon and Lower Mancos Formations into three different depositional sequences. The Dakota Formation was studied in detail, but the study presented limited details about the sequence stratigraphic framework of the Burro Canyon Formation.

Although several authors have defined the sedimentology of the deposits of the Burro Canyon Formation, there is no detailed sequence stratigraphic framework that allows us to explain the fluvial architecture and evolution of the systems based on sea-level and tectonic changes in the basin. To build upon previous studies of the Burro Canyon Formation, this study (1) explores characteristics of the fluvial deposits and their spatial distributions, (2) examines the fluvial system type and stratigraphic variability, and (3) establishes a sequence stratigraphic framework.

To address these topics, we use a combination of conventional field methods and UAS-based digital-outcrop imaging technique. We map the spatial variation of the net-to-gross ratio

and develop a sequence stratigraphic framework to interpret the fluvial architecture in terms of accommodation space relative to sediment supply.

Geological setting

The Lower Cretaceous Burro Canyon Formation formed as a result of multiple tectonic events that occurred from the Barremian to the Aptian. The collision of the Farallon and Kula plates against the North American plate during the Late Jurassic and Early Cretaceous produced the uplift and development of the Sevier Thrust Belt in what is now western Utah (DeCelles et al., 1995). During the tectonic events, erosion of more than 6 mi (10 km) of Mesozoic and Paleozoic rocks filled the foredeep, forebulge, and back-bulge regions of the sedimentary wedge. The Aptian-Albian evolution of the foreland system formed as response of a lithospheric flexure associated with the developing of the Sevier trust belt to the west. The regional thickness changes within the Cretaceous strata are associated with a depocenter zone developed toward the forebulge region in western Colorado, whereas thinning of the strata is connected to the flexural forebulge in eastern Utah (Currie et al., 1997). Slight thickening of the lower Cretaceous intervals in the western zone is attributed to the position of the back-bulge depozone and fault controls in sedimentation affecting the accommodation space (Currie, 2002).

The definition of the Burro Canyon Formation is being discussed by several authors (Figure 1). The formation is age-equivalent to the Cedar Mountain Formation in Utah and the West Wasatch Plateau (Young, 1960; Stokes, 1944, 1952; Currie, 1997; Aubrey, 1996; Kirkland et al., 1999; Kirkland and Madsen, 2007). Equivalent formations in northern Wyoming are the Clovely Formation, Thermopolis Shale, and Mowry Shale and Dakota Formation, Fall River

Formation, Skull Creek Shale, and Newcastle Sandstone in South Dakota (Kirkland et al., 1999, Kirkland and Madsen, 2007).

Stokes (1952) names the interval Cedar Mountain Formation on the San Rafael Swell and later names the same interval the Burro Canyon Formation in southeastern Utah and southwestern Colorado. Young (1960) defines the complete interval as the Dakota group, which consists of the Naturita Formation (Dakota equivalent) above and the Cedar Mountain Formation (Burro Canyon equivalent) through a regional study that involved several measured sections. Aubrey (1996) does detailed work in the lower part of the Burro Canyon and concludes that this Formation was deposited interfingered with the Brushy Basin Member (the Upper Morrison Formation). Aubrey (1996) reported Early Cretaceous fossils preserved in the upper part of the formation and interpreted them to be equivalent to the Cedar Mountain Formation in Utah and Western Colorado. However, this work reported that the lower part of the formation does not have fossils to establish specific age of deposition. In contrast, Kirkland et al., (1997) define the base of the Cedar Mountain Formation as Early Cretaceous based on three distinct dinosaur fossils faunas (ankylosaurs, iguanodons, and sauropods) at the base of the interval and divided the formation in stratigraphic members based on specific classifications of the fossil record.

Currie (1997) and Cole and Moore (1994) use the name of the Burro Canyon Formation for the fluvial deposits that unconformably overlie the Morrison Formation between the K1 and K2 unconformities in western Colorado (Figure 1). These studies highlighted the equivalence of the Cedar Mountain Formation of Utah and the Burro Canyon Formation. The top of the formation (K2 unconformity) was defined by Young (1960) where the carbonaceous content increases in the section reflecting the change of the depositional setting from a floodplain environment to a more paludal-lacustrine environment for the overlying Dakota Formation.

The depositional environment of the formation has been interpreted as a fluvial-floodplain that covered most of the foreland basin (Young, 1960). Initially, the region was crossed by huge braided low sinuosity streams that deposited conglomeratic sediment. The interchannel areas were narrow, and silt and mud materials

were transported to the sea. The late deposition of the formation was dominated by meandering fluvial systems separated by broad interchannel areas. Overall, the Burro Canyon Formation consists of fine- to coarse-grained sandstones and conglomeratic sandstones with green-red, often calcareous, mudstones that occasionally contain carbonate nodules. Sandstones dominate the lower part of the formation, whereas mudstones dominate the upper section (Cole and Moore, 1994). On the western basin margin, oxidic conditions dominated and resulted in the deposition of red overbank mudstone deposits (Young, 1973; Young, 1975).

Methodology

Lithologies, lithofacies, and facies associations

To evaluate the lithologies, lithofacies, and facies associations of the Burro Canyon Formation, we evaluated six outcrop localities in northwestern Colorado along a 48 mi (77 km) transect that approximately parallels the Gunnison River (Figure 2). We described and measured (~1500 ft; ~457 m) eight stratigraphic sections with detailed descriptions of the lithology, grain size, sedimentary structures, bounding surfaces, and paleocurrent directions for five of the six outcrops. A handheld SuperSpec RS-125 scintillometer (Radiation Solutions, Inc.) was used to measure the total- count gamma-ray (GR) values at 1 ft (0.3 m) intervals for each measured section to assist in lithology identification and for comparison and correlation to subsurface well logs. To identify and document significant stratigraphic changes within the outcrop belt, we visited additional locations between the selected outcrops.

We defined lithologies and lithofacies describing the composition, texture, sedimentary structures, and stratification of rocks along the measured sections at each location. Outcrop evaluation provided information about the vertical distribution and relationships between the defined lithofacies, therefore, the types of fluvial deposits in the Burro Canyon Formation. Architectural elements were defined by groupings related to characterize their vertical stacking patterns on a larger scale for the alluvial depositional system.

We evaluated the information collected from the outcrop exposures to identify variations in thickness, the dominance of facies associations, and the horizontal and vertical continuity of the elements at the different localities along the transect. The definition of key surfaces (main unconformities or erosive surfaces) was done at each section and correlated along the transect. These surfaces were also used to constrain the 3D outcrop models described below.

A core description of the Mitchell Energy 8-1 Federal well located in Mesa County, Colorado (Figure 2), was used to correlate the lithologies and lithofacies from the outcrop to the subsurface. We acquired GR profiles for each measured section, and we used them for stratigraphic correlation to logs from 48 wells northeast (~3 mi; ~4.8 km) of the outcrop. The digitized well logs were normalized using a graphical end-point calibration technique.

Well log cross sections were constructed approximately parallel and perpendicular to the inferred paleoflow direction (~30°–70° azimuth) (Figures 2 and 3) to correlate the Burro Canyon Formation. We used a regional datum to make an accurate interpretation of the stratigraphy for this formation. This marker corresponds to a siltstone bed represented by a GR peak above a coarsening-upward section between the lower Mancos Formation and the underlying Dakota Formation (Figure 3A). This is a regionally persistent marker that occurs above the Dakota Formation and has been historically used by other researchers (McPherson et al., 2006, 2008).

The selected datum was identified and correlated regionally in each of the 48 well logs (Figure 2). We interpreted the regional surfaces (K1 and K2 unconformities) in the well logs and use them to generate structure-contour and isopach maps (Figure 3b) to make interpretations about the thickness variations.

Architectural elements

Architectural elements in fluvial deposits contain a hierarchy of depositional elements that range in scale from individual lamina to basin-scale composite sequences. The small- to intermediate-scale elements (bars, bar sets, and channel fills) are influenced by autogenic processes such as channel avulsion or local base-level changes, which formed during short and intermediate time periods. We defined architectural elements by their sedimentologic and geomorphologic characteristics. The large-scale architectural elements (sequences and composite sequences) extended across the depositional basin are the result of accumulation over several million years (Patterson et al., 2012). Based on the lithofacies and morphological characteristics, we established facies associations and architectural elements within two categories for confined-flow elements and unconfined-flow elements. The unconfined-flow elements correspond to floodplain deposits, whereas the confined-flow elements correspond to bars, channels fill, and amalgamated and non amalgamated channel-complex deposits. The combination of field observations with digital-outcrop models allowed us to classify architectural elements through the recognition of distinctive assemblages of lithofacies, lower and upper bounding surfaces, internal geometries, and thicknesses (Miall, 1988). Sandstone bars and bar sets were defined as small-scale elements, whereas channel-fill de- posits were defined as intermediate-scale elements, and channel complexes, sequences, sequence sets, and composite sequences were defined as large-scale elements (Table 1) (Patterson et al., 2012).

To map and interpret the architectural elements, 3D digital outcrop models were generated for the six outcrop localities: Mack Ridge, Whitewater, Deer Creek, Escalante North, Escalante, and Rattlesnake Canyons. The outcrops are oriented approximately perpendicular to the paleoflow direction (~120°–190°) of the fluvial system. We collected high-resolution photographs using a DJI Phantom 3 Professional drone (UAS) with a mounted digital camera equipped with an f/2.8 lens and a 94° field of view. Images were acquired from distances that ranged from 165 to –490 ft (50 to 150 m) from the outcrop to capture the small- and large-scale features (Tellez and Pranter, 2016).

We used the collected UAS-derived images to generate 3D georeferenced point-cloud models with texture (digital outcrop models). The points were defined by the x, y, and z coordinates to represent the external surface of the outcrop face. The high-precision (0.6 ft [0.2 m]) digital elevation models represent outcrop faces that are constrained by ground-point measurements. UAS flights included at least a 70% aerial overlap to avoid data gaps and the generation of data holes before rendering the models. The digital outcrop models cover a lateral distance of approximately 41,650 ft (12,700 m).

The digital outcrop models exhibit texture and color characteristics from the imagery, resulting in high-resolution mosaics. We combined field observations and digital outcrop models to identify key stratigraphic surfaces, measure dimensions (apparent width and thickness), and identify how architectural elements vary stratigraphically. I used the distance between sandstone-element terminations as the "apparent width" in the model interpretations. The apparent width of sandstone elements in the outcrop depends on (1) the preservation of the sandstone element at the time of deposition, (2) the orientation of the sandstone element with respect to the outcrop exposure, and (3) the degree of material that has been eroded. Thus, the apparent width of a

sandstone element does not precisely represent the actual width or length of the element. However, these sets of measurements are valuable for limiting the range of values to reduce uncertainty in estimating the sandstone element's actual dimensions (Pranter et al., 2009)

To build the digital outcrop models, we used Pix4Dmapper to measure the sandstone dimensions and interpret the key surfaces. Each digital outcrop model was georeferenced and used to interpret the top of the Burro Canyon and the Morrison Formations (the K1 and K2 unconformities) that correspond to the top and base of the sequence, respectively. We identify scour surfaces within the ACC and NACC elements to define their boundaries. Isolated channel-fill elements were easy to identify within mudstone-prone intervals, due to the color contrast observed on the 3D reconstructions. The interpretation of georeferenced polygons on the models was used to measure the thickness and lateral extent of small- and large-scale architectural elements. Therefore, we recognized relevant changes in the architectural element distribution and thickness within the section.

Sequence stratigraphy

We developed a sequence stratigraphic framework based on the hierarchical description of alluvial strata following the methodology proposed by Sprague et al. (2002) and Patterson et al. (2003) (Figure 5). This hierarchical approach relates facies successions and their stratal bounding surfaces. For the Burro Canyon Formation, the sequence stratigraphic interpretation was made as follows: (1) description of alluvial stratigraphy based on the physical characteristics of the strata, (2) delineation of stratal surfaces bounding sedimentary units, (3) definition of alluvial strata and their coeval floodplain strata, (4) sequence definition considering if sequences exhibit a characteristic stacking pattern and define a conformable succession of genetically

related strata bounded by erosive surfaces, and (5) interpretation of the defined hierarchical elements and sequences.

To identify the K1 and K2 unconformities, we used the description and observations from the Mitchell Energy 8-1 Federal core (API 05-077-08026) along with the well log profiles for the GR, density, and resistivity logs. The K1 unconformity in the outcrop marks the change between the light basal conglomerates of the Burro Canyon Formation and the variegated paleosols and mudstones of the Morrison Formation. In the well logs, the GR signature shows a strong contrast from high GR values of mudstones in the Morrison Formations to cleaner GR values of conglomerates in the Burro Canyon Formation. The K2 unconformity was recognized in the outcrop considering (1) the change from noncalcareous to calcareous deposits from the Burro Canyon to the Dakota Formations and (2) the transition to carbonaceous mudstones within the Dakota Formation. Well correlation of the K2 interval was constrained using an intra-Mancos siltstone datum used successfully in previous publications (McPherson et al., 2006, 2008). Additionally, the response of the density and resistivity well logs was used to recognize changes from the calcareous and carbonaceous Dakota Formation to the noncalcareous and non carbonaceous strata of the Burro Canyon Formation.

Results

Lithofacies

The outcrops of the Burro Canyon Formation are generally dominated by trough cross-stratified sandstones and structureless sandstones at all locations; however, lateral variations occur. The floodplain deposits tend to be slope-forming and significantly contrast with the cliff-prone sandstone deposits.

We defined seven lithofacies in the Burro Canyon Formation: (1) trough cross-stratified conglomerate (Gt), (2) laminated siltstone-mudstone (FI), (3) low angle cross-stratified sandstone (SI), (4) trough cross stratified sandstone (St), (5) structureless sandstone (Sm), (6) horizontally stratified sandstone (Sh), and (7) structureless mudstone-siltstone (Fm) (Figure 6) (Table 2).

Facies associations

We group the defined lithofacies into three groups of genetically related facies associations. These facies associations allow for the description and characterization of the system in terms of its architectural elements. The facies associations are (1) coarse sandy bar, (2) sandy bar, and (3) floodplain mudstone.

Coarse sandy-bar facies

This facies association consists of fining upward packages with a predominance of cross-stratified conglomerate (Gt) fining upward to coarse sandstone (St) with trough cross-stratification and later to low angle cross-stratified sandstone (SI). The thickness of these bar sets varies from 2 to 5 ft (0.6 to 1.5 m). From base to top, coarse sandy-bar facies exhibit a scour surface on top of floodplain deposits, mud-chip clasts dispersed within the sequence, a coarse lag deposit composed of pebbles and cobbles with trough sets that become thinner and low angle to horizontally stratified toward the top.

Sandy-bar facies

The sandy-bar facies consist of very coarse to coarse-grained, cross-stratified sandstone at the base transitioning upward into medium- to fine-grained, horizontally stratified sandstone at

the top. The thickness varies from 1 to 3 ft (0.3 to 0.9 m), and it occasionally exhibits thin mudstone deposits throughout the bar sequences and minor conglomeratic sandstones (Gt) at the base.

Floodplain facies

This facies association consists of green to red, fissile, thinly laminated mudstones, silicified due to pedogenic processes and/or minor burrowing. These deposits do not have discrete boundaries, are laminated with non silicified siltstones, and exist as a fined -grained matrix in channel deposits.

Fluvial architecture

Architectural elements

The definition of architectural elements followed a hierarchy of fluvial strata similar to that defined by Patterson et al. (2010) (Figure 5; Table 1). The methodology defines elements based on their physical appearance and bounding surfaces. The hierarchy of small-scale elements extents from the lamina and lamina-set deposits that formed locally during relatively short time periods. These small-scale elements occur within intermediate- scale elements that were developed over large areas and longer time periods. Large-scale elements correspond to sequences composed of intermediate-scale elements that accumulated across the basin over millions of years (Patterson et al., 2012). We classified the small-scale architectural elements as bars and bar sets, and we divided the intermediate-scale architectural elements in (1) channel fill and (2) floodplain, whereas we described one large-scale element composed of one single sequence of deposition. definition of architectural elements follows a hierarchy of fluvial strata similar to the defined by Patterson et al., (2010) (Table 1). Therefore, the small-scale hierarchical

elements constitute the intermediate and large-scale elements within the fluvial system. We described the small-scale architectural elements as bars and bar sets. The intermediate-scale architectural elements were divided in: 1) channel fill and 2) floodplain, and the large-scale depositional elements are described as one single sequence of deposition.

Bars and bar sets

Bar and bar-set elements are composed of coarse sandy and sandy facies associations with an average thickness of 1–2 ft (0.3–0.6 m). In the core, these elements are vertically stacked within the lower part of the cored section (~70 ft; 20 m) (Figure 7). Two types of bars are identified on the outcrop: (1) lateral- accretion bars and (2) downstream accretion bars (Figure 8A and 8B). Lateral-accretion bar and bar sets are mostly composed of tan to white, moderately sorted, fining upward, trough cross-stratified sandstone with subrounded and subangular grains. These elements stack laterally and exhibit interbeds of mudstone and siltstone. In contrast, downstream accretion bars stack vertically following the paleoflow direction (mean ~55° azimuth). These deposits exhibit poorly sorted clasts (mainly pebbles) at the bottom changing upward to medium to coarse sandstone. In the outcrop, bar and bar sets show a sigmoidal geometry that varies depending on the stacking direction. Stacked bar and bar sets have cylinder-shaped GR profiles (signatures) and may have composite thicknesses of up to 55 ft (19 m). In contrast, a bell-shape signature is observed when bar sets form isolated channel-fill elements that are 5–10 ft (1.5–3 m) thick.

Channel-fill

Channel fills are composed of coarse sandy bar-set facies associations conformably stacked laterally and vertically within the extensions of a channel scour. These elements consist

of fining upward packages with a predominance of medium- to fine-grain sandstones with low angle to horizontal cross stratification (SI). Channel-fill elements are bounded at their base by erosional scour surfaces and contain rip-up clast within a thin layer of very coarse sandstone at the base. Occasional thin-layer mudstone (FI) remnants of floodplain deposits form thin mudstone deposits at the base of this elements. The thickness varies from 5 to 10 ft (1.5 to 3 m), and the width ranges from 137 to 380 ft (40 to 100 m). These deposits are embedded in floodplain deposits and are prominent along the transect within the upper Burro Canyon Formation.

Amalgamated and non-amalgamated channel complexes

These large elements consist of vertically and horizontally stacked sandstone-dominated channel-fill deposits. Typically, Amalgamated Channel Complex (ACC) elements exhibit coarse bars sandy facies association deposits at the base, grading upward to sandy bar facies. ACC elements within the Burro Canyon formation compose an overall fining upward sequence with a lack of floodplain deposits similar to the low sinuosity channels upstream deposits described by Patterson et al., (2012) within a braided fluvial system. Dimensions of ACC elements range from 20-55 ft (6-20 m) in thickness and have average apparent width of ~1500 ft (460 m). Multiple scour surfaces indicate lateral and vertical bounding of several bar-sets to form the channel complexes. These deposits, which are prominent in the lower interval of the Burro Canyon Formation near the erosional contact with the Morrison (K1 unconformity) exhibit an increase in thickness towards the Whitewater and Deer Creek Canyon areas, which is the main reason for the high net-to-gross ratio and thickness in these areas.

On contrast, Non-Amalgamated Channel Complex (NACC) elements have shorter lateral dimensions and are thinner. These elements contain an overall fining upward sequence composed of thin coarse sandy bar facies deposits at the base followed by laterally and vertically stacked sandy bar facies deposits overlain by floodplain deposits. Thickness for these elements, ranges from 7-30 ft (2-9 m) and apparent-width ranges of 450-790 ft (137-240 m). NACC are predominant in the Escalante, Escalante north, and Rattlesnake canyons mostly within the upper interval and occasionally the lower interval.

Floodplain

Floodplain deposits represent all the fine-grained lithologies related to the ancient fluvial system. In the Burro Canyon Formation these deposits are dominated by interbedded green and red mudstone with brown medium- to fine- grained, siltstone and gray to green mudstone deposited during intervals of flow regime changes. High gamma-ray response (> 250 cps in outcrop - >120 API in well logs) is a common characteristic of these deposits. However, floodplain deposits in well logs are often masked and hard to characterize. For analysis and interpretation over the three-dimensional outcrop reconstructions, parts of the covered intervals in the outcrop were assumed as floodplain deposits. These architectural elements do not have well defined geometries and morphologies and encase channel-fill deposits.

Depositional environment

Based on the results obtained from the combination of measured sections, UAS-based outcrop models, and well log data, we suggest that the depositional environment is a fluvial system dominated by straight to low sinuosity braided rivers. The relatively continuous exposure of the outcrop belt (8 mi–12.8 km) allowed us to interpret and correlate the major bounding

surfaces from canyon to canyon. These surfaces extend across the outcrops and often overlie thin mud drapes on top of the underlying elements. Surfaces that are not continuous represent smaller scale events within the system. Facies associations display similar paleocurrent orientations and internal bounding surfaces that extend from the base to the top of the bar-set elements. The stratification style of interbedded trough and low angle cross-beds within these fining upward sandstones, as well as the predominance of erosion surfaces, are characteristic of deposits of low to moderately sinuous rivers.

Evidence of braided fluvial systems comes from the internal architecture of the channel complex elements. The complex architectures of the bar and bar sets are due to downstream and oblique accretion produced during scour-fill cycles (Figure 8a). This architecture resembles modern braided systems regarding its internal structure and sedimentological characteristics (Miall, 1988; Holbrook et al., 2006; Lunt et al., 2013). Conversely, in a more sinuous fluvial system, bar and bar sets display oblique to lateral accretions typical of bars within the NACC and channel-fill elements (Figure 8b). These characteristics are commonly described within the upper interval of the Burro Canyon Formation and coincide with previous observations made by Young (1960) and Cole and Moore (1994, 2012).

Paleocurrent measurements from six outcrop locations (N = 586) (Figure 2) show consistency with the paleoflow directions to the southwest to northeast with larger azimuth ranges for measured values within the upper interval of the formation.

Minimum channel-depth estimations for the channel fill deposits within the braided system are complicated and often ambiguous due to the presence of multiple channels. The measurement of the thickness does not consider intermittent channels that may be active only during high-discharge periods. In addition, the convergence of several channels that may produce

higher scouring resulting in anomalous thickness values (Miall, 1996). For this study, only channel-fill elements with clearly defined limits were traced and measured (N = 413) with a reasonable degree of confidence. Channel-fill dimensions measured from the upper section have an average apparent thickness value of 8.5 ft (2.6 m) and an average apparent width of 160 ft (49 m). For the lower interval, these values are 18 ft (5.5 m) and 361 ft (110 m), respectively (Figure 9).

Sequence stratigraphy

Sequence bounding unconformities

Two fundamental sequence boundaries were defined to recognize the hierarchy of architectural elements in the Burro Canyon Formation. We define the base of the alluvial sequence overlying the K1 regional unconformity previously documented by several authors (Young, 1960, 1973; Aubrey, 1986, Aubrey and Skipp, 1992; Currie, 1993, 1994, 1997; Currie et al., 2002; Cole and Moore, 2012) and found within the study area. The K1 unconformity in the outcrop marks the change between the light basal conglomerates of the Burro Canyon Formation and the variegated paleosols and mudstones of the Brushy Basin member of the Morrison Formation. Above the K1 surface, an abrupt increase in sandstone amalgamation, grain size, and composition from the underlying Morrison Formation is noticeable. In well logs, the GR signature shows a strong contrast from high GR values of mudstone lithologies in the Morrison Formations to cleaner GR lectures from the basal conglomerates in the Burro Canyon Formation.

The top of the sequence is defined by the K2 unconformity. We recognize this surface in the outcrop with a change in the calcareous and carbonaceous content of the section. The Burro

Canyon Formation is mostly composed of noncalcareous deposits, whereas the Dakota Formation exhibits a higher fraction of calcareous cemented deposits and carbonaceous mudstones. The well correlation of the K2 unconformity helps to characterize the widespread and low relief of the surface (Figure 3a).

Sequence stratigraphic model

Alluvial continental settings are highly influenced by allogenic factors such as climate, tectonism, and sediment supply; and they are less influenced by absolute sea-level changes (Shanley and McCabe, 1994; Miall, 1996). We consider that the deposition of the Burro Canyon Formation represents multiple fluvial events controlled by the interplay between the (1) accommodation space and (2) sediment supply in the fluvial system that formed a sequence as a result of three main stages of base-level change: (1) base-level fall, (2) early baselevel rise, and (3) late base-level rise as suggested by Catuneanu et al. (2008) and Shanley and McCabe (1994) (Figures 10 and 14).

We describe the three stages for the deposition of the Burro Canyon Formation in the southwestern Piceance Basin. Stage 1 (Figure 10a and 10d) is identified in the K1 unconformity. The surface exhibits erosion and widespread incision of the underlying Morrison Formation across the outcrop belt in western Colorado. The K1 unconformity is a traceable surface in outcrop and well logs that exhibits a concave-up geometry across the study area (Figure 3a). The preexisting fluvial surface was abandoned, and the interfluve locations were eroded (Figure 14a). The resulted erosion surface was documented before and represents at least 20 My of absent geologic record (Roca and Nadon, 2007).

The second stage of deposition corresponds to the transition from early to late rise of base-level (Figure 10b) that filled up the accommodation space and concentrated the deposition of the fluvial system within the valley margins. Early Cretaceous rocks with coarse material formed the basal deposits of the Burro Canyon Formation. Straight and braided fluvial streams deposited channel-fill elements stacked vertically and horizontally to form large-scale ACC elements (Figure 14b). Poorly preserved floodplain deposits and high-energy fluvial deposits (Figure 8a) dominated the environment during this time of deposition.

The late base-level rise marks the third and last stage of the deposition (Figure 10c and 10e). The rise of the base level produced deposits that reflect a change of the fluvial style in the system from straight to low to-moderate sinuosity channels. Sandstone deposits are often NACC elements (Figure 14c) that vertically transition to isolated, narrow, and relatively thin channel fill elements embedded within mudstones of preserved floodplains deposits (Figure 14d).

The resulting architecture represents one stratigraphic sequence that displays an overall fining upward trend bounded at the base and top by the K1 and K2 unconformities, respectively. Above the K2 unconformity, the sequence is overlaid by rocks of the Dakota Formation that exhibit a paludal, estuarine, and shallow marine influence.

Discussion

Lithofacies and sedimentary structures

The lithofacies found within the Burro Canyon Formation are composed of conglomeratic to coarse sandstones grading from fine- to medium-grained sandstones with high- and low angle cross-stratification as well as horizontal bedding. The fractions of laminated

structureless mudstones and siltstones are variable within the formation. Sandy and coarse sandy bar sets exhibit arrays of coarse-grained lithofacies. The base of the bar sets contains lag deposits with cobble-pebble well cemented conglomeratic sandstones, topped with stacked fine-grained sandstone lithofacies. These deposits are characteristic of braided and low to moderate sinuous fluvial channels, whereas fine-grained lithologies resulted from lateral migration of the streams. The high fraction of fine-grained lithologies occurred in stages of a less steep profile during the evolution of the fluvial system that allowed for the preservation of floodplain deposits.

Paleocurrent data confirmed a southwest paleoflow direction previously documented by Young (1960), De- Celles et al. (1983), Currie (1993), and Cole and Moore (2012). Measurements from the lower interval of the ACC elements have azimuthal ranges of approximately 40°–50°, whereas the upper NACC elements have a larger range of approximately 30°–70° (Figure 2). The sedimentary structures described within the upper and lower Burro Canyon Formation and the statistical sandstone body measurements suggest a change in the fluvial style. The lower interval characteristics correspond to straight and low sinuosity channels (Figure 8a), whereas the upper interval represents low to moderate-sinuosity channels (Figure 8b).

Fluvial architecture

The Burro Canyon Formation contains hierarchical elements that allowed us to use the methodology proposed by Patterson et al. (2002) to define a hierarchical sequence stratigraphic framework. The stratigraphic sequence consists of a sandstone-rich lower interval composed of vertically stacked downstream bar-set elements. In contrast, the upper interval is mudstone prone and composed of a mixture of lateral and downstream accreted bars and floodplain deposits. The statistical measurements of apparent thickness and width of the sandstone bodies show an overall

decrease from the base to the top of the sequence and reflect the lateral continuity and variable net-to-gross sandstone within the stratigraphic section (Figure 9).

The lower Burro Canyon Formation rests on the K1 unconformity and was deposited by braided fluvial streams. The deposits exhibit multiple accreted bars and bar sets with high-angle cross-stratification. Bar-set packages formed in up dip areas and are typical of midstream or bank-attached deposits within single-thread streams where deposition occurred during high-energy, possibly shallow discharge events in the fluvial system (Miall, 1977, 1988). The lower interval is composed of laterally continuous sandstones with an average apparent width of 18 ft (5.5 m) and an average thickness of 362 ft (110 m) (Figure 9c). Multiple events are stacked on top of each other within the braid-plain, forming ACC elements that contain a high degree of internal complexity and display multiple fining upward successions and scour surfaces. These elements, which occur across the study area, have characteristics indicative of limited accommodation space as is typical of incised valley fills. The thickness and continuity in the lower interval of the Burro Canyon Formation suggest that sediment supply was constant and allowed for the deposition of thick packages of coarse sandy bar facies deposits. Statistical dimensions of channel-fill elements exhibit larger width and thickness values within the lower section often resulting in a high net-to-gross ratio within the formation (Figure 9).

The upper Burro Canyon Formation contains downstream bar sets at the base of the channel fill and NACC elements. Measurements of sandstone body dimensions in the interval average 160 ft (48 m) width and 8.5 ft (2.6 m) thick (Figure 9b). The architecture of the interval is dominated by isolated channel fill and NACC elements embedded in floodplain deposits. We relate the smaller amounts of sandstone deposits within the interval to the interplay of low

sediment supply relative to the accommodation space in a gentle slope gradient that decreased aggradation while enhancing the preservation of floodplain deposits.

Fluvial stratigraphy

The Burro Canyon Formation represents one stratigraphic sequence deposited during the Aptian-Albian

time. The sequence is clearly limited by two sequence boundaries (K1 and K2 unconformities) previously documented by Currie (1997) and Cole and Moore (2012) and described within the study area. The sequence exhibits three characteristic stages of deposition similar to those described by Catuneanu et al. (2008): (1) degradational, (2) transitional, and (3) aggradational.

Stage 1 represents a change in the basin configuration produced by the Sevier Thrust Belt uplift. A basin-wide erosion and widespread incision of the forebulge uplifted areas in Utah and western Colorado (DeCelles and Currie, 1996; Currie, 1997, 2002) generated a type 1 sequence bounding unconformity (K1). The K1 unconformity developed due to restricted accommodation space and widespread erosion into the underlying Morrison Formation producing an incised valley (Figure 14a). In the meantime, flexural subsidence of the foredeep depozone increased the accommodation space in west-central and northern Utah (Currie, 1997) (Figure 4).

Stage 2 was the system transition from degradational to aggradational

(Figure 14b). The accommodation space generated in the forebulge depozones was filled up with coarse material concentrated within the limits of the incised valley with a poor preservation of floodplain and paleosoil deposits due to lateral migration, aggradation, and limited accommodation space relative to sediment supply (Figure 10b).

Stage 3 represents the late rise and higher base level due mainly to the flooding of the Western Interior seaway. The resulting fluvial system deposits reflect a late base-level rise with

deposition of NACC (Figure 14c) and a stage of the higher base level that shows the aggradation of isolated channels encased within floodplain deposits and truncated at the top by the K2 unconformity and overlaid by fluvial deposits of the Dakota Formation (Figure 14d). The K2 unconformity was formed due to a decrease in the accommodation space relative to the sediment supply at the end of the higher stage of aggradation. It changed the amalgamation in the system and produced widespread and shallow erosion of the preexisting deposits of the Burro Canyon Formation. The sequence is capped by the K2 unconformity classified by Currie (1997) as a type 2 unconformity and confirmed with the observation in this research due to the widespread but shallow nature of the erosion displayed in the outcrops without producing an incised valley. The interpreted sequence is overlaid by rocks of the Dakota Formation that show ripples, carbonaceous, and calcareous deposits that suggest a stronger marine influence and represent the flooding of the Western Interior Seaway (Young, 1960, 1970; Kirkwood, 1976).

The tectonic evolution and geometry of the foreland basin controlled the deposition and thickness of the Early Cretaceous rocks as reported by Currie (1997). Our results indicate a similar control for the Burro Canyon Formation. The stratigraphic sequence displays the effects of forebulge uplifting and flexural subsidence that created foredeep depozones. Erosional and depositional events favored the development of local areas for deposition of thicker intervals (Figures 11 and 12) resulting in lateral changes within the architecture of the fluvial system. The study area isopach map (Figure 4) confirms the regional thickness trends in the Cretaceous strata (Young, 1970, 1975; Currie et al., 2002) within the study area. Overall, the formation displays a local thinning to the west (Utah-Colorado limit) in the forebulge uplift zone and a thicker section in the forebulge depozone similar to that described by Currie et al. (1997) (Figure 4).

The thickness decrease of the Burro Canyon sequence is well documented in the Mack Ridge outcrop reconstruction and measured section. In contrast, a significant thickening of the formation is mapped south of Grand Junction in the central area (Whitewater and Deer Creek Canyons, Figure 11a and 11b) similar to the stratigraphic profile documented by Currie et al. (2002) (Figure 4). We interpret the thickening of the zone as a result of a paleovalley axis within the fluvial system (Figures 3 and 4). The eastern region of the study area over the Escalante and Rattlesnake canyons (Figures 12 and 13) exhibits a slight thickness decrease that suggest a more restricted accommodation space relative to the sediment supply in that area at the time of deposition. Regional changes in the formation thickness are also depicted perpendicular to the paleoflow direction well cross sections (Figure 3a and 3b). The combination of outcrop reconstruction, well sections, and isopach and structural maps indicates that the K1 unconformity has greater relief (more incision) than the K2 unconformity. The concave-up geometry of this surface (Figure 3a and 3b) supports the interpretation of an incised valley. The thicker measured section within the outcrop belt is interpreted in the Whitewater canyon (Figure 11), whereas the thinner section is shown in the Mack Ridge area (Figures 13). We suggest a schematic interpretation of the suggested paleogeographical positions for the outcrop locations within the fluvial system to illustrate the changes in thickness across the study area (Figure 14).

Conclusions

This research evaluated the sequence stratigraphic framework of the Burro Canyon Formation based on UAS-based outcrop models, well log data, fieldwork observations, and the definition of hierarchical elements. Two intermediate-scale architectural elements were defined, channel fill and floodplain, and compose larger scale architectural elements such us channel complex (amalgamated and nonamalgamated). One stratigraphic sequence was interpreted and

characterized in terms of tectonics, climate, and base-level changes that influenced the (1) accommodation space and (2) sediment supply. The interplay of these variables resulted in a fluvial architecture composed of a single stratigraphic sequence that was traced along the study area and subdivided into a lower interval (transitional) and an upper interval (aggradational). The sequence boundaries defined within this framework are traceable across the entire study area where the basal unconformity corresponds to a type 1 sequence formed by a reduction in accommodation space and representing an incised valley, whereas the top of the sequence corresponds to a type 2 unconformity formed in a period of minor reduction in the accommodation space relative to the sediment supply of a nonmarine depositional setting.

The lower interval of the sequence is composed of coarse-grained deposits that formed laterally extensive ACC elements with the thickness ranging between 10 and 55 ft (3 and 20 m) and an average apparent width of approximately 1500 ft (460 m) within the incised valley. The upper interval displays a change from laterally continuous braided channels to low to -moderate sinuous to anastomosing NACC elements with thicknesses ranging between 7 and 30 ft (3 and 9 m) and apparent width ranges of 450–790 ft (137–240 m). The uppermost deposits within the sequence contain isolated sandstones with abundant fine-grained floodplain lithologies with thicknesses ranging between 5 and 10 ft (1.5 and 3m) and apparent width ranges of 137–380 ft (40–100m).

Fluvial sandstone bodies deposited during the lower interval of the sequence exhibit common amalgamation of channel-fill elements, whereas sandstones deposited in the upper interval show a decrease in amalgamation These observations are supported by the statistical measurements obtained from channels fills in the studied outcrops.

The approach used to address this study illustrated an efficient workflow to characterize large outcrop exposures. In this research, we examined a total of 8 mi (12.7 km) of outcrop exposure of the Burro Canyon Formation. The lateral information provided by our UASoutcrop reconstruction techniques offered key information about the architecture and lateral variability of sandstone-bodies that might have been missed using traditional outcrop and well log data.

Acknowledgments

Funding was provided through the Reservoir Characterization and Modeling Laboratory at the University of Oklahoma, COLCIENCIAS, and the Agencia Nacional de Hidrocarburos Scholarship. Additional funding was provided through the AAPG Foundation Grants-in-Aid (Jon R. Withrow Named Grant). Software was provided by Schlumberger (PETREL), Pix4D (Pix4Dmapper Pro) and Mirage Technologies (PointCloudViz plug-in), also to Unocal Corporation and lastly to Sarah Clark, Kelsey Lewis and Layne Hardisty for their valuable help during the fieldwork.

Figures

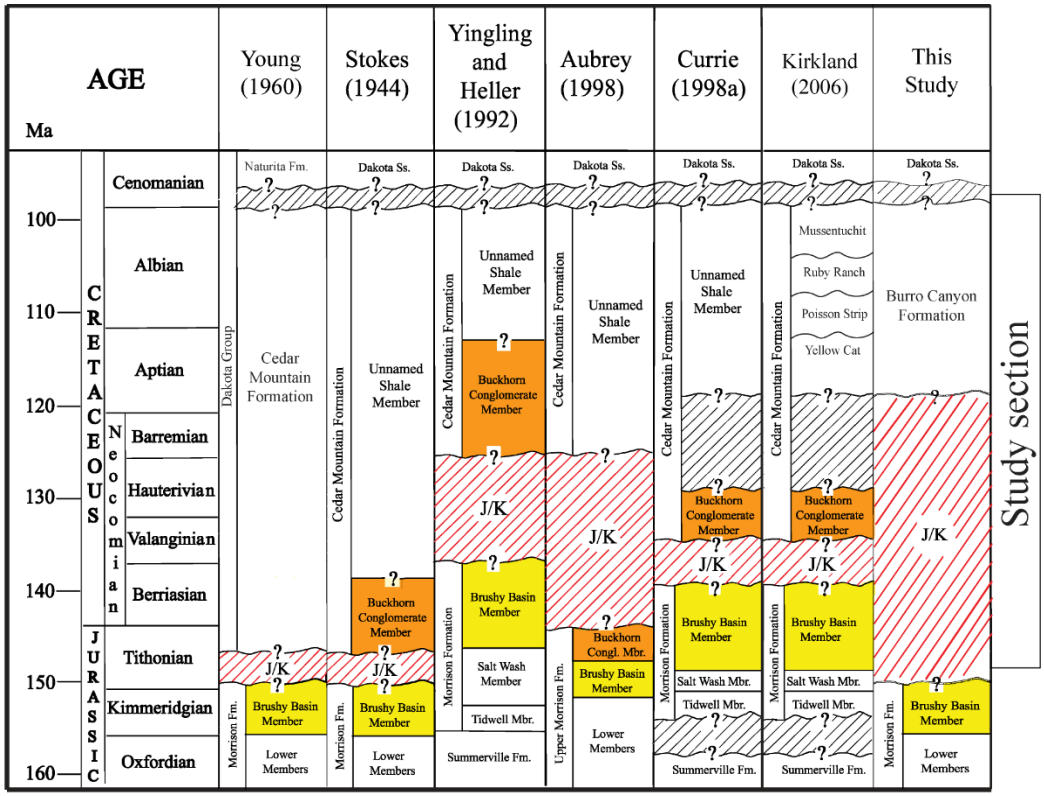

Figure 1-1: Early Cretaceous chronostratigraphic column in the Piceance and Uinta Basins showing terminology used by different authors. Within the study area, the Burro Canyon Formation is bounded by the K1 and K2 unconformities (hiatus periods). The Late Cretaceous Dakota Formation unconformably overlies the Burro Canyon Formation, and the Late Jurassic Morrison Formation unconformably underlies it. Modified after Roca and Nadon (2007).)

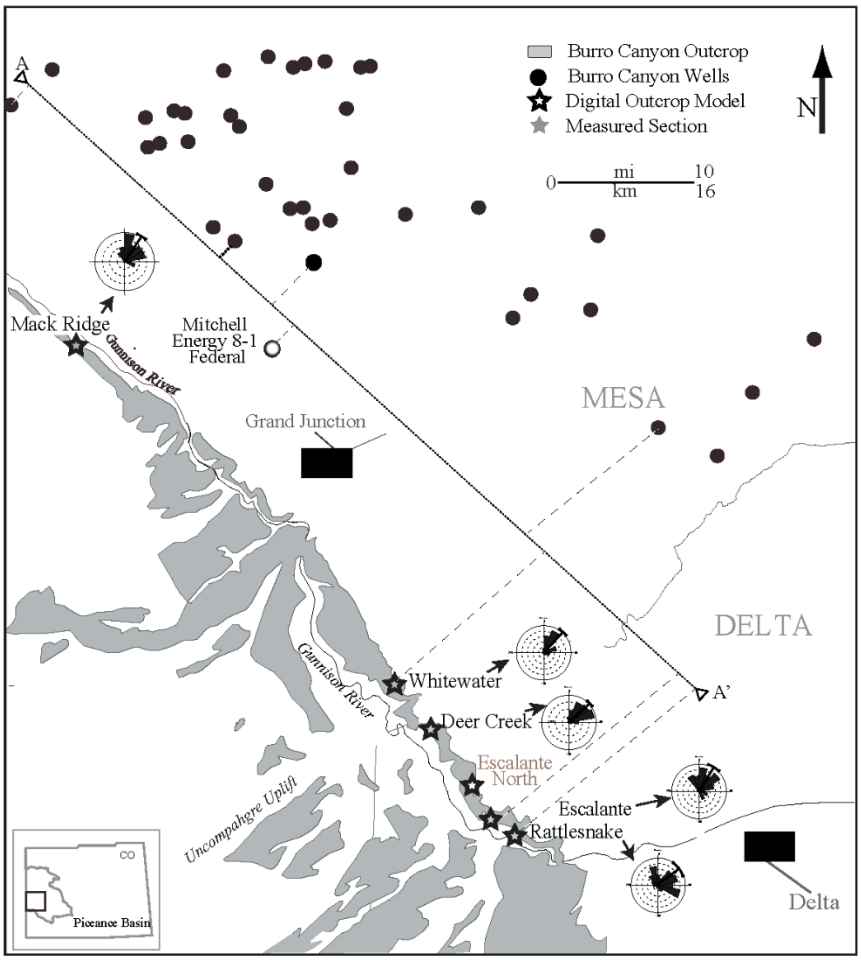

Figure 1-2: Location map for the study area. The outcrop belt extends from Mesa to Delta Counties, Colorado, and comprises a traverse from Mack Ridge to Rattlesnake Canyon. Cored data from the Mitchell Energy 8-1 Federal core (API 05-077-08026), in Mesa County, Colorado, is used as reference information in this study. The map shows locations with outcrop reconstructions, measured sections, and rose diagrams from paleocurrent measurements. The black dots represent 48 well logs used in this study. Section A-A′ is shown in Figure 3b. The light-gray color defines the outcrop distribution of the Burro Canyon Formation within western Colorado.

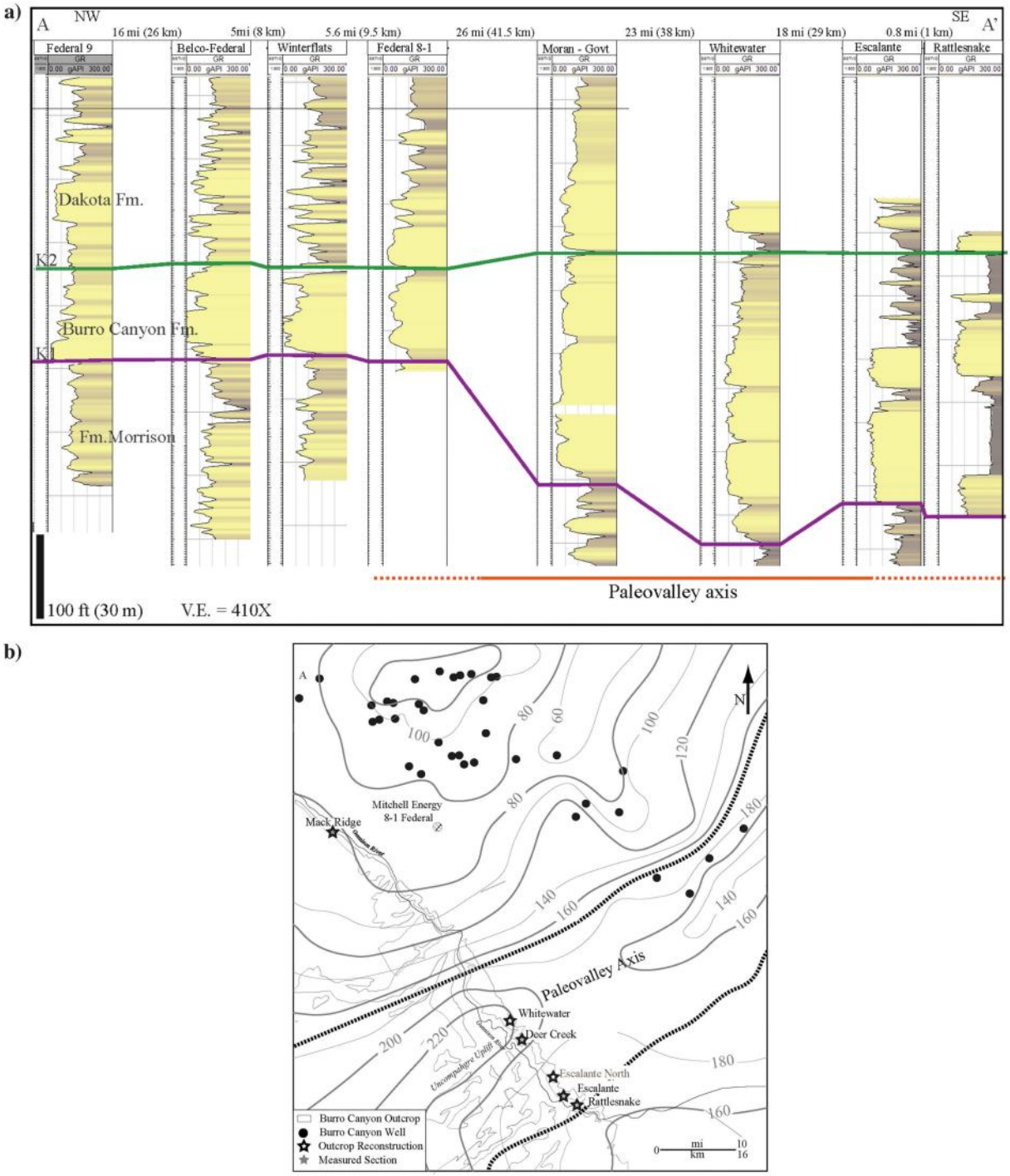

Figure 1-3: (a) Stratigraphic cross section perpendicular to the average paleocurrent direction using well log and outcrop GR data. Correlation of the top of the Burro Canyon and the top of the Morrison Formation was performed over 48 well logs available in the study area. A persistent GR deflection in the shallow marine lower Mancos Shale was used as a datum (the thin purple line). This cross section is flattened to this datum within the Mancos Formation easy to identify across the entire study area. The datum is shown in purple. The section shows the lateral variations in

thickness from northwest to southeast. The orange line below the section represents the interpreted limits of the paleovalley. The top of the K1 unconformity in purple was interpreted at the end of the mudstone-dominated section that represents the Morrison Formation. The top of the K2 unconformity in green was marked in the higher GR response after the sandstone-rich section of the Burro Canyon. The GR fill shows an approximation of the mudstone content. (b) Isochore map of the Burro Canyon Formation in the study area based on 48 well logs and measured sections from the outcrop belt. Contours show a depocenter toward the Whitewater section following the paleoflow trend southwest northeast. The estimated location of the paleovalley axis area is shown by the dashed-lines gray lines. The lateral variations observed along the outcrop belt indicate a decrease in thickness toward the northeast and an increase in the central area.

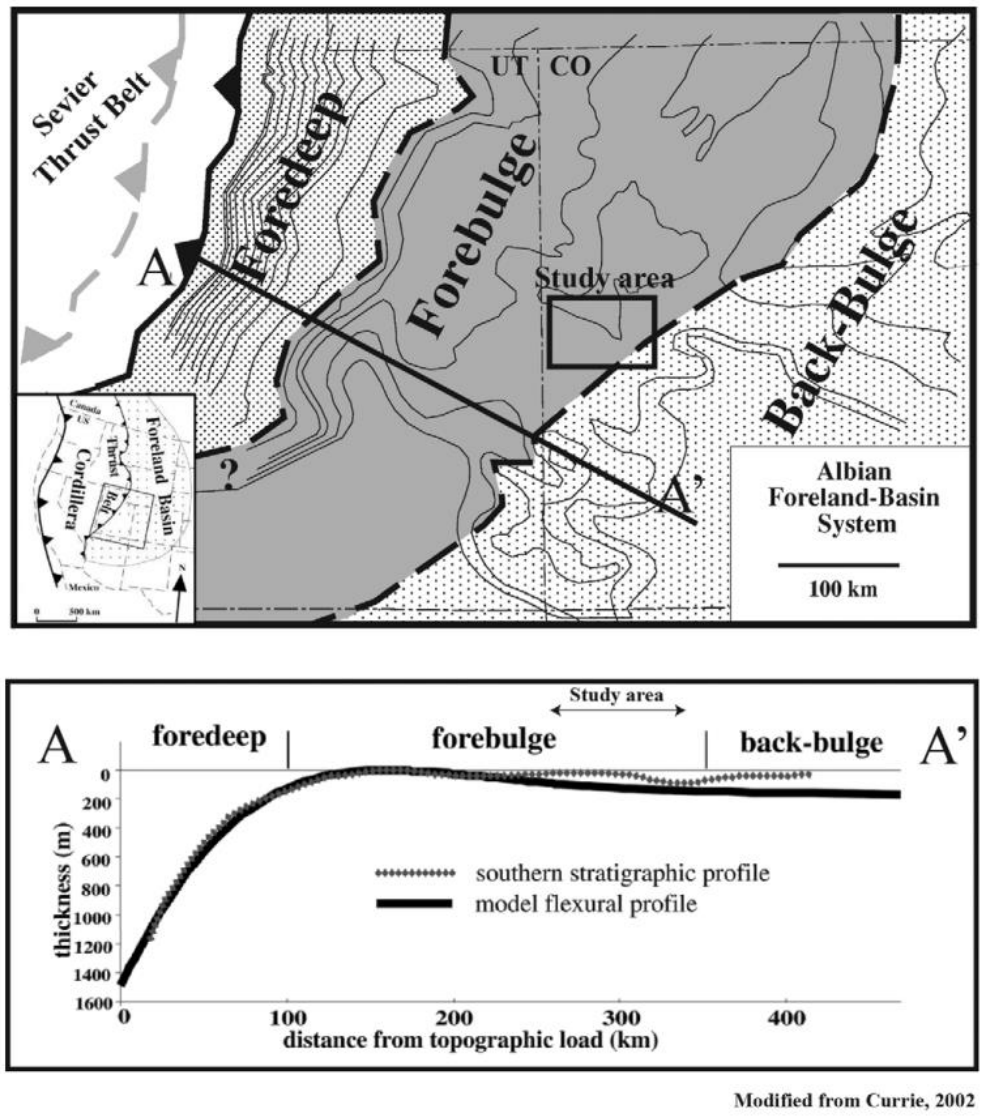

Figure 1-4: The upper figure shows a generalized paleogeographic map of the Sevier thrust belt and foreland-basin system in Utah and Colorado during Albian time. The dark barbed line corresponds to the estimated frontal position of the Sevier thrust belt. The gray barbed line represents the frontal position of the Sevier thrust belt during the Aptian. PT, Pavant Thrust; CRT, Canyon Range Thrust. The A-A′ line corresponds to the cross section below. The lower figure shows the model-generated foreland-basin flexural profile with the observed lower Cretaceous stratigraphic thickness along the transect A-A′ (modified from Currie, 2002).

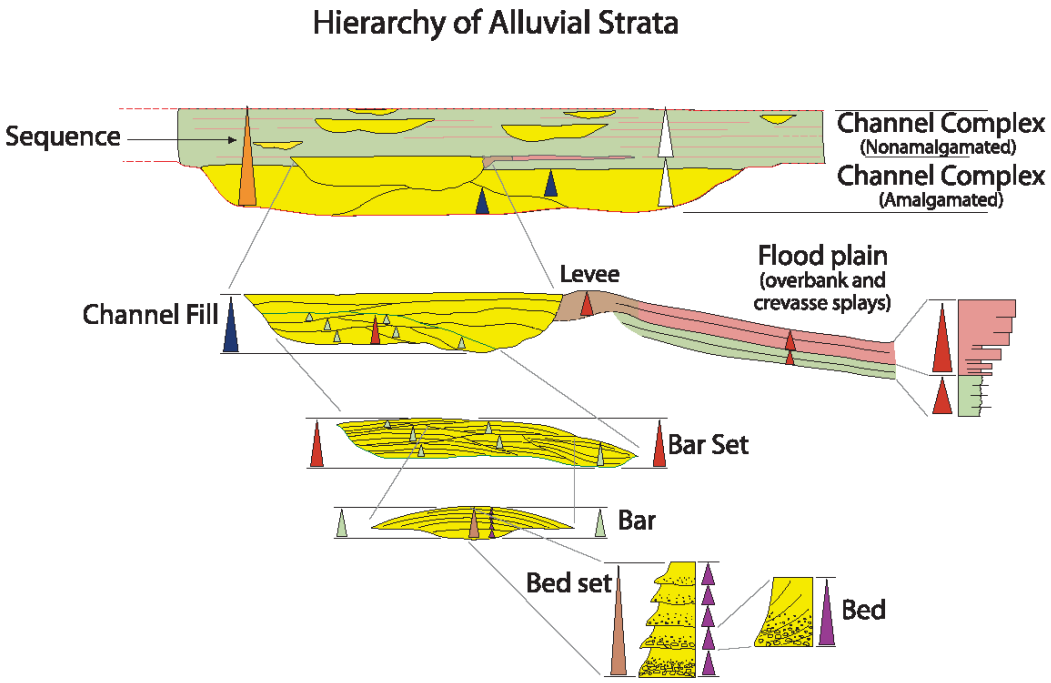

Figure 1-5: Idealized illustration of hierarchical architectural elements. Channel sandstones are shown in yellow, floodplain mudstones are shown in green, levee sandstones are in brown, and crevasse splays are in pink. Dashed-red lines indicate sequence sets, whereas continuous red lines indicate sequence boundaries. Colored triangles represent each hierarchical element. This methodology was used for small to intermediate-scale to large-scale hierarchical elements, such as bars and bar-sets, channel-fills, and channel complexes. From Patterson et al. (2010).

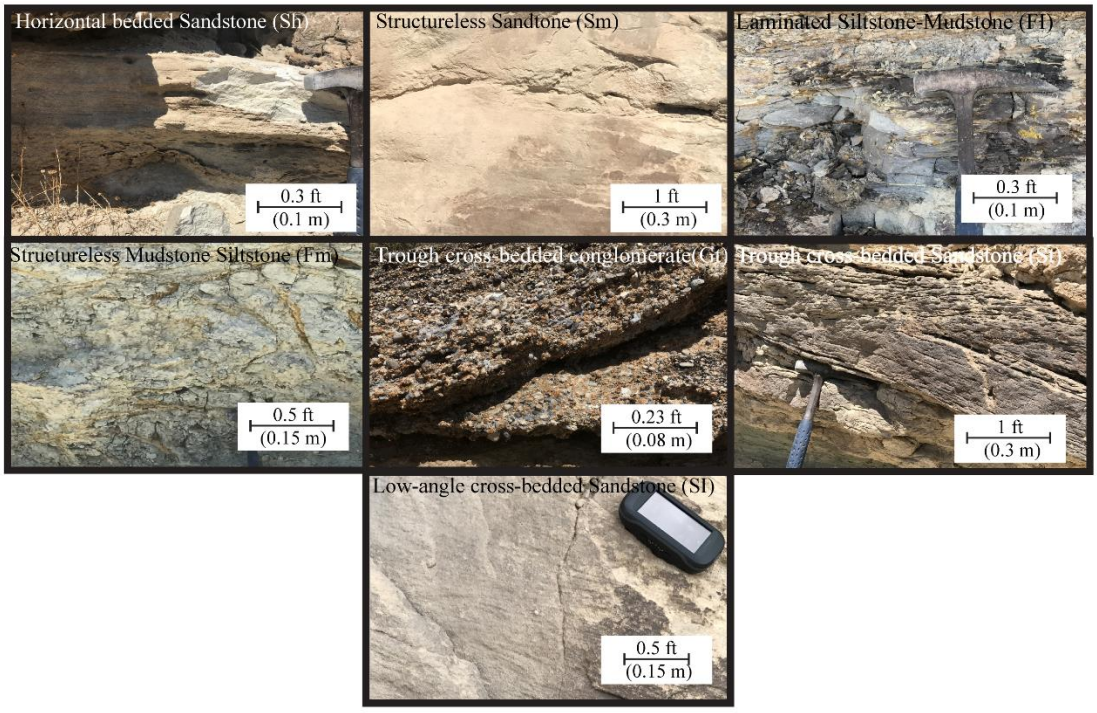

Figure 1-6: Key facies of the Burro Canyon Formation shown in outcrop. Horizontal bedded sandstone (Sh), structureless sandstone (Sm), laminated siltstone mudstone (FI), structureless mudstone siltstone (Fm), Trough cross-bedded conglomerate (Gt), Trough cross-bedded sandstone (St), and low angle cross-bedded sandstone (SI).

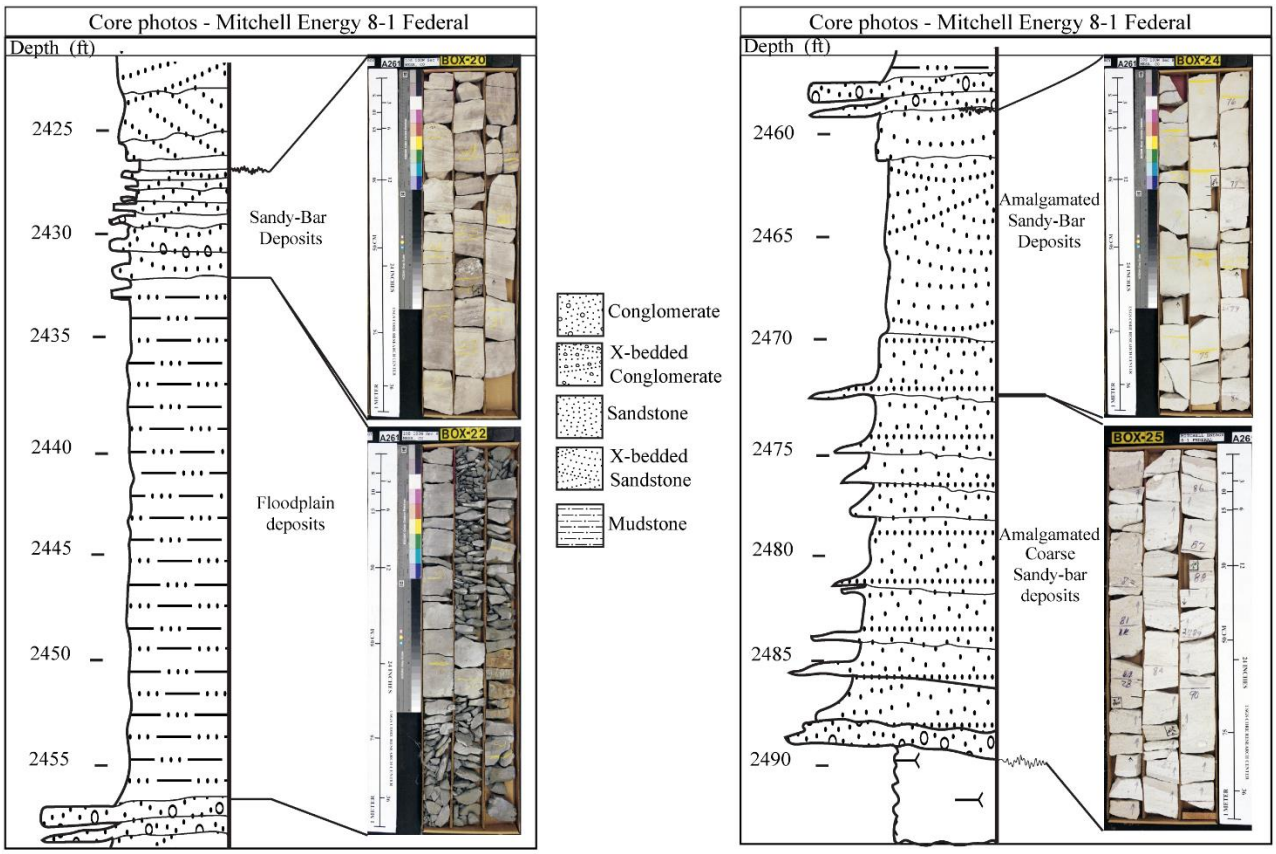

Figure 1-7: Photographs and the stratigraphic column for the Mitchell Energy 8-1 Federal core (API 05-077-08026), in Mesa County, Colorado, used as reference information in this study.

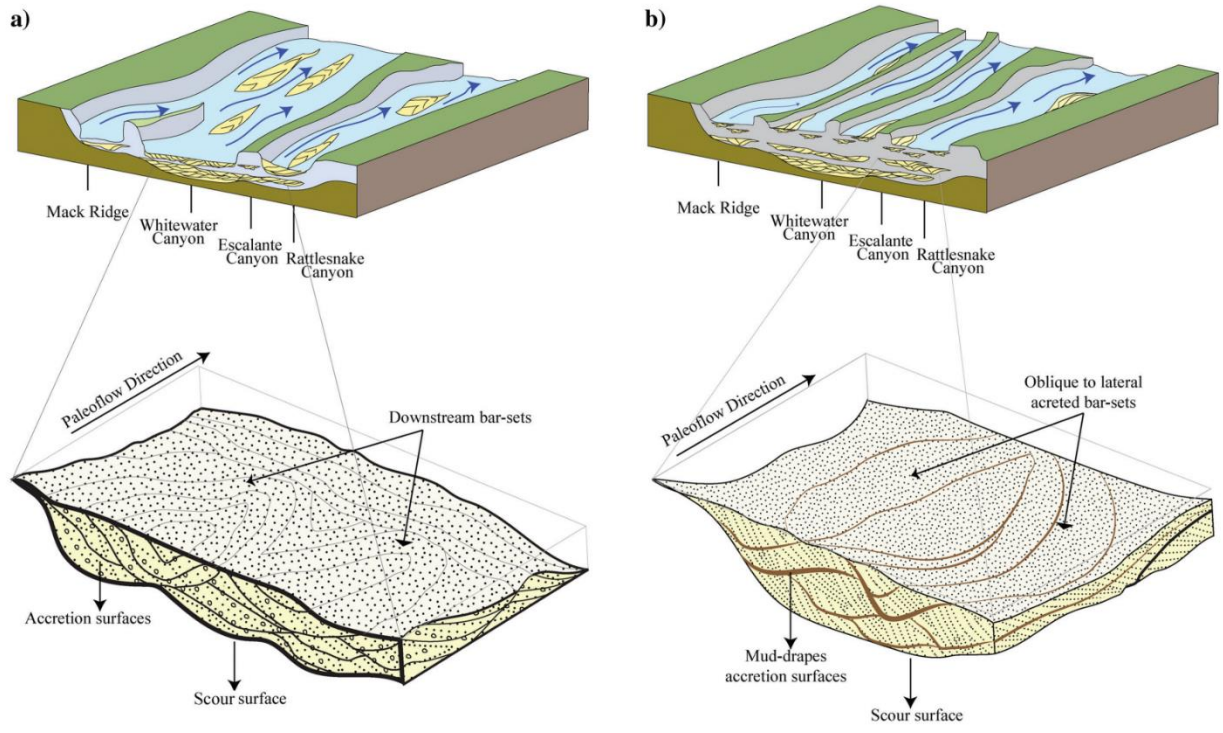

Figure 1-8: Schematic diagrams of the depositional environment and sandstone-bodies described within the lower and upper intervals of Burro Canyon Formation. (a) The lower interval of the Burro Canyon Formation is interpreted as being deposited by braided channel systems in response to low accommodation relative to sediment supply. This section exhibits ACC deposits with high net-to-gross ratios and large lateral extents. (b) The upper interval of the formation exhibits a mud-prone interval with isolated and non-amalgamated channel deposits encased in floodplain mudrocks.

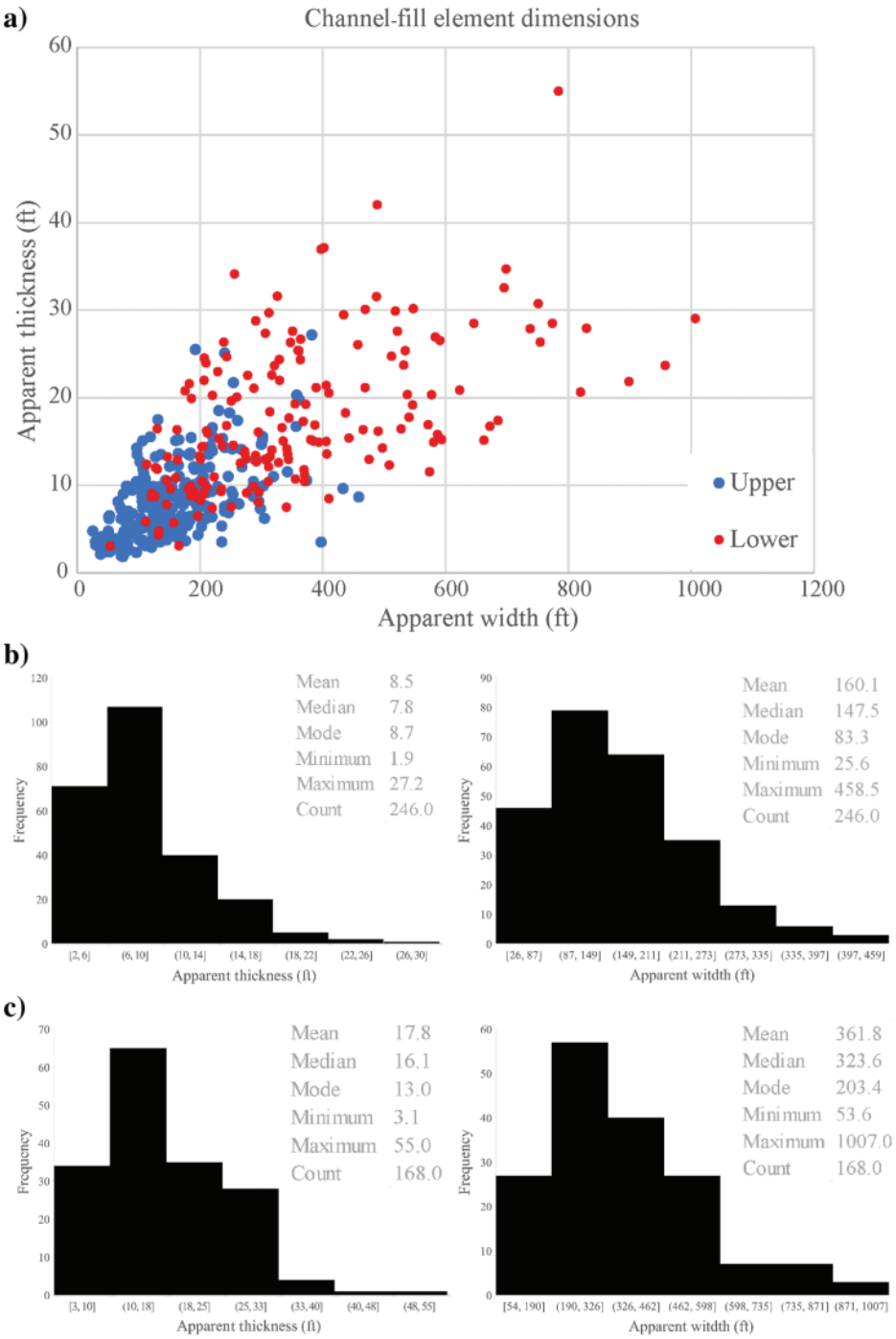

Figure 1-9: Statistics for sandstone body dimensions in the Burro Canyon Formation collected within the study area. (a) Cross-plot of the apparent width versus the apparent thickness for 414 channel-fill measurements. (b) Histograms for the apparent width and thickness values of the upper interval of the channel-fill elements. (c) Histogram for the apparent width and thickness values for the lower interval channel-fill elements.

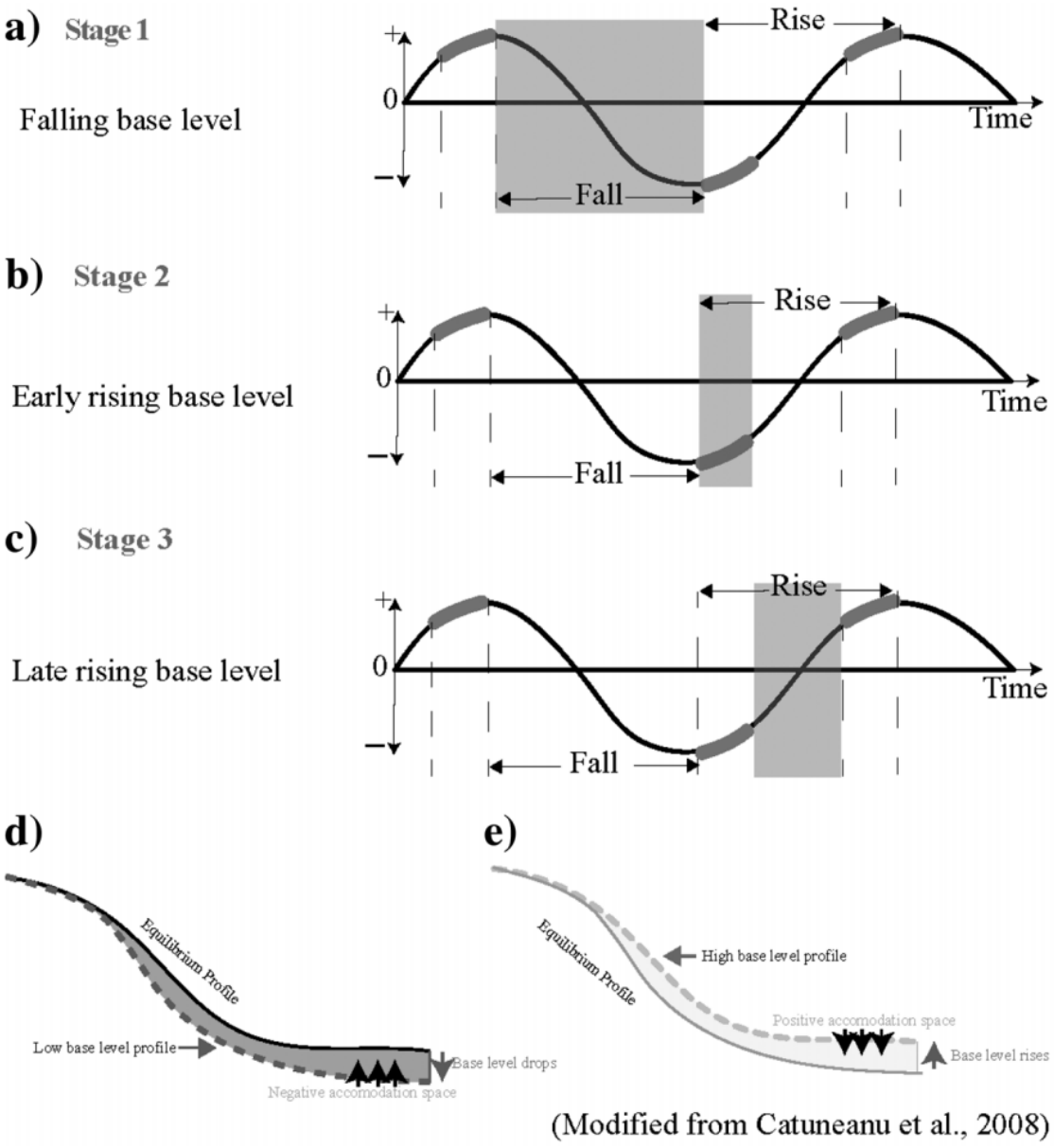

Figure 1-10: Schematic sea-level curves used as applied to the fluvial sequence stratigraphy. The sea-level curves in the gray square area are highlighted: (a) the base-level fall, (b) the slow start of the base-level rise, (c) the balance between the sediment supply and the accommodation space is reached at the late stage of base-level rise, (d) the negative accommodation space during a low base-level stage, and (e) the positive accommodation space during a high base-level stage.

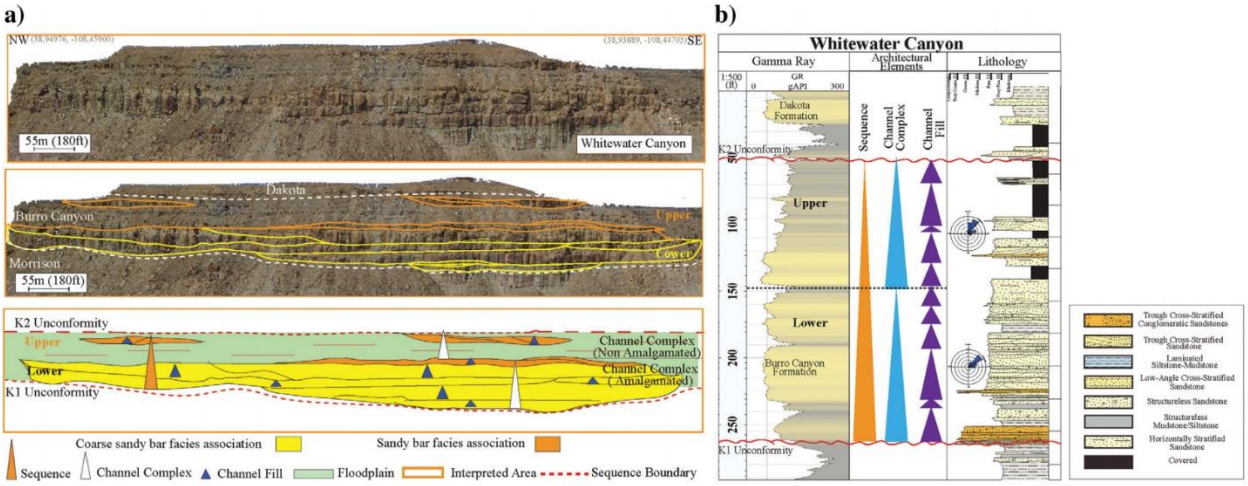

Figure 1-11: (a) The UAS-based photogrammetry model is shown in the top of the image in Whitewater location. The top and base of the Burro Canyon Formation (the K2 and K1 unconformities) are represented by red lines. The hierarchical interpretation of this outcrop shows non-amalgamated architectural elements in the upper section and ACC elements in the lower interval. The Model boundaries are shown as orange lines; the ACC elements and NACC and isolated channel-fill elements are shown in yellow. Floodplain deposits are shown in light green. Hierarchical elements are shown as triangles. This section exhibits an overall high net-to-gross ratio (0.8). This sandstone-prone section is interpreted as being located near the axis of a paleovalley formed due to erosion during the low base level. This erosion is represented by the K1 unconformity that coincides with the top of the Morrison Formation. (b) Composite graphic showing the Whitewater stratigraphic section. The gamma ray was obtained using a handheld scintillometer. Values increase from left to right, and the information was normalized before correlation with well logs. Paleocurrent azimuths range from 40° to 55°. The section is composed of two intervals. The upper interval is characterized by NACC and isolated channel-fill elements. The lower interval shows highly amalgamated channel elements without significant floodplain deposits. This section has the greatest thickness from the six studied outcrops. Architectural elements are shown as triangles. Blue represents channel-fill elements, light blue represents channel complexes, and orange represents sequences.

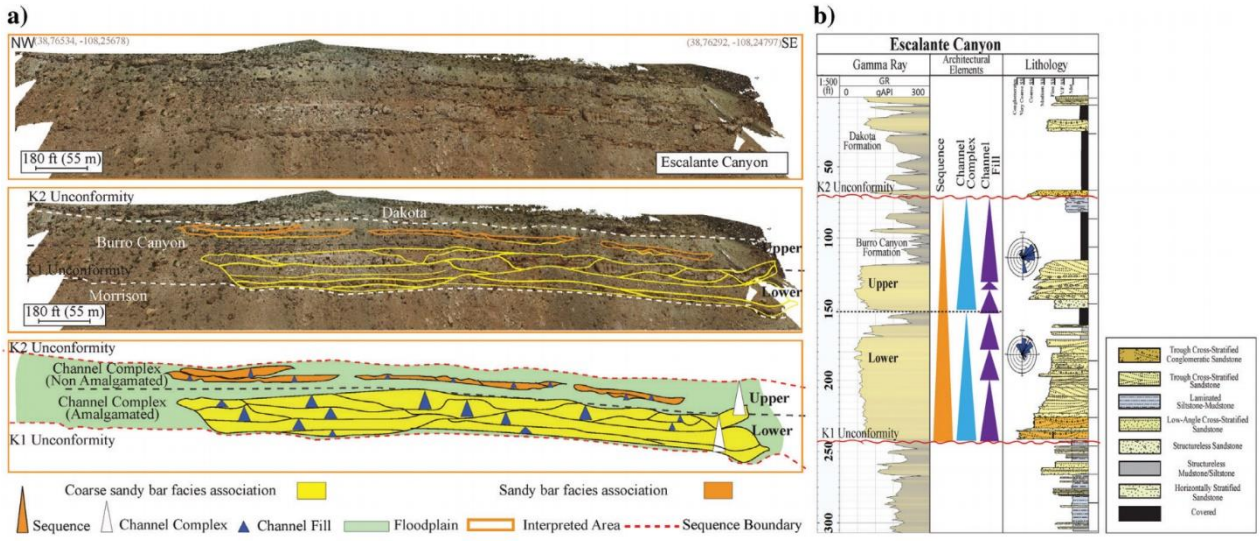

Figure 1-12: (a) The UAS-based photogrammetry model in the upper image was taken at the Escalante Canyon section. The top and base of the Burro Canyon Formation (K2 and K1 unconformities) are represented by the red lines. The hierarchical interpretation associated with this outcrop shows a non-amalgamated architectural element in the upper section and an ACC element in the lower. The model boundaries are shown as orange lines; the ACC elements and NACC elements and isolated channel-fill elements are shown in yellow. Floodplain deposits are shown in light green. Hierarchical elements are shown as triangles. This section exhibits an overall moderate net-to-gross ratio (0.6). (b) Composite stratigraphic section obtained at Escalante Canyon. The gamma ray was obtained using a handheld scintillometer. Values increase from left to right. The paleocurrent azimuth ranges from 40° to 65°. This section has an intermediate thickness among the studied outcrops. The section is composed by two intervals. The upper interval is characterized by a lower net-to-gross interval with NACC and isolated channel fill elements. The lower interval shows ACC elements resulting in a high net-to-gross ratio with some floodplain deposits. Architectural elements are shown as triangles. Blue color represents channel-fill elements; light white represents channel complexes, and orange represents sequences.

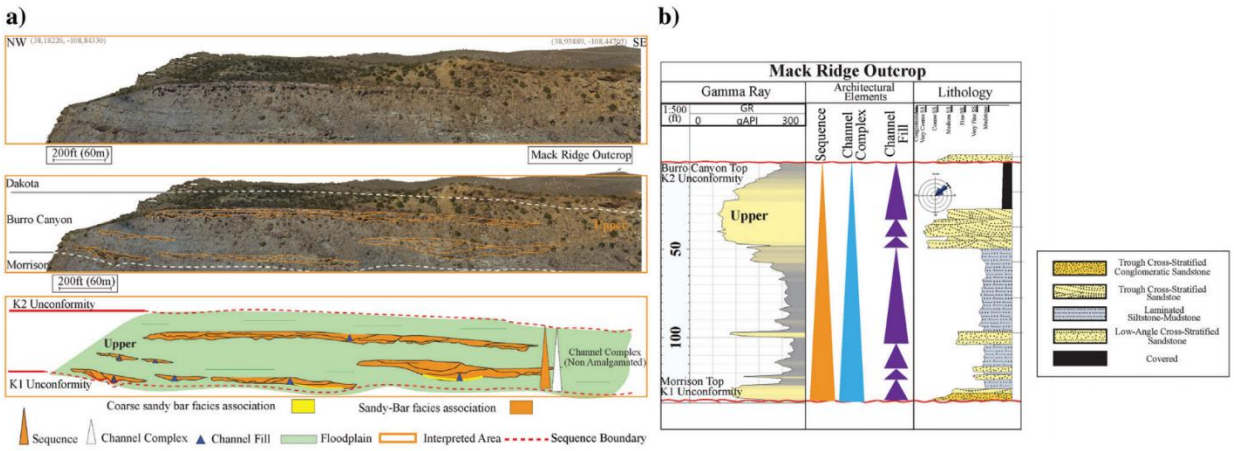

Figure 1-13: (a) A UAS-based photogrammetry model of the Mack Ridge. The top and base of the Burro Canyon Formation (K2 and K1 unconformities) are represented by the red lines. Intermediate- to large-scale architectural elements are interpreted using UAS-based photogrammetry renderings. The hierarchical interpretation associated for this outcrop shows non amalgamated to isolated channel-fill architectural elements in the section. Model boundaries are shown as orange lines; the non amalgamated channel complex and isolated channel-fill elements are shown in orange, and the floodplain deposits are in light green. The hierarchical elements are represented by triangles according to the interpretation of each architectural element. (b) Composite graphic of the Mack Ridge section. The gamma ray was obtained using a handheld scintillometer. The values increase from left to right. Paleocurrent azimuths have a mean value of 50°. The section consists of an upper interval that is characterized by a low net-to-gross ratio, a smaller thickness, and dominated to floodplain deposits. The architectural elements are shown as triangles. Purple represents channel-fill elements, light blue represents channel complexes, and orange represents sequences.

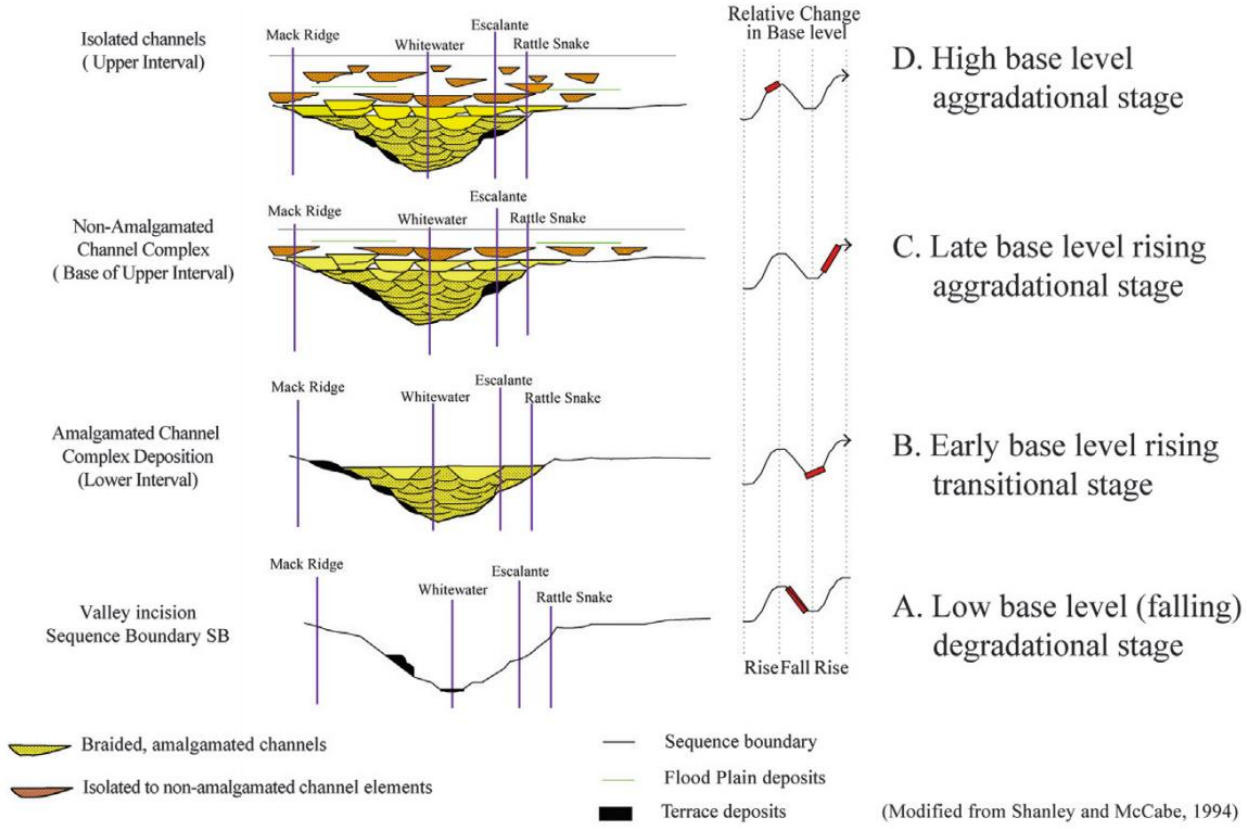

Figure 1-14: Summary diagram illustrating the relationships between the fluvial architecture and the base-level change. The red rectangular areas show baselevel stages of the base level in the sea-level curve. (a) Slow rates of base-level rise leading to base-level fall. (b) Reduced rates of base-level fall and the change to a rising base level. (c) Increased rates of base-level rise. (d) Reduced rates of base-level rise that are approximately balanced by rates of sedimentation. The interpretation of the possible locations for the sections described in this study area is shown in the diagram. Mack Ridge is located on the edge of the paleovalley, Whitewater is located close to the axis of the paleovalley, and the Escalante and Rattlesnake Canyons are in middle positions along the paleovalley. Modified from Shanley and McCabe (1994).

Tables

Table 1-1: Summary of hierarchical elements

Alluvial Hierarchical Elements	Description
Bar	The aggregate of genetically related beds and bedsets deposited within a confined channel. May form by lateral- or downstream-accretion, or as vertically aggrading fields of migrating bedforms.
Bar Set	A relatively conformable succession of genetically related bars that amalgamate vertically and/or laterally within the channel. Typically exhibit a fining-upward grain-size trend.
Channel-Fill	A relatively conformable succession of genetically related bar or bar-set elements that are deposited and preserved within a river channel that is defined by bankful discharge. Typically exhibit a fining-upward grain-size trend which reflects scouring, filling, and abandonment of the channel.
Channel Complex	Two or more channel-fill elements of similar fill type and their coeval floodplain deposits. Stratal stacking patterns may be described as amalgamated, semi-amalgamated, or non-amalgamated.
Depositional Sequence	A relatively conformable succession of genetically related channel-complex elements and their coeval floodplain strata bounded by regional surfaces of erosion or their correlative conformities ("sequence boundaries"). Typically composed of an amalgamated sand-rich channel complex element that is conformably overlain by a non-amalgamated mud-rich channel complex element.
Sequence Set	Two or more sequences that possess a similar stratal stacking pattern, bounded above and below by regional erosional surfaces or their correlative conformities. Three types are recognized: amalgamated, semi-amalgamated, and non-amalgamated. Allogenic mechanisms, such tectonism or climate, are the primary influences on sequence set accumulation.
Composite Sequence	A succession of sequence sets recording a basin-scale cycle of decreasing and increasing accommodation relative to sedimentation. Rapidly decreasing accommodation results in regional surfaces of erosion which are overlain by amalgamated or semi-amalgamated sequence sets reflecting a return to positive accommodation. These deposits are overlain by non-amalgamated sequence sets which reflect a pronounced increase in accommodation. The non-amalgamated sequence set may be succeeded by a semi-amalgamated sequence set resulting from a decrease in accommodation prior to development of the overlying regional surface of erosion.

Table 1-2: Summary of key lithofacies observed in the Burro Canyon Formation along the study area from the Mack Ridge outcrop to Rattlesnake Canyon.

Lithofacies	Description	Interpretation
Trough Cross-bedded Gravel Gt	Granule size conglomerate fining upwards to tanned - white medium size sandstone, thought cross bedding predominant to the base and tangential cross bedding to the top. The conglomeratic sandstone consists of sub-rounded, poorly sorted dark granules and pebbles embedded in a sub-angular, poor sorted, and medium size sandstone matrix. Poorly cemented and kaolinite possibly due to weathering	Base of Channel system (3-D) dunes or bed-sets
Laminated Siltstone, Mudstone Fl	Interbedded green and red mudstone with brown medium to fine grain, siltstone. Well cemented, parallel laminated with bioturbation.	Floodplain
Low Angle Cross-Bedded SS Sl	Coarse to medium tanned – white sandstone well sorted, sub-rounded and sub-angular. Iron oxides. Low angle cross bedding sometimes parallel to the top. Variations in grain size is fining –upward in small packages of 1ft.	Upper plane bed
Trough Cross-Bedded SS St	Coarse to fine tanned – white sandstone moderated sorted, Sub-rounded and sub-angular. Trough cross bedding . Fining–upward sequences. At the bottom, pebbles and poorly sorted clasts within the sandstone packages of 1ft.	Sinuous-crested or linguoid (3-D) dunes or bed sets
Structureless SS Sm	Medium grain size sandstone cemented. Fining upward to the top and lag of pebbles poorly sorted to the bottom	Amalgamated bed-sets separated by high flow granule beds
Horizontally Bedded SS Sh	Tan to white fine to medium grain sandstone, well sorted planar laminations sub-rounded to sub-angular	Straight-crested (2-D) dunes or bed-sets
Structureless Mdstn Siltstn Fm	Sedimentary structures destroyed by burrowing/rooted organisms, pedogenic modification, or outcrop weathering	Settlement for suspension

References

Aubrey, W. M., 1986, The nature of the Dakota-Morrison boundary, southeastern San Juan Basin, in C. E.Turner-Peterson, ed., A basin analysis case study: The Morrison Formation, Grants Uranium Region, New Mexico: AAPG, Studies in Geology 22, 93–104.

Aubrey, W. M., 1989, Mid-Cretaceous alluvial-plain incision related to Eustasy, southeastern Colorado Plateau: Geological Society of America Bulletin, 101, 443–449, doi: 10.1130/0016-7606(1989)101<0443:MCAPIR>2.3.CO;2.

Aubrey, W. M., 1996, Stratigraphic architecture and deformational history of Early Cretaceous foreland basin, Eastern Utah and Southwestern Colorado: Geology and Resources of the Paradox Basin, 211–220.

Aubrey, W. M., and G. Skipp, 1992, New interpretations of the stratigraphy and sedimentology of uppermost Jurassic to lowermost Upper Cretaceous strata in the San Juan Basin of northwestern New Mexico no. 1808: US Department of Interior, US Geological Survey DC, U.S. G.P.O.

Banes, A., K. G. Alvarez Ortega, M. Henry, and T. Niemi, 2017, Using drone imagery and photogrammetry to map basin stratigraphy and structures exposed in Mine, Road, and Arroyo Outcrops, Santa Rosalia, Baja California Sur, Mexico: AGUFM, T23B-0613.

Bliscaux, N., R. A. Guillois, M. Brocheray, and S. Paron, 2018, How useful are drones to derive digital stratigraphic logs? Validation of a drone's based Digital Geological Orthophotographic Model with field data: EGU General Assembly Conference Abstracts, Vol. 20, 19861.

Catuneanu, O., V. Abreu, J. P. Bhattacharya, M. D. Blum, R.W. Dalrymple, P. G. Eriksson, C. R. Fielding, W. L.Fisher, W. E. Galloway, M. R. Gibling, and K. A. Giles,2008, Toward the standardization of the sequence stratigraphy: Earth-Science Reviews, 92, 1–33, doi: 10.1016/j.earscirev.2008.10.003.

Cole, R., and G. Moore, 1994, Sequence stratigraphy ofCedar Mountain-Dakota interval, western and southern Piceance Creek basin, Colorado: AAPG Annual Convention Program, vol. 3, 124.

Cole, R., and G. Moore, 2012, Lithofacies, depositional systems, and reservoir elements in the Burro Canyon-Dakota interval, southwest Piceance Basin, Colorado:Rocky Mountain Section of AAPG.

Currie, B. S., 1993, Sequence stratigraphy of the Jurassic–Cretaceous Morrison and Cedar Mountain Formations,NE Utah–NW Colorado: Geological Society of AmericaAbstracts with Programs, 25, no. 5, 26–27.

Currie, B. S., 1994, “Back-bulge” to foredeep evolution ofthe Late Jurassic–Early Cretaceous Cordilleran forelandbasin: Evidence from the Morrison and Cedar MountainFormations, central-eastern Utah: Geological Society ofAmerica Abstracts with Programs, 26, no. 6, 9.

Currie, B. S., 1997, Sequence stratigraphy of non-marineJurassic-Cretaceous rocks, central Cordilleran foreland-basin system: Bulletin of the Geological Societyof America, 109, 1206–1222, doi: 10.1130/0016-7606(1997)109<1206:SSONJC>2.3.CO;2.

Currie, B. S., 1998, Upper Jurassic-Lower Cretaceous Morrison and Cedar Mountain Formations, NE Utah-NW Colorado; relationships between non-marine deposition and early Cordilleran foreland-basin development: Journal ofSedimentary Research, 68, 632–652, doi: 10.2110/jsr.68.632.

Currie, B. S., 2002, Structural configuration of the early cretaceous Cordilleran foreland basin system and Sevier thrust belt, Utah and Colorado: The Journal of Geology, 110, 697–718, doi: 10.1086/342626.

DeCelles, P. G., R. P. Langford, and R. K. Schwartz, 1983,Two new methods of paleocurrent determination from trough cross-stratification: Journal of Sedimentary Petrology, 53, 629–642.

DeCelles, P. G., T. F. Lawton, and G. Mitra, 1995, Thrust timing, growth of structural culminations, and synorogenic sedimentation in the type Sevier orogenic belt, western United States: Geology, 23, 699–702, doi: 10.1130/0091-7613(1995)023<0699:TTGOSC>2.3.CO;2.

DeCelles, P. G., and B. S. Currie, 1996, Long-term sediment accumulation in the Middle Jurassic–early Eocene Cordilleran retroarc foreland-basin system: Geology, 24, 591–594.

Durkin, P. R.,Holbrook, and R. Boyd, 2017, Evolution of fluvial meander-belt deposits and implications for the completeness of the stratigraphic record: GSA Bulletin, 130, 721–739, doi: 10.1130/B31699.1.

Holbrook, J. M., 1996, Complex fluvial response to low gradients at maximum regression: A genetic link between smooth sequence boundary morphology and architecture of overlying sheet sandstone: SEPM Journal of Sedimentary Research, 66, 713–722, doi: 10.1306/D42683EC-2B26-11D7-8648000102C1865D.

Holbrook, J. M., R. W. Scott, and F. E. Oboh-Ikuenobe,2006, Base-level buffers and buttresses: A model for upstream versus downstream control on fluvial geometry and architecture within sequences: Journal of Sedimentary Research, 76, 162–174, doi: 10.2110/jsr.2005.10.

Kirkland, S. G., 1976, Stratigraphy and petroleum potential of the Cedar Mountain and Dakota Formations, northwestern Colorado, Golden, Colorado School of Mines, 193.

Kirkland, J. I., B. B. Britt, D. L. Burge, K. Carpenter, R. L. Cifelli, F. L. DeCourten, J. G. Eaton, S. T. Hasiotis, andT. F. Lawton, 1997, Lower to middle Cretaceous dinosaur faunas of the central Colorado Plateau: A key to understanding 35 million years of tectonics, sedimentology, evolution and biogeography: Brigham Young University, Geology Studies, 42, 69–103.

Kirkland, J. I., R. L. Cifelli, B. B. Britt, D. L. Burge, F. L. DeCourten, J. G. Eaton, and J. M. Parrish, 1999, Distribution of vertebrate faunas in the Cedar Mountain Formation, east-central Utah: Utah Geological Survey, 99, 201–217.

Kirkland, J. I., and S. K. Madsen, 2007, The Lower Cretaceous Cedar Mountain Formation, Eastern Utah, Guidebook: The view up an always interesting learning curve: Geological Society of America Rocky Mountain Section, 35, 1–108.

Kirkwood, S.G., 1976, Stratigraphy and petroleum potential of the Cedar Mountain and Dakota Formations, northwestern Colorado [M.S. thesis]: Golden, Colorado, Colorado School of Mines, 193 p.

Labourdette, R., and R. R. Jones, 2007, Characterization of fluvial architectural elements using a three-dimensional outcrop data set: Escanilla braided system, South-Central Pyrenees, Spain: Geosphere, 3, no. 6, 422, doi: 10 .1130/ges00087.1.

Lunt, I. A., G. H. S. Smith, J. L. Best, P. J. Ashworth, S. N. Lane, and C. J. Simpson, 2013, Deposits of the sandy braided South Saskatchewan River: Implications for the use of modern analogs in reconstructing channel dimensions in reservoir characterization: AAPG Bulletin, 97, 553–576, doi: 10.1306/09251211152.

McPherson, M. L., B. S. Currie, and J. S. Pierson, 2006, Reservoir characterization of the Cretaceous Cedar Mountain and Dakota formations, southern Uinta Basin, Utah: YearOne Report: Utah Geological Survey, Open File Report 492.

McPherson, M. L., B. S. Currie, J. P. Dark, and J. S. Pierson, 2008, Outcrop-to-subsurface correlation of the Cretaceous Cedar Mountain and Dakota Formations, southern Uinta basin: Rocky Mountain Association of Geologists and Utah Geological Association, 37, 43–63.

Miall, A. D., 1977, Lithofacies types and vertical profile models in braided river deposits: A summary, vol. 5: Canadian Society of Petroleum Geologists.

Miall, A. D., 1988, Architectural elements and bounding surfaces in fluvial deposits: Anatomy of the Kayenta Formation (Lower Jurassic), southwest Colorado: Sedimentary Geology, 55, 233–262, doi: 10.1016/0037-0738(88)90133-9.

Miall, A. D., 1996, The geology of fluvial deposits: Sedimentary facies, basin analysis and petroleum geology: Heidelberg, Springer-Verlag Inc., 582.

Miall, A. D., 2006, Reconstructing the architecture and sequence stratigraphy of the preserved fluvial record as a tool for reservoir development: A reality check: AAPG Bulletin, 90, 989–1002, doi: 10.1306/02220605065.

Owen, D. E., A. M. Forgas, S. A. Miller, R. J. Stelly, and D. E. Owen Jr., 2005, Surface and subsurface stratigraphy of the Burro Canyon Formation, Dakota Sandstone, and intertongued Mancos Shale of the Chama Basin, New Mexico, in S. G. Lucas, K. E. Zeigler, V. W. Lueth, and D. E. Owen, eds., Geology of the Chama Basin, vol. 56: New Mexico Geological Society, 218–226.

Patterson, P. E., T. A. Jones, C. J. Donofrio, A. D. Donovan, and J. D. Ottmann, 2002, Geologic modeling of external and internal reservoir architecture of fluvial systems, in M. Armstrong, C. Bettini, N. Champigny, and A. Galli, eds., Geostatistics Rio 2000: Proceedings of the Geostatistics Sessions of the 31st International Geological Congress: Kluwer Academic Publishers, 41–43.

Patterson, P. E., C. R. Jones, and R. L. Skelly, 2010, Hierarchical description and sequence stratigraphy of Cretaceous alluvial strata, Hawkins Field, Texas, in V. Abreu, J. E. Neal, K. M. Bohacs, and J. L. Kalbas, eds., Sequence stratigraphy of siliciclastic systems — The ExxonMobil methodology: SEPM (Society for Sedimentary Geology), 226.

Patterson, P. E., K. Kronmueller, and T. D. Davies, 2003, Sequence stratigraphy of the Mesaverde Group and Ohio Creek conglomerate, northern Piceance Basin, Colorado: Piceance Basin, 115–128.

Patterson, P. E., R. L. Skelly, and C. R. Jones, 2012, Climatic controls on depositional setting and alluvial architecture, Doba Basin, Chad: Lacustrine sandstone reservoir and hydrocarbon systems: AAPG Memoir, 95, 265–298, doi: 10.1306/13291393M953237.

Pranter, M. J., R. D. Cole, H. Panjaitan, and N. K. Sommer, 2009, Sandstone-body dimensions in a lower coastalplain depositional setting: Lower Williams Fork Formation, Coal Canyon, Piceance Basin, Colorado: AAPG Bulletin, 93, no. 10, 1379–1401, doi: 10.1306/ 06240908173.

Pranter, M. J., A. C. Hewlett, R. D. Cole, H. Wang, and J. R.Gilman, 2014, Fluvial architecture and connectivity of the Williams Fork Formation: Use of outcropanalogues for stratigraphic characterization and reservoir modelling, in T. Good, J. Howell, and A. W. Martinius, eds., Sediment body geometry and heterogeneity: Analogue studies for modelling the subsurface: Geological Society, London, Special Publications, vol. 387, 57–83.

Roca, X., and G. C. Nadon, 2007, Tectonic Control on the sequence stratigraphy of non-marine retroarc foreland basin fills: Insights from the Upper Jurassic of central Utah, U.S.A.: Journal of Sedimentary Research, 77, 239–255, doi: 10.2110/jsr.2007.021.

Shanley, K. W., and P. J. McCabe, 1994, Perspectives on the sequence stratigraphy of continental strata: Report of a working group at the 1991 NUNA Conference on High Resolution Sequence Stratigraphy: AAPG Bulletin, 74, 544–568, doi: 10.1306/BDFF9258-1718-11D7-8645000102C1865D.

Sprague, A. R., P. E. Patterson, R. E. Hill, C. R. Jones, K. M. Campion, J. C. Van Wagoner, M.D. Sullivan, D. K. Larue, H. R. Feldman, T. M. Demko, R. W. Wellner, and J. K. Geslin, 2002, The physical stratigraphy of fluvial strata: A hierarchical approach to the analysis of genetically related stratigraphic elements for improved reservoir prediction: AAPG Annual Meeting, A167–A168.

Stokes, W. L., 1944, Morrison formation and related deposits in and adjacent to the Colorado Plateau: Geological Society of America Bulletin, 55, no. 8, 951–992, doi: 10 .1130/gsab-55-951.

Stokes, W.L. and D.A. Phoenix, 1948, Geology of the Egnar-Gypsum Valley area, San Miguel and Montrose Counties, Colorado. U.S. Geological Survey Oil and Gas Investigations Map, OM-93, 1 sheet, scale 1:48,000

Stokes, W. L., 1952, Lower Cretaceous in Colorado Plateau: AAPG Bulletin, 36, 1766–1776, doi: 10.1306/5CEADB93- 16BB-11D7-8645000102C1865D.

Tellez, J. J., and M. J. Pranter, 2016, Application of UAVbased photogrammetry for outcrop characterization of fluvial deposits of the Burro Canyon Formation, Piceance Basin, GTW, new opportunities with drones: New Needs, FAA Rule Changes, New Technologies.

Young, R. G., 1960, Dakota Group of Colorado Plateau: AAPG Bulletin, 44, 156–194.

Young, R. G., 1970, Lower Cretaceous of Wyoming and the Southern Rockies: AAPG Bulletin, 7, 105–121, doi: 10 .1306/5D25C1E7-16C1-11D7-8645000102C1865D.

Young, R. G., 1973, Depositional environments of basal Cretaceous rocks of the Colorado Plateau, in J. E. Fassett, ed., Cretaceous and Tertiary Rocks of the Southern Plateau: A memoir of the Four Corners Geological Society: Four Corners Geological Society, 10–27.

Young, R. G., 1975, Lower Cretaceous rocks of northwestern Colorado and northeastern Utah: Rocky Mountain Association of Geologists Symposium, 141–147.Aubrey, W. M., 1986, The nature of the Dakota-Morrison boundary, southeastern San Juan Basin, in Turner-Peterson, C. E., ed., A Basin Analysis Case Study: The Morrison Formation, Grants Uranium Region, New Mexico: American Association of Petroleum Geologists, Studies in Geology 22, p. 93-104.

Appendix

I added the following images and text for a better understanding of the published manuscript. They compile specific details and work you complement this chapter.

UAS-based photogrammetry workflow summary

I generated three-dimensional outcrop reconstructions across the study area in locations perpendicular to the fluvial system paleoflow direction south-west to north-east. The high-resolution photographs were obtained using a DJI Phantom 3 Professional drone UAS (Unmanned Aerial Systems) with a mounted photography camera equipped with an f/2.8 lens and 94º field view. The process used to generate a three-dimensional outcrop reconstruction required the following steps:

Pre-flight considerations:

Before the flighting process, I considered wind conditions, light and weather conditions, visibility, battery status, and data storage of the UAS.

Ground points markers (GPM) collection:

I identified relevant, large-scale features in the outcrop and marked them for GPM use. I utilized fluorescent tape to mark with a large "X" prominent boulders and trees easy to identify in photographs from the outcrops.

Acquisition:

The acquisition process followed established flight paths with distances to the outcrop face from 50 to 150 m (165-490 ft). I defined multiple paths forming grids that covered the area, considering large- and small-scale features to identify within the models. The grid size considers an overlap above 70% among photographs to avoid gaps within the data used to generate the model reconstructions. The collected images required specific light conditions avoiding shadow

zones in the photographs to produce a reliable high-resolution dataset to create three-dimensional models. The quality, contrast, and brightness of the images played a vital role during the model generation.

Photo editing:

The image editing includes removing sky, clouds, and dynamic objects from the photographs using Adobe Photoshop. Photographs with variable incident sunlight over the outcrop are commonly overexposed or underexposed objects. I adjusted contrast, color saturation, and brightness to illuminate outcrop features diminished due to extremely high or low light contrast.

Cloud point generation:

The imagery was used to generate three-dimensional (3-D) georeferenced point-cloud models with texture. The model building process defines X, Y, and Z coordinates to represent the external surface of the outcrop face. The result of the point clouds were high precision digital elevation models of the terrain. During this process, I included the information collected from ground point measurements (GPM) to constrain the outcrop locations and scale.

Interpretation:

I used the three-dimensional outcrop reconstructions and combined them with field observations to identify key stratigraphic surfaces, measure architectural element dimensions, and identify stratigraphic and lateral variations along the outcrop belt. A software package (PIX4d™) was used to make the stratigraphic interpretations (key surfaces and scour contacts) over the generated three-dimensional models. Georeferenced polygons tracing the location and extension of the sandstone bodies and channel complexes were drawn over the point cloud models generated from the collected image inventory. Additional UAS-photographs were also used to

complement the identification and description of channel systems hard to trace over the point-cloud models due to limited visibility.

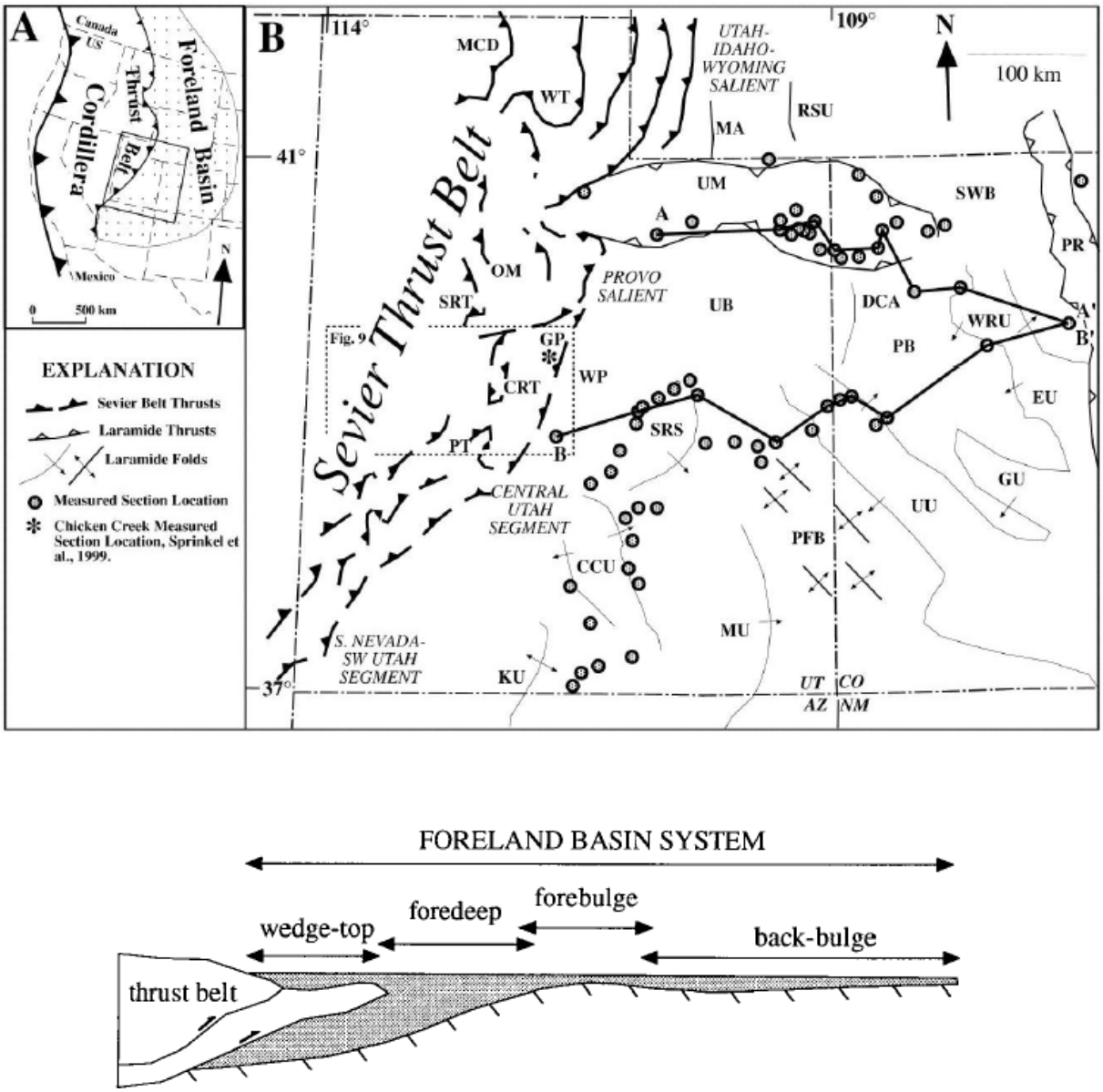

Figure 1-15A: Generalized paleogeographic map of the Sevier thrust belt and foreland-basin system in Utah and Colorado during Albian time. Dark dashed-line corresponds to estimated frontal position of the Sevier thrust belt. Gray barbed line represents frontal position of Sevier thrust belt during the Aptian. PT, Pavant Thrust; CRT, Canyon Range Thrust. Original thickness of Lower Cretaceous rocks in southwest Utah north of zero isopach contour are unknown due to lack of exposure and later thrust-related uplift in the southwestern Utah segment of the Sevier belt. (Currie, 2002).

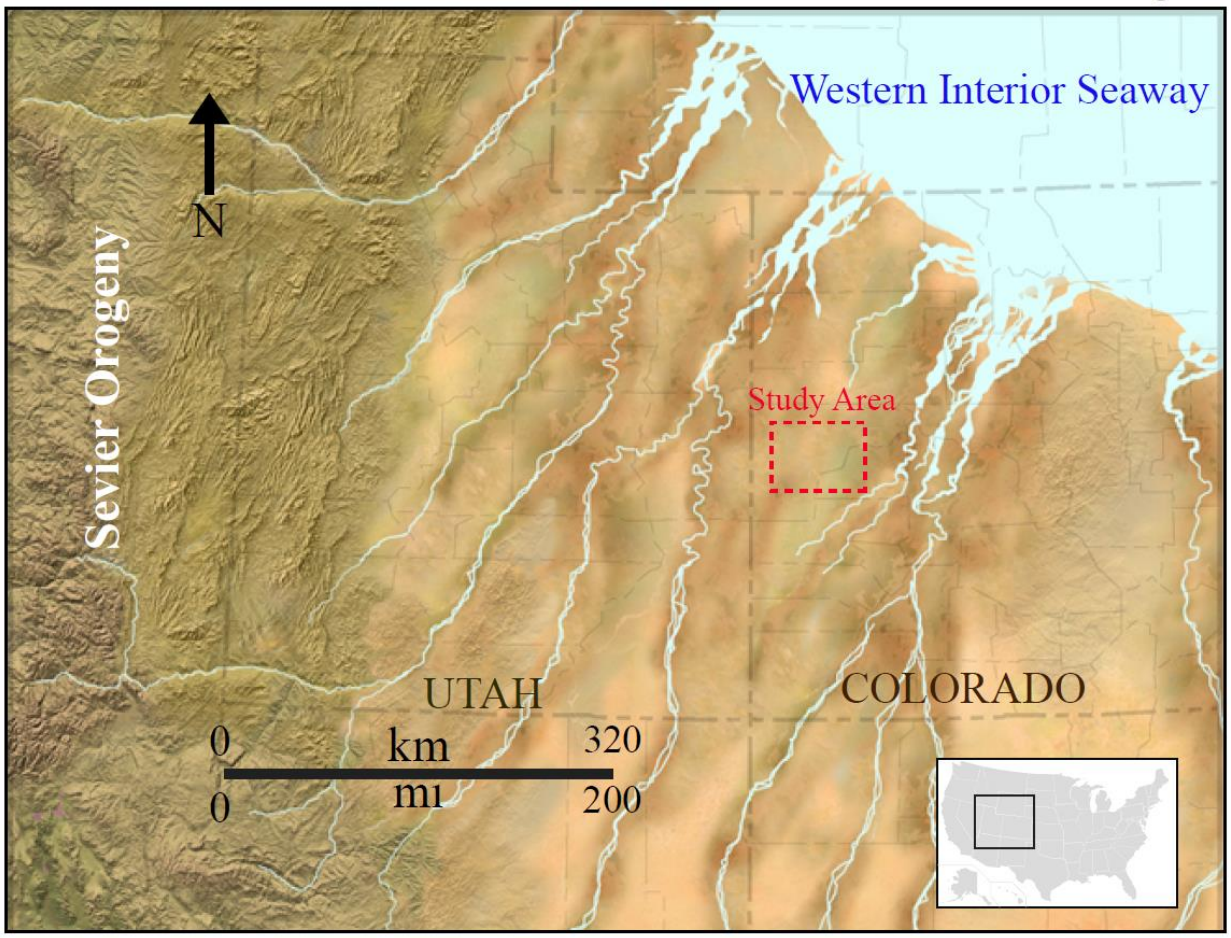

Figure 1-16A: Paleogeographic map of the study area during the time of deposition for the Burro Canyon Formation, Aptian-Albian (~110 Ma), The evolution of the Sevier orogenic belt during the Aptian-Albian of the foreland system formed the fluvial-channel architecture present in the Lower Cretaceous formations within the basin. The study area is highlighted in red. Modified from Blakey (2014).

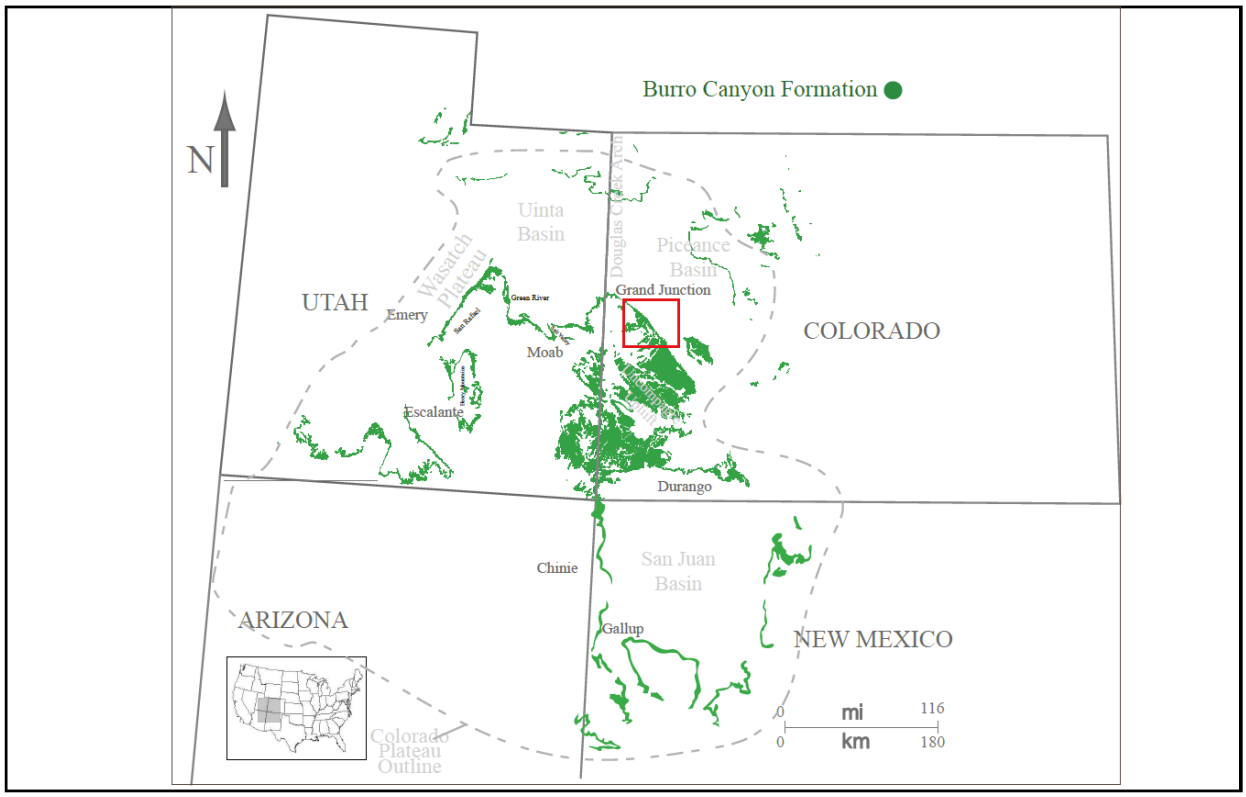

Figure 1-17A: Regional map for the Early Cretaceous formations. The outcrop belt of the Burro Canyon Formation is present in eastern Utah, Western Colorado and Northwestern New Mexico. The map shows in dashed lines the limits of the Colorado Plateau. The light green color shows the distribution of outcrops for the Burro Canyon Formation within western Colorado.

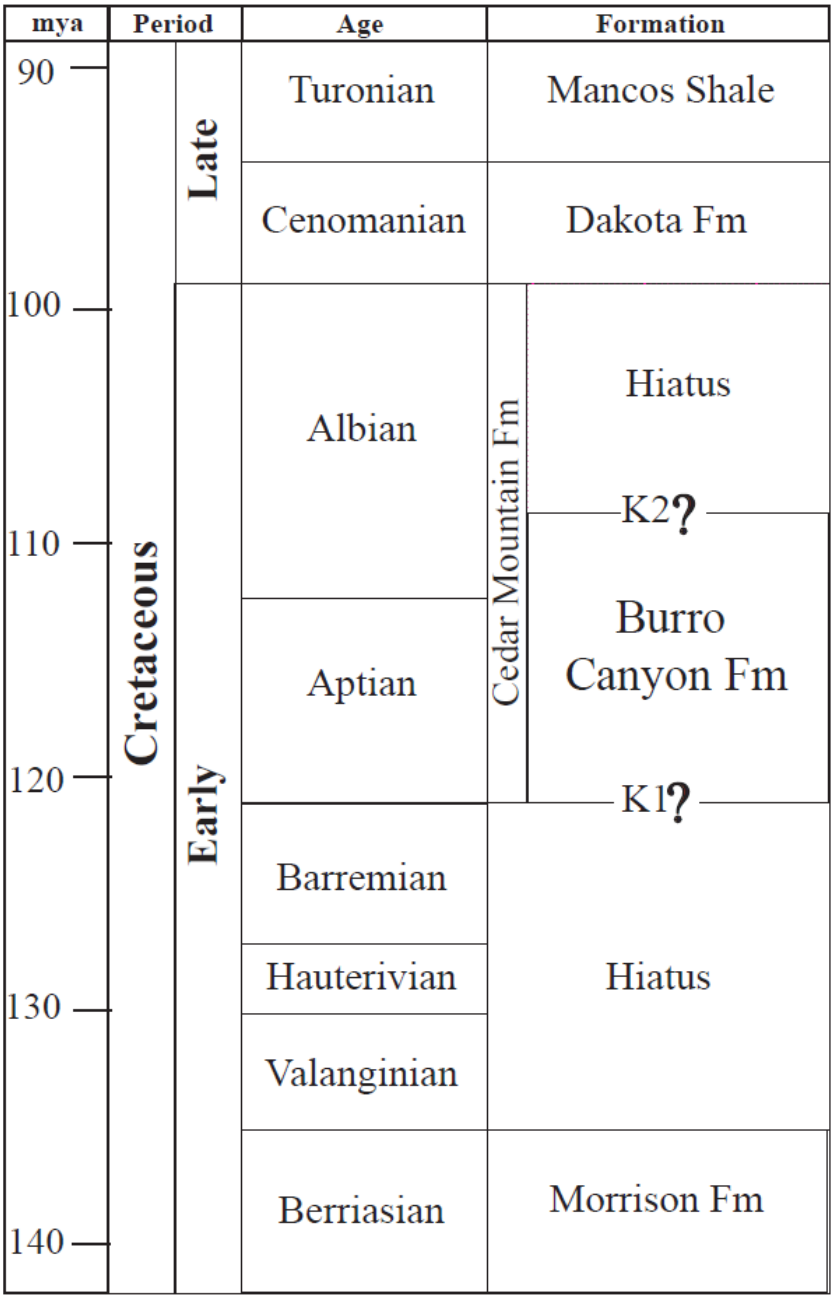

Figure 1-18A: Stratigraphic nomenclature used in this study. The Burro Canyon Formation is the target of this study. Modified from Cole (2016, personal communication)

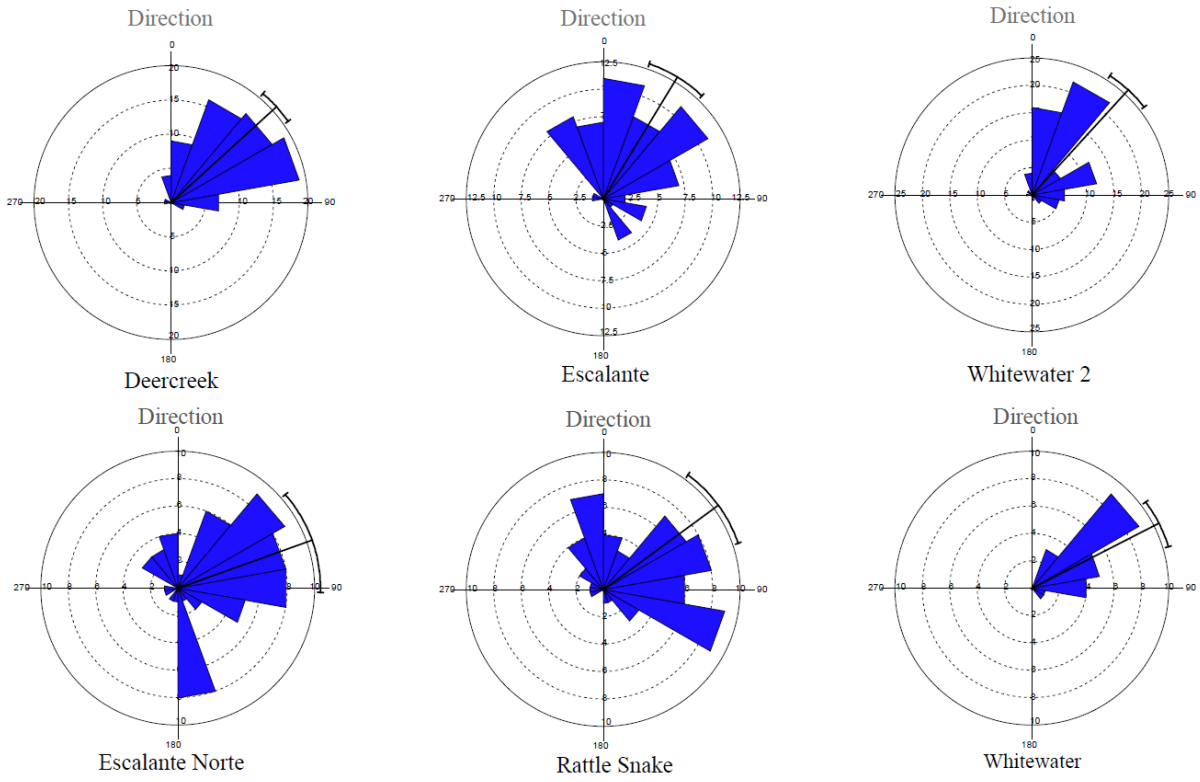

Figure 1-19A: Paleocurrent rose diagrams from measurements taken in each of the outcrop locations. Mack Ridge outcrop, Whitewater, Deer Creek, Escalante north, Escalante and Rattlesnake Canyons. N=589.

Figure 1-20A: Mack Ridge study area. Green highlight indicates extent of the outcrop reconstruction mapped using UAV (Unmanned Aerial Vehicle) photogrammetry. The location of the measured section traverse is indicated in red line. The exposed side of Mack Ridge outcrop analyzed within the Burro Canyon Formation includes the wall perpendicular to the paleoflow.

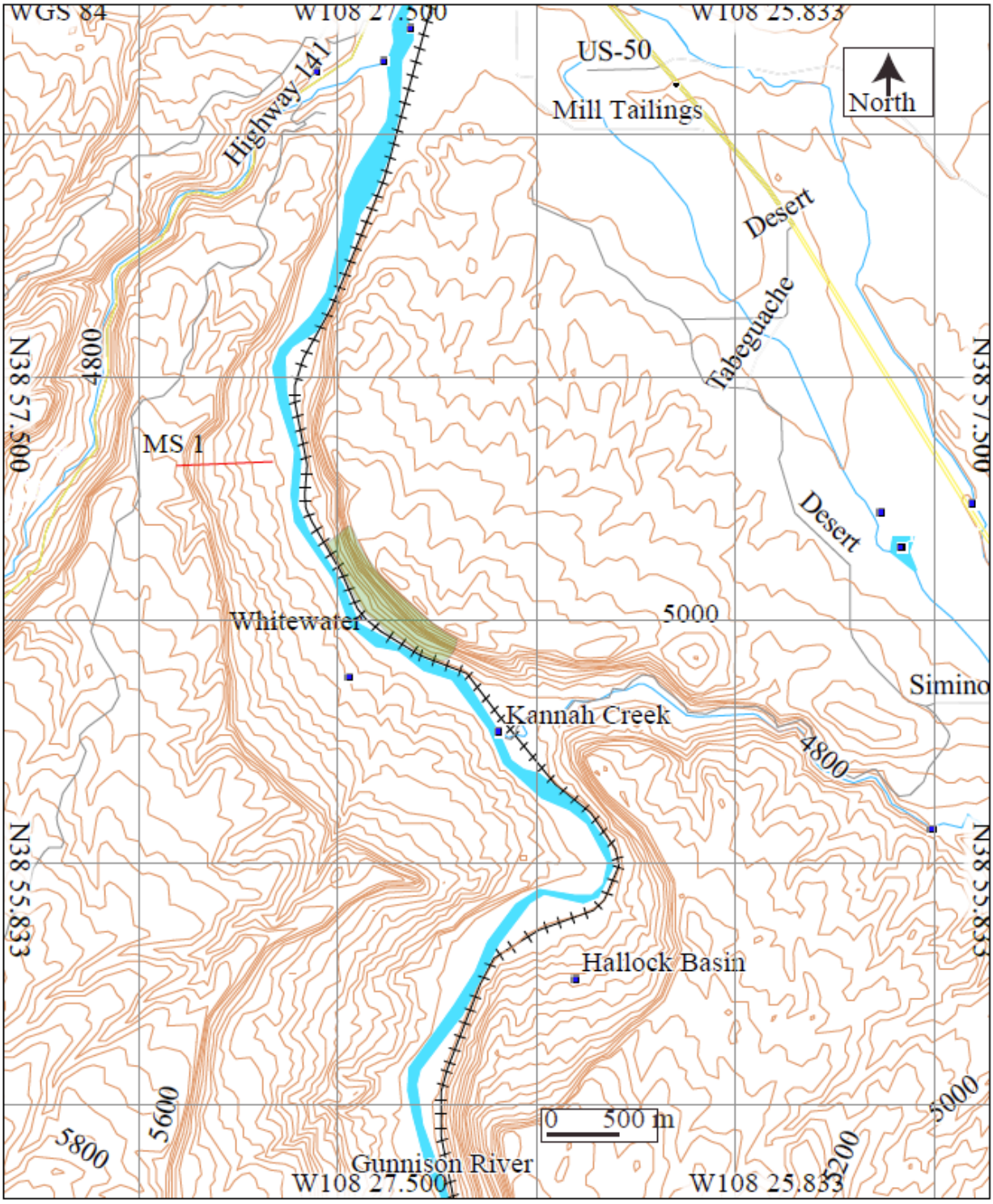

Figure 1-21A: Whitewater canyon study area. Green highlight shows extent of the outcrop reconstruction mapped using UAV (Unmanned Aerial Vehicle) photogrammetry. The location of the measured section traverse is indicated in red line. The exposed side of Whitewater canyon analyzed within the Burro Canyon Formation exposures includes only the wall closely perpendicular to the paleoflow of the system.

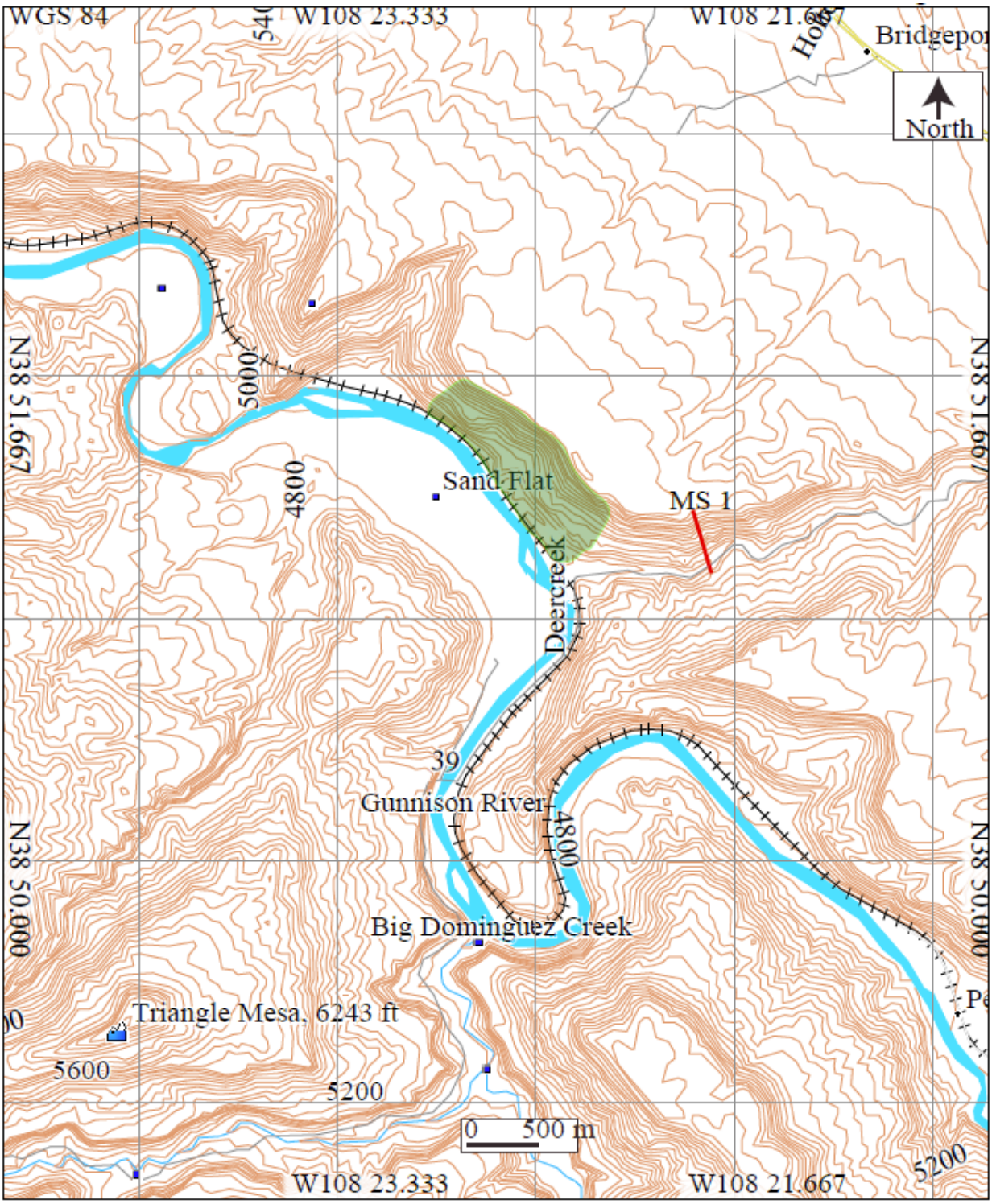

Figure 1-22A: Deer Creek canyon study area. Green highlight shows extent of the outcrop reconstruction mapped using UAV (Unmanned Aerial Vehicle) photogrammetry. The location of the measured section traverse is indicated in red line. The exposed side of Deer Creek canyon analyzed within the Burro Canyon Formation exposures includes the wall perpendicular to the paleflow of the system.

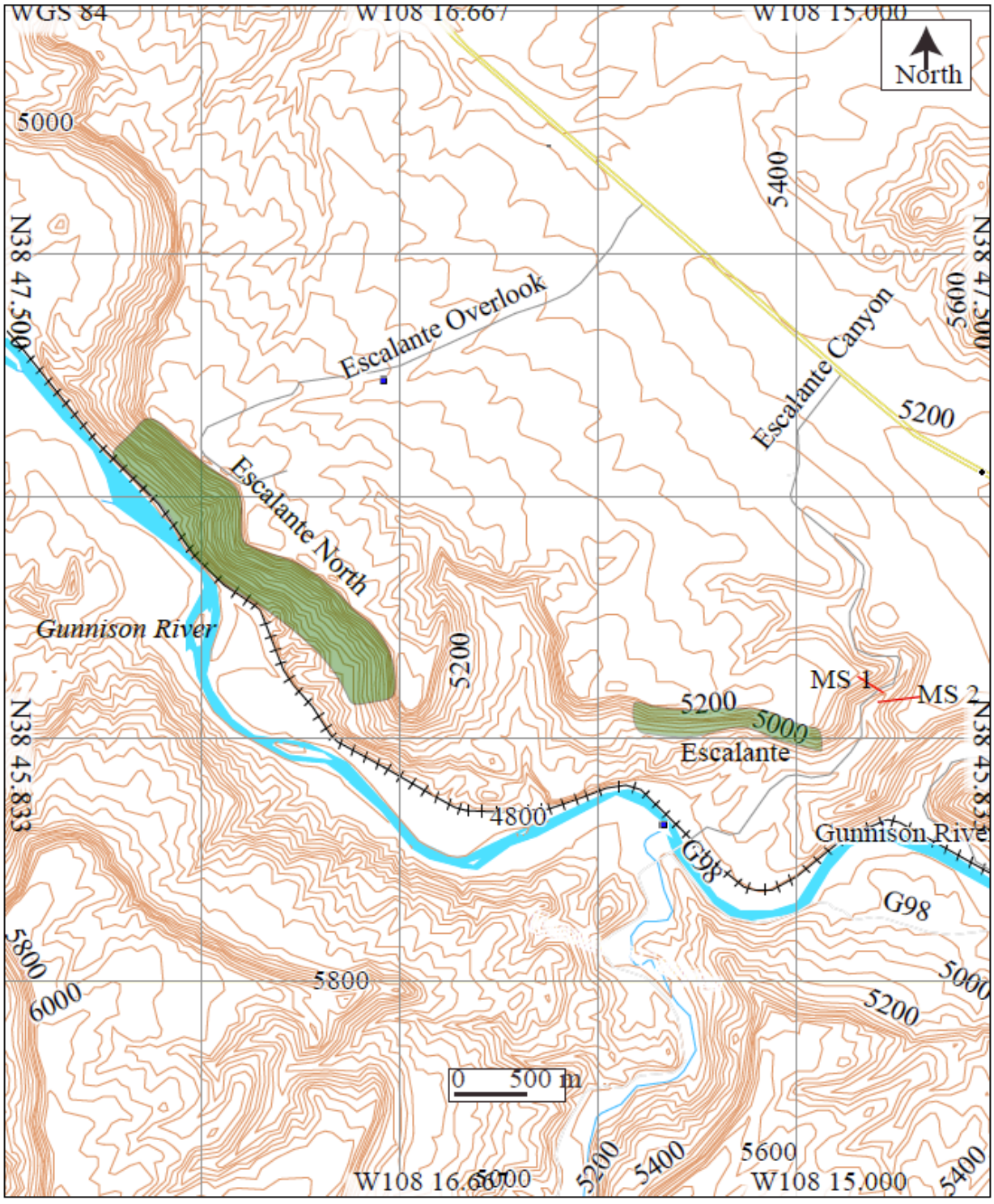

Figure 1-23A: Escalante and Escalante north canyons study area. Green highlights show extent of the outcrop reconstructions mapped using UAV (Unmanned Aerial Vehicle) photogrammetry. The locations of the measured sections traverse are indicated in red line. Three exposed sides of Escalante canyon were analyzed within the Burro Canyon Formation exposures. They include the walls within the parallel to paleoflow sections of the system.

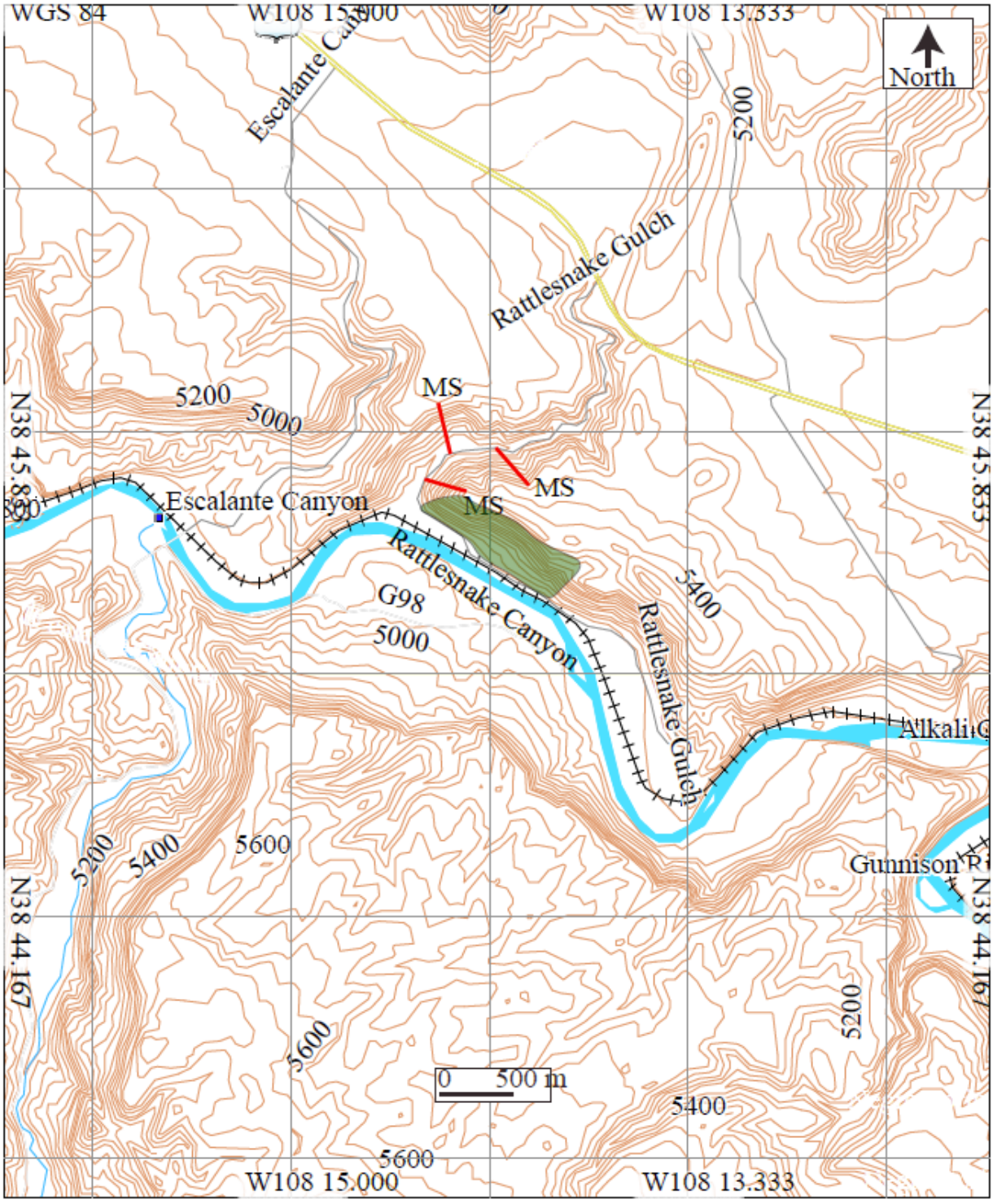

Figure 1-24A: Rattlesnake study area. Green highlight indicates the extent of the outcrop reconstruction mapped using UAV (Unmanned Aerial Vehicle) photogrammetry. The location of the measured section traverse is indicated in the red line. The exposed side of Rattlesnake Canyon analyzed within the Burro Canyon Formation exposures includes only the South-east

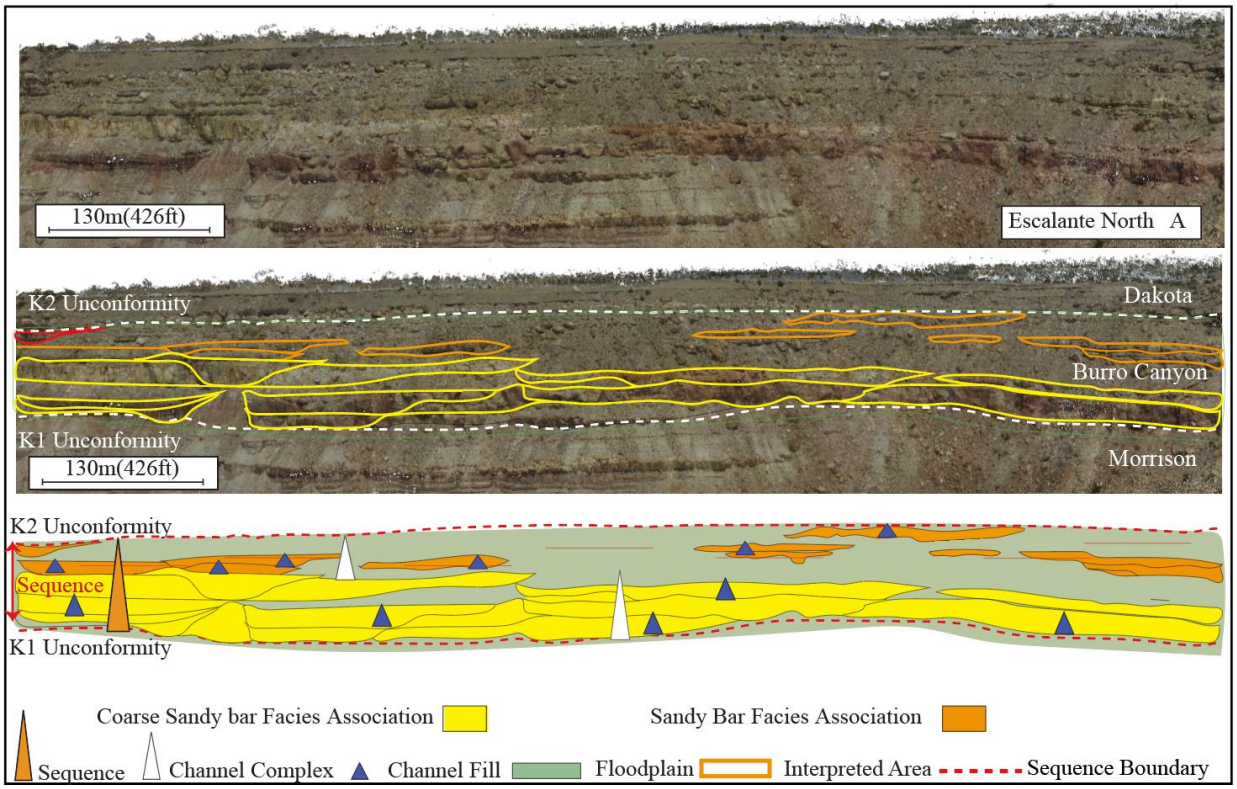

Figure 1-25A: UAV- based photogrammetry model is shown in the top of the image of the Escalante North section 1. The top and base of Burro Canyon Formation (K2 and K1 unconformities) are represented in red lines. Architectural elements are interpreted using UAV-based outcrop renderings. The interpretation is consistent with the other outcrops and shows non-amalgamated architectural element in the upper section of the Burro Canyon Formation and amalgamated channel complex elements in the lower interval of the formation. Model boundaries are shown as orange lines; coarse sandy bar facies association are shown in yellow and the sandy bar facies association in orange. Floodplain deposits are shown in light green. This section exhibits a high net-to-gross ratio (0.75).

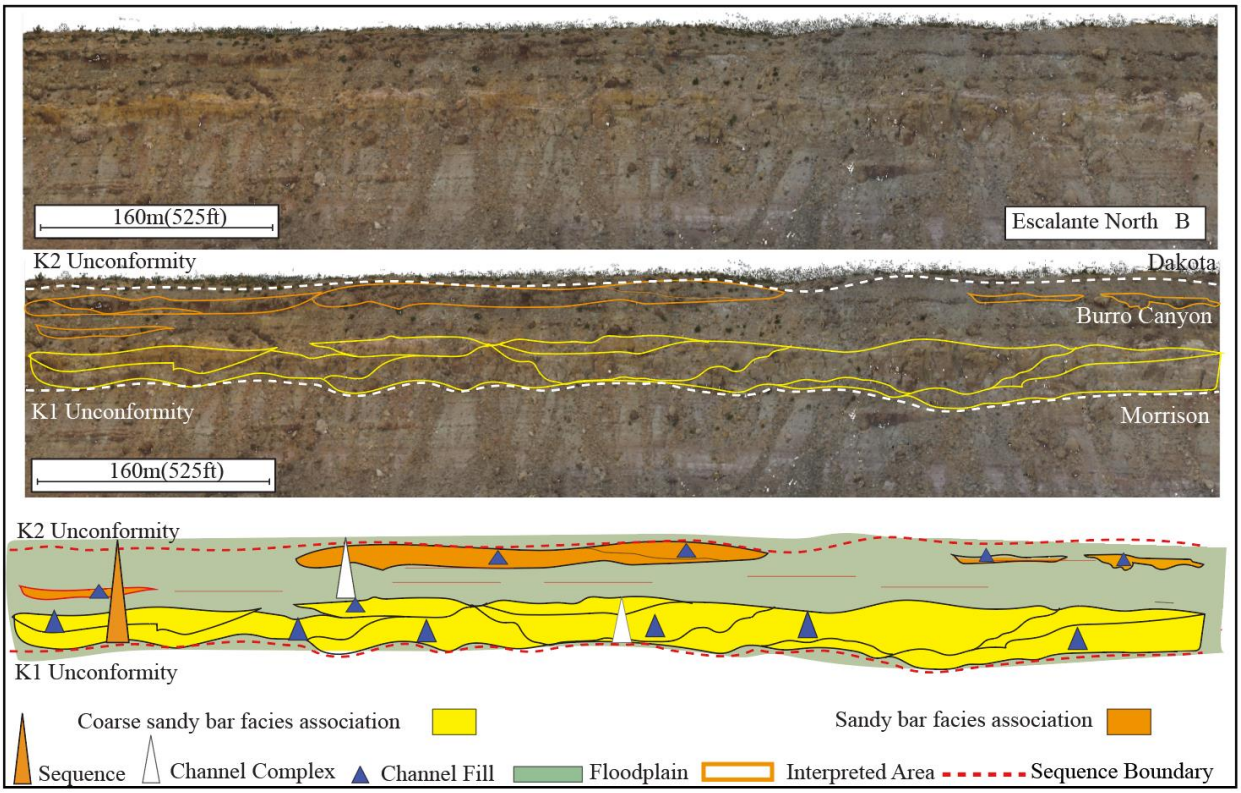

Figure 1-26A: UAV- based photogrammetry model is shown in the top of the image of the Escalante North section 2. The top and base of Burro Canyon Formation (K2 and K1 unconformities) are represented in red lines. Architectural elements are interpreted using UAV-based outcrop renderings. The interpretation is consistent with the other outcrops and shows non-amalgamated architectural element in the upper section of the Burro Canyon Formation and amalgamated channel complex elements in the lower interval of the formation. Model boundaries are shown as orange lines; the coarse sandy bars facies associations are shown in yellow and the sandy bar facies association elements in orange. Floodplain deposits are shown in light green. These location does not have a measure section associated. However, the trend is consistent with the regional interpretation. This section exhibits a high net-to-gross ratio (0.7).

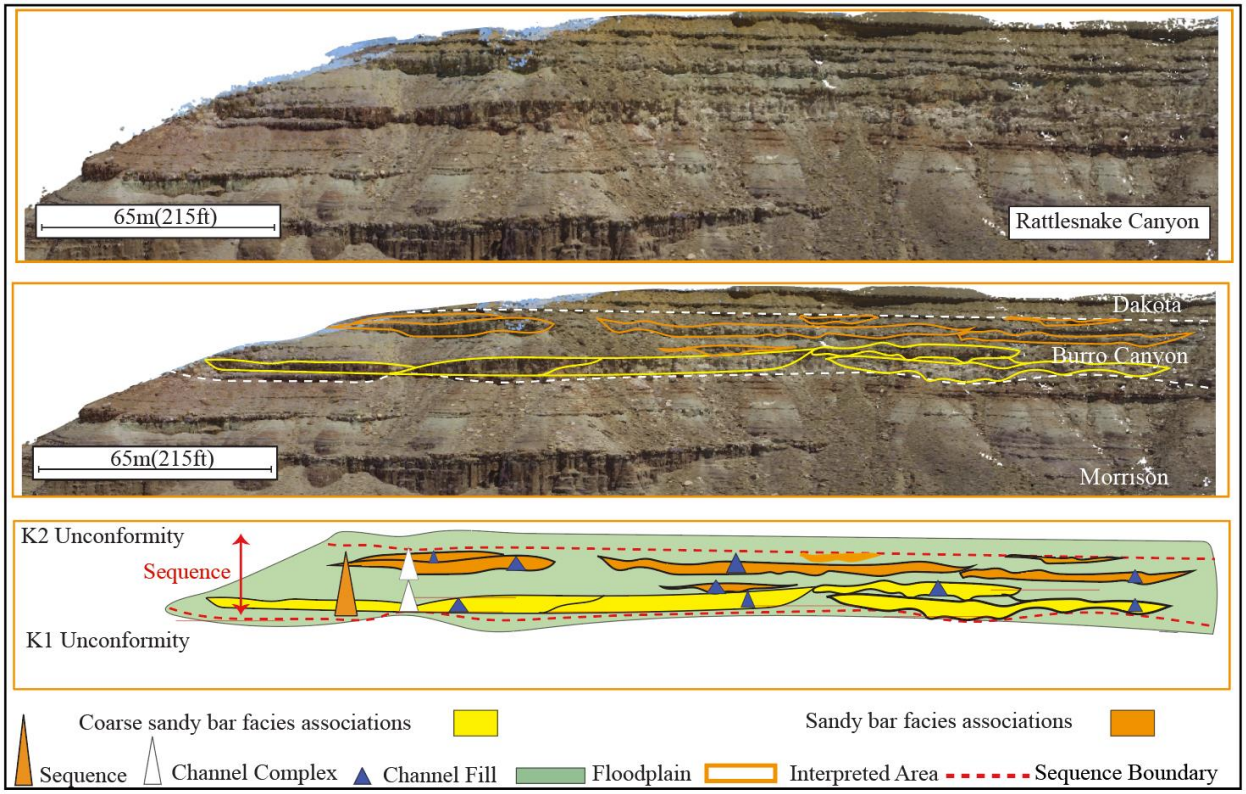

Figure 1-27A: UAV- based photogrammetry model for the Rattlesnake canyon. The top and base of Burro Canyon Formation (K2 and K1 unconformities) are represented in red lines. Intermediate-to- large-scale architectural elements are interpreted using UAV-based outcrop renderings. The hierarchical interpretation associated for this outcrop shows a non-amalgamated architectural element in the upper section of the Burro Canyon Formation and amalgamated channel complex element in the lower interval of the formation. Model boundaries are shown as orange lines; the coarse sandy bar facies associations are shown in yellow and the sandy bar facies associations in orange. Floodplain deposits are shown in light green. Hierarchical elements are shown as triangles. For this section three measured sections were evaluated and used to constrain the mosaic interpretations.

.

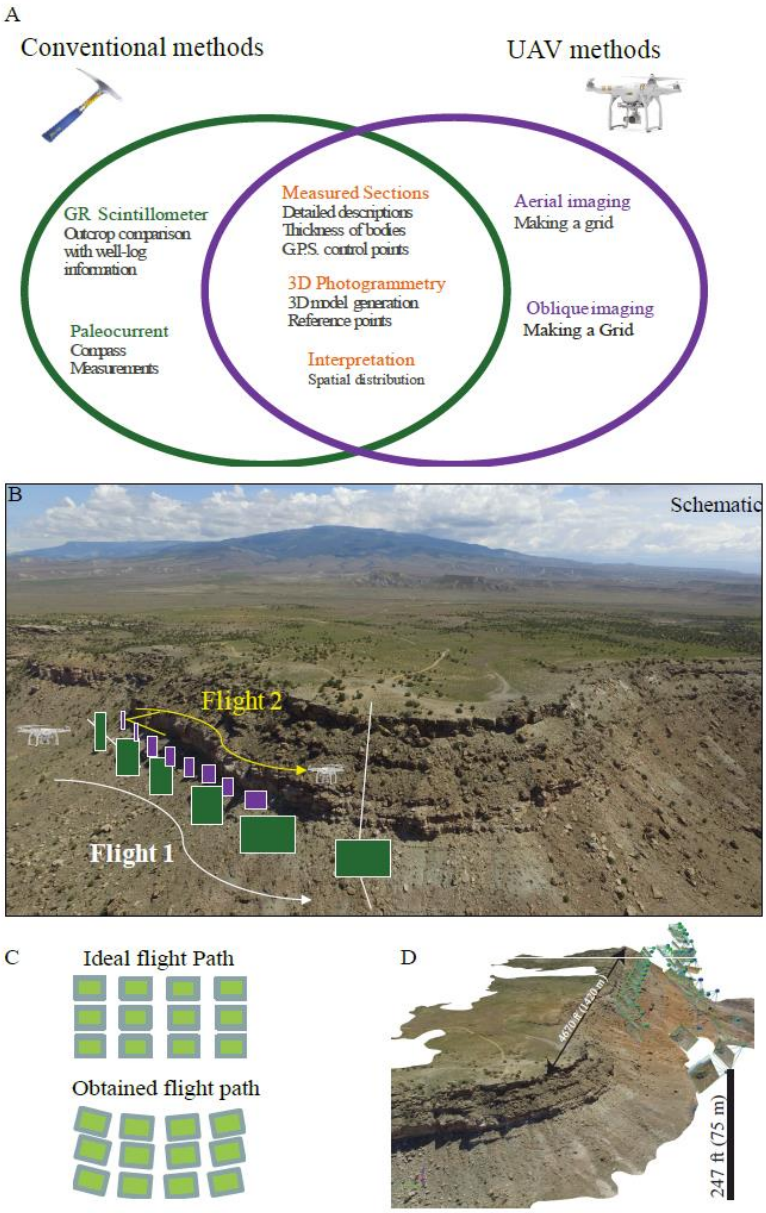

Figure 1-28A: (A) Diagram of the methodology used in this study. Green circle contains the steps used in conventional fieldwork methods. Purple circle contains the steps used for UAV-based photogrammetry modeling approach. (B) To create the UAV-based photogrammetry models at least two flight paths were performed in every outcrop. Flight one shows a schematic flight path 50 m (165 ft) close to the outcrop flight two shows a path 150 m (490 ft) apart from the outcrop. The separation from the outcrop face was done to obtain different details in the images taken using the drone. (C) Top shows green squares representing an idealized grid of images, however, due to climatic and environmental conditions the obtained grid is often deformed as it is shown in the bottom image. The planned grid required a minimum of 75% overlapping for successful creation of the outcrop reconstruction models. (D) Outcrop reconstruction of the Escalante Canyon. The images show the approximate dimensions of the reconstructed model. Outcrop reconstruction models were done using Pix4DMapper Pro.

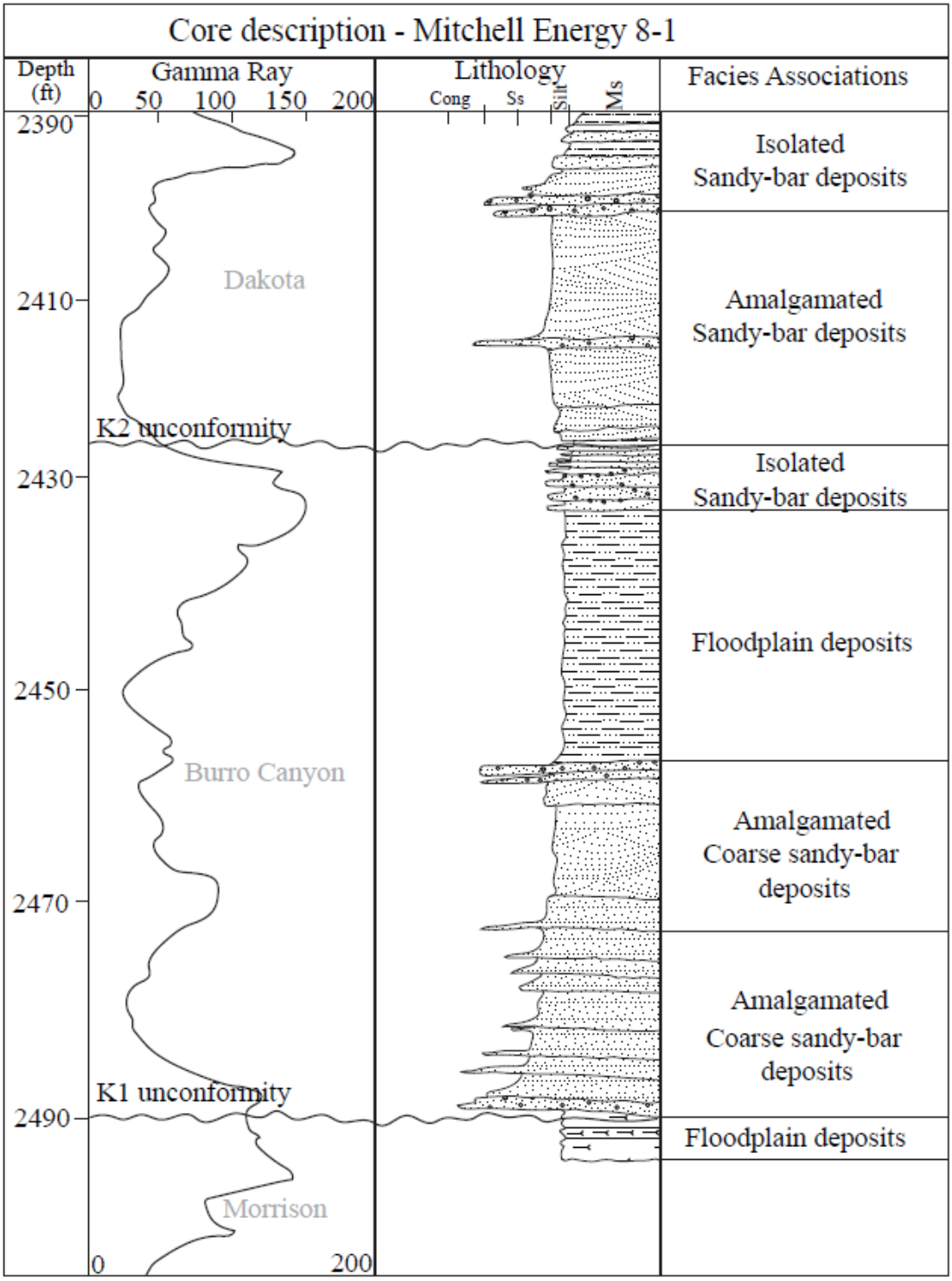

Figure 1-29A: Core description for the Mitchell Energy 8-1 Federal well. Gamma-ray increases from left to right. Facies associations are described along the Burro Canyon Formation. The overall sequence is fining upward in the study area and contains high-energy, low-sinuosity to lower-energy, fluvial deposits with thick intervals of mudstone floodplain deposits.

Table 2-3: Dimension measurements for channel fill elements within the Burro Canyon Formation from the studied outcrops

Channel fill dimensions

Channel fill	Location	Channel complex	Apparent Width (ft)	Apparent Thickness (ft)	Interval
1	Mack Ridge	1	167.28	8.21	U
2	Mack Ridge	1	154.16	9.79	U
3	Mack Ridge	1	115.78	9.76	U
4	Mack Ridge	1	248.46	18.27	U
5	Mack Ridge	1	70.19	7.50	U
6	Mack Ridge	2	96.60	4.74	U
7	Mack Ridge	2	50.74	2.40	U
8	Mack Ridge	2	133.17	7.64	U
9	Mack Ridge	2	214.51	9.42	U
10	Mack Ridge	3	131.46	17.48	U
11	Mack Ridge	3	84.30	6.46	U
12	Mack Ridge	3	164.66	13.65	U
13	Mack Ridge	4	170.56	4.79	U
14	Mack Ridge	4	73.01	4.23	U
15	Mack Ridge	4	108.37	11.34	U
16	Mack Ridge	4	92.27	5.47	U
17	Mack Ridge	4	147.67	6.12	U
18	Mack Ridge	4	76.00	6.15	U
19	Mack Ridge	4	123.59	4.46	U
20	Mack Ridge	4	180.07	5.44	U
21	Mack Ridge	4	119.06	3.58	U
22	Mack Ridge	4	116.41	7.50	U
23	Mack Ridge	4	127.92	6.23	U
24	Mack Ridge	4	74.78	6.82	U
25	Mack Ridge	4	107.19	11.84	U
26	Mack Ridge	4	177.12	9.59	U
27	Mack Ridge	4	126.28	5.44	U
28	Mack Ridge	4	110.54	3.58	U
29	Mack Ridge	4	145.96	3.78	U
30	Mack Ridge	4	138.25	9.45	U
31	Mack Ridge	4	93.35	9.59	U
32	Mack Ridge	4	108.47	5.16	U
33	Mack Ridge	4	96.40	10.43	U

34	Mack Ridge	5	74.46	3.24	U
35	Mack Ridge	5	98.30	4.71	U
36	Mack Ridge	5	52.15	6.20	U
37	Mack Ridge	5	58.38	3.95	U
38	Mack Ridge	U	134.91	3.53	U
39	Mack Ridge	U	77.41	2.31	U
40	Mack Ridge	6	50.81	4.79	U
41	Mack Ridge	6	142.35	4.48	U
42	Mack Ridge	6	105.88	3.44	U
43	Mack Ridge	6	107.81	3.72	U
44	Mack Ridge	6	90.36	6.77	U
45	Mack Ridge	7	196.80	4.34	U
46	Mack Ridge	7	183.68	5.98	U
47	Mack Ridge	7	152.85	5.08	U
48	Mack Ridge	7	112.83	5.36	U
49	Mack Ridge	7	97.28	4.82	U
50	Mack Ridge	8	41.98	3.95	U
51	Mack Ridge	8	40.34	4.15	U
52	Mack Ridge	9	71.50	1.97	U
53	Mack Ridge	9	53.69	2.45	U
54	Mack Ridge	10	59.86	3.53	U
55	Mack Ridge	10	76.85	7.05	U
56	Mack Ridge	10	109.72	5.89	U
57	Mack Ridge	10	87.15	4.43	U
58	Mack Ridge	11	124.64	8.01	U
59	Whitewater	1	593.68	15.23	L
60	Whitewater	1	820.00	20.64	L
61	Whitewater	1	695.36	32.54	L
62	Whitewater	1	685.52	17.40	L
63	Whitewater	1	521.52	27.58	L
64	Whitewater	1	295.20	16.07	L
65	Whitewater	1	662.56	15.14	L
66	Whitewater	1	508.40	12.32	L
67	Whitewater	1	574.00	11.56	L
68	Whitewater	1	672.40	16.75	L
69	Whitewater	1	1006.96	29.05	L
70	Whitewater	1	957.76	23.69	L
71	Whitewater	1	774.08	28.48	L

72	Whitewater	1	534.64	25.38	L
73	Whitewater	1	203.36	14.38	L
74	Whitewater	1	783.92	54.99	L
75	Whitewater	1	546.45	19.18	L
76	Whitewater	1	490.36	16.19	L
77	Whitewater	1	370.64	11.22	L
78	Whitewater	1	344.40	12.97	L
79	Whitewater	1	751.12	30.74	L
80	Whitewater	1	457.23	26.06	L
81	Whitewater	1	380.48	15.23	L
82	Whitewater	1	580.56	14.95	L
83	Whitewater	1	754.40	26.37	L
84	Whitewater	1	898.72	21.86	L
85	Whitewater	1	829.84	27.92	L
86	Whitewater	1	475.60	12.97	L
87	Whitewater	1	410.00	8.49	L
88	Whitewater	1	389.34	21.15	L
89	Whitewater	1	698.64	34.69	L
90	Whitewater	1	518.24	29.89	L
91	Whitewater	1	577.28	20.33	L
92	Whitewater	1	328.00	12.61	L
93	Whitewater	1	465.76	16.36	L
94	Whitewater	1	587.12	15.79	L
95	Whitewater	1	370.64	10.43	L
96	Whitewater	1	120.38	8.74	L
97	Whitewater	2	202.70	5.30	U
98	Whitewater	2	114.80	3.38	U
99	Whitewater	2	82.98	2.76	U
100	Whitewater	3	458.54	8.69	U
101	Whitewater	3	242.72	7.05	U
102	Whitewater	3	164.00	4.00	U
103	Whitewater	3	161.74	9.05	U
104	Whitewater	4	104.99	9.53	U
105	Whitewater	4	83.31	7.05	U
106	Whitewater	4	211.20	9.17	U
107	Whitewater	4	357.82	20.30	U
108	Whitewater	4	102.34	12.69	U
109	Whitewater	4	301.76	15.23	U

110	Whitewater	4	251.64	9.31	U
111	Whitewater	4	136.61	13.54	U
112	Whitewater	5	206.90	7.61	U
113	Whitewater	5	261.28	17.40	U
114	Whitewater	6	203.49	10.72	U
115	Whitewater	6	129.63	6.77	U
116	Whitewater	6	124.02	6.60	U
117	Whitewater	6	125.20	6.77	U
118	Whitewater	6	249.77	7.90	U
119	Whitewater	6	192.50	25.52	U
120	Whitewater	6	342.43	11.56	U
121	Whitewater	6	319.80	11.00	U
122	Whitewater	6	290.28	12.92	U
123	Whitewater	6	287.00	10.43	U
124	Whitewater	6	303.40	9.95	U
125	Whitewater	6	220.28	13.93	U
126	Whitewater	6	254.53	21.71	U
127	Whitewater	7	143.40	7.78	U
128	Whitewater	7	235.50	5.36	U
129	Whitewater	7	168.99	8.74	U
130	Deercreek	0	145.96	7.81	L
131	Deercreek	0	157.05	5.72	L
132	Deercreek	0	355.72	10.72	L
133	Deercreek	0	201.39	8.32	L
134	Deercreek	0	234.19	9.31	L
135	Deercreek	1	646.16	28.48	L
136	Deercreek	1	165.77	3.10	L
137	Deercreek	1	223.11	10.97	L
138	Deercreek	2	133.33	4.79	L
139	Deercreek	2	132.48	4.34	L
140	Deercreek	2	53.60	3.07	L
141	Deercreek	3	341.12	7.50	L
142	Deercreek	3	369.66	11.79	L
143	Deercreek	3	401.90	37.14	L
144	Deercreek	3	341.78	14.18	L
145	Deercreek	3	738.00	27.86	L
146	Deercreek	4	393.27	14.95	L
147	Deercreek	4	184.63	9.87	L

148	Deercreek	4	512.14	24.73	L
149	Deercreek	4	623.20	20.87	L
150	Deercreek	4	469.04	21.15	L
151	Deercreek	5	373.92	10.58	U
152	Deercreek	5	432.96	9.64	U
153	Deercreek	5	305.04	6.23	U
154	Deercreek	5	298.38	7.33	U
155	Deercreek	5	285.26	9.62	U
156	Deercreek	5	155.18	7.44	U
157	Deercreek	6	235.50	3.55	U
158	Deercreek	6	105.75	8.74	U
159	Deercreek	7	204.34	11.93	U
160	Deercreek	7	97.22	14.27	U
161	Deercreek	6	130.12	6.97	U
162	Deercreek	6	177.58	10.32	U
163	Deercreek	7	114.47	7.92	U
164	Deercreek	6	127.40	13.25	U
165	Deercreek	7	139.99	6.35	U
166	Deercreek	6	157.74	4.91	U
167	Deercreek	7	189.85	10.07	U
168	Deercreek	6	240.65	14.33	U
169	Deercreek	8	263.68	7.90	U
170	Deercreek	8	268.30	12.13	U
171	Deercreek	8	203.43	9.11	U
172	Deercreek	8	165.80	11.05	U
173	Deercreek	8	153.08	7.28	U
174	Deercreek	8	172.86	7.78	U
175	Deercreek	8	80.26	5.64	U
176	Deercreek	8	66.58	8.15	U
177	Deercreek	8	97.74	13.54	U
178	Deercreek	8	208.05	6.15	U
179	Deercreek	8	172.36	5.70	U
180	Deercreek	8	209.17	7.70	U
181	Deercreek	8	129.46	6.01	U
182	Deercreek	8	74.55	1.89	U
183	Deercreek	8	176.46	3.67	U
184	Deercreek	8	84.49	2.68	U
185	Deercreek	8	82.23	3.50	U

186	Deercreek	8	140.97	8.18	U
187	Deercreek	8	75.11	3.67	U
188	Deercreek	8	96.37	2.34	U
189	Deercreek	8	36.97	2.85	U
190	Deercreek	U	71.44	6.20	U
191	Deercreek	U	52.87	6.54	U
192	Deercreek	U	47.30	3.38	U
193	Deercreek	U	29.82	3.58	U
194	Deercreek	U	30.08	3.21	U
195	Deercreek	9	66.26	2.90	U
196	Deercreek	9	100.47	3.81	U
197	Deercreek	9	50.22	3.10	U
198	Deercreek	9	64.48	3.07	U
199	Deercreek	9	38.11	2.14	U
200	Deercreek	9	77.54	3.72	U
201	Deercreek	9	85.08	4.51	U
202	Deercreek	9	101.61	5.27	U
203	Deercreek	9	51.40	6.40	U
204	Deercreek	9	128.51	5.75	U
205	Deercreek	10	220.45	15.59	U
206	Deercreek	10	160.52	15.12	U
207	Deercreek	10	114.93	5.78	U
208	Deercreek	10	111.32	3.10	U
209	Deercreek	10	103.58	6.29	U
210	Deercreek	10	75.21	9.02	U
211	Deercreek	10	136.55	6.91	U
212	Deercreek	10	213.33	6.35	U
213	Deercreek	10	153.90	7.36	U
214	Deercreek	10	122.77	9.67	U
215	Deercreek	10	132.54	9.81	U
216	Deercreek	10	121.16	2.93	U
217	Deercreek	10	72.16	7.22	U
218	Deercreek	10	83.31	5.08	U
219	Deercreek	10	25.58	4.79	U
220	Deercreek	10	167.51	8.60	U
221	Deercreek	10	119.00	15.54	U
222	Escalante North	1	310.68	13.11	L
223	Escalante North	1	276.04	9.14	L

224	Escalante North	1	205.10	14.47	L
225	Escalante North	1	228.98	22.98	L
226	Escalante North	1	306.52	27.35	L
227	Escalante North	1	488.72	42.02	L
228	Escalante North	1	182.53	21.60	L
229	Escalante North	1	211.26	9.81	L
230	Escalante North	1	126.61	8.74	L
231	Escalante North	1	130.51	16.47	L
232	Escalante North	1	205.39	9.14	L
233	Escalante North	1	162.69	16.36	L
234	Escalante North	1	220.09	7.39	L
235	Escalante North	1	175.91	20.78	L
236	Escalante North	1	196.24	8.54	L
237	Escalante North	1	251.05	19.63	L
238	Escalante North	2	251.02	7.56	L
239	Escalante North	2	189.72	9.39	L
240	Escalante North	2	121.46	9.08	L
241	Escalante North	2	212.41	15.96	L
242	Escalante North	2	287.33	9.87	L
243	Escalante North	2	203.36	10.46	L
244	Escalante North	3	206.80	24.53	L
245	Escalante North	3	275.26	13.00	L
246	Escalante North	3	537.92	20.36	L
247	Escalante North	4	277.72	22.56	L
248	Escalante North	4	344.99	17.68	L
249	Escalante North	4	387.37	16.89	L
250	Escalante North	4	405.87	15.00	L
251	Escalante North	4	583.48	26.93	L
252	Escalante North	4	497.28	14.27	L
253	Escalante North	4	532.08	23.72	L
254	Escalante North	4	363.56	24.34	L
255	Escalante North	4	326.00	31.58	L
256	Escalante North	4	312.52	29.69	L
257	Escalante North	4	256.17	34.12	L
258	Escalante North	4	487.41	31.53	L
259	Escalante North	4	547.43	30.17	L
260	Escalante North	4	350.96	27.58	L
261	Escalante North	4	321.28	23.66	L

262	Escalante North	4	329.64	22.00	L
263	Escalante North	4	434.17	29.47	L
264	Escalante North	4	540.64	17.77	L
265	Escalante North	4	364.01	26.68	L
266	Escalante North	4	287.98	21.09	L
267	Escalante North	4	359.82	25.41	L
268	Escalante North	4	238.82	26.34	L
269	Escalante North	4	397.24	36.94	L
270	Escalante North	4	361.23	25.35	L
271	Escalante North	4	354.99	19.29	L
272	Escalante North	4	591.02	26.54	L
273	Escalante North	4	405.77	21.40	L
274	Escalante North	4	469.34	30.09	L
275	Escalante North	4	196.44	6.51	L
276	Escalante North	5	206.12	9.00	L
277	Escalante North	5	152.09	4.23	U
278	Escalante North	5	195.03	7.67	U
279	Escalante North	5	189.58	12.13	U
280	Escalante North	5	170.82	8.49	U
281	Escalante North	5	252.82	14.16	U
282	Escalante North	5	88.59	9.59	U
283	Escalante North	5	164.92	12.30	U
284	Escalante North	5	219.01	9.31	U
285	Escalante North	5	165.54	15.23	U
286	Escalante North	5	121.29	8.88	U
287	Escalante North	5	134.25	9.36	U
288	Escalante North	5	119.42	8.77	U
289	Escalante North	5	246.07	11.03	U
290	Escalante North	5	213.40	7.28	U
291	Escalante North	5	131.92	6.88	U
292	Escalante North	6	185.55	15.45	U
293	Escalante North	6	216.12	12.07	U
294	Escalante North	6	190.24	8.18	U
295	Escalante North	6	163.70	8.74	U
296	Escalante North	6	137.07	5.67	U
297	Escalante North	6	106.70	7.47	U
298	Escalante North	6	123.85	9.87	U
299	Escalante North	6	139.40	9.08	U

300	Escalante North	6	174.82	9.87	U
301	Escalante North	0	191.06	11.84	U
302	Escalante North	0	206.15	10.35	U
303	Escalante North	0	111.00	10.72	U
304	Escalante North	0	140.71	9.31	U
305	Escalante North	0	147.63	10.15	U
306	Escalante North	0	194.83	6.77	U
307	Escalante North	0	145.89	10.43	U
308	Escalante North	0	80.49	9.93	U
309	Escalante North	0	300.05	14.66	U
310	Escalante North	0	156.95	8.74	U
311	Escalante North	0	105.91	8.18	U
312	Escalante North	0	147.27	9.17	U
313	Escalante North	0	228.62	9.87	U
314	Escalante	1	235.18	9.59	L
315	Escalante	1	210.05	23.97	L
316	Escalante	1	291.99	12.69	L
317	Escalante	1	111.52	5.87	L
318	Escalante	1	127.76	12.01	L
319	Escalante	1	273.42	13.59	L
320	Escalante	1	199.29	13.34	L
321	Escalante	2	230.65	15.34	L
322	Escalante	2	146.06	10.55	L
323	Escalante	2	311.99	12.13	L
324	Escalante	2	130.61	11.84	L
325	Escalante	2	152.39	9.59	L
326	Escalante	2	160.88	10.86	L
327	Escalante	2	181.12	9.59	L
328	Escalante	2	147.27	13.25	L
329	Escalante	2	186.14	19.91	L
330	Escalante	2	313.93	18.39	L
331	Escalante	0	163.31	12.92	L
332	Escalante	0	113.16	12.41	L
333	Rattlesnake	1	314.49	13.31	L
334	Rattlesnake	1	185.25	8.83	L
335	Rattlesnake	1	236.29	14.52	L
336	Rattlesnake	1	206.71	22.00	L
337	Rattlesnake	1	347.68	26.31	L

338	Rattlesnake	1	296.18	9.28	L
339	Rattlesnake	1	220.42	20.28	L
340	Rattlesnake	1	527.75	16.44	L
341	Rattlesnake	1	316.88	22.59	L
342	Rattlesnake	1	311.08	10.43	L
343	Rattlesnake	1	243.38	16.81	L
344	Rattlesnake	1	329.38	24.36	L
345	Rattlesnake	1	290.94	28.76	L
346	Rattlesnake	1	260.10	20.08	L
347	Rattlesnake	1	240.33	25.10	U
348	Rattlesnake	1	361.78	19.77	U
349	Rattlesnake	1	382.12	27.18	U
350	Escalante	1	265.88	12.55	L
351	Escalante	1	272.60	13.90	L
352	Escalante	1	290.54	13.42	L
353	Escalante	1	295.30	8.07	L
354	Escalante	1	372.28	19.26	L
355	Escalante	1	342.89	13.56	L
356	Escalante	1	368.34	17.29	L
357	Escalante	1	442.80	15.40	L
358	Escalante	1	317.14	14.04	L
359	Escalante	1	436.90	18.27	L
360	Escalante	1	571.70	16.92	L
361	Escalante	1	305.93	12.97	L
362	Escalante	1	335.45	15.06	L
363	Escalante	1	333.58	16.58	L
364	Escalante	1	410.00	20.53	L
365	Escalante	1	406.72	13.59	L
366	Escalante	1	384.42	15.06	L
367	Escalante	2	243.31	24.68	L
368	Escalante	2	254.30	14.58	L
369	Escalante	2	210.90	16.22	L
370	Escalante	2	200.74	13.00	L
371	Escalante	1	192.54	8.29	U
372	Escalante	1	184.27	13.71	U
373	Escalante	1	240.10	7.05	U
374	Escalante	2	181.32	13.54	U
375	Escalante	2	178.37	8.26	U

376	Escalante	2	150.39	12.15	U
377	Escalante	2	106.50	15.09	U
378	Escalante	2	140.29	9.64	U
379	Escalante	2	154.09	10.41	U
380	Escalante	2	169.87	6.60	U
381	Escalante	2	205.56	11.00	U
382	Escalante	2	191.95	9.84	U
383	Escalante	3	158.52	6.15	U
384	Escalante	3	217.30	14.49	U
385	Escalante	3	239.93	7.59	U
386	Escalante	3	76.26	4.77	U
387	Rattlesnake	2	202.15	6.23	U
388	Rattlesnake	2	181.19	6.35	U
389	Rattlesnake	2	101.58	4.96	U
390	Rattlesnake	2	356.77	16.72	U
391	Rattlesnake	2	302.32	15.57	U
392	Rattlesnake	3	287.00	8.74	U
393	Rattlesnake	3	294.22	9.17	U
394	Rattlesnake	3	296.09	8.18	U
395	Rattlesnake	3	89.41	9.45	U
396	Rattlesnake	3	85.15	4.85	U
397	Rattlesnake	3	183.55	13.45	U
398	Rattlesnake	3	267.35	14.10	U
399	Rattlesnake	4	196.31	8.49	U
400	Rattlesnake	4	217.10	7.47	U
401	Rattlesnake	4	236.78	15.37	U
402	Rattlesnake	4	220.38	16.58	U
403	Rattlesnake	4	230.62	18.53	U
404	Rattlesnake	4	397.54	3.53	U
405	Rattlesnake	5	197.69	10.29	U
406	Rattlesnake	5	214.22	13.56	U
407	Rattlesnake	5	246.75	6.88	U
408	Rattlesnake	5	154.19	5.84	U
409	Rattlesnake	6	253.68	8.97	U
410	Rattlesnake	6	219.66	6.40	U
411	Rattlesnake	6	143.99	10.58	U
412	Rattlesnake	6	183.81	6.49	U
413	Rattlesnake	6	158.72	12.30	U

414	Rattlesnake	6	107.72	8.83	U

Paleocurrent measurements

Table 2-4: Compiled paleocurrent measurements within the study area. Data collected along each of the six measured sections and nearby outcrop locations.

No.	Dip		Direction	Latitude	Longitude
1	18.5		22.2	38.97	-108.46
2	15.8		70.5	38.97	-108.46
3	22.9		81.6	38.97	-108.46
4	21.9		73.9	38.97	-108.46
5	10.2		71.7	38.97	-108.46
6	16.7		59.1	38.97	-108.46
7	35.0		62.1	38.97	-108.46
8	14.7		33.5	38.97	-108.46
9	25.4		50.0	38.97	-108.46
10	25.7		56.8	38.97	-108.46
11	27.0		103.8	38.97	-108.46
12	24.1		91.7	38.97	-108.46
13	21.6		92.8	38.97	-108.46
14	9.5		45.8	38.97	-108.46
15	9.5		45.8	38.97	-108.46
16	14.6		34.4	38.97	-108.46
17	19.4		47.9	38.97	-108.46
18	17.5		48.5	38.97	-108.46
19	28.3		131.3	38.97	-108.46
20	17.6		40.9	38.97	-108.46
21	30.0		60.3	38.97	-108.46
22	28.1		54.0	38.97	-108.46
23	33.8		82.9	38.97	-108.46
24	10.8		297.9	38.86	-108.34
25	15.2		6.5	38.86	-108.34
26	14.8		2.5	38.86	-108.34
27	20.6		261.4	38.86	-108.34
28	6.8		18.8	38.86	-108.34
29	5.5		42.6	38.86	-108.34
30	26.6		30.5	38.86	-108.34
31	23.6		358.6	38.86	-108.34
32	22.1		0.1	38.86	-108.34
33	22.9		12.0	38.86	-108.34
34	20.7		352.0	38.86	-108.34

35	14.3		356.2	38.86	-108.34
36	19.9		38.3	38.86	-108.34
37	6.7		22.6	38.86	-108.34
38	14.7		49.0	38.86	-108.34
39	20.2		61.9	38.86	-108.34
40	29.7		48.5	38.86	-108.34
41	4.2		28.8	38.86	-108.34
42	14.3		88.3	38.86	-108.34
43	20.8		64.6	38.86	-108.34
44	14.2		55.7	38.86	-108.34
45	21.0		65.1	38.86	-108.34
46	29.4		40.8	38.86	-108.34
47	33.7		32.7	38.86	-108.34
48	16.3		70.6	38.86	-108.34
49	27.2		74.9	38.86	-108.34
50	21.3		57.9	38.86	-108.34
51	11.5		58.1	38.86	-108.34
52	14.4		98.5	38.86	-108.34
53	5.7		48.9	38.86	-108.34
54	24.9		36.4	38.86	-108.34
55	24.5		61.2	38.86	-108.34
56	12.7		79.5	38.86	-108.34
57	23.4		28.1	38.86	-108.34
58	28.1		37.3	38.86	-108.34
59	29.1		350.1	38.86	-108.34
60	29.6		9.8	38.86	-108.34
61	14.3		86.8	38.86	-108.34
62	15.7		91.0	38.86	-108.34
63	15.8		78.2	38.86	-108.34
64	10.3		47.9	38.86	-108.34
65	25.8		82.5	38.86	-108.34
66	12.0		47.5	38.86	-108.34
67	27.9		43.1	38.86	-108.34
68	34.1		12.6	38.86	-108.34
69	18.0		78.9	38.86	-108.34
70	18.0		62.3	38.86	-108.34
71	18.4		67.2	38.86	-108.34
72	32.5		52.1	38.86	-108.34
73	20.7		67.4	38.86	-108.34
74	20.3		84.8	38.86	-108.34
75	22.2		65.6	38.86	-108.34
76	25.7		79.0	38.86	-108.34
77	50.8		56.9	38.86	-108.34

78	13.8		104.6	38.86	-108.34
79	8.9		99.8	38.86	-108.34
80	20.1		76.7	38.86	-108.34
81	15.5		71.2	38.86	-108.34
82	9.5		104.0	38.86	-108.34
83	20.1		59.2	38.86	-108.34
84	29.1		39.1	38.86	-108.34
85	31.8		22.3	38.86	-108.34
86	30.1		38.2	38.86	-108.34
87	16.2		79.9	38.86	-108.34
88	18.7		69.6	38.86	-108.34
89	24.0		27.0	38.86	-108.34
90	14.8		22.7	38.86	-108.34
91	10.6		63.4	38.86	-108.34
92	20.0		58.7	38.86	-108.34
93	26.0		10.0	38.86	-108.34
94	21.3		8.0	38.86	-108.34
95	17.5		37.1	38.86	-108.34
96	20.1		27.3	38.86	-108.34
97	14.4		46.1	38.86	-108.34
98	20.1		38.5	38.86	-108.34
99	15.4		55.5	38.86	-108.34
100	7.0		218.4	38.77	-108.24
101	11.8		332.3	38.77	-108.24
102	5.9		5.5	38.77	-108.24
103	11.5		37.2	38.77	-108.24
104	16.8		9.7	38.77	-108.24
105	30.6		25.5	38.77	-108.24
106	5.2		90.3	38.77	-108.24
107	5.8		164.5	38.77	-108.24
108	8.7		72.3	38.77	-108.24
109	9.0		13.4	38.77	-108.24
110	14.9		65.6	38.77	-108.24
111	1.6		277.0	38.77	-108.24
112	7.7		59.1	38.77	-108.24
113	6.4		90.8	38.77	-108.24
114	4.9		190.8	38.77	-108.24
115	7.4		312.1	38.77	-108.24
116	8.5		120.1	38.77	-108.24
117	6.7		145.5	38.77	-108.24
118	6.2		77.3	38.77	-108.24
119	4.6		350.5	38.77	-108.24
120	2.0		224.7	38.77	-108.24

121	28.0		85.0	38.77	-108.24
122	19.0		88.0	38.77	-108.24
123	17.0		96.0	38.77	-108.24
124	16.0		82.0	38.77	-108.24
125	16.0		85.0	38.77	-108.24
126	20.0		181.0	38.77	-108.24
127	30.0		60.0	38.77	-108.24
128	30.0		30.0	38.77	-108.24
129	23.0		32.0	38.77	-108.24
130	23.0		80.0	38.77	-108.24
131	5.0		358.0	38.77	-108.24
132	6.0		65.0	38.77	-108.24
133	25.0		32.0	38.77	-108.24
134	12.0		344.0	38.77	-108.24
135	15.0		45.0	38.77	-108.24
136	30.0		25.0	38.77	-108.24
137	20.0		40.0	38.77	-108.24
138	22.0		40.0	38.77	-108.24
139	17.0		67.0	38.77	-108.24
140	32.0		33.0	38.77	-108.24
141	19.0		28.0	38.77	-108.24
142	27.0		70.0	38.77	-108.24
143	24.0		65.0	38.77	-108.24
144	20.0		25.0	38.77	-108.24
145	22.0		60.0	38.77	-108.24
146	3.5		35.8	38.76	-108.25
147	2.4		107.9	38.76	-108.25
148	8.5		68.0	38.76	-108.25
149	15.2		81.8	38.76	-108.25
150	15.2		81.6	38.76	-108.25
151	2.3		326.0	38.76	-108.25
152	1.6		339.6	38.77	-108.26
153	61.2		145.0	38.77	-108.24
154	32.2		10.0	38.77	-108.25
155	21.9		343.3	38.77	-108.25
156	11.3		36.0	38.77	-108.25
157	12.2		13.0	38.77	-108.25
158	16.4		359.5	38.77	-108.25
159	10.5		58.8	38.77	-108.25
160	20.0		66.7	38.77	-108.25
161	20.5		58.9	38.77	-108.25
162	11.4		354.6	38.77	-108.25
163	16.3		46.3	38.77	-108.25

164	7.4		36.6	38.77	-108.25
165	4.3		108.3	38.77	-108.25
166	13.2		62.1	38.76	-108.25
167	14.2		50.4	38.76	-108.25
168	9.8		7.2	38.76	-108.25
169	15.4		130.6	38.76	-108.25
170	6.8		141.5	38.76	-108.25
171	2.4		55.0	38.76	-108.25
172	6.7		71.5	38.76	-108.25
173	34.0		11.6	38.77	-108.25
174	17.1		336.6	38.77	-108.25
175	13.2		279.2	38.77	-108.25
176	13.4		295.1	38.77	-108.25
177	18.7		339.8	38.77	-108.25
178	28.1		343.0	38.77	-108.25
179	30.6		321.5	38.76	-108.26
180	24.8		324.7	38.76	-108.25
181	20.9		48.1	38.77	-108.26
182	19.3		48.7	38.77	-108.25
183	20.5		337.0	38.77	-108.26
184	6.4		332.0	38.77	-108.26
185	23.7		359.9	38.77	-108.26
186	31.5		15.1	38.77	-108.26
187	24.8		26.0	38.77	-108.26
188	22.8		32.7	38.77	-108.26
189	34.1		42.4	38.77	-108.26
190	3.2		11.4	38.77	-108.26
191	9.1		146.4	38.77	-108.26
192	28.0		45.6	38.77	-108.26
193	20.8		25.4	38.76	-108.25
194	17.3		5.2	38.76	-108.25
195	17.3		352.1	38.76	-108.25
196	28.3		24.5	38.76	-108.25
197	21.7		36.5	38.76	-108.25
198	33.9		13.2	38.77	-108.25
199	25.0		155.0	38.77	-108.24
200	24.0		110.0	38.77	-108.24
201	19.0		42.0	38.77	-108.24
202	14.0		60.0	38.77	-108.24
203	11.0		41.0	38.77	-108.24
204	6.0		104.0	38.77	-108.24
205	27.0		60.0	38.77	-108.24
206	9.0		1.0	38.77	-108.24

207	5.0		60.0	38.77	-108.24
208	15.0		6.0	38.77	-108.24
209	19.0		8.0	38.77	-108.24
210	28.0		358.0	38.77	-108.24
211	2.8		155.0	38.77	-108.28
212	1.0		356.2	38.77	-108.28
213	0.4		322.5	38.77	-108.28
214	10.9		251.8	38.77	-108.28
215	12.7		175.3	38.77	-108.28
216	16.3		327.3	38.77	-108.28
217	26.9		33.1	38.77	-108.28
218	25.4		56.0	38.77	-108.28
219	7.2		174.1	38.77	-108.28
220	24.9		114.3	38.77	-108.28
221	10.8		271.5	38.77	-108.28
222	6.7		60.7	38.77	-108.28
223	10.9		115.7	38.77	-108.28
224	8.6		116.2	38.77	-108.28
225	7.3		176.7	38.77	-108.28
226	7.8		164.2	38.77	-108.28
227	4.4		12.5	38.77	-108.28
228	16.6		111.9	38.77	-108.28
229	2.9		165.8	38.77	-108.28
230	12.4		125.2	38.77	-108.28
231	13.5		96.3	38.77	-108.28
232	6.4		203.1	38.77	-108.28
233	7.9		166.5	38.77	-108.28
234	2.3		182.3	38.77	-108.28
235	13.0		110.4	38.77	-108.28
236	6.9		97.9	38.77	-108.28
237	1.8		27.6	38.77	-108.28
238	16.5		352.9	38.77	-108.28
239	15.1		170.9	38.77	-108.28
240	4.0		63.9	38.77	-108.28
241	16.1		61.2	38.77	-108.28
242	8.5		314.7	38.77	-108.28
243	16.0		351.4	38.77	-108.28
244	9.3		98.9	38.77	-108.28
245	10.4		169.4	38.77	-108.28
246	17.9		66.5	38.77	-108.28
247	28.1		40.1	38.77	-108.28
248	25.0		39.6	38.77	-108.28
249	5.7		20.2	38.77	-108.28

250	32.7		48.7	38.77	-108.28
251	27.7		44.6	38.77	-108.28
252	9.4		322.6	38.77	-108.28
253	18.0		46.6	38.77	-108.28
254	22.8		31.8	38.77	-108.28
255	8.2		349.7	38.77	-108.28
256	10.1		55.1	38.77	-108.28
257	9.7		94.3	38.77	-108.28
258	24.2		45.0	38.77	-108.28
259	10.1		68.1	38.77	-108.28
260	14.6		85.5	38.77	-108.28
261	11.5		84.5	38.77	-108.28
262	12.6		91.6	38.77	-108.28
263	7.8		311.8	38.77	-108.28
264	8.6		48.2	38.77	-108.28
265	8.3		310.7	38.77	-108.28
266	9.7		135.5	38.77	-108.28
267	11.3		22.9	38.77	-108.28
268	19.2		60.4	38.77	-108.28
269	25.8		71.2	38.77	-108.28
270	23.6		80.4	38.77	-108.28
271	25.3		73.6	38.77	-108.28
272	22.7		54.9	38.77	-108.28
273	15.2		65.6	38.96	-108.46
274	14.2		40.1	38.96	-108.46
275	9.3		114.6	38.96	-108.46
276	15.9		350.7	38.96	-108.46
277	23.1		16.7	38.96	-108.46
278	18.9		20.2	38.96	-108.46
279	25.8		357.9	38.96	-108.46
280	28.0		351.4	38.96	-108.46
281	29.8		2.3	38.96	-108.46
282	26.9		12.8	38.96	-108.46
283	26.8		9.2	38.96	-108.46
284	25.4		342.8	38.96	-108.46
285	20.6		308.4	38.96	-108.46
286	2.6		89.6	38.96	-108.46
287	9.6		77.3	38.96	-108.46
288	7.0		62.4	38.96	-108.46
289	4.7		24.3	38.96	-108.46
290	8.4		76.1	38.96	-108.46
291	6.9		114.1	38.96	-108.46
292	13.5		35.3	38.96	-108.46

293	10.5		42.6	38.96	-108.46
294	24.3		3.5	38.96	-108.46
295	10.4		81.7	38.96	-108.46
296	8.1		28.7	38.96	-108.46
297	25.0		14.7	38.96	-108.46
298	26.9		23.8	38.96	-108.46
299	24.6		73.1	38.96	-108.46
300	3.2		133.5	38.96	-108.46
301	16.9		4.7	38.96	-108.46
302	25.1		19.5	38.96	-108.46
303	19.7		10.3	38.96	-108.46
304	26.1		3.5	38.96	-108.46
305	18.8		16.5	38.96	-108.46
306	28.3		13.6	38.96	-108.46
307	28.0		16.8	38.96	-108.46
308	3.8		13.5	38.96	-108.46
309	37.7		24.8	38.96	-108.46
310	15.0		21.5	38.96	-108.46
311	27.2		23.1	38.96	-108.46
312	13.6		103.1	38.96	-108.46
313	23.6		97.4	38.96	-108.46
314	24.8		105.2	38.96	-108.46
315	11.5		261.3	38.96	-108.46
316	15.2		35.4	38.96	-108.46
317	14.9		23.1	38.96	-108.46
318	14.9		23.3	38.96	-108.46
319	20.1		97.2	38.96	-108.46
320	28.3		96.7	38.96	-108.46
321	23.3		87.3	38.96	-108.46
322	21.3		176.4	38.96	-108.46
323	19.3		39.6	38.96	-108.46
324	17.5		27.9	38.96	-108.46
325	17.2		26.5	38.96	-108.46
326	28.2		73.3	38.96	-108.46
327	24.9		62.4	38.96	-108.46
328	31.1		78.2	38.96	-108.46
329	18.0		130.2	38.96	-108.46
330	18.7		66.0	38.76	-108.23
331	21.2		68.1	38.76	-108.23
332	15.2		59.5	38.76	-108.23
333	23.9		47.3	38.76	-108.23
334	6.3		91.5	38.76	-108.24
335	10.0		30.5	38.76	-108.24

336	24.7		40.4	38.76	-108.24
337	9.6		73.8	38.76	-108.24
338	5.4		124.1	38.76	-108.24
339	10.7		87.5	38.76	-108.24
340	8.1		104.9	38.76	-108.24
341	20.3		79.3	38.76	-108.23
342	15.1		79.2	38.76	-108.23
343	18.9		356.7	38.76	-108.23
344	16.9		351.2	38.76	-108.23
345	11.4		322.9	38.76	-108.23
346	14.5		295.9	38.76	-108.23
347	8.7		51.2	38.76	-108.23
348	7.0		98.7	38.76	-108.23
349	4.9		103.3	38.76	-108.23
350	11.7		121.8	38.76	-108.23
351	16.7		97.1	38.76	-108.23
352	27.4		40.8	38.76	-108.23
353	6.7		94.2	38.76	-108.23
354	5.4		102.8	38.76	-108.23
355	12.9		107.4	38.76	-108.23
356	14.0		90.8	38.76	-108.23
357	10.7		114.8	38.76	-108.23
358	16.8		66.4	38.76	-108.23
359	24.2		67.0	38.76	-108.23
360	32.8		60.0	38.76	-108.23
361	16.0		104.3	38.76	-108.23
362	17.1		105.4	38.76	-108.23
363	13.7		107.2	38.76	-108.23
364	18.4		22.6	38.76	-108.23
365	9.4		14.9	38.76	-108.23
366	22.0		49.8	38.76	-108.23
367	12.1		17.4	38.76	-108.23
368	12.2		78.6	38.76	-108.23
369	2.8		126.8	38.76	-108.23
370	1.3		165.6	38.76	-108.23
371	2.4		147.8	38.76	-108.23
372	13.2		111.4	38.76	-108.23
373	27.2		24.6	38.76	-108.23
374	14.6		266.0	38.76	-108.23
375	4.4		252.3	38.76	-108.23
376	11.3		307.8	38.76	-108.23
377	13.7		332.3	38.76	-108.23
378	25.0		358.4	38.76	-108.23

379	3.1		320.0	38.76	-108.23
380	7.6		342.6	38.76	-108.23
381	5.6		341.9	38.76	-108.23
382	28.1		0.1	38.76	-108.23
383	22.9		353.6	38.76	-108.23
384	27.0		336.5	38.76	-108.23
385	15.2		16.9	38.76	-108.23
386	24.7		354.8	38.76	-108.23
387	27.5		338.1	38.76	-108.23
388	3.5		35.8	38.76	-108.25
389	2.4		107.9	38.76	-108.25
390	8.5		68.0	38.76	-108.25
391	15.2		81.8	38.76	-108.25
392	15.2		81.6	38.76	-108.25
393	2.3		326.0	38.76	-108.25
394	1.6		339.6	38.77	-108.26
395	61.2		145.0	38.77	-108.24
396	7.0		218.4	38.77	-108.24
397	11.8		332.3	38.77	-108.24
398	5.9		5.5	38.77	-108.24
399	11.5		37.2	38.77	-108.24
400	16.8		9.7	38.77	-108.24
401	30.6		25.5	38.77	-108.24
402	5.2		90.3	38.77	-108.24
403	5.8		164.5	38.77	-108.24
404	8.7		72.3	38.77	-108.24
405	9.0		13.4	38.77	-108.24
406	14.9		65.6	38.77	-108.24
407	1.6		277.0	38.77	-108.24
408	7.7		59.1	38.77	-108.24
409	6.4		90.8	38.77	-108.24
410	4.9		190.8	38.77	-108.24
411	7.4		312.1	38.77	-108.24
412	8.5		120.1	38.77	-108.24
413	6.7		145.5	38.77	-108.24
414	6.2		77.3	38.77	-108.24
415	4.6		350.5	38.77	-108.24
416	2.0		224.7	38.77	-108.24
417	32.2		10.0	38.77	-108.25
418	21.9		343.3	38.77	-108.25
419	11.3		36.0	38.77	-108.25
420	12.2		13.0	38.77	-108.25
421	16.4		359.5	38.77	-108.25

422	10.5		58.8	38.77	-108.25
423	20.0		66.7	38.77	-108.25
424	20.5		58.9	38.77	-108.25
425	11.4		354.6	38.77	-108.25
426	16.3		46.3	38.77	-108.25
427	7.4		36.6	38.77	-108.25
428	4.3		108.3	38.77	-108.25
429	13.2		62.1	38.76	-108.25
430	14.2		50.4	38.76	-108.25
431	9.8		7.2	38.76	-108.25
432	15.4		130.6	38.76	-108.25
433	6.8		141.5	38.76	-108.25
434	2.4		55.0	38.76	-108.25
435	6.7		71.5	38.76	-108.25
436	34.0		11.6	38.77	-108.25
437	17.1		336.6	38.77	-108.25
438	13.2		279.2	38.77	-108.25
439	13.4		295.1	38.77	-108.25
440	18.7		339.8	38.77	-108.25
441	28.1		343.0	38.77	-108.25
442	30.6		321.5	38.76	-108.26
443	24.8		324.7	38.76	-108.25
444	20.9		48.1	38.77	-108.26
445	19.3		48.7	38.77	-108.25
446	20.5		337.0	38.77	-108.26
447	6.4		332.0	38.77	-108.26
448	23.7		359.9	38.77	-108.26
449	31.5		15.1	38.77	-108.26
450	24.8		26.0	38.77	-108.26
451	22.8		32.7	38.77	-108.26
452	34.1		42.4	38.77	-108.26
453	3.2		11.4	38.77	-108.26
454	9.1		146.4	38.77	-108.26
455	28.0		45.6	38.77	-108.26
456	20.8		25.4	38.76	-108.25
457	17.3		5.2	38.76	-108.25
458	17.3		352.1	38.76	-108.25
459	28.3		24.5	38.76	-108.25
460	21.7		36.5	38.76	-108.25
461	33.9		13.2	38.77	-108.25
462	13.0		12.0	38.76	-108.24
463	91.0		14.0	38.76	-108.24
464	18.0		20.0	38.76	-108.24

465	78.0		19.0	38.76	-108.23
466	82.0		23.0	38.76	-108.23
467	81.0		15.0	38.76	-108.23
468	85.0		20.0	38.76	-108.23
469	78.0		22.0	38.76	-108.24
470	61.0		15.0	38.76	-108.24
471	37.0		22.0	38.76	-108.24
472	71.0		21.0	38.76	-108.24
473	61.0		19.0	38.76	-108.24
474	87.0		18.0	38.76	-108.24
475	94.0		19.0	38.76	-108.24
476	48.0		18.0	38.76	-108.23
477	88.0		18.0	38.76	-108.23
478	51.0		7.0	38.76	-108.23
479	64.0		18.0	38.76	-108.23
480	88.0		16.0	38.76	-108.23
481	127.0		13.0	38.76	-108.23
482	111.0		20.0	38.76	-108.23
483	95.0		16.0	38.76	-108.23
484	93.0		16.0	38.76	-108.23
485	79.0		14.0	38.76	-108.23
486	80.0		15.0	38.76	-108.23
487	64.0		13.0	38.76	-108.23
488	55.0		16.0	38.76	-108.23
489	84.0		17.0	38.76	-108.23
490	93.0		20.0	38.76	-108.23
491	104.0		15.0	38.76	-108.23
492	83.0		22.0	38.76	-108.23
493	81.0		24.0	38.76	-108.23
494	58.0		19.0	38.76	-108.23
495	78.0		28.0	38.76	-108.23
496	72.0		16.0	38.76	-108.23
497	98.0		14.0	38.76	-108.23
498	94.0		16.0	38.76	-108.23
499	18.0		23.0	38.76	-108.23
500	9.0		15.0	38.76	-108.23
501	22.0		50.0	38.76	-108.23
502	12.0		17.0	38.76	-108.23
503	12.0		79.0	38.76	-108.23
504	111.0		15.0	38.76	-108.23
505	101.0		14.0	38.76	-108.23
506	110.0		15.0	38.76	-108.23
507	6.0		15.0	38.76	-108.23

508	86.0		19.0	38.76	-108.23
509	2.0		14.0	38.76	-108.23
510	18.0		6.0	38.76	-108.23
511	42.0		5.0	38.76	-108.23
512	30.0		26.0	38.76	-108.23
513	1.0		22.0	38.76	-108.23
514	12.0		22.0	38.76	-108.23
515	38.0		19.0	38.76	-108.23
516	22.0		6.0	38.76	-108.23
517	49.0		14.0	38.76	-108.23
518	9.0		9.0	38.76	-108.23
519	11.0		9.0	38.76	-108.23
520	61.0		20.0	38.76	-108.23
521	17.0		12.0	38.76	-108.23
522	55.0		6.0	38.76	-108.23
523	33.0		13.0	38.76	-108.24
524	48.0		29.0	38.76	-108.24
525	28.0		13.0	38.76	-108.24
526	12.0		9.0	38.76	-108.24
527	46.0		14.0	38.76	-108.24
528	52.0		7.0	38.76	-108.24
529	48.0		12.0	38.76	-108.24
530	30.0		11.0	38.76	-108.24
531	22.0		12.0	38.76	-108.23
532	28.0		4.0	38.76	-108.23
533	88.0		14.0	38.76	-108.23
534	64.0		20.0	38.76	-108.23
535	55.0		14.0	38.76	-108.23
536	65.0		20.0	38.76	-108.23
537	40.0		29.0	38.76	-108.23
538	32.0		33.0	38.76	-108.23
539	70.0		16.0	38.76	-108.23
540	74.0		27.0	38.76	-108.23
541	57.0		21.0	38.76	-108.23
542	58.0		11.0	38.76	-108.23
543	98.0		14.0	38.76	-108.23
544	48.0		5.0	38.76	-108.23
545	36.0		24.0	38.76	-108.23
546	61.0		24.0	38.76	-108.23
547	79.0		12.0	38.76	-108.23
548	28.0		23.0	38.76	-108.23
549	37.0		28.0	38.76	-108.23
550	350.0		29.0	38.76	-108.23

551	9.0		29.0	38.76	-108.23
552	86.0		14.0	38.76	-108.23
553	91.0		15.0	38.76	-108.23
554	78.0		15.0	38.76	-108.23
555	47.0		10.0	38.76	-108.23
556	82.0		25.0	38.76	-108.23
557	47.0		11.0	38.76	-108.23
558	43.0		27.0	38.76	-108.23
559	12.0		34.0	38.76	-108.23
560	78.0		18.0	38.76	-108.23
561	62.0		17.0	38.76	-108.23
562	67.0		20.0	38.76	-108.23
563	52.0		32.0	38.76	-108.23
564	67.0		20.0	38.76	-108.23
565	84.0		20.0	38.76	-108.23
566	65.0		22.0	38.76	-108.23
567	79.0		25.0	38.76	-108.23
568	56.0		50.0	38.76	-108.23
569	104.0		13.0	38.76	-108.23
570	99.0		8.8	38.76	-108.23
571	76.0		20.0	38.76	-108.23
572	71.0		15.0	38.76	-108.23
573	17.0		298.0	38.76	-108.23
574	12.0		302.0	38.76	-108.23
575	6.0		270.0	38.76	-108.23
576	13.0		275.0	38.76	-108.23
577	17.0		332.0	38.76	-108.23
578	10.0		275.0	38.76	-108.23
579	9.0		296.0	38.76	-108.23
580	14.0		283.0	38.76	-108.23
581	7.0		260.0	38.76	-108.23
582	12.0		255.0	38.76	-108.23
583	11.0		240.0	38.76	-108.23
584	12.0		351.0	38.76	-108.23

Table 2-5: List of wells used for mapping and correlation in this study.

Name	UWI	Latitude	Longitude
102FEDERAL	5103089670000	40°02'36.0500"N	108°53'28.6800"W
ALBERTSON	5045064810000	39°26'20.2900"N	108°38'27.7400"W
ALBERTSONRANCHES	5045063400000	39°27'45.9700"N	108°35'25.0400"W
BEARGULCHUNIT	5045060920000	39°35'2.6800"N	108°39'42.0400"W
BELCO-FEDERAL	5077085510000	39°20'38.5400"N	108°35'23.0600"W
DEBEQUE	5077084830000	39°17'11.2900"N	108°14'26.7000"W
DOUGHERTY	5045063290000	39°27'4.7500"N	108°34'50.5100"W
DRYFORKFEDERAL	5045068760000	39°22'8.9000"N	108°17'59.4200"W
FEDERAL1	5103082120000	39°40'6.8100"N	108°39'20.5900"W
FEDERAL2	5077086880000	39°21'27.0000"N	108°36'51.2600"W
FEDERAL3	5077085400000	39°21'31.3900"N	108°29'53.7700"W
FEDERAL4	5077089630000	39°20'23.6700"N	108°09'35.6700"W
FEDERAL5	5045064470000	39°26'15.1000"N	108°40'30.9000"W
FEDERAL6	5045064770000	39°27'57.5600"N	108°38'44.7700"W
FEDERAL7	5045064950000	39°28'6.4500"N	108°39'26.2400"W
FEDERAL8	5045064780000	39°26'3.2900"N	108°41'21.6900"W
FEDERAL9	5045063440000	39°28'38.5300"N	108°51'0.0300"W
FEDERAL10	5045065070000	39°27'45.5700"N	108°41'29.0000"W
FEDERAL11	5045063200000	39°23'50.6300"N	108°33'1.9400"W
FEDERAL12	5045067690000	39°30'14.7900"N	108°35'50.6300"W
FEDERAL13	5045062910000	39°30'35.9900"N	108°48'1.0000"W
FEDERAL 8-1	507708026	39°12'13.5700"N	108°34'25.7800"W
FEE	5103090730000	39°59'28.0300"N	109°00'56.6200"W
HANCOCKGULCH	5077081550000	39°21'52.1600"N	108°23'15.3600"W
KULP-LYONS	5077085480000	39°16'10.5200"N	108°10'20.4500"W
LATHAM1	5077083170000	39°21'38.5900"N	108°28'32.5500"W
LATHAM2	5045062440000	39°22'24.2300"N	108°31'24.5900"W
LATHAM3	5045063600000	39°22'25.9300"N	108°30'25.2000"W
MESAGAR-FEDERAL	5045062960000	39°25'15.8800"N	108°36'40.8200"W
MORAN-GOVT	5077080420000	39°09'27.1800"N	108°05'53.9100"W
NARCOFEDERAL	5045066970000	39°30'59.8300"N	108°32'38.1100"W
NIGH	5077086690000	39°15'52.4500"N	108°15'48.1300"W
ROANCREEK-GOVT	5045060420000	39°33'42.0800"N	108°37'26.3200"W
SOLDIERCANYONUNIT	5045061130000	39°36'34.3700"N	108°40'3.7900"W
SSPC	5045069130000	39°27'58.5300"N	108°27'8.8100"W

SWETLAND	5077084580000	39°07'44.5000"N	108°01'42.6700"W
TATE1	5045064220000	39°30'31.6800"N	108°30'1.8000"W
TATE2	5045063470000	39°30'40.2800"N	108°28'33.9200"W
TATEGFEDERAL	5045063410000	39°30'21.3800"N	108°30'51.5800"W
TEXACOFEE	5045066160000	39°30'16.8100"N	108°26'6.1000"W
THUNDERH	5077085810000	39°17'59.9640"N	107°27'3.6000"W
THUNDERHAWKUNIT	5077085810000	39°17'59.9600"N	107°27'4.2800"W
TURNER	5045063240000	39°30'19.1100"N	108°25'25.0600"W
USA	5045063730000	39°24'35.0600"N	108°26'56.1800"W
WINTERFLATS	5077085180000	39°17'8.3300"N	108°32'27.9900"W

Chapter 2: Structural and stratigraphic characterization of Mississippian strata using seismic-constrained reservoir modeling, STACK play, Anadarko Basin, Oklahoma

Preface

This chapter presents multiple workflows for stratigraphic and structural characterization, thoroughly integrating multi-scale data sources. I used supervised machine learning techniques to create constrained three-dimensional reservoir models and evaluate relationships between geology and hydrocarbon production in the Meramec STACK unconventional reservoir.

This chapter was presented in an invited talk for the Dallas Geological Society. March 9th, 2021. and it will be sent in for publication to a geoscience journal in late 2021.

Abstract

The STACK (Sooner Trend in the Anadarko [Basin] in Canadian and Kingfisher counties) play in Oklahoma primarily produces oil and gas from unconventional Devonian and Mississippian rocks. The argillaceous mudstones and calcareous siltstones within the Meramec strata consist of a mixed and gradational carbonate-siliciclastic composition. These rocks provide aerially extensive tight reservoirs challenging to delineate and characterize since lithologies do not have discrete boundaries or specific geometries. Therefore, the contrast in rock composition makes the reservoir challenging to map, resulting in a high uncertainty on placing horizontal wells for hydrocarbon production.

The integration of core descriptions, thin-section observations, and seismic analysis along with a combination of machine learning techniques allowed us to address the heterogeneity problem and characterize the spatial variability of lithologies and petrophysical properties. The generated seismic-constrained models of lithologies/rock types and petrophysical properties integrated a sequence stratigraphic and structural interpretation for the Meramec rocks. The models show the relationship between the sequence stratigraphic framework at different scales and the lithologies distribution and the reservoir rock lateral and vertical continuity.

The production analysis of selected horizontal wells drilled within the Meramec strata suggests that two factors drive the production of hydrocarbons in area 1) the rock lithology percentages along the well path drilled, and 2) the proximity of drilled wells to faults and damage zones within the region.

Introduction

The Mississippian Meramec strata in central Oklahoma is part of the STACK (Sooner Trend Anadarko Canadian-Kingfisher) play in the Anadarko Basin (Figure 2-1). The mixed carbonate-siliciclastic composition of these deposits exhibits interbedded mudstone-siltstone facies that provide aerially extensive tight reservoirs. These rocks, along with the underlying organic-rich Woodford Shale, complete a prolific petroleum system (Figure 2-2). Due to the economic importance of this play, several authors have studied these strata to understand and characterize the lithology, lithofacies (Price et al., 2017; Drummond, 2018; Duarte, 2018; Hardwick, 2018; Hickman, 2018; Leavitt, 2018; Miller, 2018; Miller, 2019), sequence stratigraphic framework and depositional environment (Price et al., 2020; Miller, 2018; Miller et al., 2019;), as well as chemofacies and reservoir quality (Duarte, 2018; Hardisty et al., 2019).

The Oklahoma Geological Survey (Marsh and Holland, 2015) and the USGS have contributed to the understanding of the structural framework and fault distribution of the Anadarko Basin, and other authors have characterized faults within the basement using seismic data (Shan and Keller, 2017; Chase et al., 2018). Patel et al., (2021) analyzed multiple seismic attributes and discussed seismic data limitations to resolve faults within the Meramec. Their study provided insights regarding a positive trend between hydrocarbon production and structural features interpreted using seismic data. Patel and Marfurt (2018) explored the seismic definition of facies and reported the presence of channelized features within Meramec that were further described by Price et al. (2020).

Despite numerous isolated studies of the Mississippian lithologies, faults, and stratigraphy that have been conducted through core and petrographic analyses or separately through seismic interpretation, multidisciplinary and integrated studies that combine core, well log, and seismic analyses to interpret the structure and sequence stratigraphy of the Mississippian strata in the STACK play are limited. To build upon previous studies of the Mississippian Meramec strata, this study addresses the following questions: 1) How does the sequence stratigraphic framework relate to the spatial distribution of lithologies? 2) How do lithology and petrophysical properties relate to hydrocarbon pore volume distribution? 3) What are the characteristics and spatial distribution of key faults and structural features? 4) How do structural elements influence petrophysical properties and reservoir-quality distribution?

To address these questions, a combination of methods was implemented to build seismic-constrained models that integrate a sequence stratigraphic framework, lithologies, and rock type definition, as well as key structural features. The data available include 288 vertical wells with log data, three described cored wells (538 ft, 164 m) with routine core laboratory measurements (N=185), and 50 selected thin sections. Log data typically include gamma Ray (GR), neutron porosity (NPHI), bulk density (RhoB), photoelectric factor (PE), and sonic (DT) well logs. Seismic data included a post-stack seismic volume covering 143 mi2 (370 km2) with a bin size of 110 ft x110 ft (33.5 m x 33.5 m). The seismic frequency ranges from 10 to 60 Hz provided a vertical resolution of ~ 45ft (0.31 m) within the Meramec strata and the information is standard American polarity. The data also include two acoustic impedance volumes (compressional and shear) obtained from an elastic impedance inversion process conducted by Marathon Oil Corporation (Figure 2-3). Results of this study show the impact of the sequence stratigraphic

framework and fault distribution on the petrophysical properties of the Meramec to assess the uncertainty and potential zones development of the unconventional Meramec reservoirs.

Geological Setting

The Anadarko Basin comprises distinct structures created after three major orogenic events that affected the North American craton. The Acadian, Antler, and proto-Ouachita tectonic events took place from the Middle Devonian to the Pennsylvanian time (~320-390 m.y.) (Gutschick and Sandberg, 1983). The succession of a continental collision to the east, followed by an oceanic plate collision to the west and later convergence of a continental plate to the south, produced the structural configuration during the Mississippian (Figure 2-1) (Beebe, 1959)

The Oklahoma basement subsided during the Ordovician until the Mississippian and created accommodation to deposit thick sedimentary sequences (Johnson, 2008). At the end of the Pennsylvanian, the Appalachian orogeny caused southwest-oriented compressive stresses that created folding and shortening within basins in southern Oklahoma (Johnson, 1988; Kolawole et al., 2019). The result of this compressional event produced a northeast-trending fold-thrust belt due to inversion of the Cambrian rift system in the southeast Oklahoma region to form the Southern Oklahoma Aulacogen (SOA) and the Ouachita Mountains (Powers, 1928; Brewer et al., 1983; Keller et al., 2007; Simpson, 2015). The accelerated uplift produced by the SOA formed the present-day foreland Anadarko Basin (Johnson, 2008; Simpson, 2015) divided into two main areas: a foredeep subsided area in the south and a gentle dipping shelf in central and northern Oklahoma known as the Anadarko Shelf.

The Meramacian rocks were deposited on the Anadarko Shelf in an overall southward direction across shelf-edge, slope, and basinal environments (Mazullo, 2009). Pennsylvanian (~320 m.y.) sediments bound the top of the interval forming an angular unconformity that decreases with the proximity to the deepest part of the basin (Beebe, 1959). The base of the section overlies Devonian rocks of the Woodford Formation unconformably. Meramec strata are part of Mississippian deposits which are divided into four series or ages: the Kinderhookian, Osagean, Meramecian, and Chesterian (Curtis et al., 1959) (Figure 2-2).

The Meramecian strata exhibit an even distribution across the basin with a northwest-southeast trend that coincides with the depositional strike (Curtis et al., 1959; Mazullo, 2009). The thickness of this series ranges from 100-900 ft (30-270 m) and is not more extensive than 100 ft (30m) in north-central Oklahoma. The deposition of these rocks occurred during a marine transgression where deposition occurred below the wave base due to local subsidence or sheltered waters. The deposits are composed of cross-bedded calcarenites, calcareous sandstones, and siltstones within the upper Meramecian beds (Curtis et al., 1959; Price et al., 2017; Miller et al., 2019; Price et al., 2020). The Chesterian Series corresponds to deposits that follow the continuation of a transgression towards the Ardmore Basin. These rocks have characteristic lithologies that suggest a high-energy environment (Curtis et al., 1959) and exhibit variable thickness from 500 ft (152 m) to zero, where the strata pinch out toward central Oklahoma.

Methodology

Lithologies, lithofacies, and rock types

This study builds on studies by Miller (2019) and Gupta (2019, personal communication). Miller defined lithologies for three cored wells, Well A, Gulf Oil Corp 1-25 Rohling, and Gulf

Oil Corp 1-23 Shaffer, by integrating petrographic data and calculated mineralogy logs from XRF analysis (Han et al., 2019). In this study, I described two additional cored wells (B, C) (1472 ft, 430 m) and interpreted lithofacies and their stacking patterns to establish a sequence stratigraphic framework for the Meramec strata.

Gupta (2019, personal communication) defined rock types using a Flow Zone Indicator technique (FZI) (Amaefule et al., 1993) with routine core laboratory porosity and permeability data measurements (N=185) to calculate Reservoir Quality Index (RQI) and pore grain volume (Rpvgv). The rock type results of this technique were incorporated in this study to classify the Meramec rocks into three primary rock types (RT1, RT2, and RT3) with their associated mineralogical and petrophysical properties.

Classification of lithologies and rock types in cored wells

The lithology and rock type classification of non-cored wells was done using an Artificial Neural Network (ANN). ANN models are part of the machine learning techniques for artificial intelligence studies (Haykin, 2000). They are composed of a group of interconnected artificial neurons that work together in an organized scheme. In this system, input data are given to the neurons, and after performing some proper operations, a desired output is provided. I used this supervised method to compute discrete data (classes or categories) trained with an input dataset (lithologies\rock types defined from core and well logs). The classification output represents the highest probability of the input data belonging to a particular class or category. I applied the ANN models described by Miller (2019) to classify the lithologies and rock types in non-cored wells within the study area. The models were derived from the relationships with a log suite that

included gamma Ray (GR), neutron porosity (NPHI), bulk density (RhoB), and photoelectric factor (PE).

Sequence stratigraphic framework

Recent studies have shown that the Meramec strata exhibit vertical variations that allow the application of sequence stratigraphy concepts for unconventional resources (Price et al., 2017, 2020; Miller, 2018; Drummond, 2018). I incorporated core descriptions from Miller (2019) and described two additional cored wells (Wells 4 and 6; Figure 2-3) to identify lithofacies, interpret depositional geometries, and describe sedimentary structures to develop a sequence stratigraphic framework for the Meramec strata. To complement and extend the observations described in the core, I used the gamma-ray log signatures to define high-frequency intervals that are interpreted as parasequences. These parasequences were interpreted based on three log-signature types 1) increasing-upwards, 2) decreasing-upwards or 3) serrated (no-change upwards). I defined key surfaces such as flooding surfaces (fs) where gamma-ray trends changed between the gamma-ray defined stacked intervals. To integrate the defined higher-order parasequences with seismic data, I used the interpreted well tops to match four interpreted seismic horizons: Meramec, parasequence 3, Osage, and Woodford as well as five conformable surfaces that represent the tops of parasequences 1, 2, 3, 4, 5, 6, and 7 (Figure 2-4).

I interpreted and defined the lower-frequency depositional sequences by analyzing the vertical stacking patterns of parasequences and correlated them with rock attributes such as lithofacies, bioturbation, sedimentary structures, and mineralogy. These cycles were established as low frequency, long-term stratigraphic cycles superimposed on higher-frequency cycles. The

partial sequences in this study were identified following laterally continuous stratigraphic surfaces, such as Maximum Flooding Surfaces (MFS) and Sequence Boundaries (SB).

Machine learning-based lithology and rock type prediction

This workflow integrates data from well logs, impedance volumes from seismic inversion, and interpretation to obtain a 3D map for lithologies and rock types with associated probability volumes using a multi-scale Bayesian approach. In this process, I defined interpretation priors such as 1) horizons and identification of major sequences, 2) probabilities from different lithologies or rock types within the sequence, 3) interpretational indicators to be used as spatial filters for classification probability, and 4) the classification of seismic data accounting for the prior information. These interpretation priors are used to normalize the probability density function (PDF) to reflect the geological interpretation bias (Bachrach et al., 2004; Buland et al., 2008). The workflow is divided into two processes, an "a priory" analysis and Bayesian prediction (Figure 2-5).

The Bayesian approach was performed using Acoustic Impedance (AI) and Shear Impedance (SI) well log data, well tops, and seismic horizons with the lithology and rock type logs previously calculated using ANN. The AI well logs were derived from sonic (DTC) and density (RHOB) well logs whereas SI well logs were calculated using an empirical equation by Fu et al. (2019) that relates compressional velocity (*Vp)* and shear velocity (*Vs)* from measurements from core plug data for the Meramec strata.

$$\boldsymbol{V_s = 1.29 + 0.35 * V_p} \qquad (1)$$

The result of the “a priory” analysis is a function that describes the probability of an event occurring within a portion of continuous space. Each priory PDF is established from cluster analysis of the log data as a representation of the variability within the Meramec strata.

The Bayesian prediction process was used to obtain a posterior conditional PDFs incorporating the spatial correlations of the lithologies and rock types estimated using variograms. The process updates the prior PDF to give a posterior PDF (Buland et al., 2008). This approach takes the covariance function of the seismic data and makes it proportional to the covariance function obtained from well data. The calibration obtained from well data, and the impedance traces is used to create a calibrated PDF (Mukerji et al., 2001). The result is a set of posterior PDFs for the elastic seismic attributes (AI and SI) to produce lithology and rock type prediction volumes as well as one probability volume per class for lithologies (4 classes) and rock types (3 classes). Each volume contains the probability of a class to occur within the seismic volume (Figure 2-5).

Structural interpretation

The structural framework for this study was developed using three steps. First, the generation of the stratigraphic framework allowed me to interpret and derive chronostratigraphic surfaces that represent flooding surfaces. Second, a detailed fault interpretation developed with a workflow allowed me to quantify the uncertainty of the fault interpretation. Lastly, a detailed fault characterization defined the damage zone using volumetric seismic attributes.

Stratigraphic framework - Horizon Interpretation

Two seismic horizons that correspond to the top of the Meramec and Woodford formations were incorporated into this workflow from Miller (2019). Additionally, parasequence 3 and Osage horizons were interpreted within the modeled area on the interfaces from peak-to-trough (zero-crossing) of the seismic amplitude. I performed a seismic-to-well tie that helped to identify the amplitude response associated with the corresponding horizons and well top markers on the well logs to support the interpretation (Figure 2-4).

Five additional surfaces were generated using conformable gridding to derive surfaces from the interpreted seismic horizons and were adjusted to the well tops for parasequences 1,2,3,4,5,6 and 7 respectively.

Velocity model

A generated velocity model helped perform a multi-attribute analysis in the depth domain and facilitate well data integration in the structural interpretation. Three horizons in time (Meramec, parasequence 3, and Woodford) were used with 894 well tops interpreted in 298 wells to build the velocity model within the study area. This model considered the interval velocity defined at the datum using the following relation:

$$z = z_{\mathrm{r}} + v_0(t - t_{\mathrm{r}})$$

Where z is the calculated depth of the point, $z_{r,}$ the depth at the well location, v_0 the calculated velocity and (t-t_{r}) the difference in time.

Fault interpretation

I evaluated the results obtained by Patel et al. (2021) using a multi-attribute analysis for fault interpretation in the study area and explore methods to make a reliable interpretation using

an integrated approach. The integrated workflow (Figure 2-6) determines an Interpretation Confidence Value (ICV) based on data analysis from a multidisciplinary approach that includes geological mapping and cross sections, seismic attribute analysis, and production data from wells. For this analysis, one (1) point was assigned to the evaluation criteria if the evaluated attribute displays a relevant response or characteristic to help define the fault interpretation. The ICV score allows us to quantify the confidence in the fault interpretation as low (score 0-3), medium (score 4-5), and high confidence (6-10).

Interpretation of structural features required a previous general overview of the tectonic history and evolution of the Anadarko Basin. The geological analysis allowed the seismic interpreter to generate "in context interpretations" (Infante and Marfurt, 2018). To include a multiscale analysis, I used well tops and stratigraphic horizons to generate structural cross sections and maps for the top of the Meramec and Woodford formations. The structural maps were plotted using a close contouring interval (5 ft, 1.5 m) combined with dip maps interpretation, highlighting abrupt horizon elevation changes as possible faulted zones (Figure 2-7).

Cross sections perpendicular to the fault planes using vertical wells also provided information about abrupt elevation changes in the section considering: 1) the regional dip of the Meramec strata (1-2 degrees) and 2) the distance from the well to the fault plane. This evaluation provided an estimate of the fault throw that was included in the modeling process to create a faulted 3-D model grid (Figure 2-8).

I used a multi-attribute analysis with geometrical attributes that highlight discontinuities such as coherence, curvature, aberrancy, amplitude, and Ant-tracking. Analysis of vertical and horizon

seismic slices helped with the fault interpretation and mapping process to increase the fault ICV score.

I analyzed general pressure trends for the entire interval as well as GOR maps incorporated from previous studies from Miller (2019) and Hickman (2018). The engineering analysis included major faults in the study area.

Variance analysis to characterize damage zones

The variance attribute is commonly used to identify discontinuities in seismic interpretation, such as channels and faults. It is defined as one minus the energy of the coherent part of seismic traces divided by the average acoustic energy of the traces (Chopra and Marfurt, 2007). This study uses a variance volume to analyze the interpreted fault damage zone following the methodology of Liao et al. (2013) and Liao et al. (2019). This methodology reveals dimensions and shapes of fault damage zones considering the variance response along with extracted profiles across the fault plane. This method uses the concept of seismic distortion zone to understand and associate damage within a fault system at the seismic scale to characterize the structure and its surrounding deformation (Lacopini et al., 2016).

I selected the interval surrounding the parasequence 3 horizon in the middle of the studied section to generate perpendicular-to-the fault profiles and extract the variance values. The spacing between the generated profiles was ~1900 ft (500 m). I used the scaling relations

established from this analysis to create permeability modifiers and incorporate them into the 3-D petrophysical modeling process (Figure 2-9).

Damage zone dimensions

To obtain a numerical characterization of each fault damage zone, I plotted the normalized distance from the fault versus the normalized variance response extracted from the perpendicular-to-the-fault profiles for each fault. Then, I compared the geometry of the variance-defined damage zones with distributions from well documented studies in the field, outcrops, and seismic data to define relationships between petrophysical properties, mechanical properties, and shapes and geometries of the damage zones (Sagy et al., 2001; Wilson et al., 2003; Powers and Jordan, 2010). These plots typically show an exponential decay of the fracture density with distance from the fault core.

I assumed that, in general, the damage decay fits a power function or an exponential function:

$$(5)\ D = a\, e^{-bx}$$

where *a* and *b* are constants that reflect the physical properties related to the brittleness of the rock or thickness (Cowie et al., 1995).

Reservoir modeling

The 3-D reservoir model grid integrated the stratigraphic surfaces created from the interpreted seismic horizons, parasequence well tops, and fault interpretations. The modeled area covers approximately 143 mi^2 (370 km^2). The horizontal cell dimensions were set considering the seismic data horizontal resolution and the vertical cell dimensions and layering scheme. To represent the modeled area structural configuration, I included thirty interpreted faults in the grid as part of the Meramec stratigraphic and structural framework.

The spatial variability of lithologies and rock types was represented using vertical and horizontal variograms derived from 1) well logs and 2) the classification volumes generated from the prediction process for lithologies and rock types. I computed vertical variograms using the ANN-generated lithology and rock type logs. Horizontal variograms were generated after resampling the classification volumes to the 3D model grid to create variograms maps for each lithology and rock type.

The lithology and rock type models were generated using sequential-indicator simulation (SIS) to reflect the spatial variability of lithologies and rock types within the Meramec strata. The constraints incorporated during the modeling process included: 1) parasequence surfaces included as part of the stratigraphic framework; 2) the structural interpretation of faults; 3) upscaled lithology and rock type logs; 4) vertical and horizontal variograms by facies and zone; 5) lithology and rock type percentage by zone, and 6) 3D seismic-based probability volumes.

I generated two 3D total porosity models, one biased to the lithology model and a second biased to the rock type model. I used an arithmetic average to upscale the porosity well logs and assign values for each cell. The porosity models were created using sequential-Gaussian simulation (SGS) and include the following constraints: 1) the 3-D lithology or rock type model, 2) upscaled PHIT well logs biased to the lithology or rock type model, 3) porosity histograms by zone and lithology or rock type, and 4) variograms parameters by zone and lithology or rock type.

Permeability modifiers

I defined exponential equations derived from the damage zone analysis to estimate the damage zone dimensions for each side of the interpreted faults included within the model. To

implement the effect of the damage zone dimensions within the petrophysical models, I created region volumes with properties that related the distance from the fault to the respective decay equation defined for each of the analyzed damage zones. The generated permeability models were then multiplied using the permeability modifier volumes to enhance the permeability values in the areas around faults.

Volumetric analysis

I used SIS stochastic modeling to assign a random global seed and create multiple model realizations (N=30) for lithologies and rock types. Then, I evaluated the uncertainty in the quantification of pore volume, calculating the pore volume for each of the model realizations generated and plotted the results on histograms to identify the P10 (conservative), P50 (most likely), and P90 (optimistic) cases of volume distribution for the lithology and the rock type models. Finally, I used the P50 model as the most representative model for the study area.

Production analysis

To evaluate the effect of lithologies, rock types, and petrophysical properties on reservoir oil productivity (normalized cumulative oil production), 10 producing horizontal wells drilled in the Meramec formation were assessed. I extracted lithology, rock type, porosity, and permeability logs along the wells horizontal path from the generated 3-D models. The lithology and rock type percentages for each well were calculated for the selected wells lateral sections. I normalized the 360-day cumulative oil production (STB) by the respective well lateral length to analyze the wells production information. Lithology, rock type, and petrophysical property averages were cross plotted against the normalized production data.

Results

Lithofacies

The Meramec in the study area is comprised of seven lithofacies (Figure 2-10). These rocks range from argillaceous claystone to very-fine sandstone with calcite and quartz cement. The lithofacies are silty grainstone, structureless siltstone/sandstone, cross-laminated siltstone/sandstone, laminated calcareous siltstone, laminated mudstone, and structureless mudstones(Table 2-1A). The lithofacies exhibit a gradational nature that makes it challenging to establish discrete boundaries using characteristics such as grain size and calcite cement. Therefore, I used petrographic observations to identify lithological variations and cement compositions.

Lithologies and rock types

Lithofacies characterization using well logs is challenging because multiple lithofacies exhibit similar well log responses. I defined five representative lithologies differentiated using well logs 1) mudstone, 2) argillaceous siltstone, 3) argillaceous-calcareous siltstone, 4) calcareous siltstone, and 5)silty limestone. The lithological definition followed the methodology developed by Miller (2019) using petrographic observations and mineralogy data from X-ray fluorescence.

I incorporated Gupta's (2019, personal communication) results to define rock types to define three representative types within the Meramec strata. Rock type 1 (RT 1) represents rocks with relatively low calcite cement, high clay content, low brittleness index, and high total porosity. Rock type 2 (RT2) shows intermediate values in calcite cement, clay content, brittleness index, and total porosity and represents the transition between RT1 and RT3. Rock

type 3 (RT3) has abundant calcite cement, low clay content, high brittleness index, and low total porosity. (Figure 2-11).

Lithology and rock type classification in non-cored wells

To classify lithologies and rock type in non-cored wells, I used an Artificial Neural Network (ANN) approach similar to that of Miller(2019) for well 1. The best model results included a well log suite comprised of Gamma-ray (GR), neutron porosity (NPHI), bulk density (RhoB), and photoelectric effect (PE) with 93% and 70% accuracy for the prediction of lithologies and rock types, respectively. I applied the model to 260 vertical wells within the model area and five additional wells used for lithological and tock type regional analysis. The classification techniques resulted in two new discrete well logs representing lithology and rock types for each of the 265 wells analyzed.

Stratigraphic framework

Parasequence characterization

The lithofacies interpreted from multiple Meramec cores and well logs show seven relatively higher frequency coarsening-upward parasequences that are superimposed on an overall fining upward stratigraphic package. Three main parasequence architectures are observed depending on the proximal to distal position within the depositional system (Figure 2-12). 1) Proximal parasequences commonly exhibit several upward-coarsening vertical facies successions that contains basal structureless, bioturbated, and laminated mudstones underlying structureless siltstones, and calcareous and cross-laminated siltstones topped with silty limestones. The lithofacies successions form asymmetric, coarsening-upward cycles with a relatively thicker regressive phase and a thin to absent transgressive phase. 2) Distal parasequences are composed

of several upward-coarsening vertical facies successions composed of structureless, bioturbated mudstones overlain by structureless and laminated siltstones. The facies successions form more symmetrical parasequences with somewhat equally thick regressive and transgressive phases. 3) An intermediate parasequence type commonly exhibit vertical facies successions characterized by fining upward or irregular blocky patterns. The lithofacies within intermediate parasequences are composed of calcareous siltstones and very fine sandstones and siltstones that rapidly grade upward into laminated siltstones-mudstones overlain by hemipelagic mudstones.

The Meramec consists of eight parasequences and the overall Meramec thickness ranges from 450 ft (137 m) in the northwest to 250 ft (76 m) in the southeast.

Lower order flooding surfaces define the base and top of the Meramec strata (Figure 2-13). The Meramec represent an overall fining upward succession that consists of three parasequence sets. The lower Meramec forms a transgressive parasequence set that includes parasequences 1, 2, 3, and 4 and is capped by a maximum flooding surface. The subsequent parasequence set comprises parasequence 5 and 6 and exhibits an aggradational to progradational stacking pattern with a serrate gamma-ray log signature and more uniform grain size. The uppermost parasequence set is a retrogradational set characterized by back-stepping of parasequences 7 and 8 (Figure 2-14).

The first transgressive parasequence set has dominantly silty limestones and calcareous lithologies that grade basinward into argillaceous mudstones. These deposits are associated with a shallow marine outer carbonate shelf. Parasequence 3 displays a thick and retrogradational to aggradational interval composed of thin interbedded siltstones and clay-rich deposits transitioning to finer-grained deposits in parasequence 4. These rocks reflect sedimentary characteristics of a lower energy setting with intermittent flows of coarser silt-size sediments

associated with gravity flows and occasional channelized deposits. The second aggradational to progradational parasequence set (parasequence 5 and 6) is dominated by siltstones with interbedded mudstones and shows an asymmetric coarsening-upward signature in gamma-ray. The third and uppermost parasequence set (parasequences 7 and 8) is retrogradational and exhibits a fining upward signature, capped by a transgressive surface of erosion that represents the top of the Meramec strata (Figure 2-14).

Structural interpretation

The analysis of 3-D seismic data displays two distinct orientations for significant structural features interpreted within the basin. Normal faults with large apparent vertical displacement up to 180 ft (54 m) and north-south-oriented follow the Nemaha uplift and El Reno fault structural trend. Second, an east-west trend with right-lateral strike-slip kinematics and a small apparent average vertical displacement of 40 ft (13 m). Faults interpreted within this orientation often display oblique secondary faults. The integrated workflow for fault definition resulted in 30 interpreted faults (Figure 2-15). Strike-slip faults display nearly vertical dip and often show minor vertical displacement. The stratigraphic zone thickness is consistent on both sides of the faults, suggesting that the fault development does not significantly affect the sedimentation. To include faults within the 3D reservoir model grid, I simplified the interpretation to single fault planes.

Damage zone characterization

Analysis of 3-D seismic variance performed over the parasequence 3 horizon shows that vertical sections that are oriented perpendicular to the fault planes display mixed characteristics depending on the fault throw, angle, and overall orientation. The amplitude sections are strongly

disturbed close to the fault zone. The distortion amount is highlighted easily in maps that display high variance. The extracted profiles (Figure 2-16) reflect the distortion intensity along the cross section. Plots show low variance values away from the fault and increase gradually while reducing the distance to the fault plane, indicating a higher structural disturbance intensity and discontinuity. The distortion effect around fault planes results from fractured rocks that affect the geological strata continuity and, therefore, the seismic reflectors.

Variance cross sections over the Meramec interval show two zones similar to those proposed by Liao et al. (2019), 1) the fault core and 2) the damage zone. Analysis of multiple perpendicular-to-fault cross sections helps to divide the interpreted faults into two structural types. Type 1 displays symmetric variance on both sides of the fault. The zone that characterizes the fault core area is narrow (~ 20% normalized distance-to-fault), and the width of the fault damage zone is equivalent on either side of the fault (Figure 2-16(a)).

In contrast, structural type 2 exhibits an asymmetric variance response along the cross section profile. Variance values show a skewed distribution associated with high seismic disturbance around the fault plane. Structural type 2 displays a narrow fault core area (~ 20% distance-to-fault), while the fault damage zone width is unequal on both sides of the fault. (Figure 2-16(b))

I plotted the normalized variance vs. the distance from fault plane values to define a function to describe the variance-defined damage zone. The resulting plots display an exponential variance decay as a function of increasing distance from the fault plane (Figure 2-17). I compared function geometries that explored relationships between fracture density and distance from the fault plane using seismic (Powers and Jordan, 2010) and outcrop data (Sagy et al., 2001; Wilson et al., 2003). The plots of exponential functions derived from normalized

profiles generated for structural types 1 and 2 in this analysis closely match previous studies with slightly different coefficients. Notably, the comparison with structural type 2 faults displays a more extensive damage zone that includes potentially sub-seismic faults characterized as isolated high variance points on the plot.

The damage zone analysis resulted in 46 decay equations used to create individual multiplier volumes and enhance the permeability due to structural deformation around each side of the interpreted faults. Multiplier volumes were limited to the damage zone width for each side of the faults (left and right). A computed distance from fault property volume was used with the available multiplier volumes during the 3D permeability modeling.

Reservoir models

3D grid

The generated 3-D reservoir model grid integrates the stratigraphic surfaces created from interpreted seismic horizons, parasequence well tops, and fault interpretations. The modeled area covers approximately 143 mi^2 (370 km^2). The horizontal cell dimensions are 110 ft x 110 ft (33.5 m x 33.5 m) to preserve the horizontal seismic resolution with a proportional layer scheme with an average thickness of 2 ft (0.6 m). The grid comprises 575 x 577 x 406 cells in the I, J, and K directions, respectively, with 134,700,650 cells. Thirty faults were included in the grid with fault throws varying from 40 to 200 ft (12 to 60 m) to represent the model area structural configuration. The model contains seven zones with one zone that combines parasequence 4 and 5 and individual zones for the rest of the other eight parasequences (Figure 2-18).

Bayesian impedance-based classification of lithologies and rock types

The results of the Bayesian classification process consist of two outputs. First, I obtained probability density functions for each lithology and rock type calculated during the "a priori" analysis process. Then, probability volumes are generated per class during the "a posteriorly" prediction process. Analysis of the Bayesian approach quality resulted in a confusion matrix containing the probability of classifying a sample that belongs to group A, given that its true group is B. (Prediction |True).

The generated probability density functions (PDF's) show the probability of predicting each lithology or rock type using a combination of acoustic impedance (P-impedance), and shear impedance (S-impedance) well logs. The PDF's curves represent the probability of lithologies and rock types being predicted based on each lithology or rock type impedance range. An ideal classification using these attributes shows low overlap and great separation in the combined PDF's curve plot for each lithology and rock type. The plots show four distinctive peaks of high probability in the PDF's of P-impedance and S-impedance for lithology definition. The function peaks represent impedance values likely to represent the corresponding lithologies. Ranges for S-impedance in mudstones are around 13000 (ft/s)*(g/cc), argillaceous siltstone 15000 (ft/s)*(g/cc), calcareous siltstone 16500 (ft/s)*(g/cc), and silty limestone 18500 (ft/s)*(g/cc). In contrast, P-impedance values show the highest probability in 36000 (ft/s)*(g/cc) for mudstones, 42000(ft/s)*(g/cc) for argillaceous siltstone, 48000(ft/s)*(g/cc) for calcareous siltstone, 52000(ft/s)*(g/cc) for silty limestone.

In the case of rock type classification, the PDF's show a distinct separation in the probability functions. High probability S-impedance values for RT1, RT2, and RT3 were 19000 (ft/s)*(g/cc), 23000 (ft/s)*(g/cc), and 25000 (ft/s)*(g/cc) respectively, whereas for P-impedance

values were 39000 (ft/s)*(g/cc) for RT1, 44000 (ft/s)*(g/cc) for RT2 and 49000 (ft/s)*(g/cc) for RT3.

The confusion matrix resulted from the Bayesian approach using the five defined lithology classes showed a low overall accuracy. To improve the classification accuracy, I performed an exploratory data analysis and simplified the lithological definition from five to four categories. The modification increased the overall accuracy from 45 % to 68% for the Bayesian classification process. Selected lithologies show user accuracy values for mudstone 90%, argillaceous siltstones 76%, calcareous siltstone 51%, and silty limestone 53%. The classification of rock type (RT) classes performed better, showing an overall 73% accuracy with user accuracy of RT1 90%, RT2 53%, and RT3 75%.

The Bayesian classification results include one classification volume that indicates the most likely class to occur in each location and the corresponding probability volume for each class. The lithology classification volume shows a trend with a predominant occurrence of calcareous siltstone, argillaceous calcareous siltstone, and a minor proportion of silty limestone to the northeast that gradually changes to dominantly mudstone and argillaceous calcareous siltstone to the southwest. Parasequences 1 and 2 (PS1 and PS2) display a persistent occurrence of calcareous siltstone and argillaceous calcareous siltstone in the modeled area. The volume resulting from the rock type classification reveals RT3 and RT2 dominance in the northeast model area, strongly changing to RT1 to the southwest with minor percentage of RT2 in parasequence 1, similar to the trend of the lithology classification volume (Figure 2-23(b)).

The Bayesian classification workflow results were used in the next section as probability volumes for lithology and rock type modeling.

Lithology, rock type models

The computed vertical and horizontal variograms from well logs and probability volumes were used to constrain the lithology and rock type models. Lithology models included vertical variograms ranges from 4.5 to 6 ft (1.4 to 1.8 m). Horizontal variograms minor and major ranges vary from 5000 to 7000 ft (1500 to 2200 m) for mudstones, 5200 to 7000 ft (1600 to 2200 m) for argillaceous siltstones, 5100 to 6500 ft (1550 to 1900 m) for calcareous siltstones, and 4200 to 6500 ft (1000 to 1300 m) for silty limestone, respectively. Variogram maps illustrated a major axis orientation ~67° azimuth degrees approximately perpendicular to the interpreted depositional-dip direction.

The rock type model vertical variogram ranges vary from 5 to 7 ft (1.5 to 2.1 m). Horizontal variogram minor and major ranges vary from 1500 to 2000 ft (457 to 610 m) for RT1, 2500 to 3500 ft (760 to 1000 m) for RT2, and 1500 to 2000 ft (457 to 610 m) for RT3, respectively. The variogram maps computed from the classification volumes show a major continuity axis orientation ~ 81° azimuth, perpendicular to the deposition direction.

Lithology and rock type vertical proportion curves (VPC) from the upscaled wells describe the stratigraphic variability within the Meramec strata (Figure 2-19). The lithology VPC displays lithology percentage changes consistent with the proposed stratigraphic framework. Parasequences 1, 2, and 3 comprise the first fining upward transgressive parasequence set with a gradational increase in mudstones and argillaceous calcareous siltstones from 0 to 10% and 10% to 90%, respectively. This transgressive parasequence set is topped by a maximum flooding surface that reflects the inflection point and beginning of a progradational to aggradational parasequence set (Parasequences 4 and 5) characterized by a significant calcareous siltstone increment from 30% to 65%. Lastly, a fining upward succession that contains a mudstone

increase from 10 to 60% represents the uppermost and regressive parasequence set (Parasequences 6 and 7) of the Meramec strata capped by a transgressive surface of erosion (Figure 2-19).

A dip-oriented model cross section illustrates the lateral continuity of the Meramec strata (Figure 2-20 and 2-21). The first parasequence set (Zone 1, Zone 2, and Zone 3) displays predominant calcareous siltstones and silty limestones to the northwest (landward) with a smooth transition to argillaceous calcareous siltstone and occasional mudstone to the southeast (basinward) (Figure 2-20). In contrast, the overlying parasequence set (Zone 4 and Zone 5) shows a quick gradational variation from silty limestone and calcareous siltstone to dominant clay-rich lithologies from northwest to southeast. The top parasequence set (Zone 6 and Zone 7) comprises overall argillaceous calcareous siltstone and mudstone lithologies that become more clay-rich to the southeast.

A generated rock type model displays similar trends to the lithological model with its related rock types. Zones 1, 2, and 3 show an upwards increase of RT1 related to fined-grained lithologies and representing the first parasequence set. Zones 4 show steady RTs proportions, whereas zone 5 displays increasing RT3 and decreasing RT1 percentages. These observations are consistent with the interpretation of an aggradational to progradational interval for the parasequence set. The top zones 6 and 7 show an increase in RT1, representing the last regressive parasequence set of the Meramec strata (Figure 2-19). Dip-oriented sections across the rock type model show the lateral gradational proximal-to-distal variability in the area from the predominant RT3 and RT2 combination in the northwest (landward) to the occasional RT2 and dominant RT1 composition to the southeast (basinward)(Figure 2-21).

Even though lithology and rock type models resulted from different input data to discretize rocks in the strata, the results show a consistent stratigraphic variation.

Porosity and permeability models

Porosity model results were constrained to lithology/rock type models and a probability volume computed from an empirical relationship between p-impedance and total porosity. I selected the model representing the P50 case after the stochastic to describe the porosity distribution associated to rock type and lithology facies models (2-22A). The model displays overall porosity values that range from 0.1 to 11% (Figure 2-22). Zones 6 and 7 exhibit the highest average porosity with 6% and 7% for each zone, whereas zones 1 and 2 reflect the lowest average porosity values with 4% and 5%, respectively. High porosity values are often related to clay-rich lithologies such as argillaceous calcareous sandstones and mudstones, while low porosity values dominate proximal silty limestones and calcareous siltstones. When I analyze total porosity values to rock types, RT1 shows the highest average porosity with 8%, whereas RT3 displays the lowest values with an average porosity of 3%. The southwest (basinward) locations within the model contain the higher porosity areas, mainly in zones 6 and 7 due to the predominant RT1 and RT2 deposits. In contrast, the northwest mixture of RT3 and RT2 deposits display lower porosity areas within the model.

The permeability model results integrate a combination of workflows that included a cloud transform using 145 samples from core data and permeability multipliers that resulted from the variance-based damage zone analysis for each fault. The Meramec strata permeability model values range from 0.001 to 5.2 μD with average permeability of 4.5 μD (Figure 2-23). Higher permeability values for RT2 and RT3 are abundant in northwest areas within zones 2, 3,

and 4, while in the southwest, zones 1, 2, 3, and 5 show highly permeable restricted regions. The permeability model displays an overall increase of permeability values in cells with proximity to fault zones product of multipliers applied during the modeling process.

Production analysis

Analysis of production data from 10 horizontal production wells resulted in possible relationships between hydrocarbon production and lithologies, rock types, or faults. The production data from 360-day cumulative production was normalized per horizontal length. Cross plots of lithology percentage in wells versus hydrocarbon production do not show clear trends between any specific lithology. The evaluation of rock type percentage versus cumulative production shows a positive correlation between wells that drilled through higher RT3 percentages along the well path. RT1 percentages show a weak positive correlation with cumulative hydrocarbon production. However, it is difficult to conclude the implications of rock type in hydrocarbon production.

The results of cumulative production versus horizontal well path distance to the fault cross plots (Figure 2-24) show a negative correlation with prolific wells drilled nearby faults zones and low cumulative hydrocarbon production in wells drilled in farther locations.

Discussion

Stratigraphic control of petrophysical properties

The vertical stratigraphic variation within the Meramec strata reflects relative changes in sea-level that result in a vertical succession of highly heterogeneous lithologies. Observation of the models suggests a strong relationship between lithology/rock type spatial variability and pore volume (Figure 2-22). Parasequence architectures reflect variable grain size and lithology percentages within high-order cycles from proximal to distal, as Suriamin (2020) reports for the

entire Mississippian stratigraphic unit. The array of lithologies displays asymmetric proximal parasequences that contain an abundance of relative coarse-grained, highly-cemented, and low porosity lithologies that dominate the northwest region as well as the basal parasequences 1 and 2. In contrast, distal portions of the study area display symmetric parasequences characterized by lithologies and rock types associated with high-clay content (mudstone, argillaceous siltstones, and RT1). Argillaceous lithologies display large pore volumes that dominate the southeast studied regions. These results are consistent with findings reported by Miller (2019) and Hardisty (2020), where dominant argillaceous lithologies deposited during transgressive cycles show high porosity. Previous studies that analyzed the composition of Meramec rocks (Miller (2019); Hardwick (2018); and Laresee, 2019 personal communication) reported that high clay content composed rocks within the Meramec strata inhibit the precipitation of calcareous cement and preserve the pore space in the rocks.

Stratigraphic controls on permeability relate to the lateral distribution of lithologies/rock types and diagenetic cementation. Calcareous sandstones and RT3 represent the most cemented rocks with low permeability values and higher proportions in the study area proximal locations and regressive parasequence sets. Likewise, submarine channels composed of calcareous siltstones and argillaceous calcareous siltstones (RT2 and RT3 rock types) were deposited in a north-south direction. The mapping of high-permeable lithologies using a bivariate analysis with total porosity as a second variable might result in permeability overestimation in clay-rich lithologies and rock types (mudstones, argillaceous calcareous mudstones, and RT1). However, a better calibration for these values is complicated to achieve because there is no clear relationship between porosity and permeability within the Meramec strata (Suriamin, 2020).

Analysis of seismic coherence highlights the lateral variability of deposits within the carbonate platform, including low sinuosity submarine channels interpreted from north to south (Figure 2-25), as previously reported by Price (2020). The diverse channel orientation suggests sediment transported from proximal locations within a semi-circular platform (Suriamin, 2020) and deposited in a low energy deep marine environment. Channels are composed of calcareous siltstones/argillaceous siltstones or RT/RT2 and produce an impedance response that allows them to be mapped using amplitude or relative acoustic impedance attributes over horizon slice extractions (Figure 2-26).

Structural framework and controls in reservoir quality distribution

Integration of seismic data and the stratigraphic framework in the model helped identify the effects of faults in the reservoir distribution and rock properties of the Meramec strata. Two fault types are observed. Type 1 faults are often related to normal faults with high vertical displacement. Analysis of normalized plots shows that the deformation effect in damage zones can be quantified using the variance analysis methodology and produce function plots that closely match previous studies using seismic (Powers and Jordan, 2010) and outcrop data (Sagy et al., 2001; Wilson et al., 2003).

The evaluation of thickness maps across each side of the type 1 faults shows no significant effect in accommodation space or sedimentation within the interval. The seismic coherence analysis extractions analyzed over selected phantom horizons suggest fault control in channel orientation from north to south. The low sinuosity submarine channels that reached type 1 fault zones aligned in a north-south direction and deposited a mixture of calcareous siltstones/argillaceous sandstones or RT2/RT3 rocks parallel to fault planes.

Structural type 2 relates to strike-slip, vertical and small throw faults that often exhibit asymmetric damage zones. Normalized plots of variance versus distance from the fault show occasional outliers related to minor Riedel faults associated with relays in strike-slip zones (Liao et al., 2017; 2019). Observations from horizon slices display Meramec submarine channels laterally displaced across strike-slip faults suggesting a post-depositional movement for east-west oriented structures affecting the lateral reservoir continuity (Figure 2-27).

Production data from the horizontal wells drilled in the Meramec formation reveal a negative correlation with distance from faults (Figure 2-24). High cumulative oil is shown to be associated with wells drilled closer to faults, whereas wells with significant distance from fault planes show lower cumulative oil values. Rocks within the damage zone display a notable increase in natural fractures as represented by seismic distortion. The mapping of damage zones and the estimation of petrophysical properties surrounding faulted areas represent one of the critical stages in identifying prospective hydrocarbon production locations in tight reservoirs within the Meramec strata.

Conclusions

The Meramec strata correspond to low energy deposits of an out-shelf mixed siliciclastic-carbonate ramp environment. The stratigraphic interval contains seven lithofacies that form eight high-frequency coarsening-upward parasequences bounded by flooding surfaces. Parasequence architectures within the Meramec strata are asymmetric and regressive-dominated cycles in proximal northwest (landward) locations and transition to symmetric cycles in distal southeast (basinward) areas. Overall, Meramec thickness decrease to the southeast due to regressive

intervals thinning down-dip, whereas clay-rich transgressive siltstones and mudstone rocks become dominant. Vertical stacking patterns within the stratigraphic interval exhibit from base to top a retrogradational, aggradational/progradational, and retrogradational array of parasequence sets.

Meramec rocks in central Oklahoma consist of five lithologies: 1) mudstone, 2) argilleceous siltstones, 3) argilleceous calcareous siltstones, 4) calcareous siltstones, and 5) silty limestones. These lithologies were successfully predicted in wells using an ANN approach to relate core data and well log information. The lithological/rock type three-dimensional spatial distribution within the Meramec was successfully achieved using a Bayesian approach to relate seismic and well scale acoustic impedance rock properties. The simplification of the lithology definition improved the accuracy of the prediction. Three rock types (RT1, RT2, and RT3) represent the Meramec deposits and show a robust relationship with the stratigraphic framework as well as with lithologies even though each model input data is independent. The petrophysical model analysis suggests a strong stratigraphic control on reservoir quality.

The use of a variance-based seismic characterization helped define two main fault orientations that dominate the Meramec strata structural configuration. Faults oriented north-south are normal syndepositional faults associated with significant structural deformation events such as the El Reno fault and the Nemaha uplift. In contrast, faults-oriented east-west often display post-depositional left lateral with smaller associated fault sets and vertical offsets. Moreover, the variance-based methodology showed an excellent approach to characterize damage zones and perform a numerical quantification of their effects on petrophysical rock properties.

Horizon slices helped to illuminate and characterize submarine channels that often show parallel orientation to the north-south fault system. These elements contain siltstones and calcareous sandstones that may be prospective reservoirs if located along fault planes.

Production analysis shows weak relationships with the lithology/rock type percentage of drilled rocks along well paths. However, the distance of horizontal well paths to the faults shows a negative correlation with cumulative hydrocarbon production, indicating that wells drilled in the proximity of damage zones are likely to be more prolific for hydrocarbon production.

Acknowledgments

This research was funded through the Reservoir Characterization and Modeling Laboratory at the University of Oklahoma, COLCIENCIAS and the Agencia Nacional de Hidrocarburos Scholarship. I thank Marathon Oil Corporation and the Integrated Core Characterization Center (IC3) for data. I thank Ishank Gupta, Jing Fu, Son Dang, and Heyleem Han for the rock type data, core plug velocity data, x-ray diffraction, and mineralogy data, respectively. Special thanks to Chris McClain and James Packwood from Marathon Oil Corporation for their valuable support in the project. Finally, I thank Schlumberger (Petrel and Techlog) for its generous license donation to the University of Oklahoma.

Figures

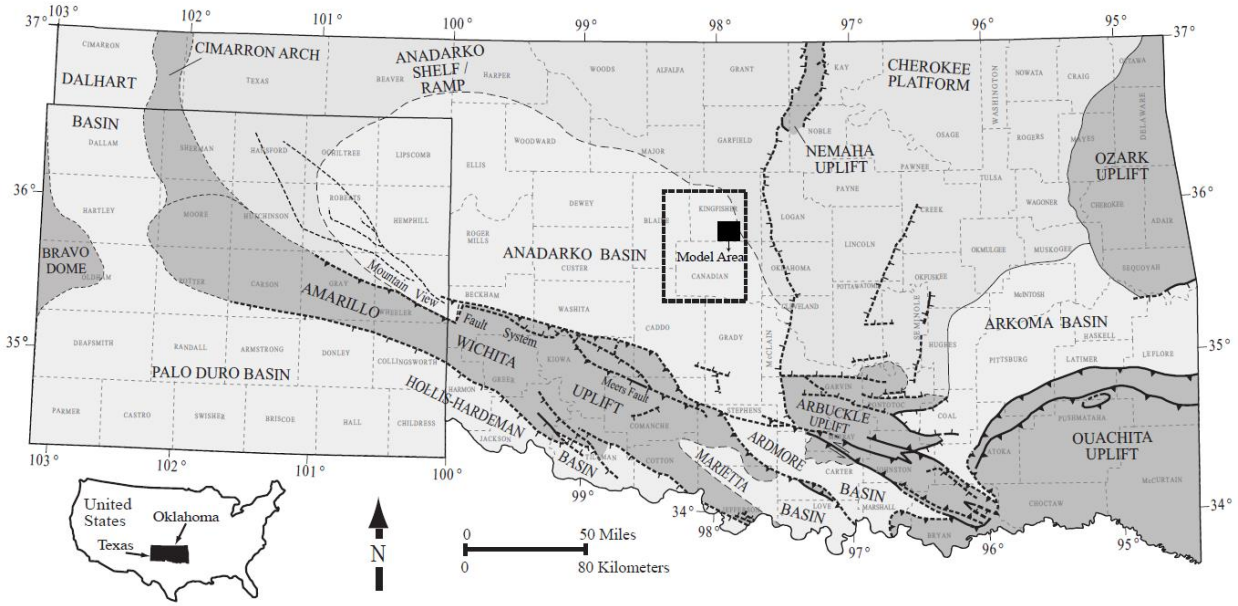

Figure 30: Map of regional tectonic provinces of Oklahoma and the Texas panhandle. The study area lies in the Anadarko Basin. (modified from Johnson and Luza, 2008; Northcutt and Campbell, 1995; Campbell, et al., 1988; Dutton, 1984; LoCriccho, 2012, McConnell, 1989).

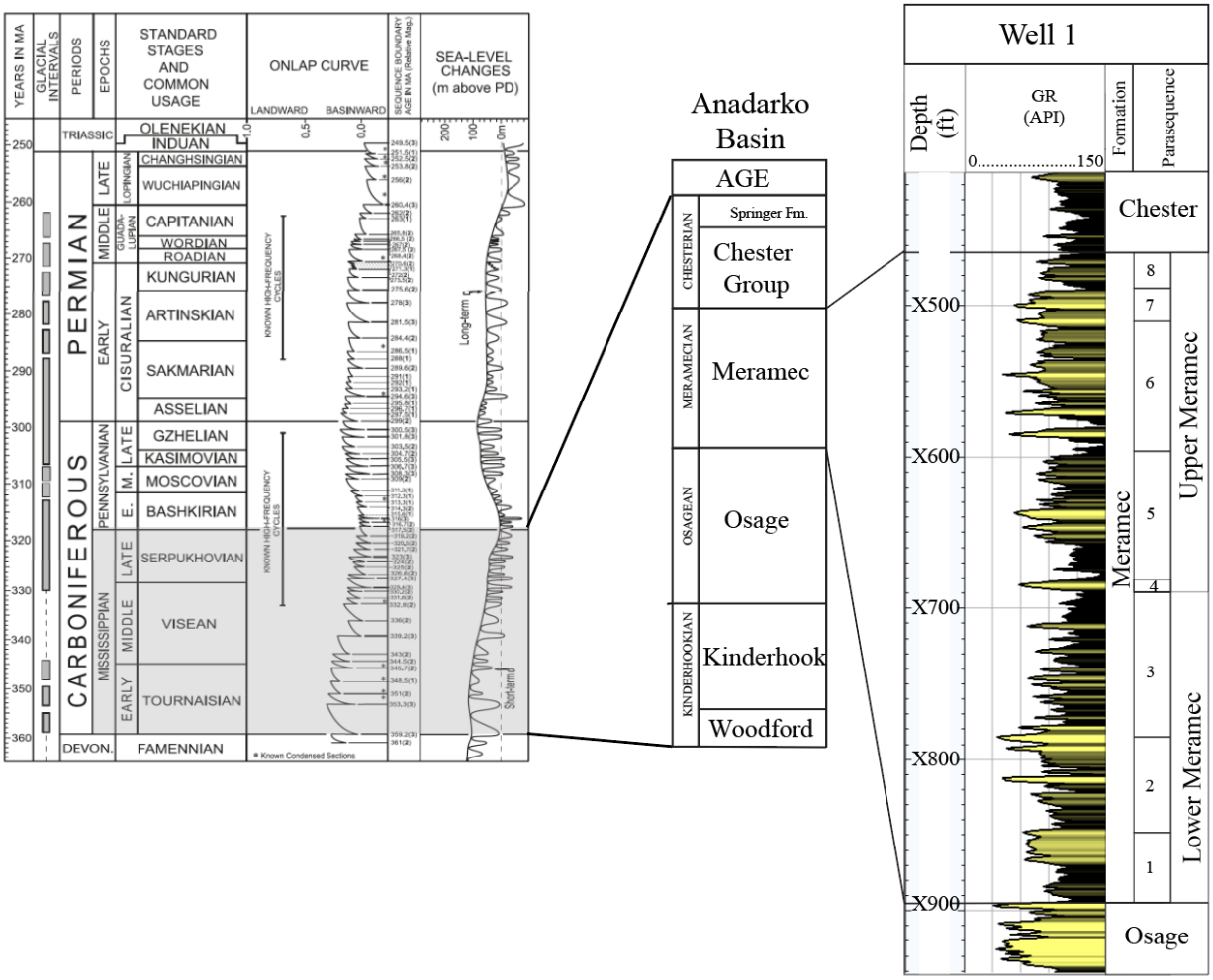

Figure 312: Generalized stratigraphic column and type log of the Mississippian section. The type log shows the interpreted parasequences from 1 to 8. (modified from Haq and Schutter, 2008).

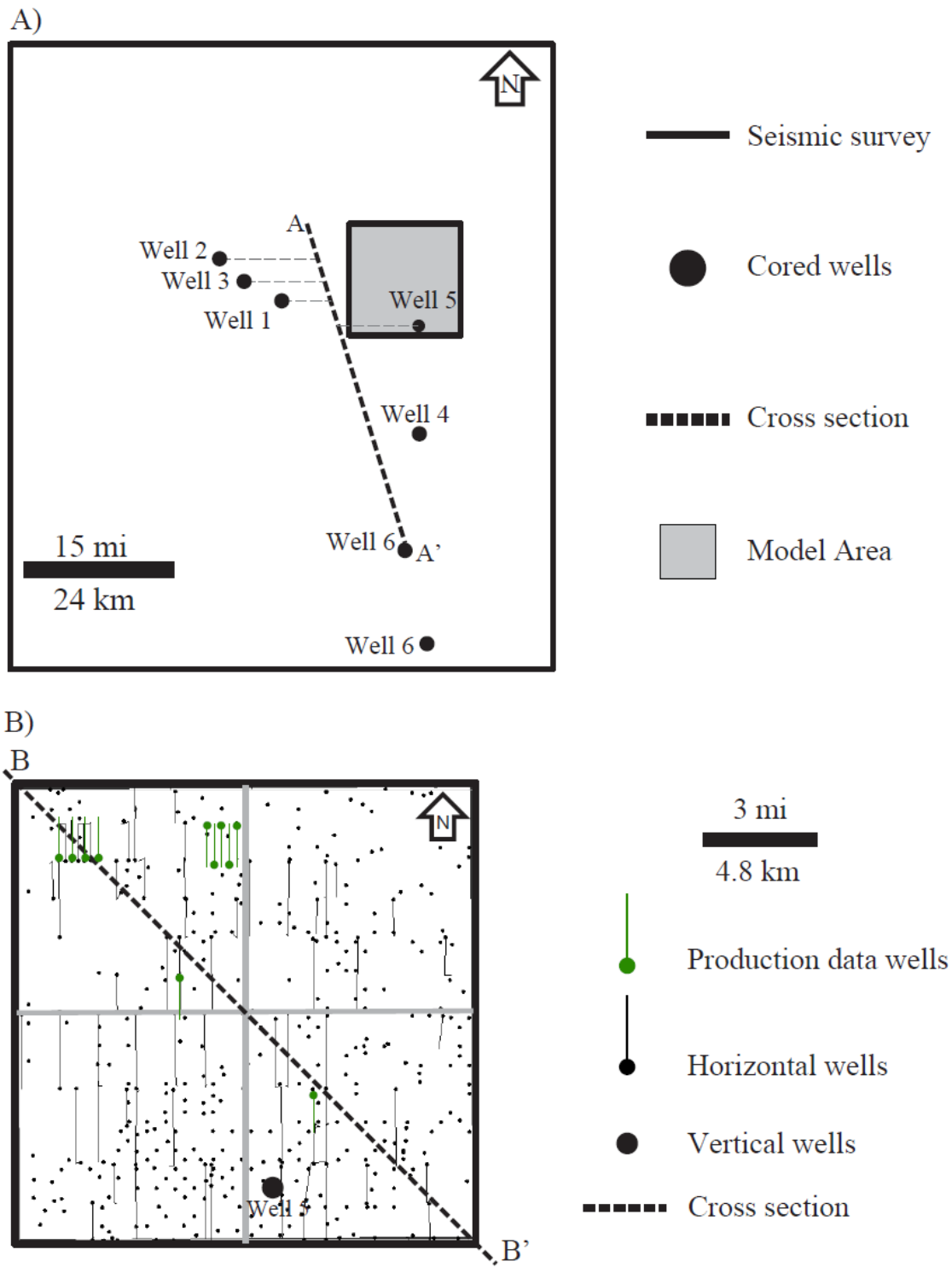

Figure 323:(A) Regional map with a cross section and the cored wells surrounding the modeled area. (B) A detailed map of the study area shows 288 wells with wireline logs (GR, NPHI, RhoB, PE, RILD, and DT), five cored wells, and two cross sections.

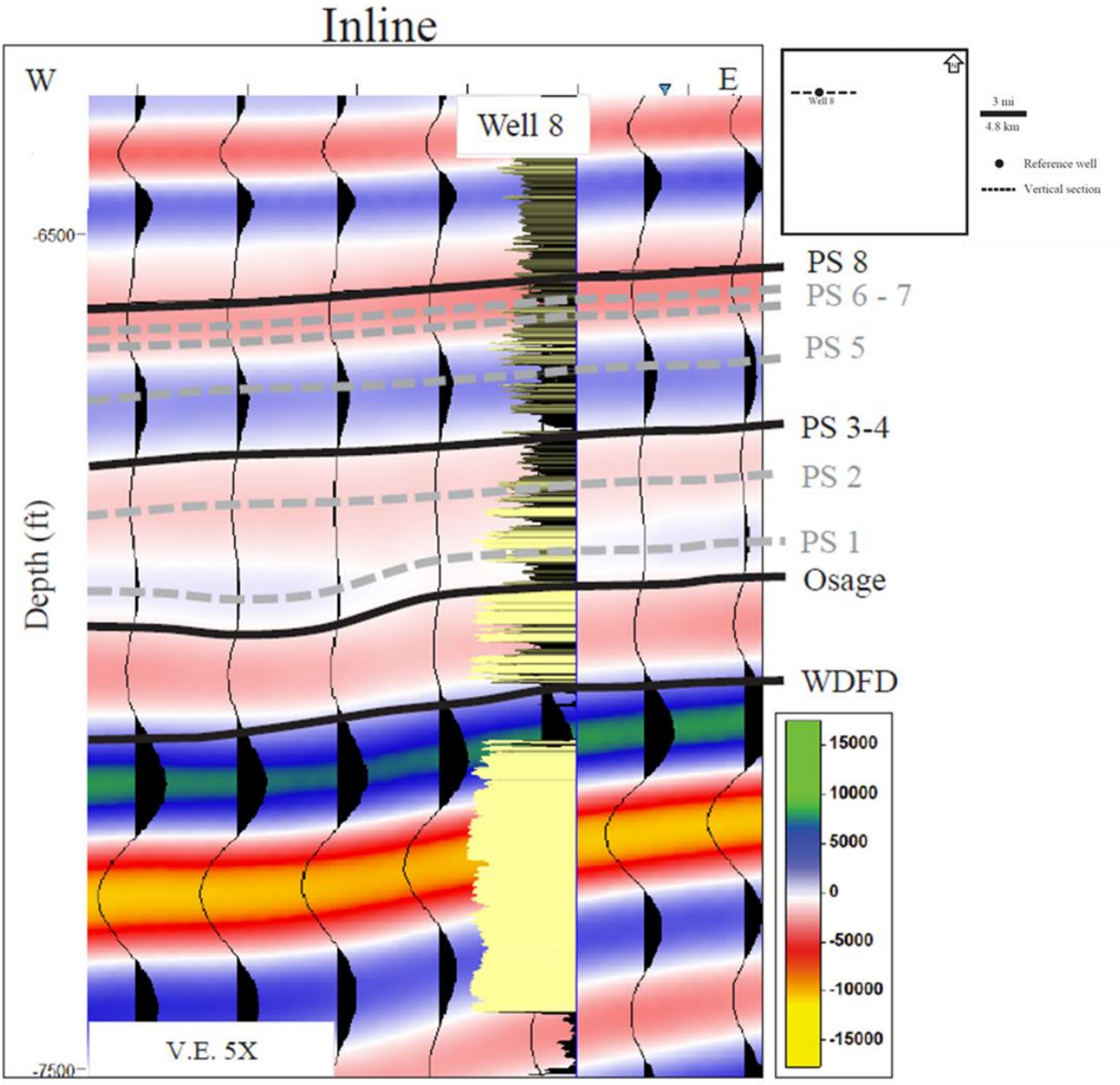

Figure 344:(A-A') Seismic inline display in-depth domain. Three seismic interpreted horizons are displayed (black lines), and the remaining surfaces were calculated using conformable gridding. (dashed lines).

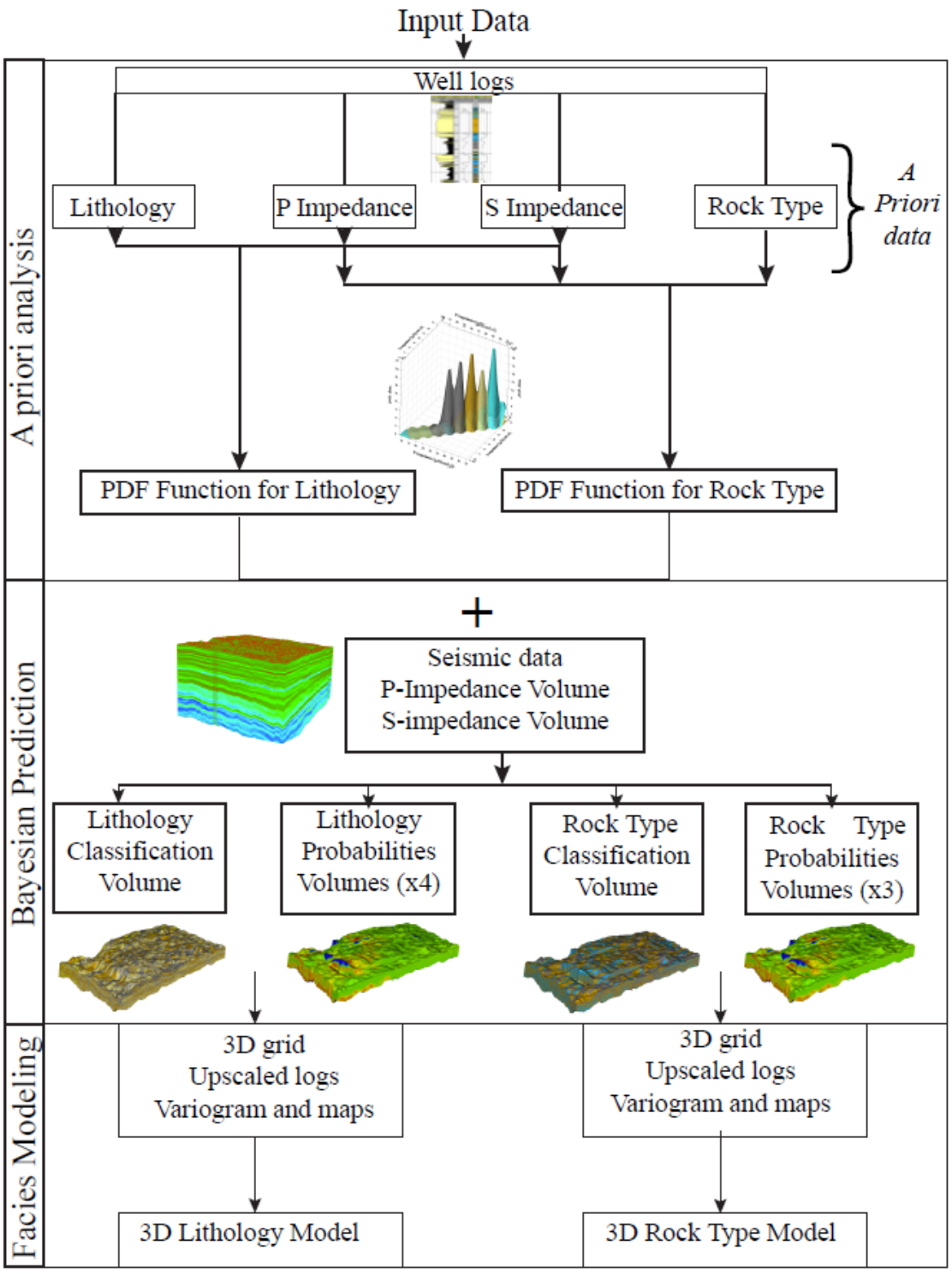

Figure 355: Schematic workflow for the Bayesian approach classification process and its application in modeling. The method comprises three steps: 1) a priory analysis, 2) the Bayesian prediction, and 3) the facies modeling using the Bayesian prediction results.

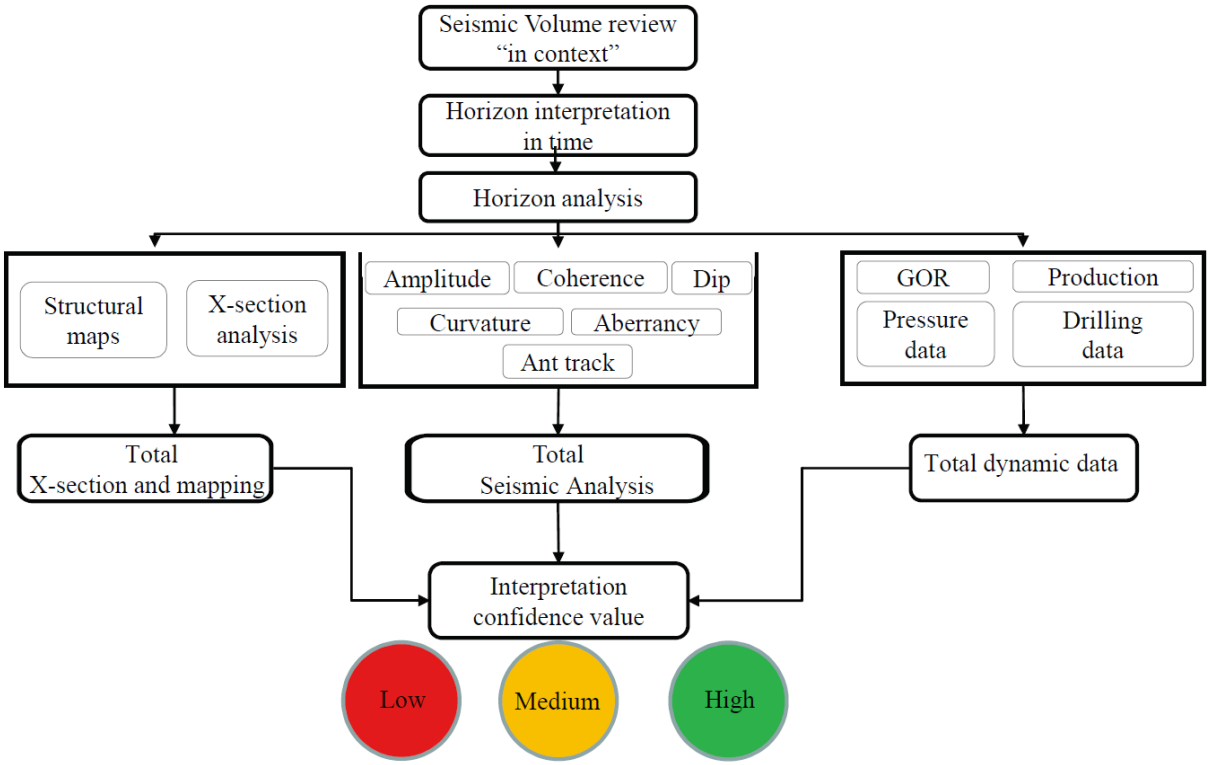

Figure 366: Schematic workflow for integrated fault interpretation. The method includes three integrated areas with X-section, mapping, seismic data analysis and dynamic data. The result of the process is an interpretation with a confidence level for each fault.

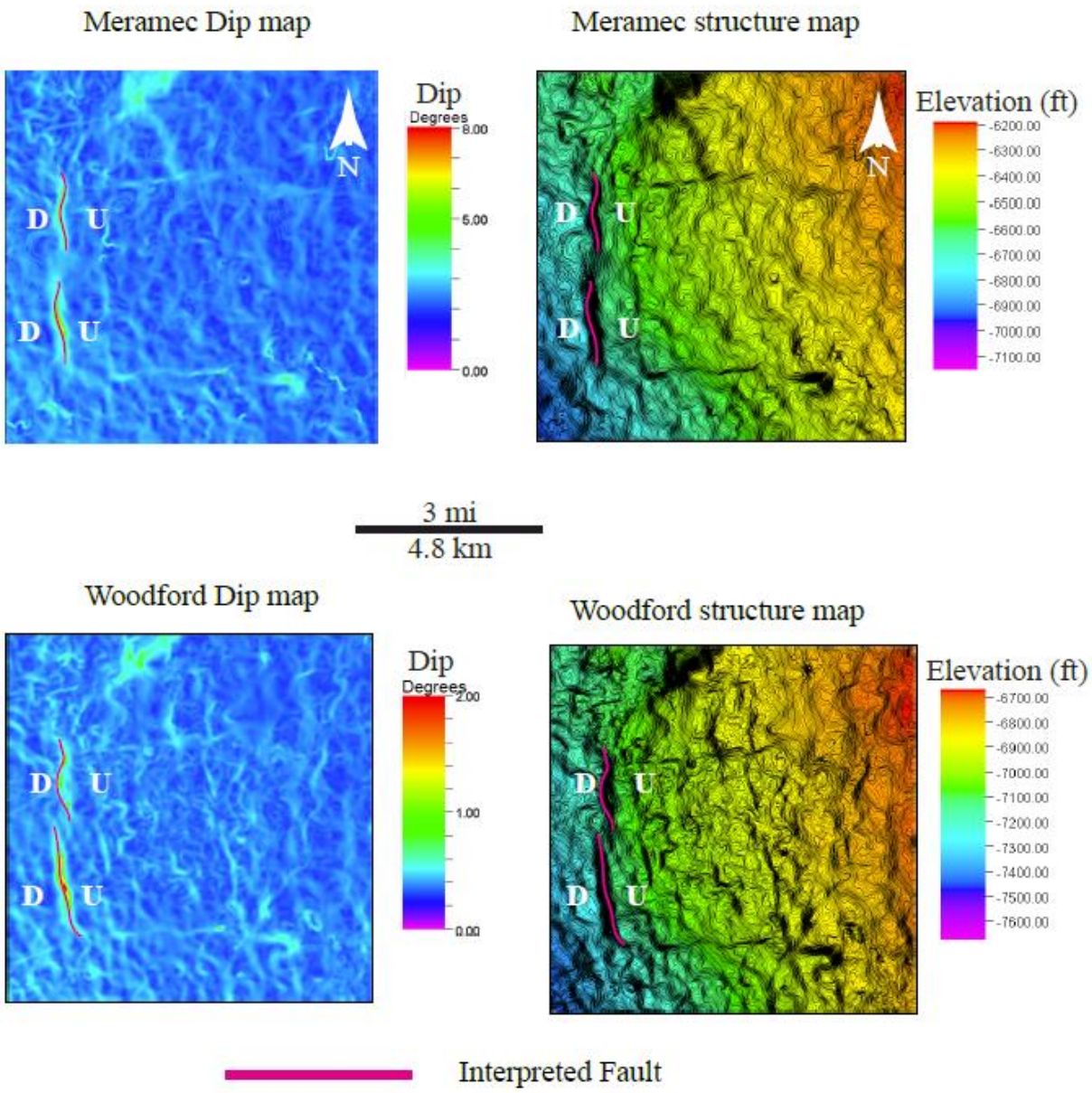

Figure 377: Structural maps with high-density contouring for the top of the Meramec and the Woodford formations. The pink line shows one example where a fault was inferred based on the high-density contours and orientation identified in the structural map. I used the top and base surface to consider faults that affected the entire stratigraphic section.

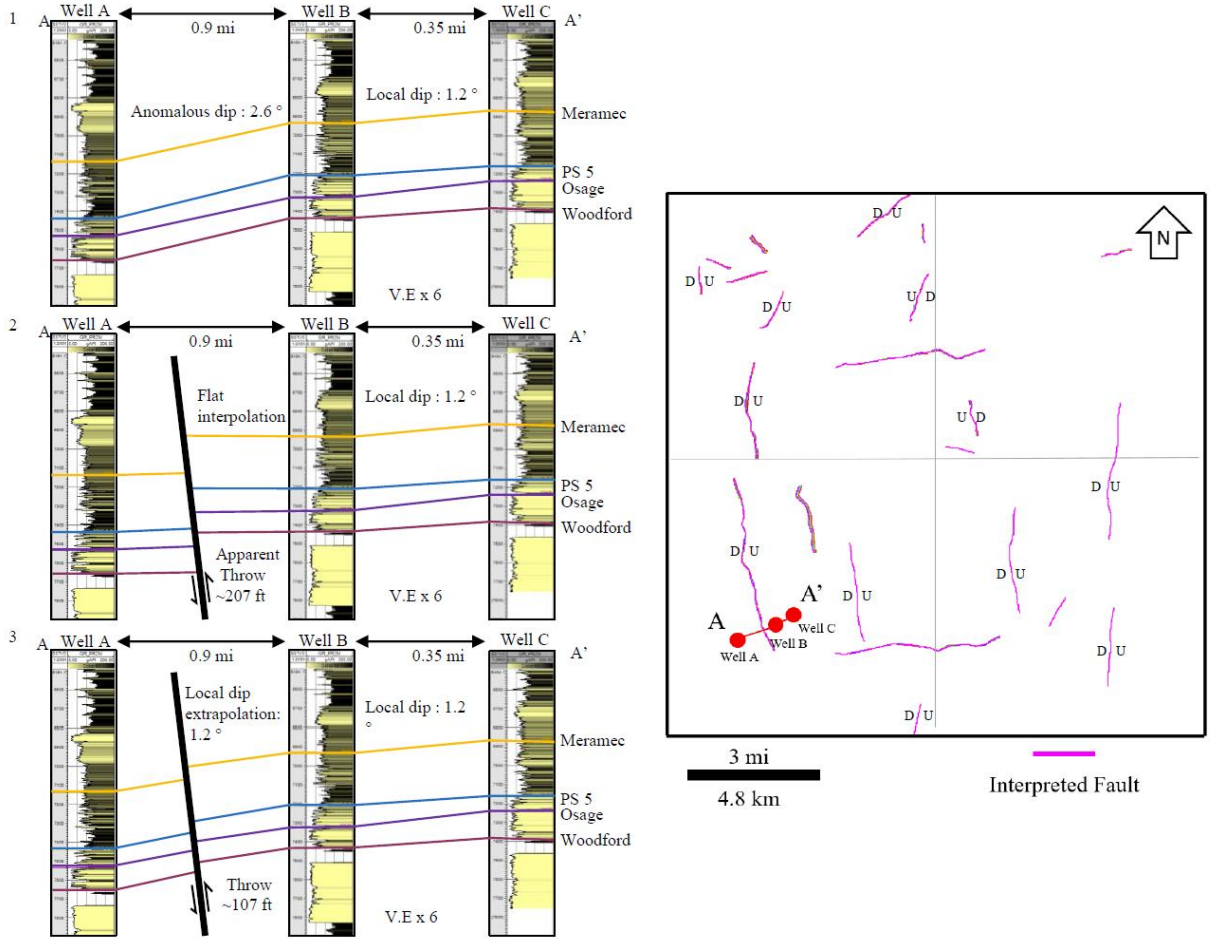

Figure 388: One example of structural cross sections used to analyze and estimate the vertical displacement of faults. 1) A cross section with a drastic dip change between adjacent wells, 2) A cross section that shows the fault interpretation using a flat surface to interpret the fault from the well tops data, and 3) A cross section displays the fault interpretation after dip correction for the regional trend.

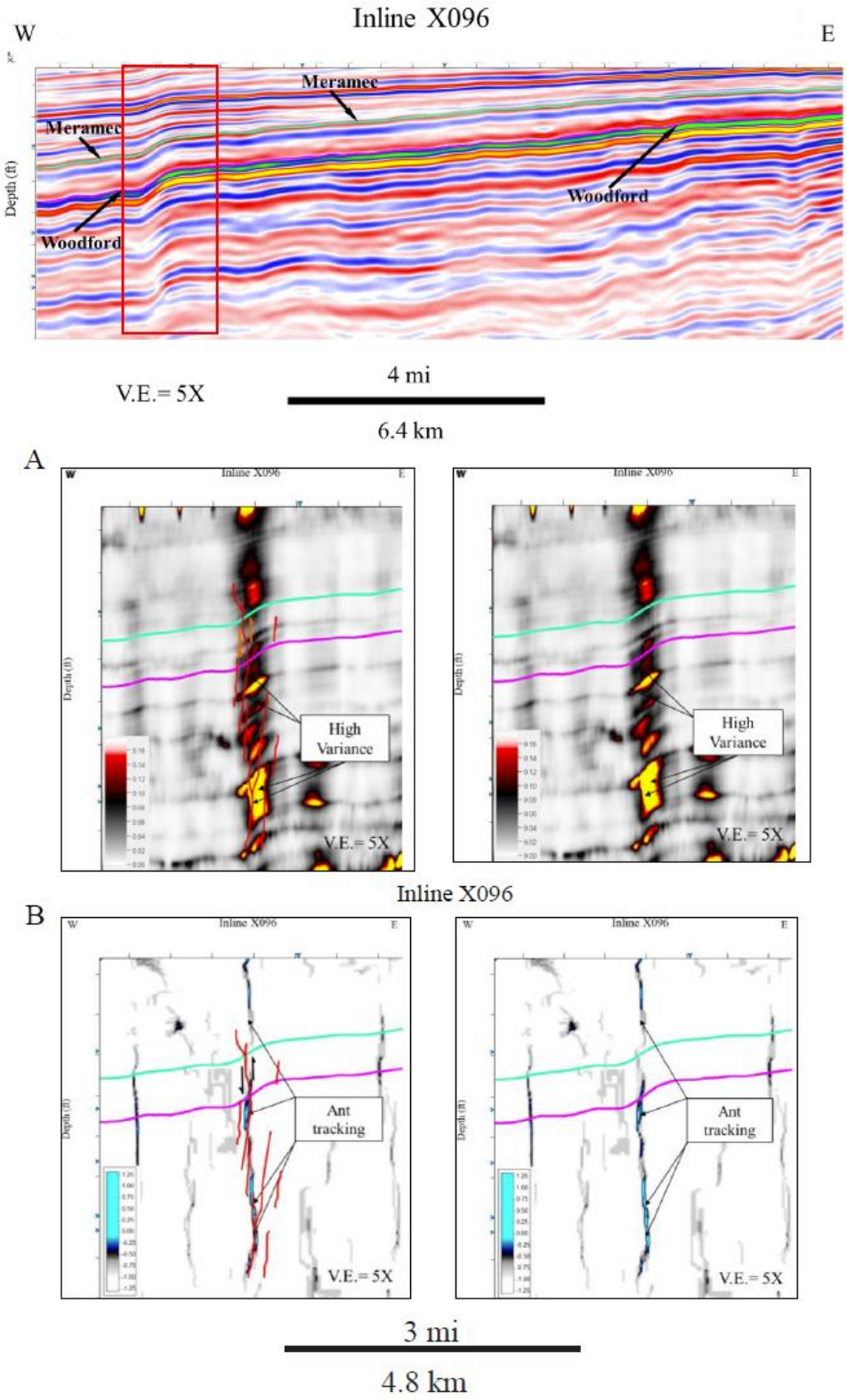

Figure 399: Detailed view of vertical seismic profiles of variance and ant-tracking attributes for fault interpretation.

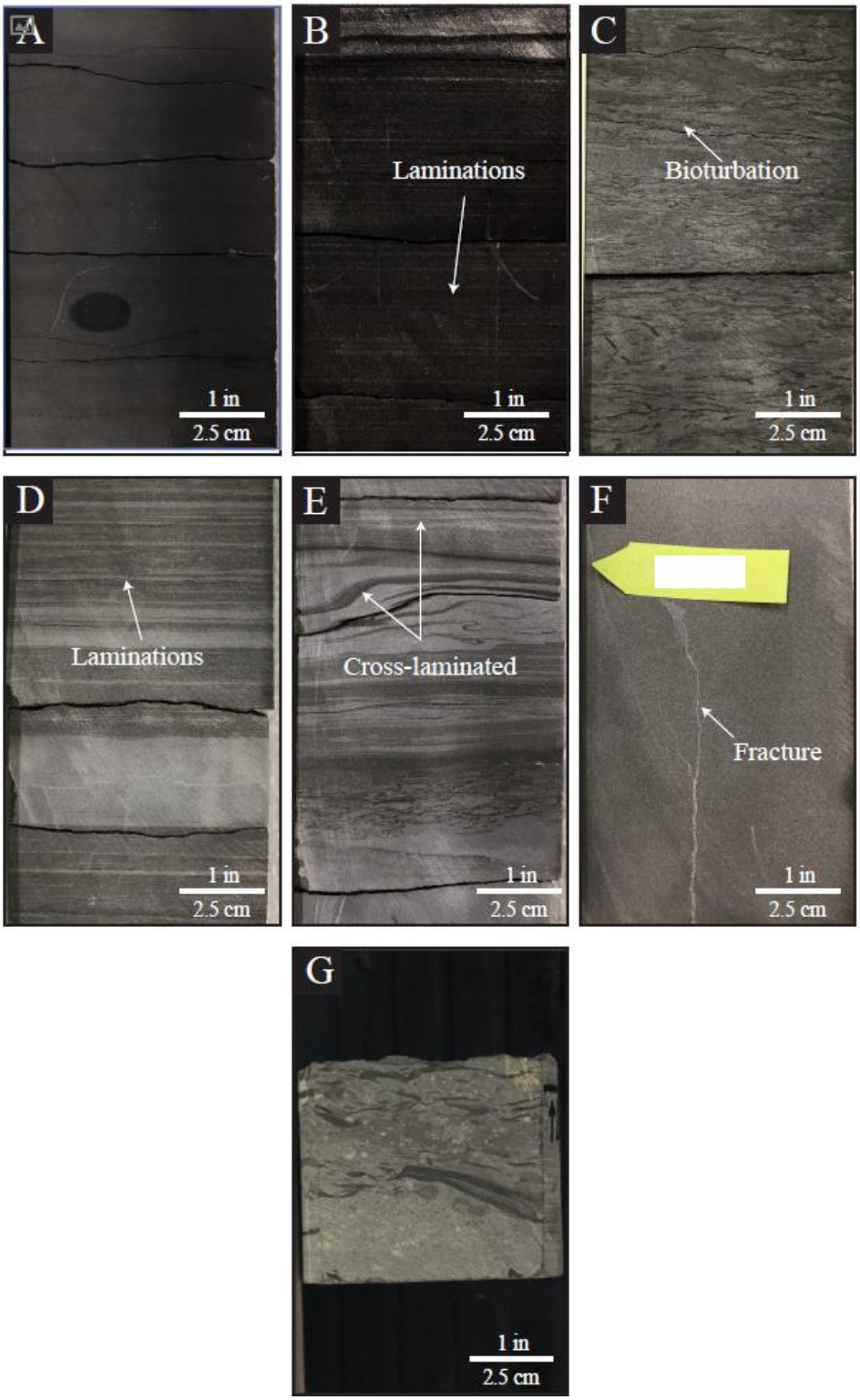

Figure 40: Core photographs of the identified Meramec lithofacies in the study area: A) Structureless mudstone B) Laminated mudstone C) Bioturbated mudstone. D) Calcareous laminated siltstone E) Cross-laminated siltstone/sandstone F) Structureless siltstone/sandstone G) Silty grainstone.

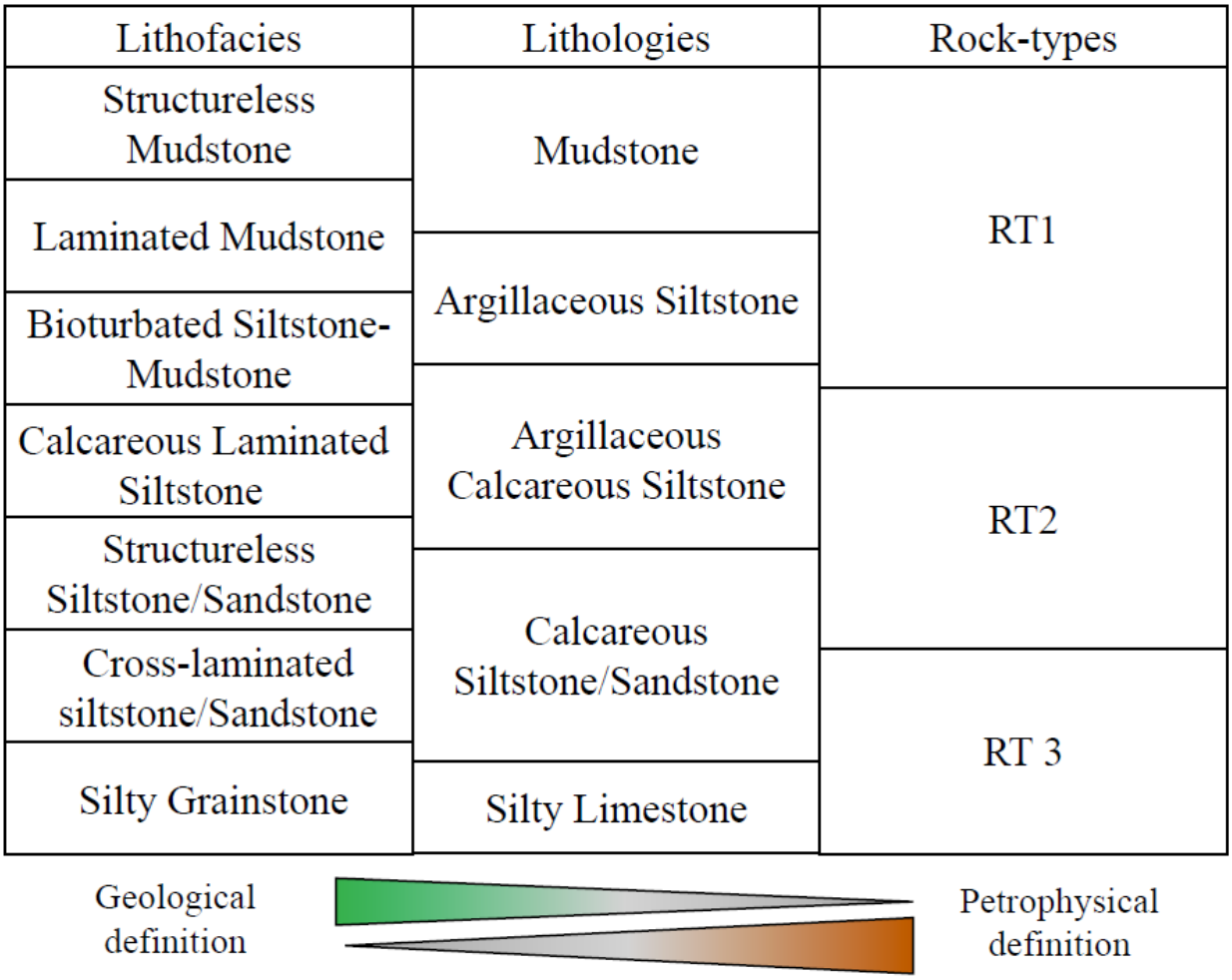

Figure 411: A summary table that shows the defined lithofacies from core and thin-section descriptions. Lithologies are used to simplify the lithofacies model and represent the geology using well log data. Rock types are defined using a flow zone indicator approach that considers only the rock porosity and permeability.

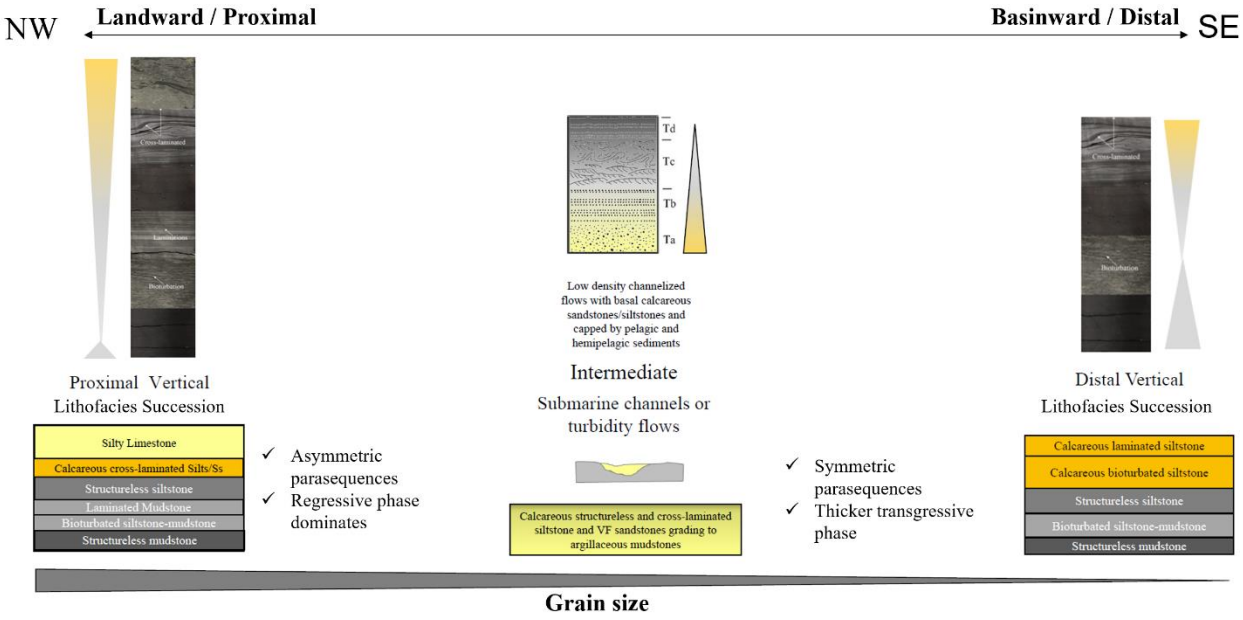

Figure 42: Proximal to distal vertical succession of lithofacies in parasequences. The proximal succession is composed of coarser and more calcareous lithologies compared to the distal succession, mainly dominated by mudstones and clay-rich lithofacies. Occasional rocks are found in intermediate positions and show a blocky of fining upward trend composed of calcareous siltstones and interpreted as a result of submarine channels deposited within the carbonate out shelf.

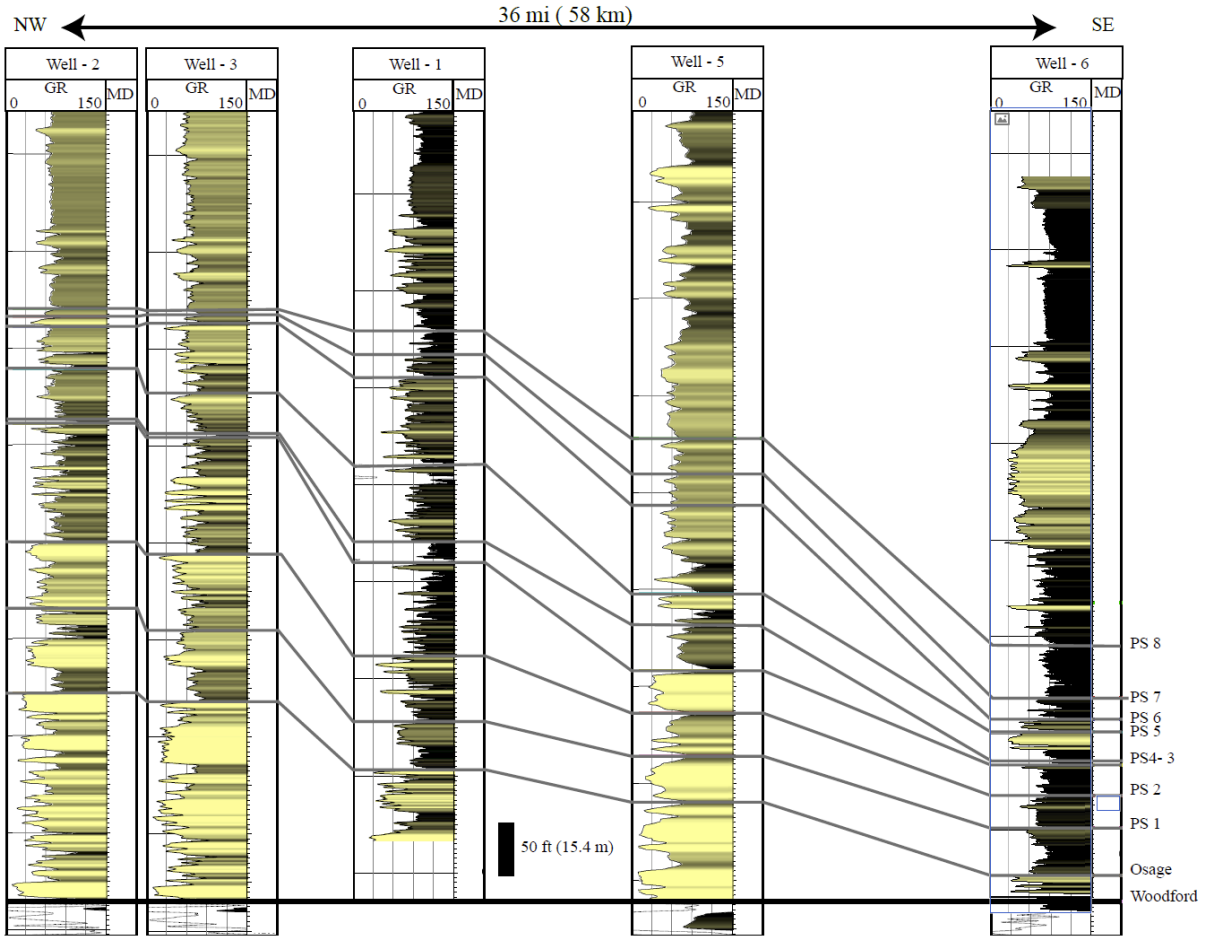

Figure 43: (A-A') Regional cross section that includes wells with available core within the study area flattened on the Woodford shale. Black lines correspond to the parasequences tops interpreted for the Mississippian Meramec. The GR track is shaded by the gamma-ray values and was used for stratigraphic correlations. The section is oriented northwest-southeast and shows the progradational clinoforms in the study area and the decrease in the overall thickness of the Meramec towards the southeast.

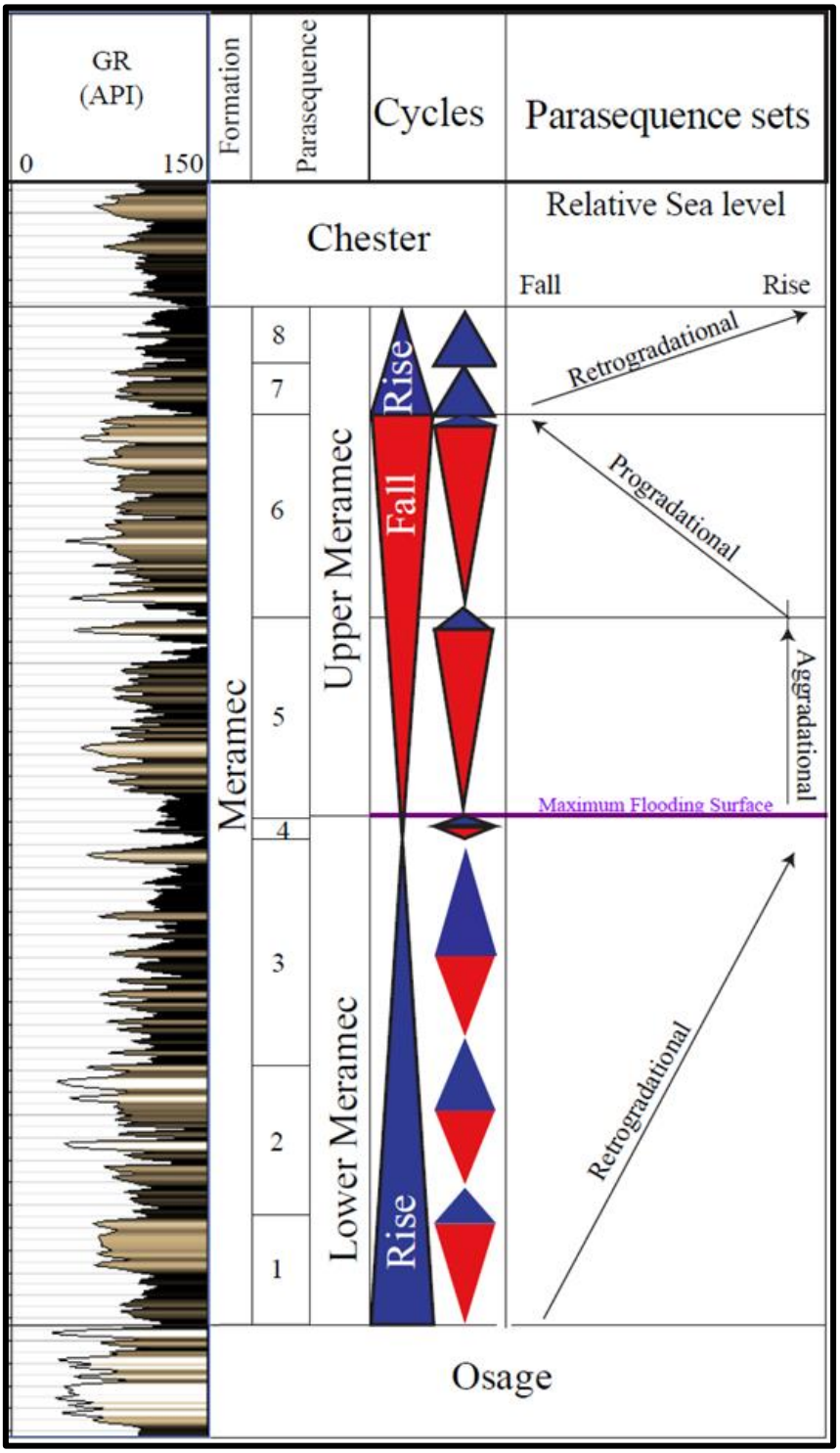

Figure 444: A summary of the parasequence sets interpreted in well 11 for the Meramec strata. From base to top, retrogradational, aggradational-progradational, and retrogradational.

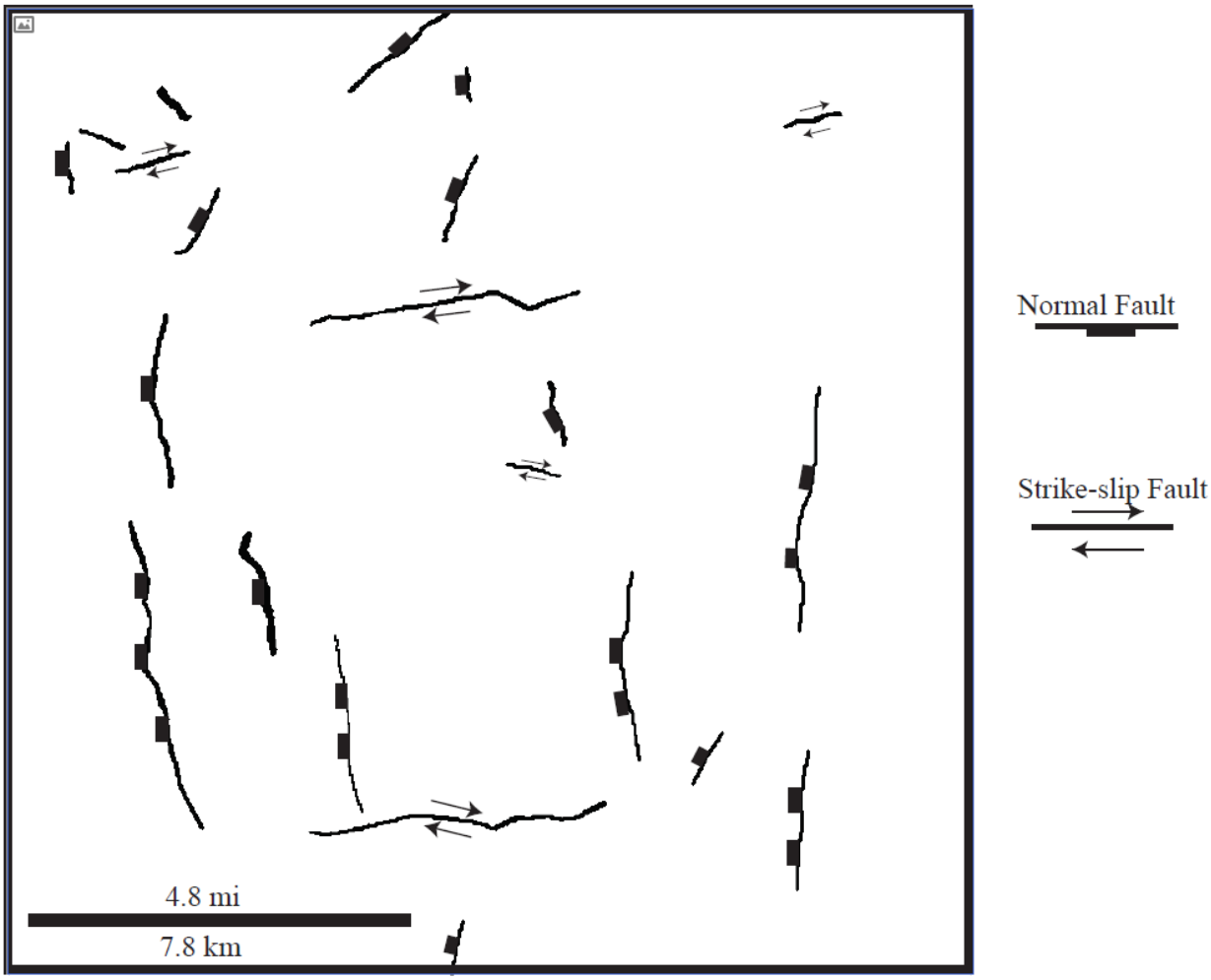

Figure 455: Map of the interpreted faults within the Meramec strata. Two main structural types were identified 1) Normal faults with a predominant north-south orientation and 2) strike-slip faults with an east-west direction.

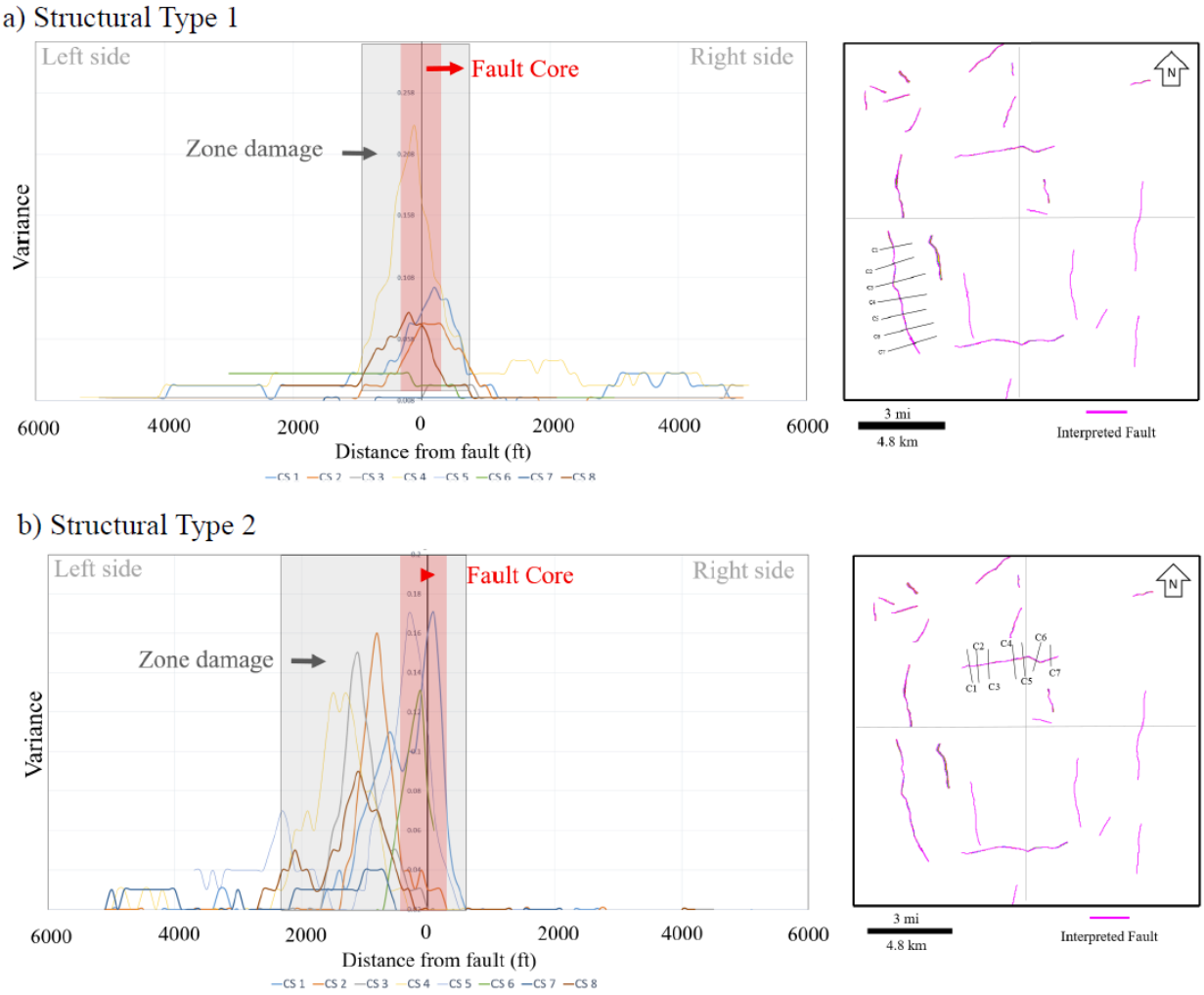

Figure 466: An example of the variance analysis performed over faults. a) shows a structural type 1 fault analysis with symmetric damage zone highlighted with the variance response b) displays a cross-plot of the analysis of a structural type 2 fault characterized by an asymmetric damage zone highlighted in higher variance values to the left side of the fault.

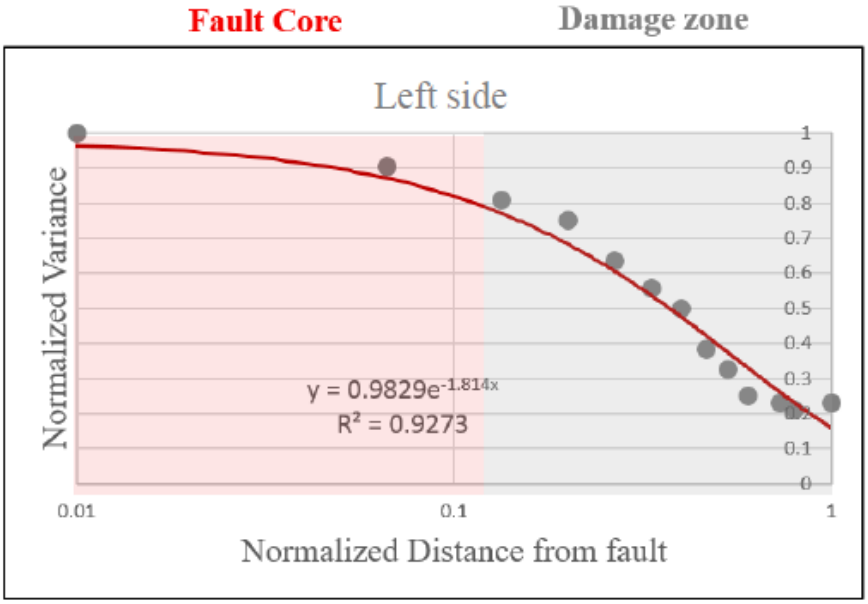

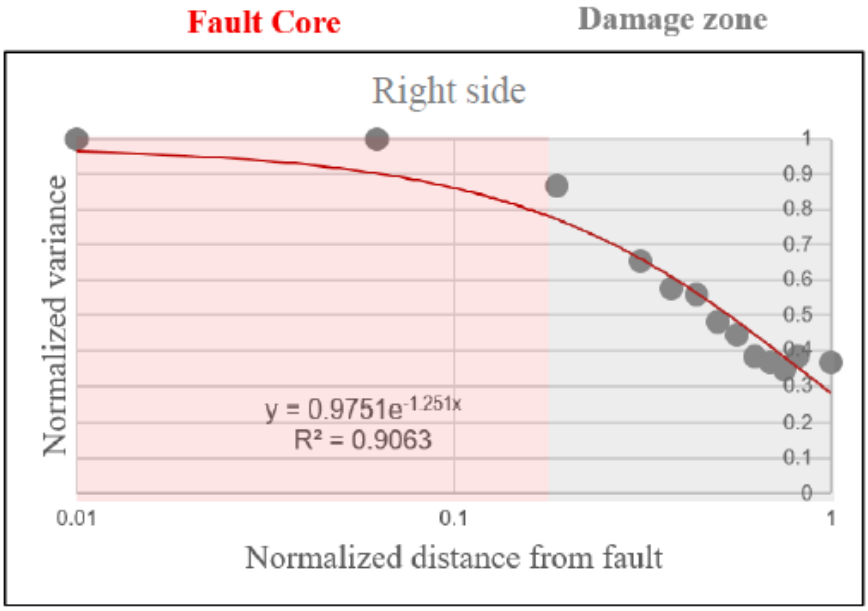

Figure 477: Normalized variance versus distance to fault cross plots generated from the variance analysis across each fault side (left or right). The results closely match similar equations reported in the literature for fracture density variations versus distance from the fault

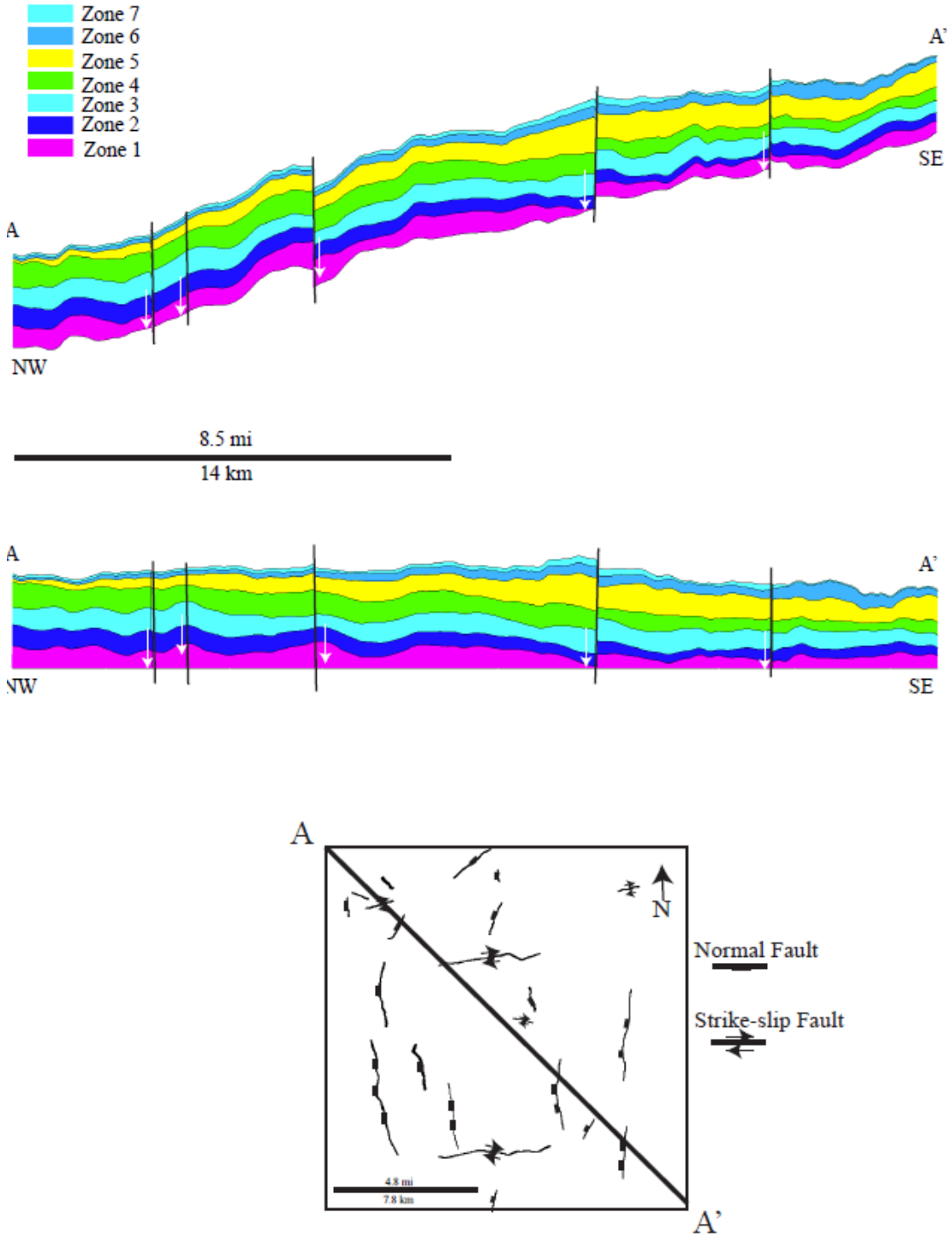

Figure 488: Northwest-southeast oriented cross sections through the 3D model flattened on the Osage horizon. The model reflects seven modeled zones and 30 interpreted faults within the structural grid.

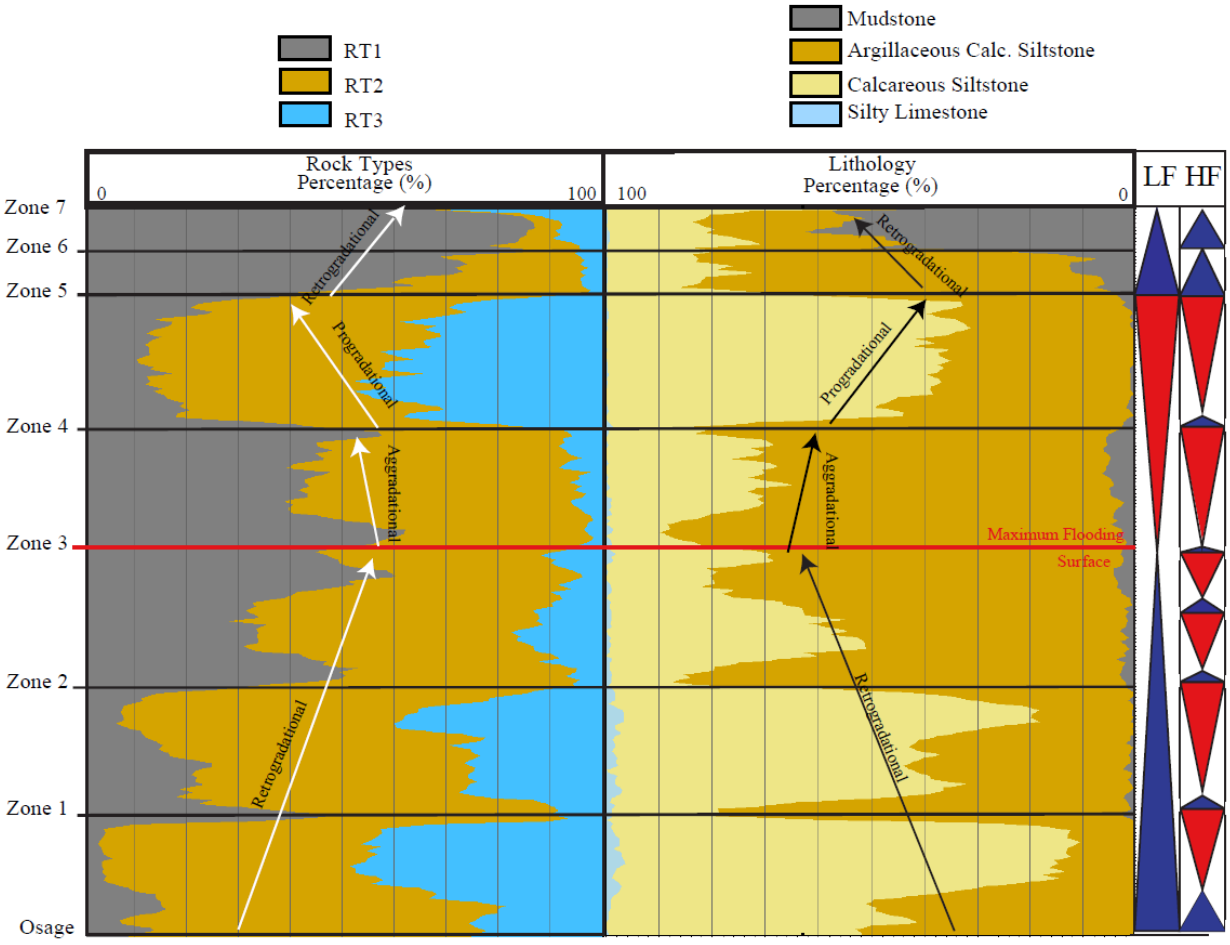

Figure 499: Vertical proportion curves for the lithology and rock type models with the interpreted 3rd and 4th order cycles. Stratigraphic variations of lithological and rock types percentages show a strong relationship between the stratigraphic framework and the reservoir model rock distribution.

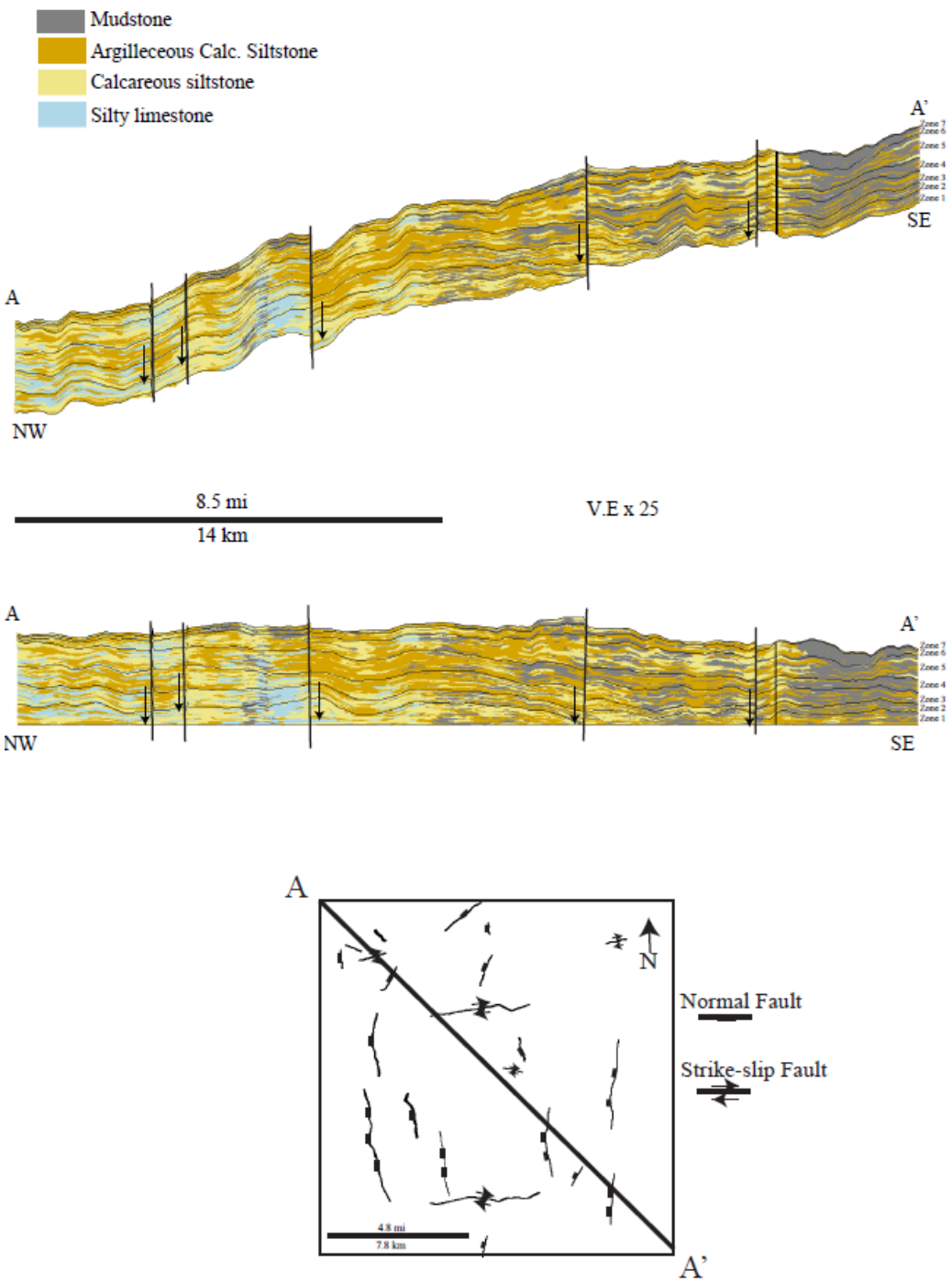

Figure 50: Northwest-southeast oriented cross section through the 3-D lithology model flattened on the Osage horizon. The cross section shows the spatial distribution of the lithologies within the study area. Zones 1, 2, 3 and 4, display an overall increase in argillaceous and clay-rich lithologies upwards with a decrease in calcareous siltstones that represent a rise in sea-level and retrogradation. Zones 5 and 6 show a slight increase in the abundance of calcareous siltstones indicative of a small regressive cycle that transitions to the top clay-rich zones 6 and 7 with predominant mudstones southwest representing the final transgressive cycle in the Meramec.

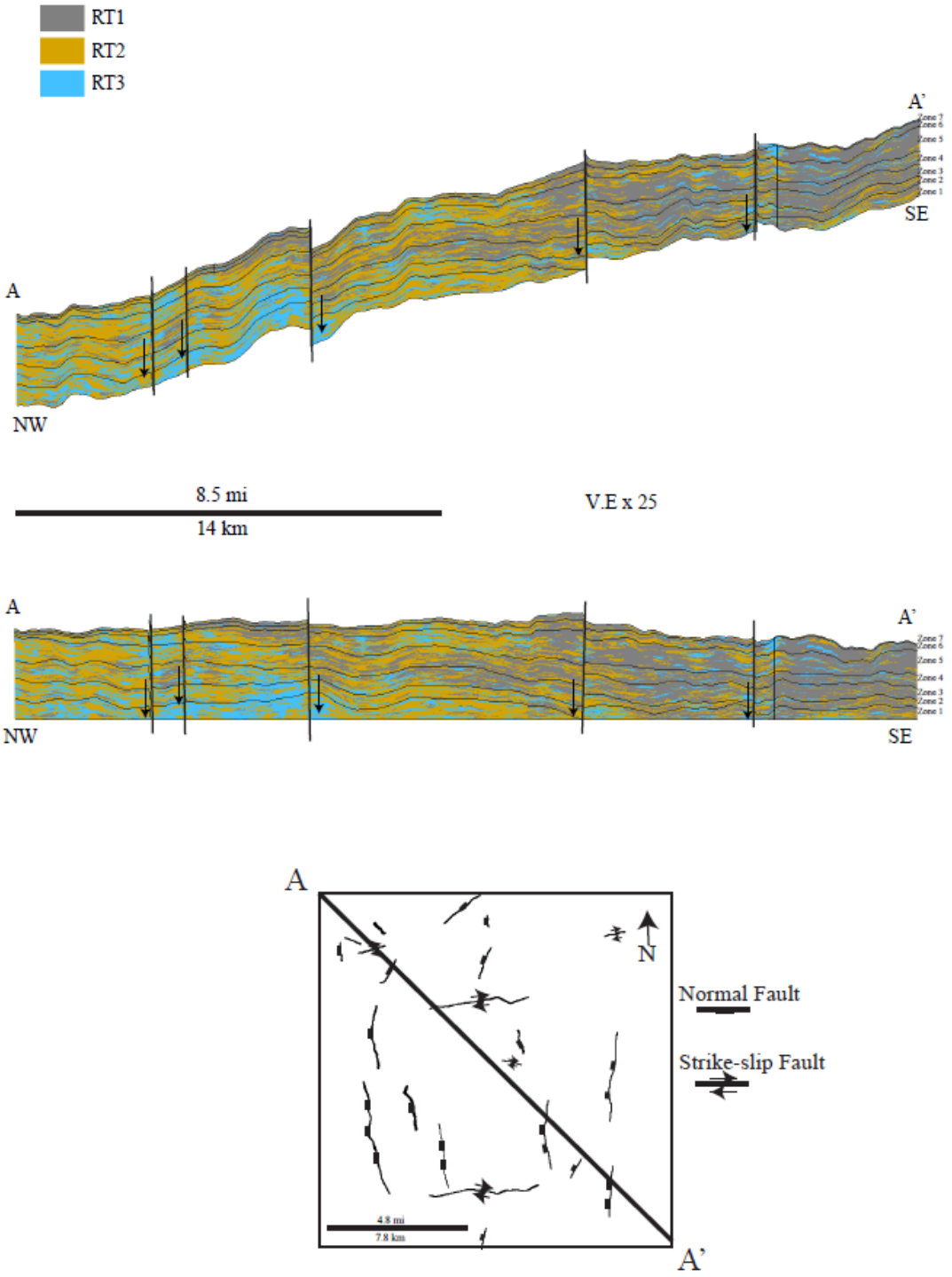

Figure 51: Northwest-southeast oriented cross section through the 3-D rock type model flattened on the Osage horizon. The cross section shows the spatial distribution of the rock types within the study area. Zones 1, 2, 3 and 4, display increasing abundance of RT1 and RT2 upwards with a decrease of RT3, representing a rise in sea-level and retrogradation. Zones 5 and 6 show an increase in the quantity of RT2 and RT3 indicative of a small regressive cycle that transitions to the top RT1 dominated zones 6 and 7.

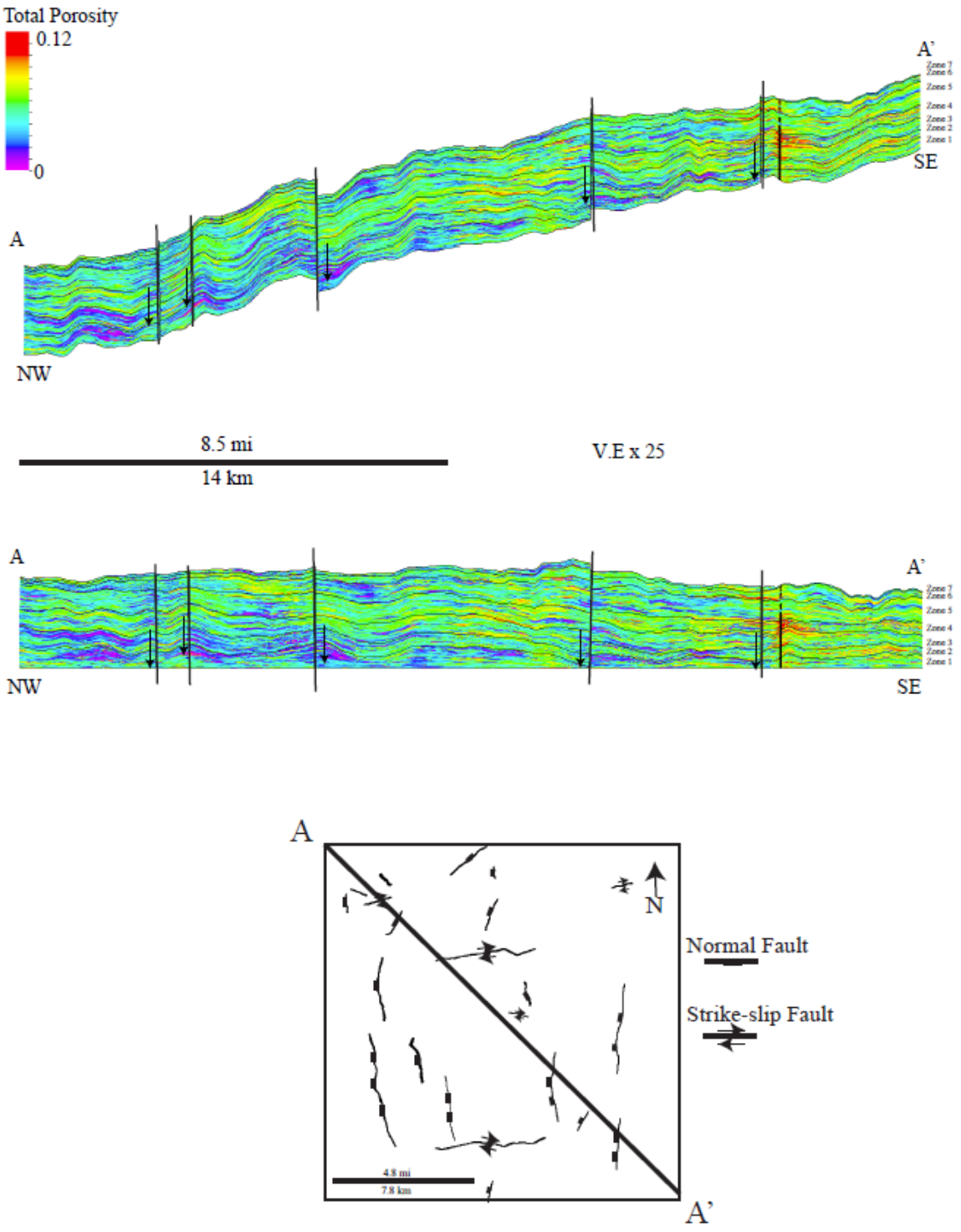

Figure 522: Northwest-southeast oriented cross section through the 3-D porosity model flattened on the Osage horizon. The section shows the spatial distribution of the porosity within the study area. High porosity areas are associated with clay-rich lithologies and RT1 that dominate the model southeast (basinward) and zones 3, 4, 6, and 7.

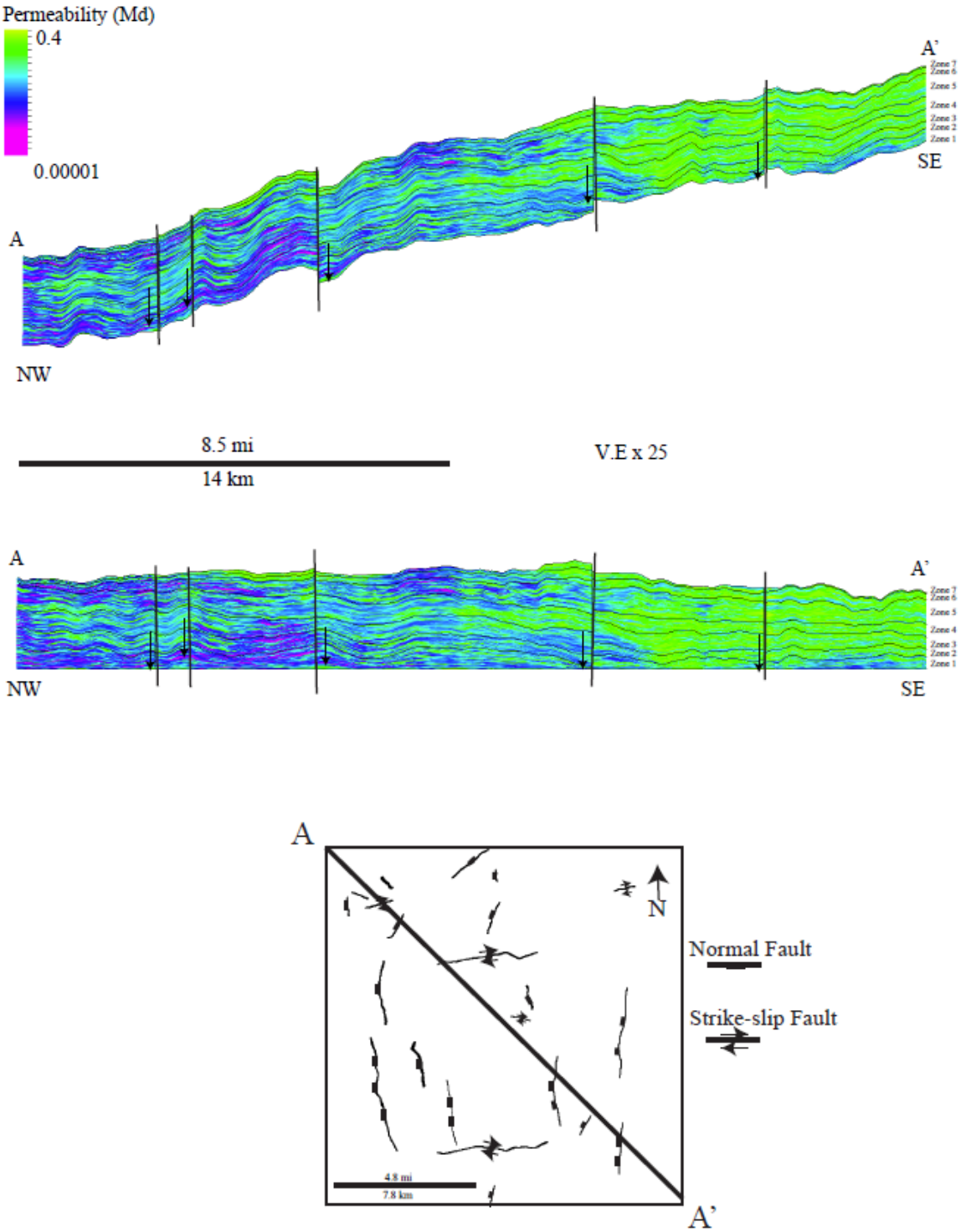

Figure 533: Northwest-southeast oriented cross section through the 3-D permeability model flattened on the Osage horizon. The section shows the spatial distribution of permeability within the study area. The permeability model resulted from a cloud transform approach and includes permeability modifiers that enhance permeability in the fault's vicinity, as shown in the cross section.

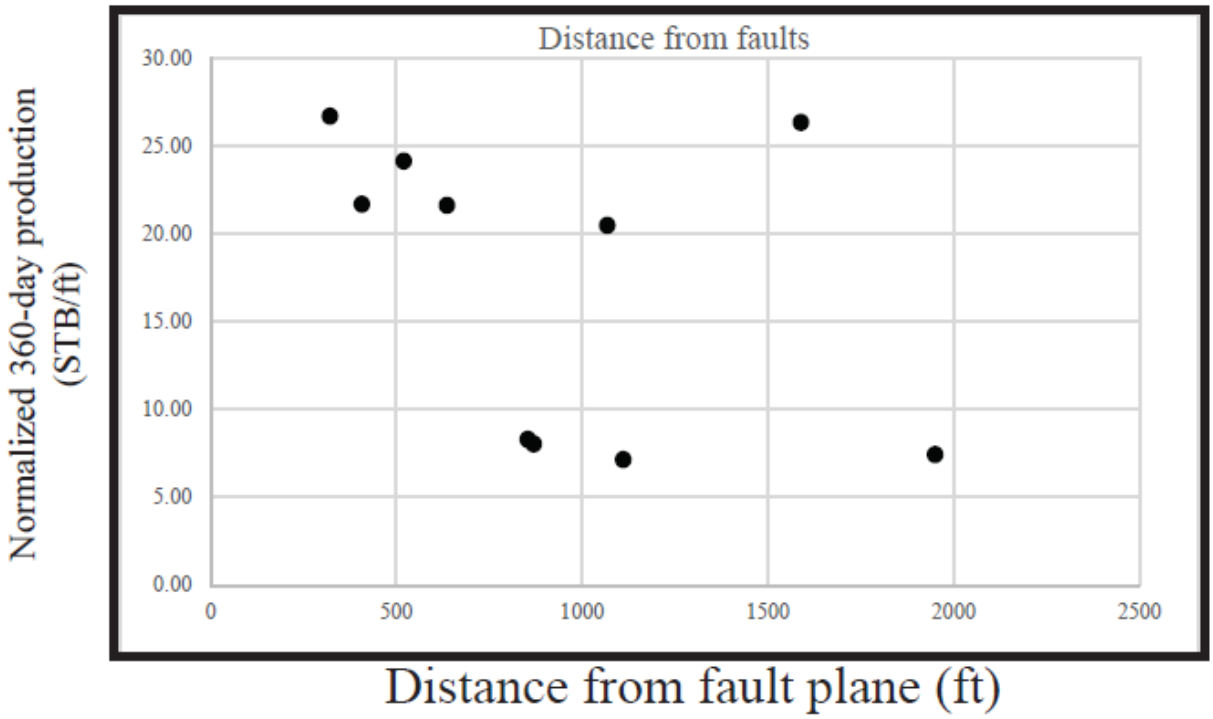

Figure 544: Cross-plots of 360-day cumulative production versus distance from the fault. The production data was normalized by dividing the cumulative production by the lateral length of the well.

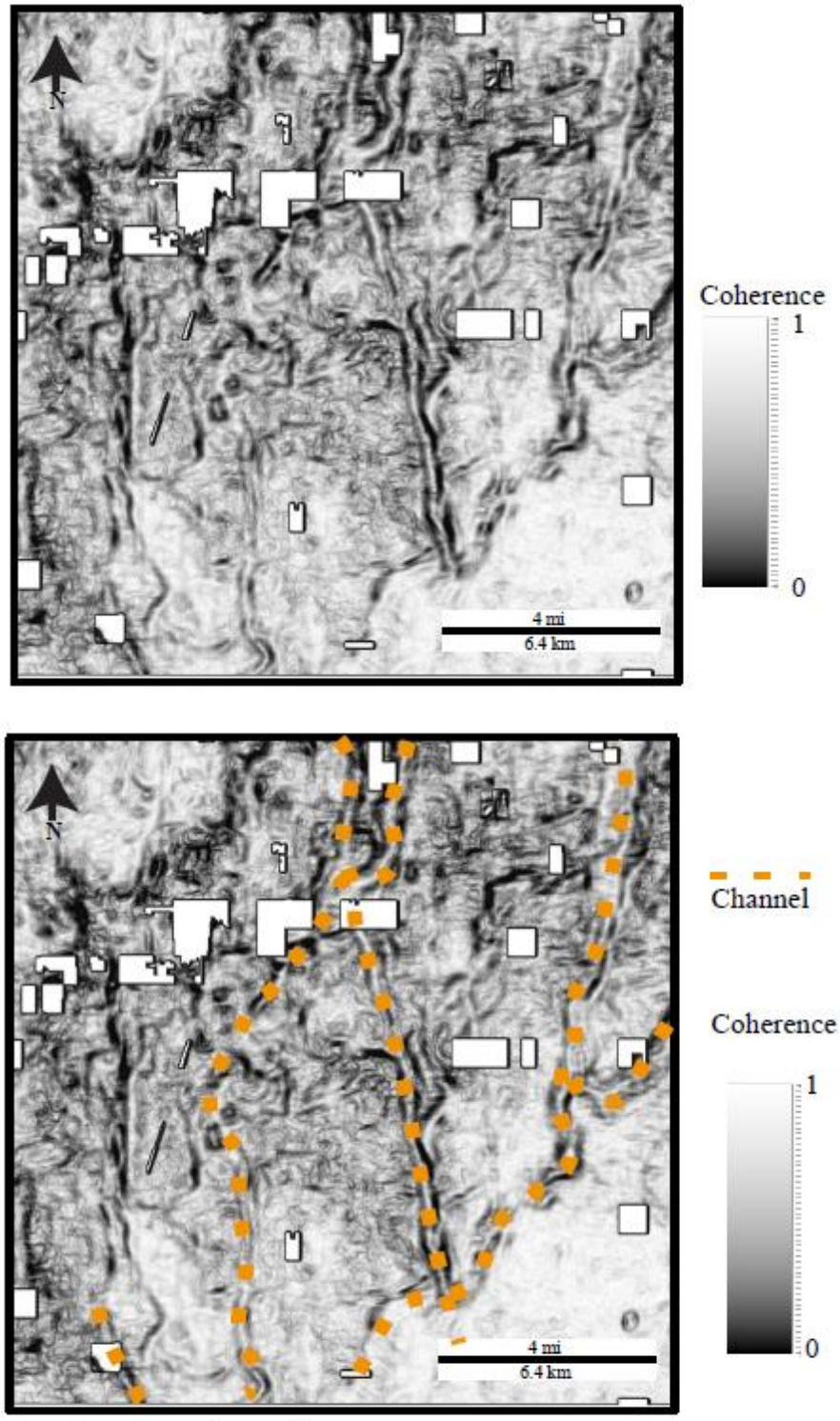

Figure 555: Coherence phantom horizon slice (uninterpreted and interpreted). Parasequence 2 and 3 contain deposition of submarine channels with paleo-flow direction north-south

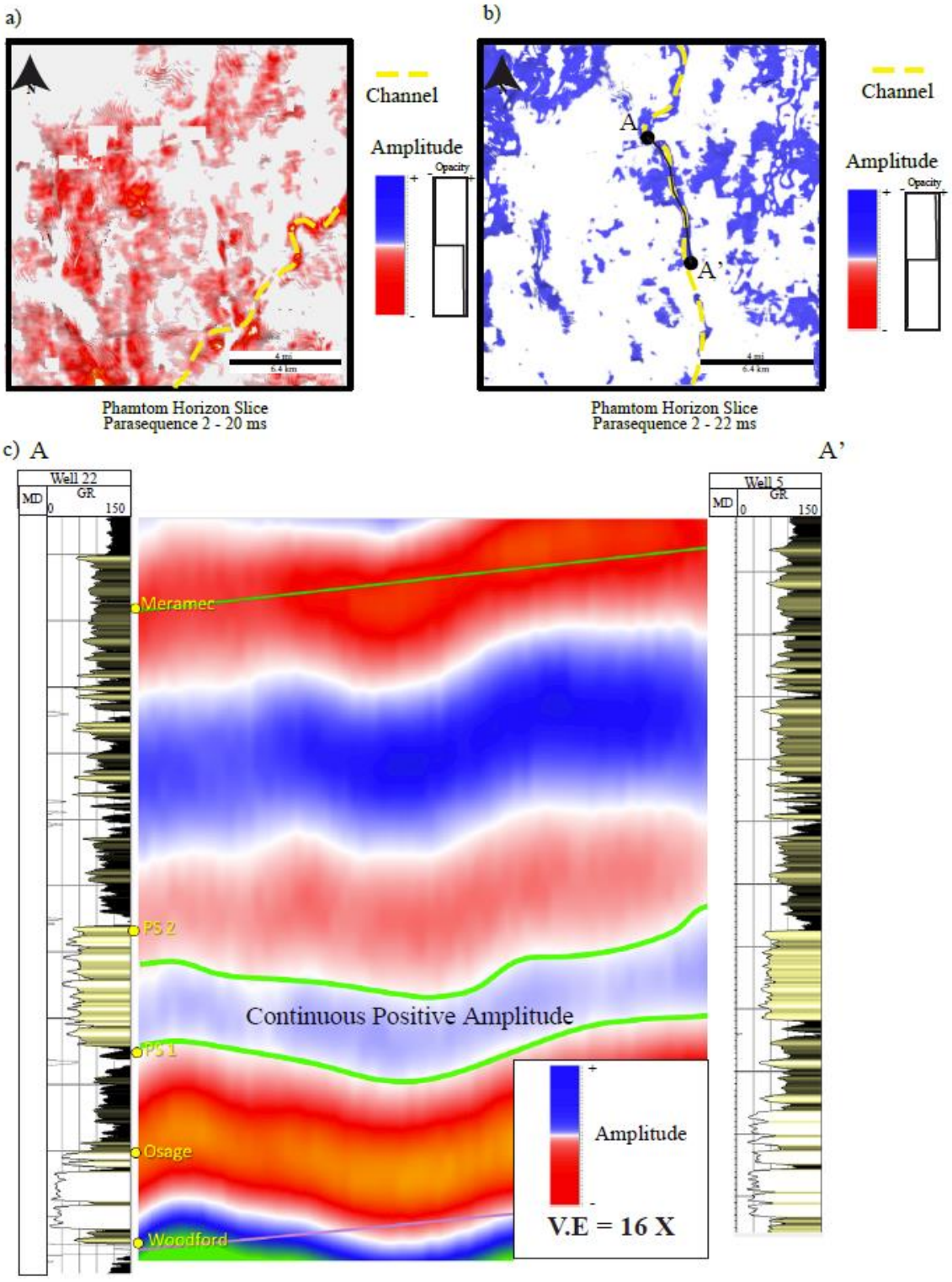

Figure 566: Amplitude extractions in phantom horizons near parasequence 2 and 3. Submarine channels are isolated, decreasing the opacity of a)positive or b)negative amplitude depending on the channel lithological composition. C) A composite vertical seismic section displays a channel composed of RT2 or calcareous siltstone (positive amplitude) drilled in wells 5 and 22.

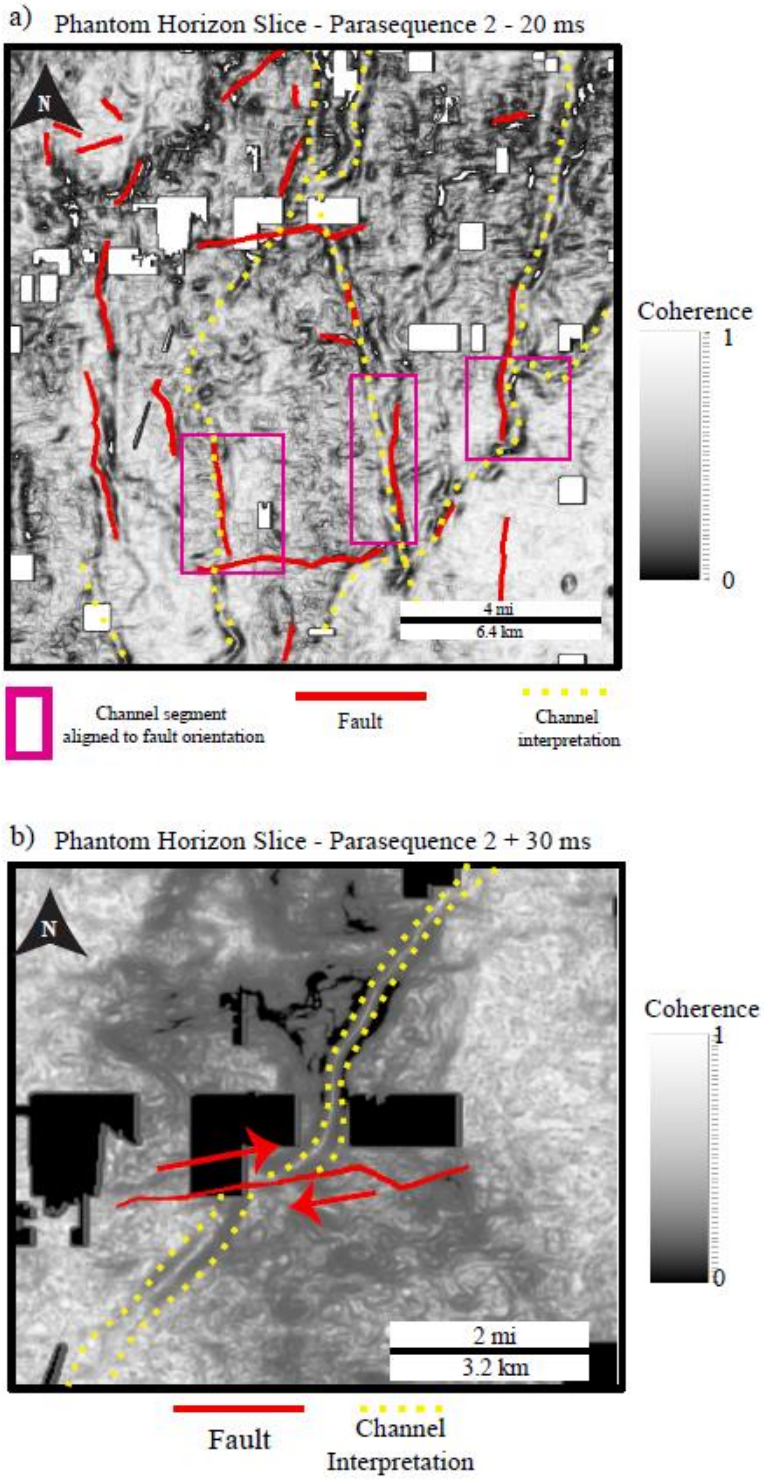

Figure 577: a) Phantom coherence horizon slice close to parasequence horizon 2 combined with structural interpretation. Purple areas reflect channel orientation aligned to north-south faults. b) Extracted coherence phantom horizon between parasequence 2 and 3 displays the right-lateral displacement of a strike-slip fault after the deposition of a submarine channel.

Appendix

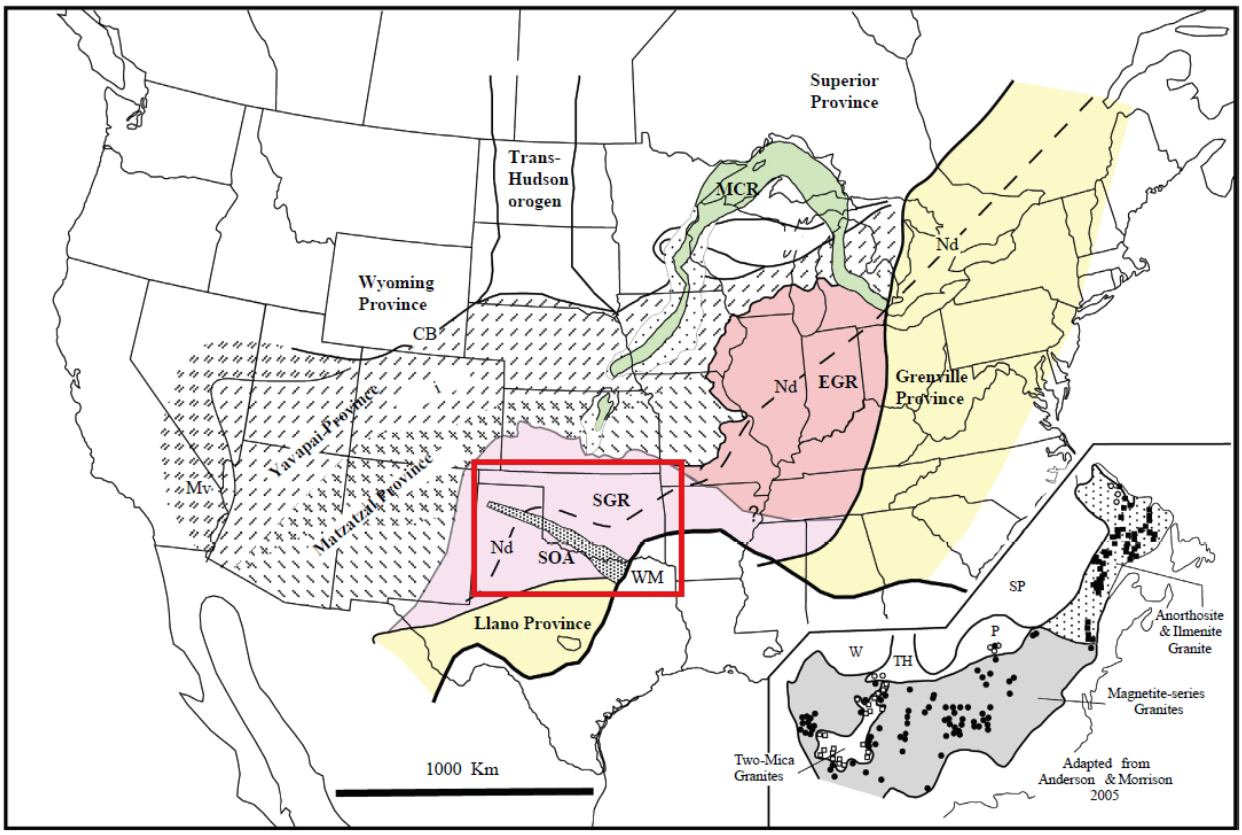

Figure 2-1A: Precambrian Terranes in the US midcontinent9; EGR, Eastern Granite–Rhyolite Province; SGR, Southern Granite–Rhyolite Province; MCR, Midcontinent Rift; SOA, Southern Oklahoma Aulacogen (Cambrian) Modified from Bickford et al., (2015)

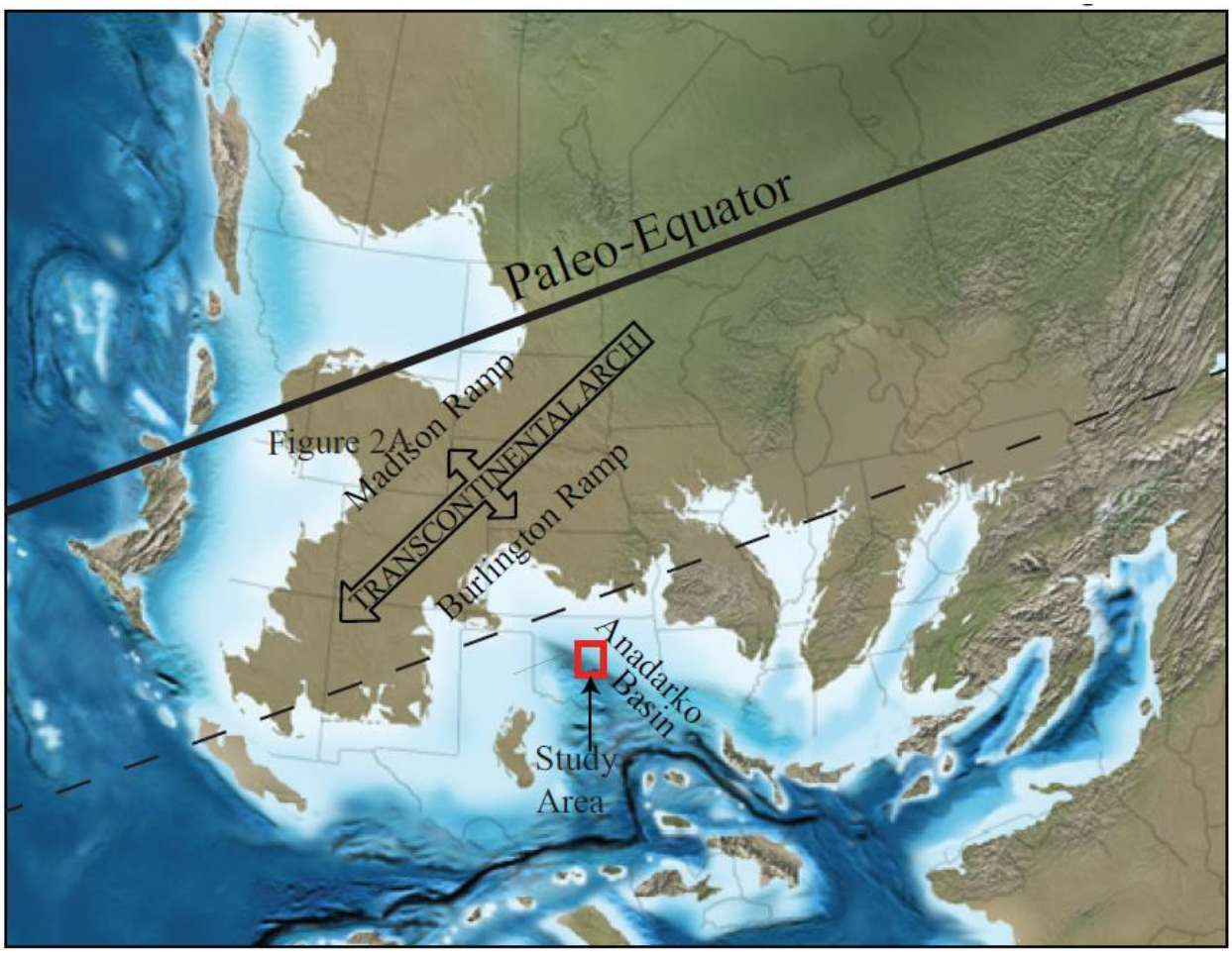

Figure 2-2A: Late Mississippian paleogeographic map. The transconticnental Arch and paleoequator were located approximately between 20-30 S, southeast of the paleoequator. (Blakey, 2013).

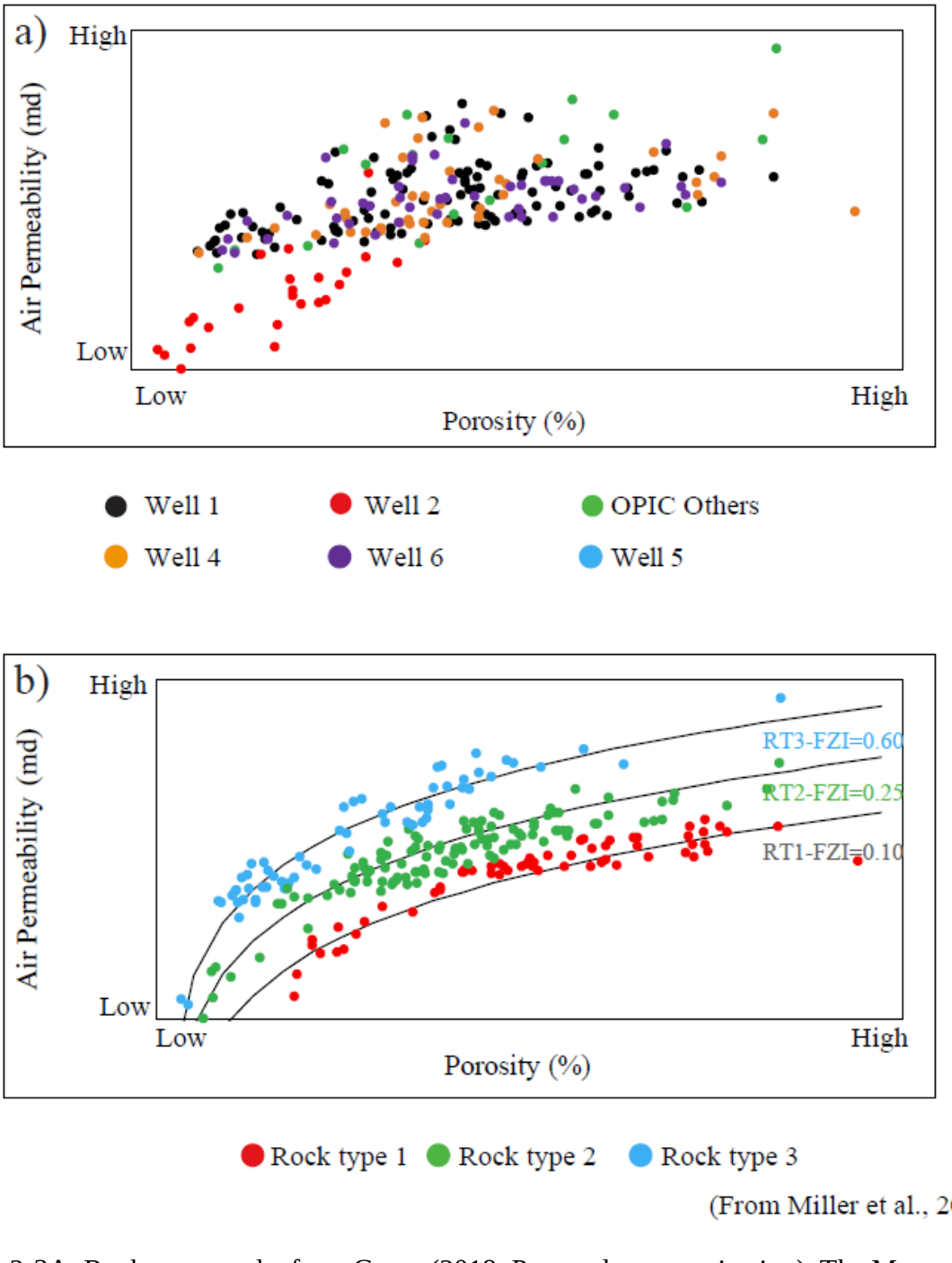

Figure 2-3A: Rock type results from Gupta (2019, Personal communication). The Meramec rocks are divided into three primary rock types (RT1, RT2, and RT3) with their associated mineralogical and petrophysical properties using a Flow Zone Indicator technique (FZI) (Amaefule et al., 1993)

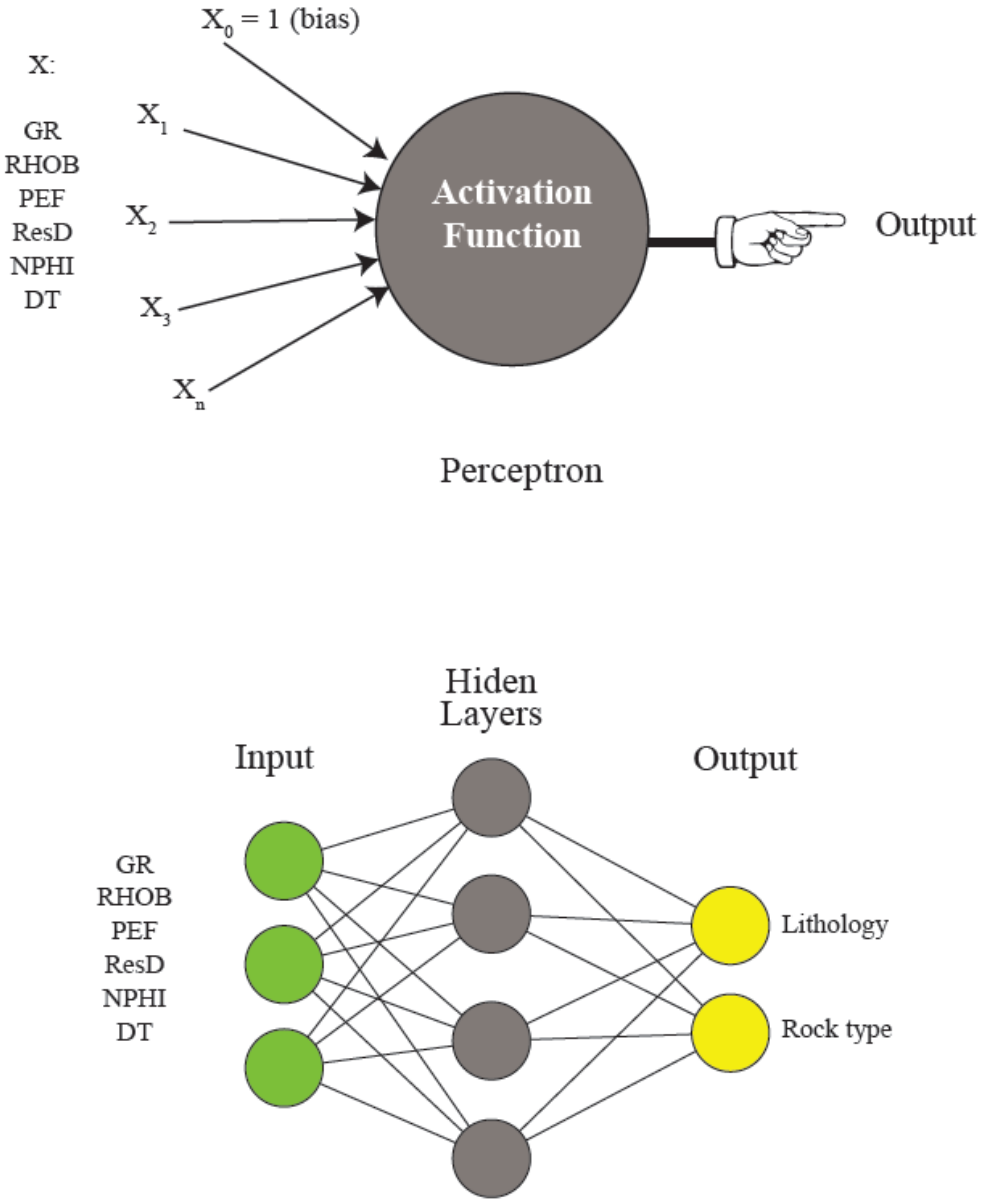

Figure 2-4A: Structure of an Artificial Neural Network. Well logs were used as input data to produce a classification model for lithology and rock types.

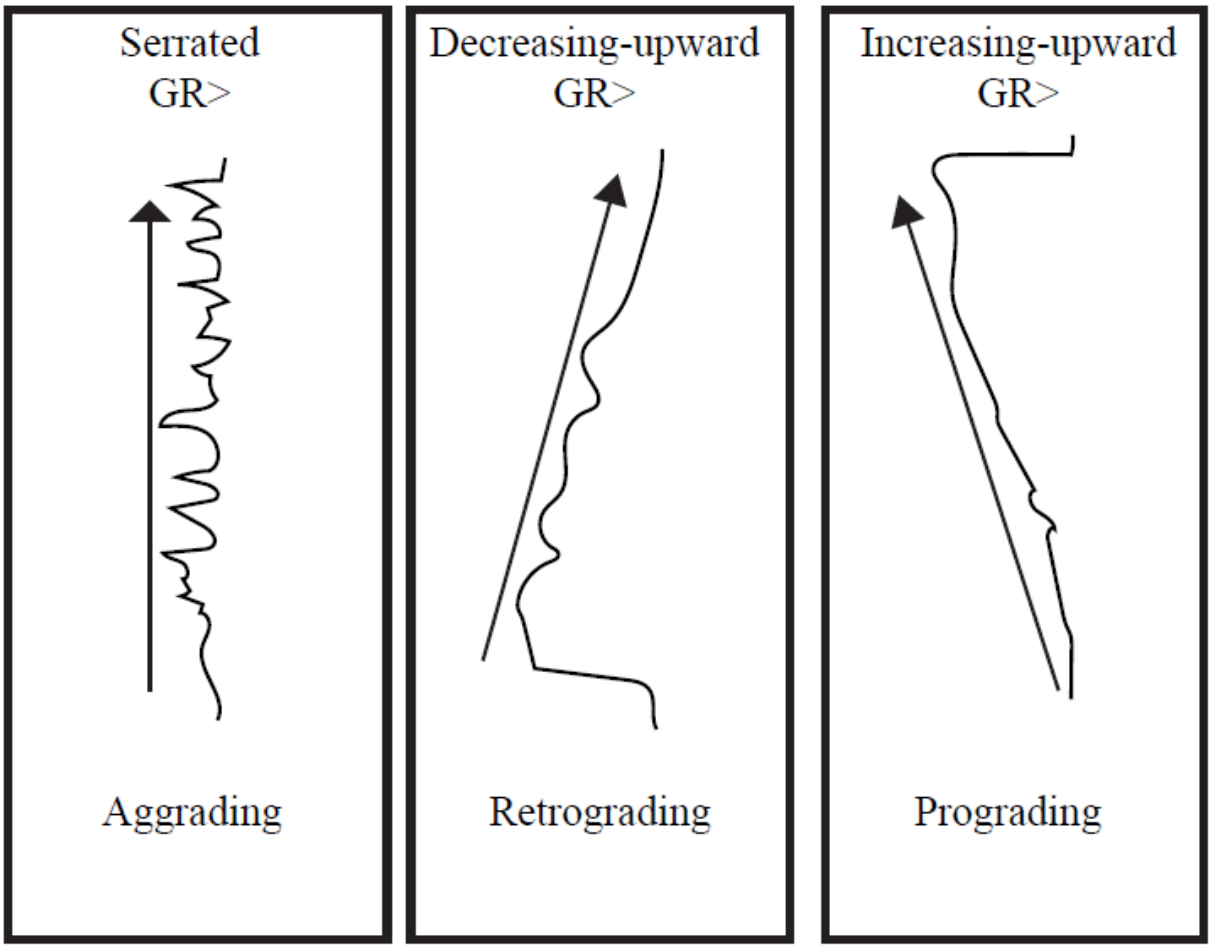

Figure 2-5A: Gamma-ray response for characterization of parasequences. Aggrading, retrograding, and prograding.

Simplified
Confusion Matrix

	Class 1 Predicted	Class 2 Predicted
Class 1 Actual	True Positives (TPs)	False Negatives (FNs)
Class 2 Actual	False Positives (FPs)	True Negatives (TNs)

Figure 2-6A: A simplified confusion matrix to evaluate the accuracy of artificial neural networks (ANN).

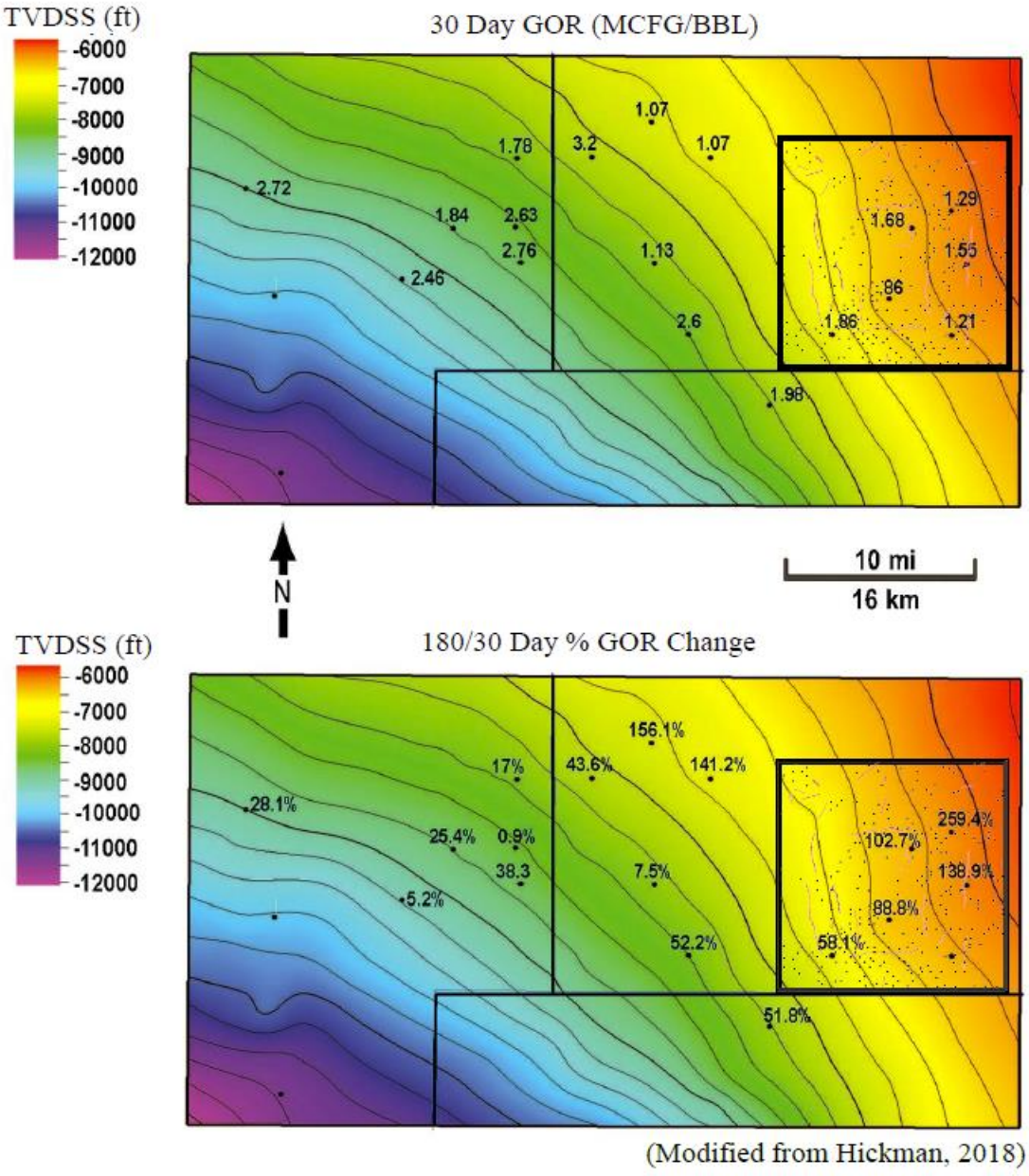

Figure 2-7A: Regional map shows GOR data available for fault analysis in the study area (Modified from Hickman, 2019).

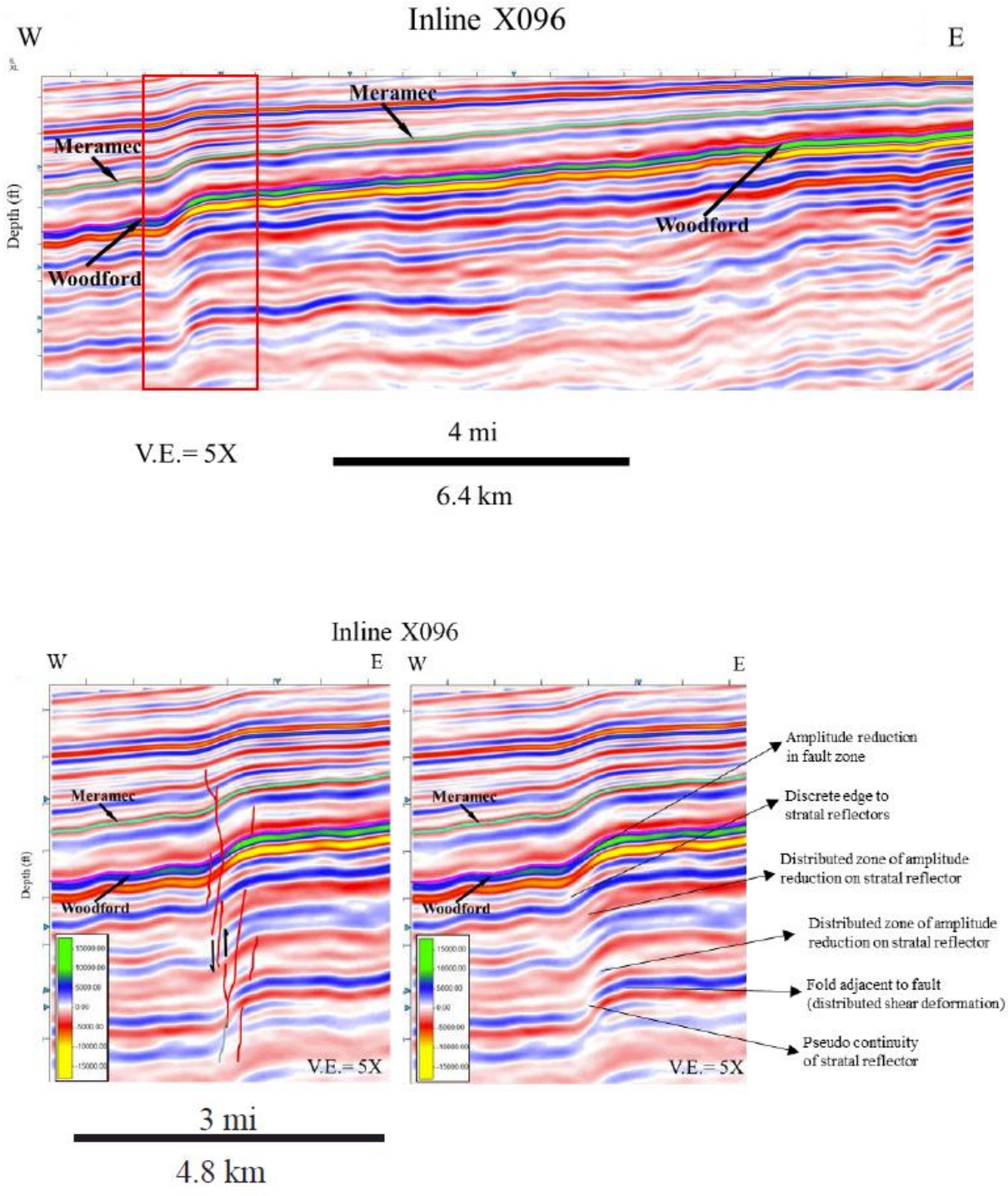

Figure 2-8A: Vertical amplitude seismic profile. The inline displays a distortion zone interpreted as a faulted zone within the Meramec strata. A detailed image displays the characteristics used for fault interpretation using an amplitude volume. (Modified from Iacopini et al. 2016)

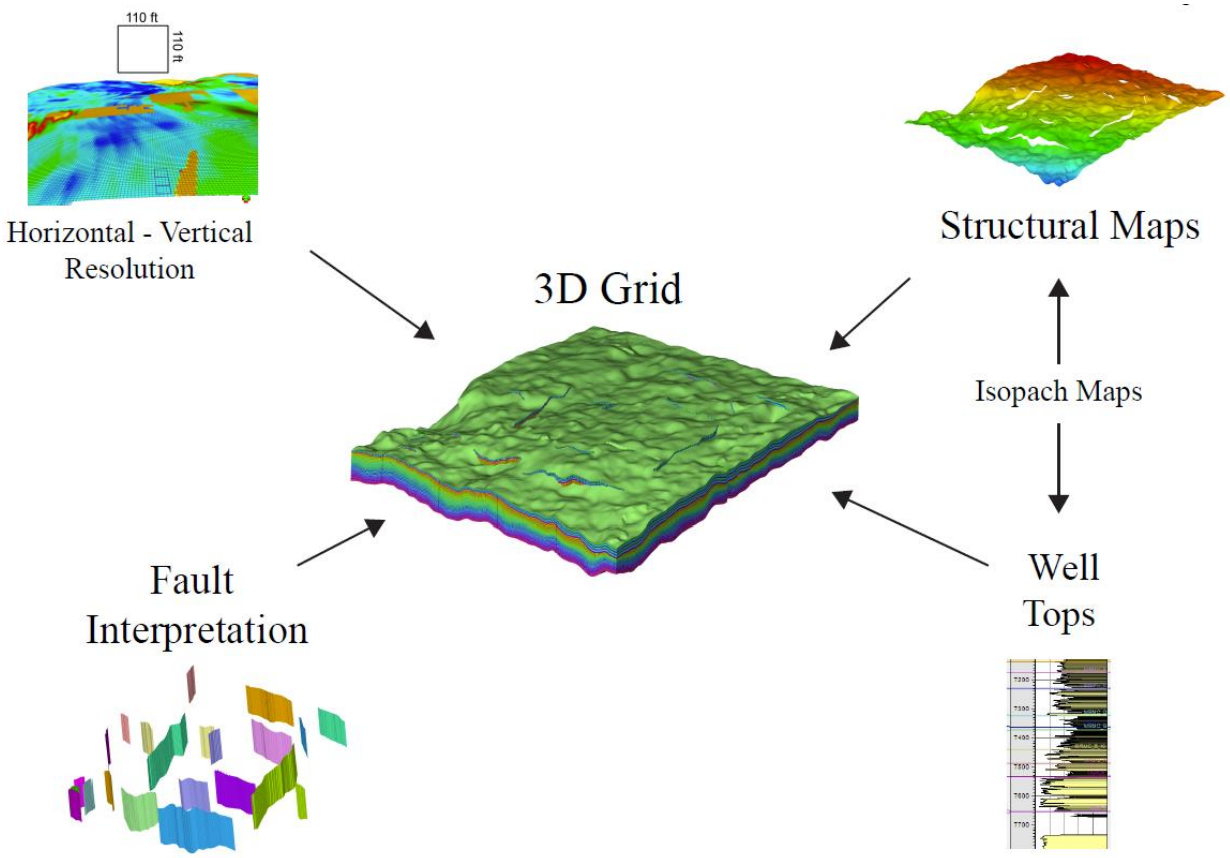

Figure 2-9A: Schematic diagram that shows elements used to constrain the construction of the three-dimensional grid

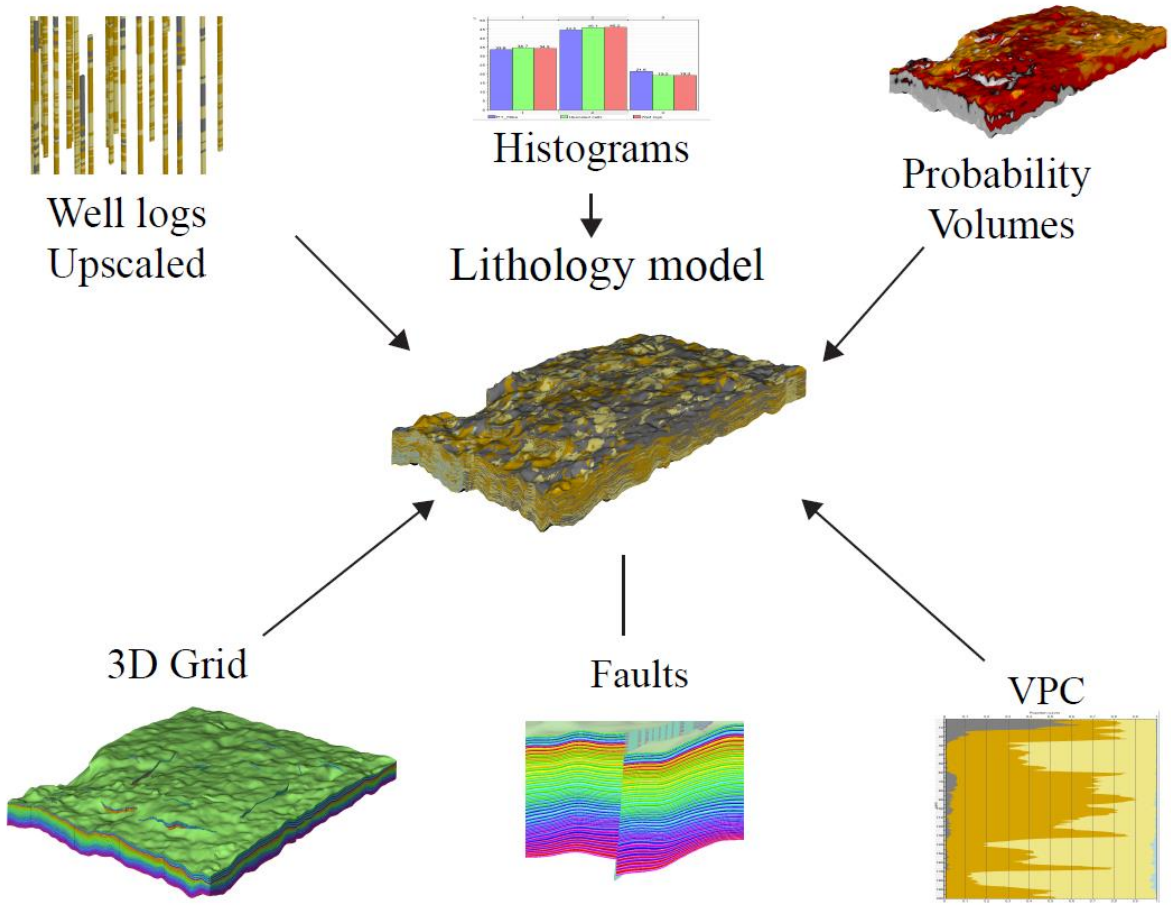

Figure 2-10A: Schematic diagram that shows data to constrain the generation of the three-dimensional facies models

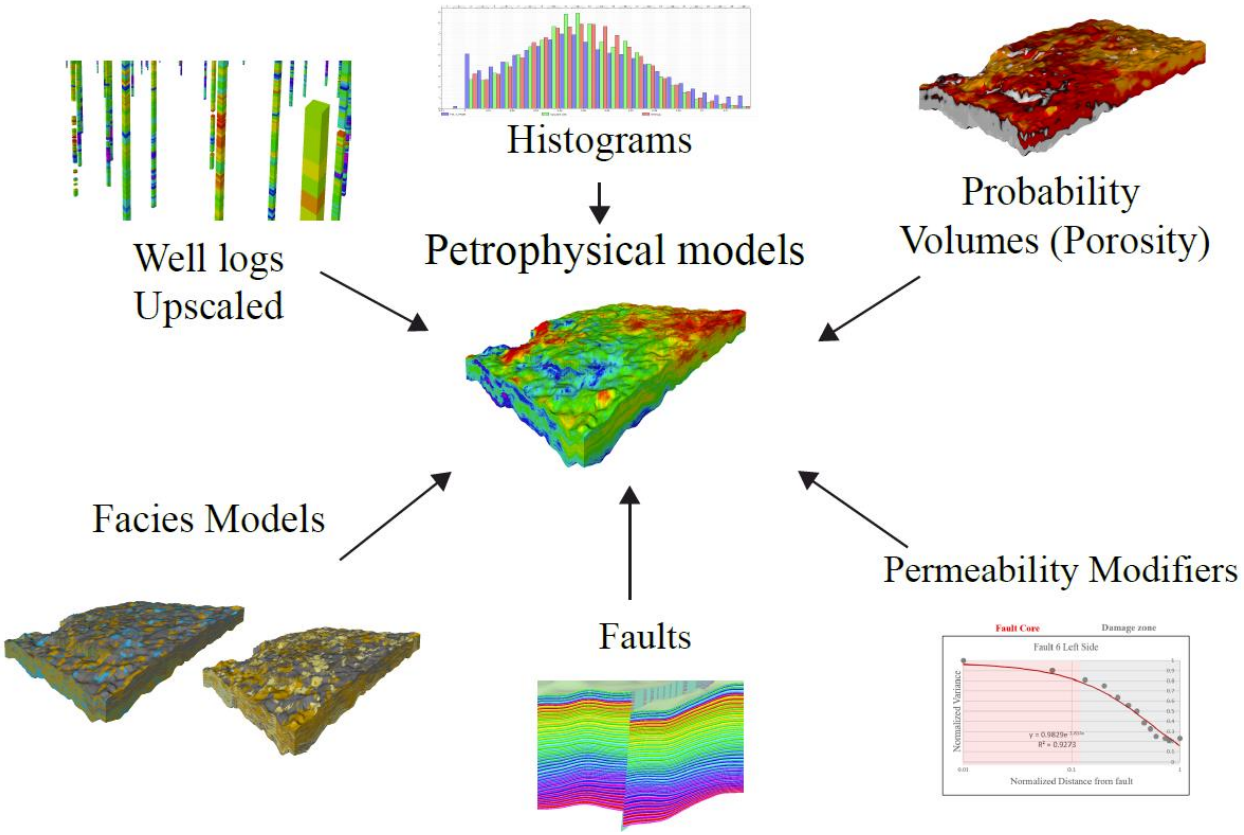

Figure 2-11A: Schematic diagram that shows data to constrain the generation of the three-dimensional petrophysical models

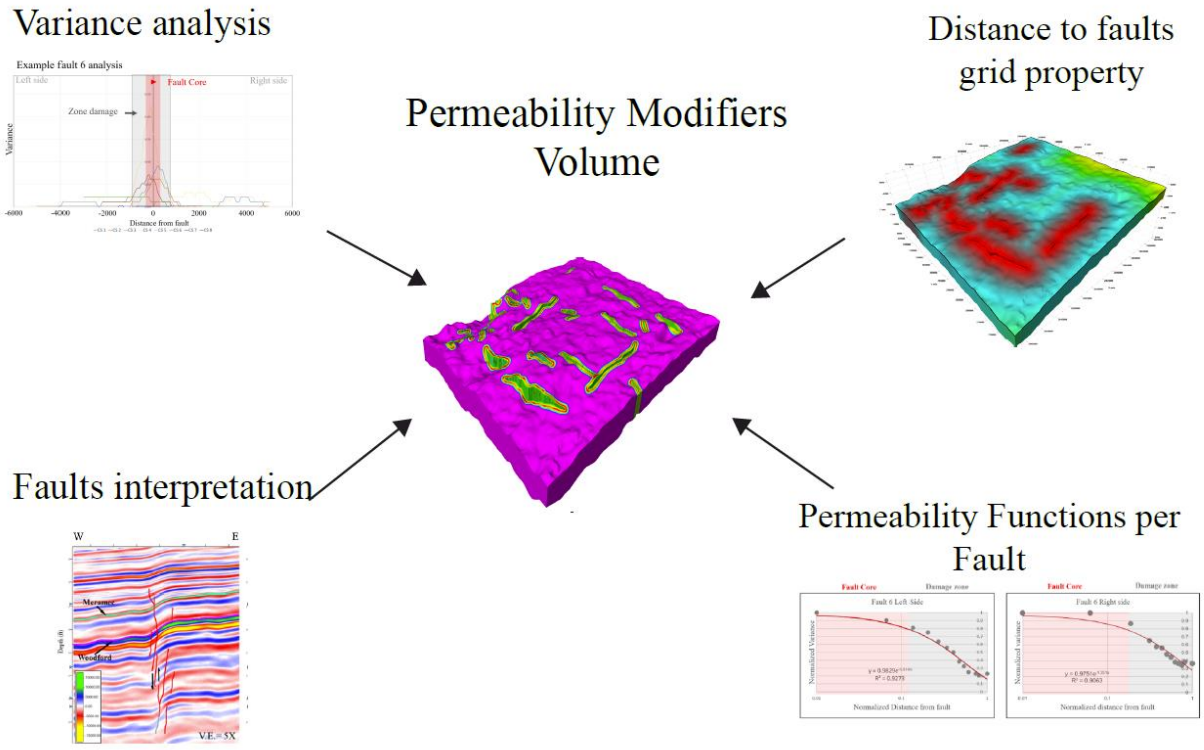

Figure 2-12A: Schematic diagram that display components used to generate to construct the volume modifiers applied to the permeability model

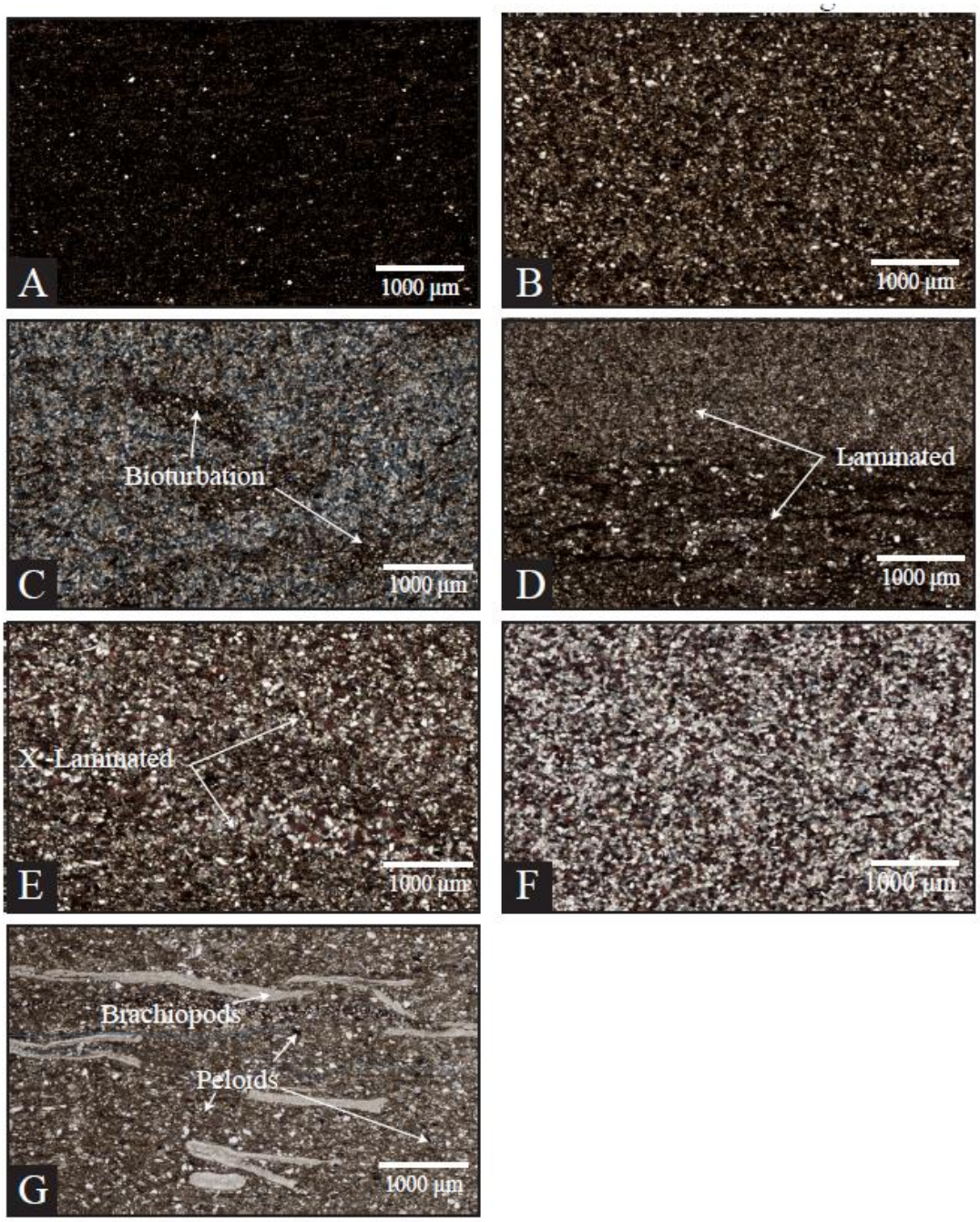

Figure 2-13A: Thin section photomicrographs of lithofacies in the study area: A) Structureless mudstone. A) Structureless mudstone - Clay rich with occasional pyrite B) Laminated mudstone - with some sub-angular, moderately-well sorted quartz siltstone size grains C) Bioturbated mudstone -Burrows filled up with clay-rich materials. D) Calcareous siltstone- predominant calcite cement present with clay-filled burrows and intergranular clay material E) Structureless Siltstone/Sandstone - Angular to subangular quartz grains with a high percentage of calcareous cement. F) Cross-laminated siltstone/sandstone – Inclined and planar clay-rich laminations G) Silty grainstone - silty packstone to grainstone. Fossil preserved with high amounts of calcite cement and grains (Only present in proximal locations).

ANN	GR, NPHI, RhoB, PE			
Core	Mudstone	Argillaceous Siltstone	Arg. Calc. Siltstone	Calcareous Siltstone
Mudstone	25	0	0	0
Argillaceous Siltstone	0	317	22	4
Arg. Calc. Siltstone	0	28	235	4
Calcareous Siltstone	0	1	14	350
User Accuracy	100 %	92 %	87 %	98 %

Overall Accuracy : 93 %

ANN	GR, NPHI, RhoB,PE		
Core	Rock Type 1	Rock Type 2	Rock Type 3
Rock Type 1	266	209	38
Rock Type 2	59	717	192
Rock Type 3	6	137	456
User Accuracy	80 %	68 %	67 %

Overall Accuracy : 70 %

Modified from Miller (2019)

Figure 2-14A: Confusion matrices that reflect accuracy for the artificial neural network models for lithologies and rock type definitions. The higher accuracy was obtained using a log suite combination of gamma-ray (GR), neutron porosity (NPHI), bulk density (RhoB), and photoelectric effect (PE)

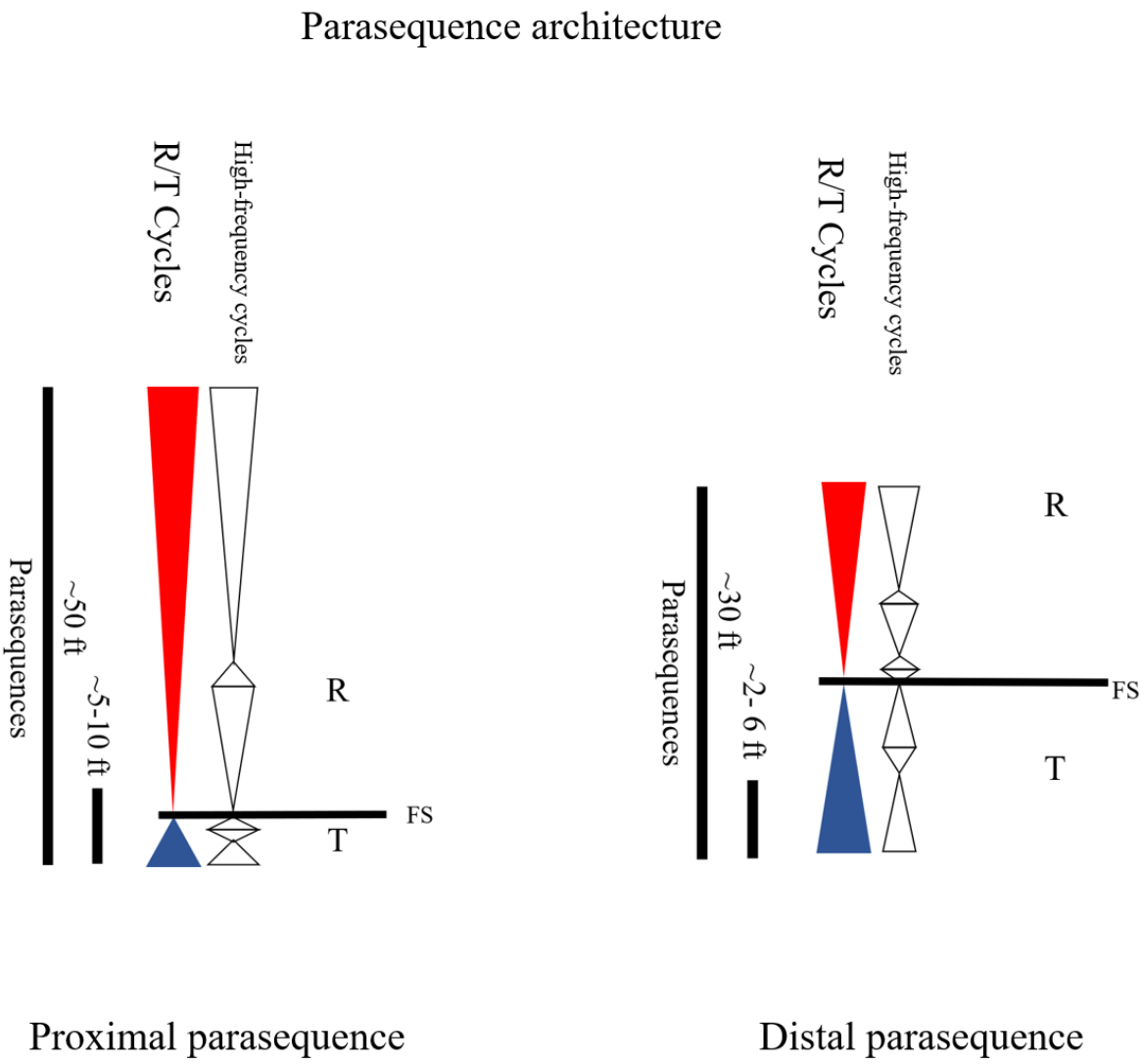

Figure 2-15A: Parasequence architecture of the Meramec strata. The overall stratigraphic section shows proximal asymmetric parasequences that grade to symmetrical and clay-rich intervals in distal locations. R=Regressive, T=Transgressive, FS=Flooding surface

a)

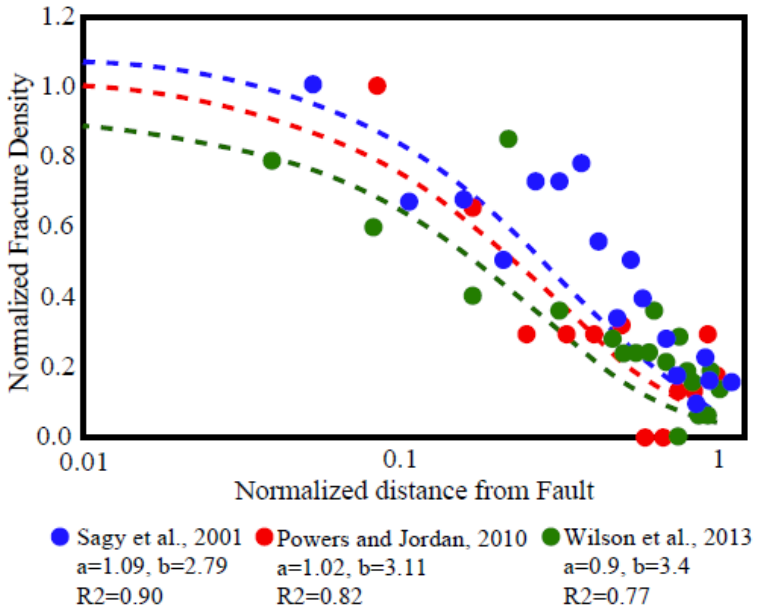

b)

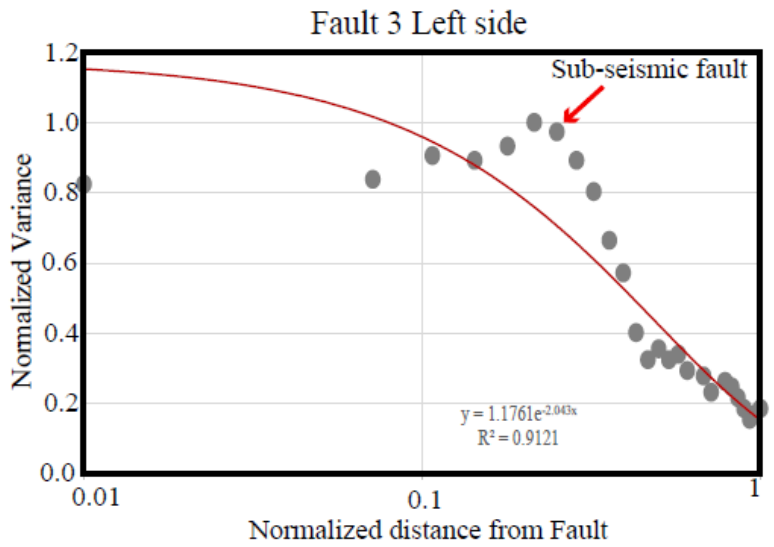

Figure 2-16A: a) Equations and cross plot constant reported by previous studies of normalized fracture density versus distance from the fault. (modified from Sag et al. 2001; Power and Jordan, 2010; Wilson et al., 2013) b) a cross plot that shows outliers found during the variance analysis typically found in structural type 2 faults. Anomalous variance values are related to sub-seismic or Riedel faults within the damage zone, as reported in previous studies by Liao et al. (2019)

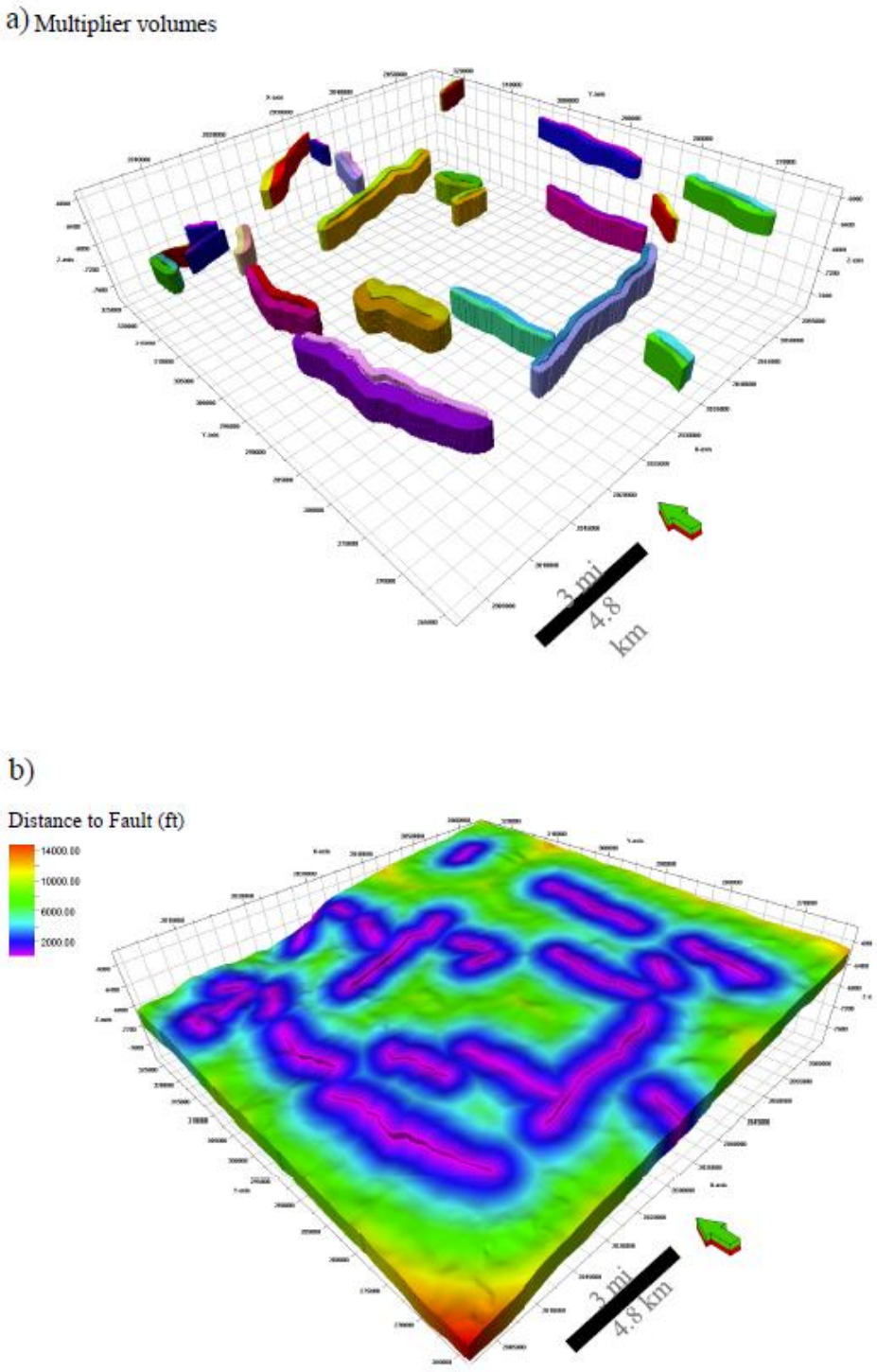

Figure 2-17A: a) Volumes to limit the distribution of permeability modifiers during the petrophysical model computation b) Distance from the fault property used to establish the effect of multiplier equations around damage zones of faults

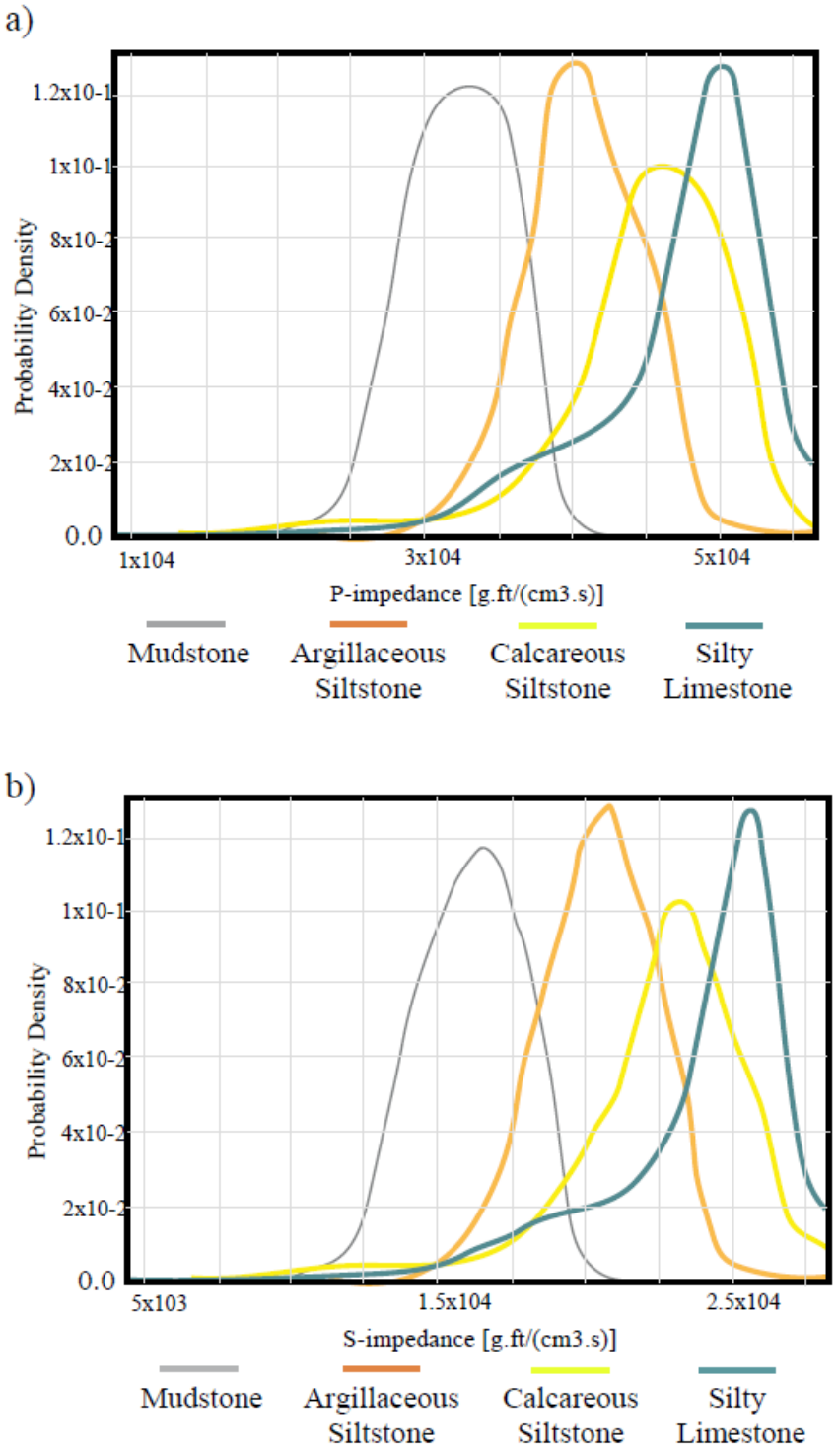

Figure 2-18A: Probability density functions PDF's generated from the Bayesian classification for lithology classification. The PDF's used a combination of well log and seismic P-impedance and S-impedance to generate probability volumes.

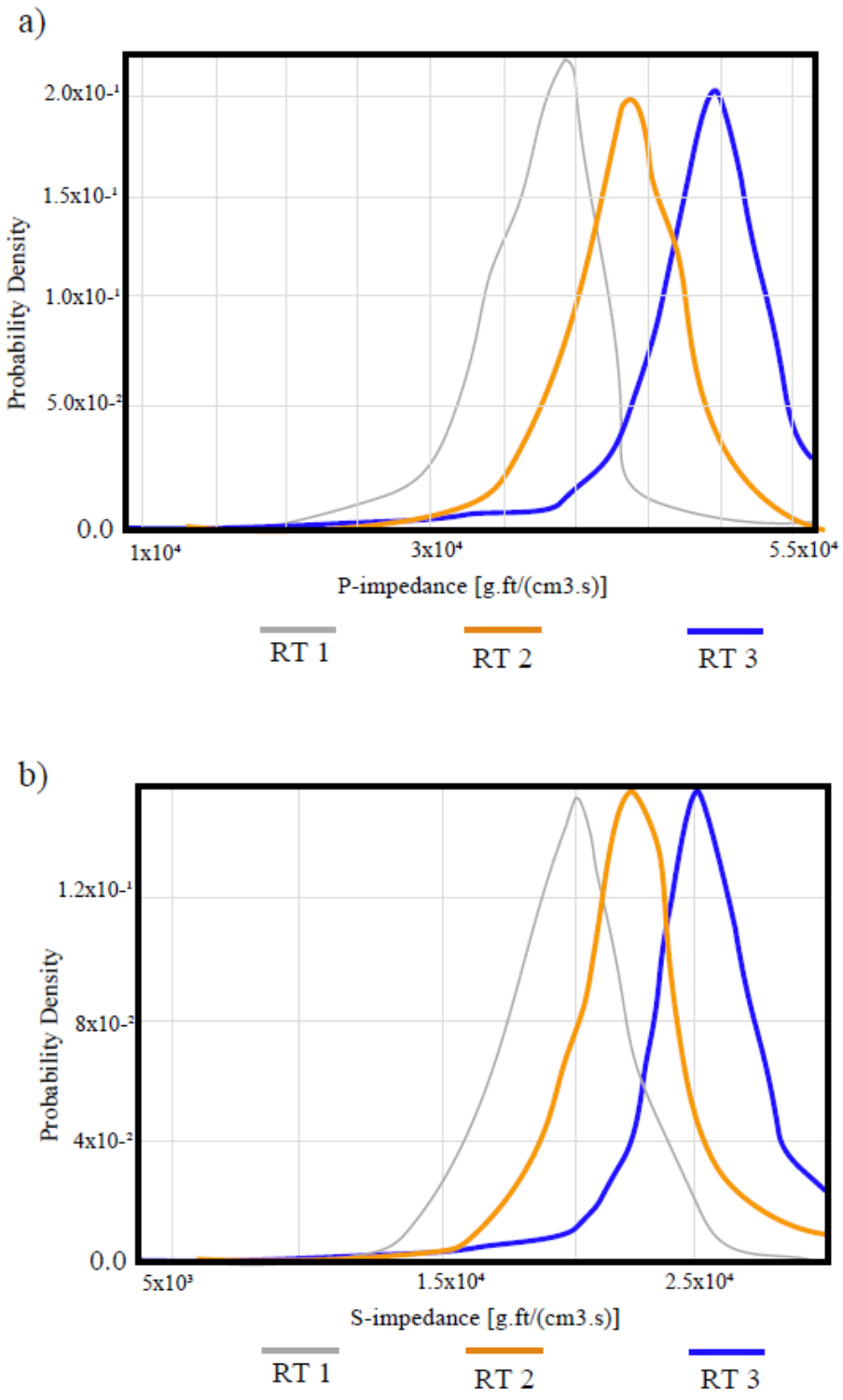

Figure 2-19A: Probability density functions PDF's generated from the Bayesian classification for rock type classification. The PDF's used to generate probability volumes.

Rock Type Confusion Matrix	Predicted		
Actual	RT 1	RT 2	RT 3
RT 1	89.7%	27.8%	8.2%
RT 2	7.7%	53.3%	16.8%
RT 3	2.6%	18.9%	75.0%

Overall Accuracy : 73%

Lithology Confusion Matrix	Predicted			
Actual	Mudstones	Arg. Calc Siltstones	Calc Siltstones	Silty Limestone
Mudstones	89.6%	8.9%	6.2%	5.9%
Arg. Calc. Siltstones	9.8%	75.7%	22.1%	15.5%
Calc Siltstones	0.3%	14.7%	50.1%	25.3%
Silty Limestone	0.3%	0.7%	21.7%	53.2%

Overall Accuracy : 67%

Figure 2-20A: Confusion matrices that reflect accuracy for the Bayesian classification models for lithologies and rock type modeling. The higher accuracy obtained using a combination of well log and seismic P-impedance and S-impedance was 73% and 67% for lithology and rock type. The results of these analyses were used along with vertical and horizontal variograms for facies modeling.

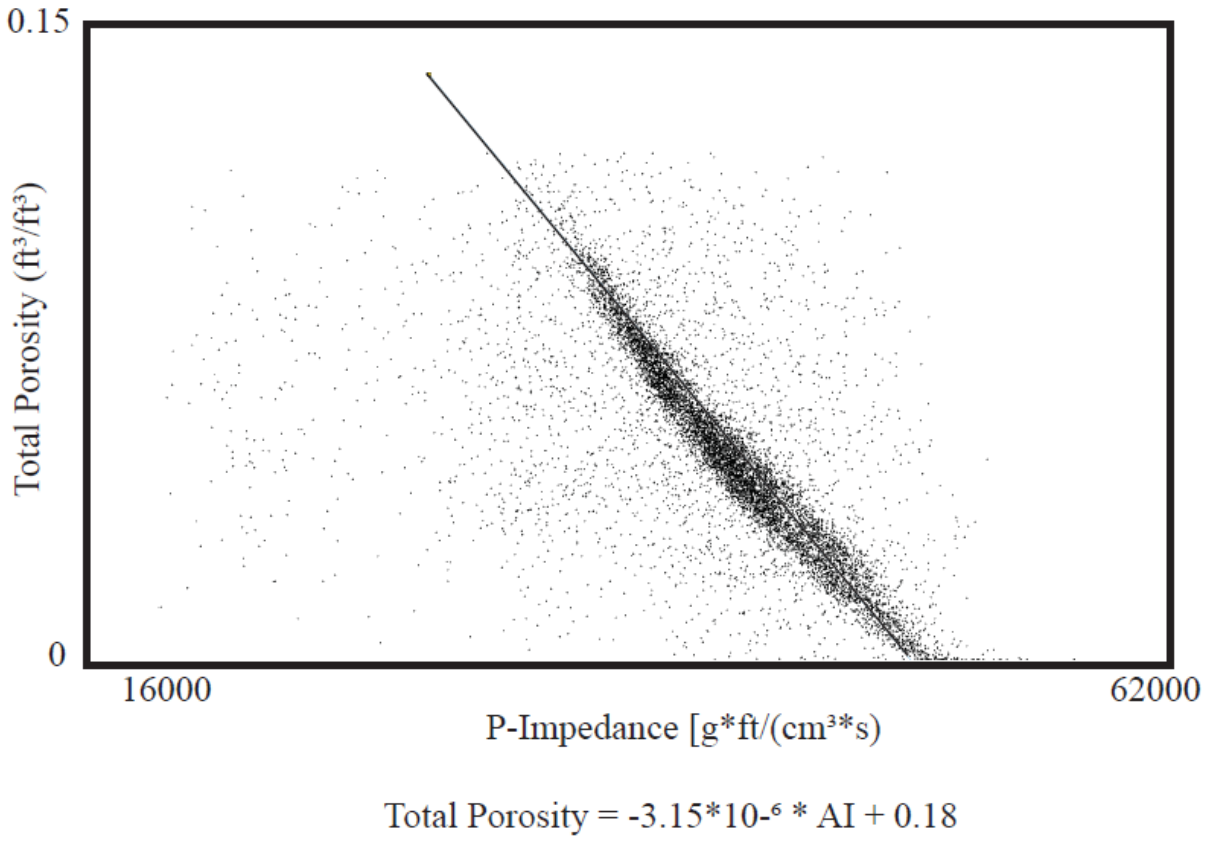

Figure 2-21A: Linear relationship used to generate a porosity trend volume for porosity modeling

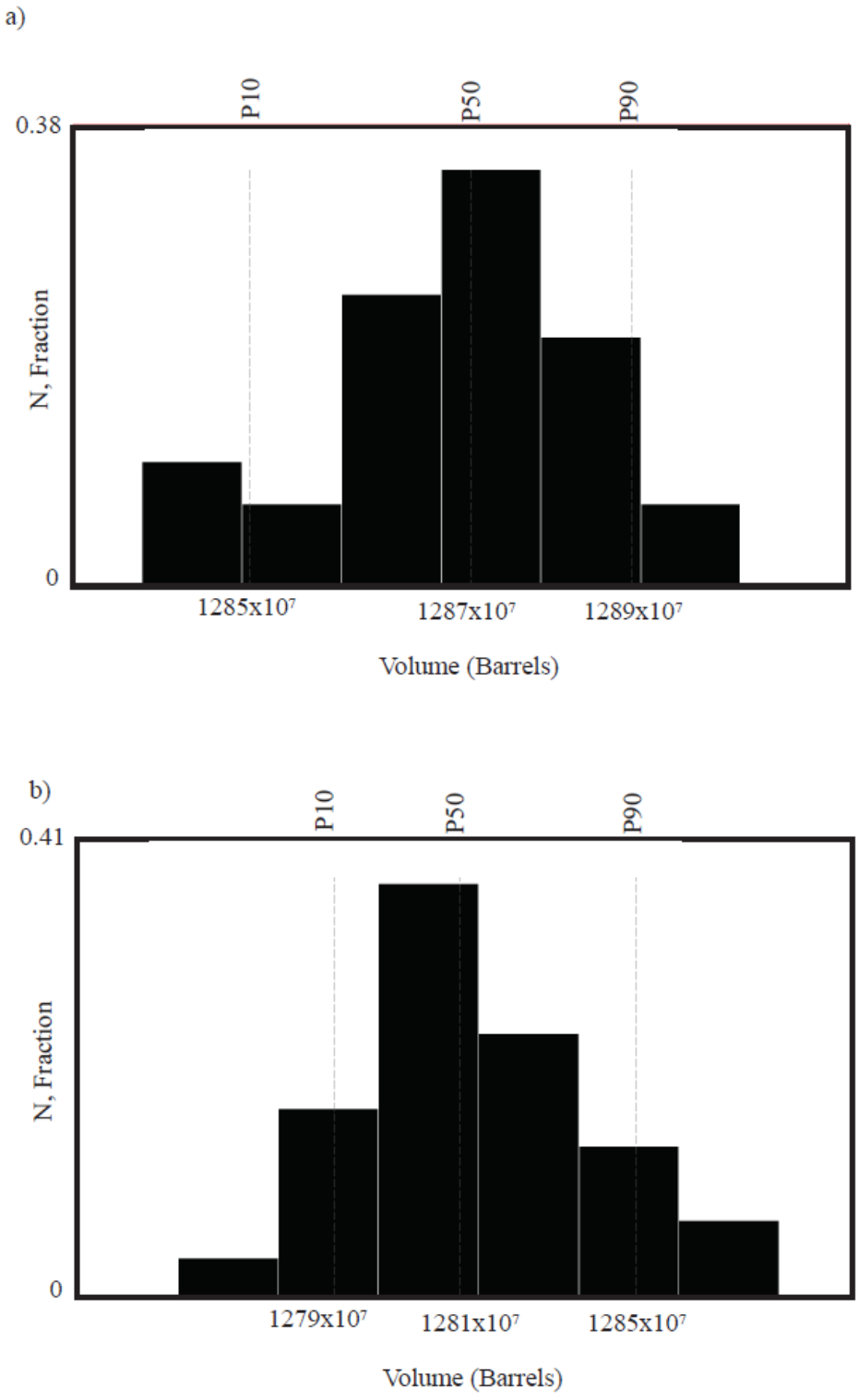

Figure 2-22A: Histogram of pore volume calculated through 30 iterations of a) rock type and b) lithology models in an uncertainty analysis. P10, P50, and P90 values of pore volume are displayed in the vertical dashed lines. Y-axis indicates the fraction of iterations that correspond to the calculated pore volume on the X-axis.

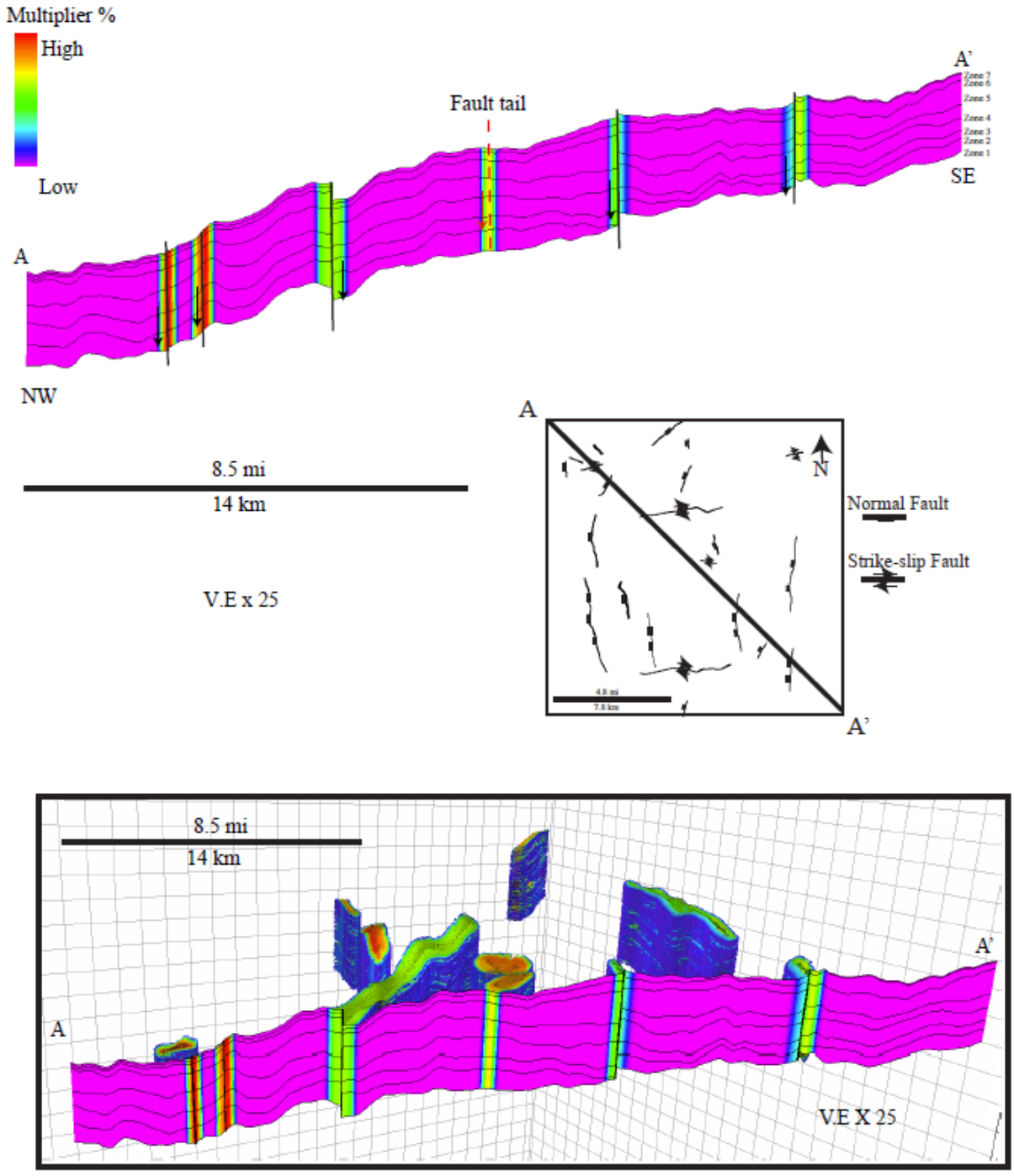

Figure 2-23A: Northwest-southeast oriented cross section through the 3-D permeability modifier. The section shows the exponential variation of permeability modifiers applied to faults crossing the section.

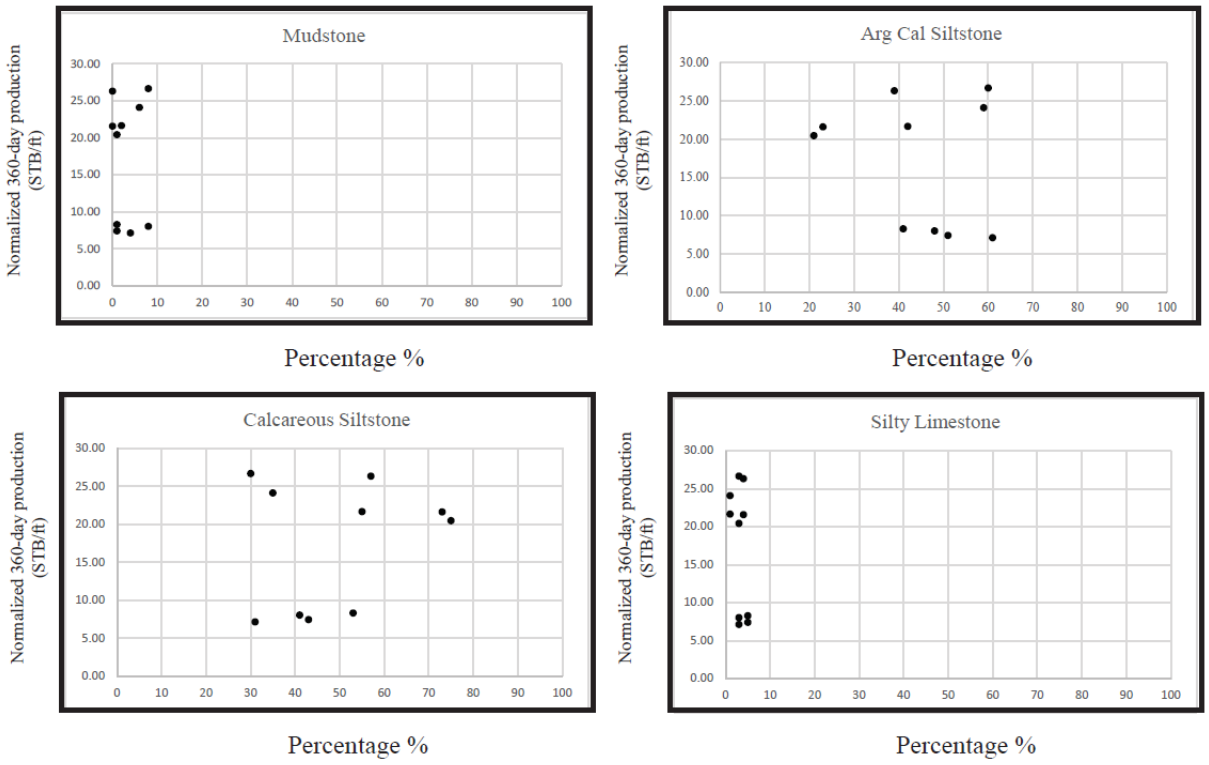

Figure 2-24A: Cross-plots of 360-day cumulative production versus lithology fractions extracted along the lateral. The production data was normalized by dividing the cumulative production by the lateral length of the well.

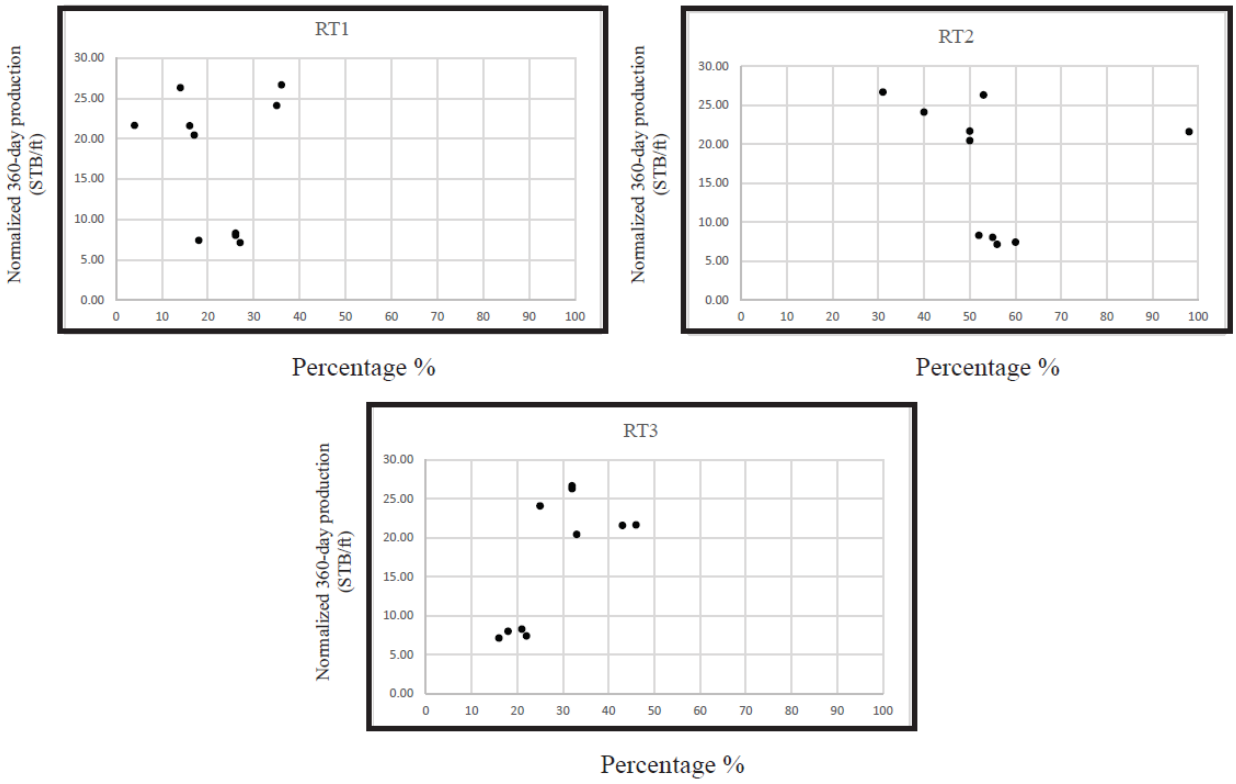

Figure 2-25A: Cross-plots of 360-day cumulative production versus rock type fractions extracted along the lateral. The production data was normalized by dividing the cumulative production by the lateral length of the well.

References

Bickford, M. E., W. R. Van Schmus, K. E. Karlstrom, P. A. Mueller, and G. D. Kamenov, 2015, Mesoproterozoic-trans-Laurentian magmatism: a synthesis of continent-wide age distributions, new SIMS U–Pb ages, zircon saturation temperatures, and Hf and Nd isotopic compositions. Precambrian Res. 265, 286–312.

Baytok, S. and M.J.Pranter, 2013, Fault and fracture distribution within a tight-gas sandstone reservoir: Mesaverde Group, Mamm Creek Field, Piceance Basin, Colorado, USA. Petroleum Geoscience, 19 no. 3, 203-222.

Beebe, B.W., 1959, Characteristics of Mississippian production in the northwestern Anadarko Basin, Tulsa Geological Society Digest, no. 27, 190–205.

Blakey, R., 2016, Paleogeography and geologic evolution of North America, http://cpgeostystems.com/paleomaps.html, (accessed March 2018).

Brewer, J. A., R. Good, J. E. Oliver, L. D. Brown, and S., Kaufman,1983, COCORP profiling across the Southern Oklahoma aulacogen: Overthrusting of the Wichita Mountains and compression within the Anadarko Basin. Geology 11, no. 2, 109-114.

Buland, A., O. Kolbjørnsen, R. Hauge, O. Skjæveland, and K. Duffaut, 2008, Bayesian lithology and fluid prediction from seismic prestack data: Geophysics, no. 3, 73.

Chase, B., E. A. Atekwana, F. Kolawole, M. S. Turko, B. M. Carpenter, R. L Evans, and C. Finn, 2018, The southern Oklahoma aulacogen: New insights from aeromagnetic, seismic reflection and magnetotelluric data analyses. AGU Fall Meeting Abstract #G51E-0523.

Chopra, S., and K. J. Marfurt, 2007, Seismic attributes for prospect identification and reservoir characterization: Tulsa, Oklahoma, Society of Exploration Geophysicists Geophysical Developments Series 11, doi:10.1190 /1.9781560801900.

Cowie, P. A., and C. H. Scholz, 1992, Displacement-length scaling relationship for faults: Data synthesis and discussion: Journal of Structural Geology, v. 14, no. 10, 1149–1156, doi:10.1016/0191 8141(92)90066-6.

Curtis, D. M. and S. C. Champlin, 1959, Depositional environments of Mississippian limestones of Oklahoma: Tulsa Geological Society Digest, no. 27, 90–103.

Drummond, K., 2018, Regional stratigraphy and proximal to distal variation of lithology and porosity within a mixed carbonate-siliciclastic system, Meramec and Osage series (Mississippian), central Oklahoma, M.S. Thesis, University of Oklahoma, Norman, Oklahoma, 165.

Duarte, D., 2018, Rock characterization and stratigraphy of the Mississippian strata, Meramec/Sycamore merge play, central Oklahoma: M.S. thesis, University of Oklahoma, 80.

Gutschick, R. C., and C. A. Sandberg, 1983, Mississippian continental margins of the conterminous United States: in D. J. Stanley, and G. T. Moore, eds., The Shelfbreak: Critical Interface on Continental Margins: SEPM Special Publication 33, 79–96.

Haykin, S., 2000, Neural networks: A guided tour. Nonlinear Biomedical Signal Processing, 1, 53-68.

Hardwick, J., 2018, Reservoir quality evaluation of the Meramec and Upper Osage units in the Anadarko Basin, M.S. thesis, University of Oklahoma, Norman, Oklahoma, 76.

Hickman, G., 2018, Parasequence scale stratigraphic variability of lithology and porosity of Mississippian Meramec reservoirs and the relationships to production characteristics, STACK trend, Oklahoma, M.S. Thesis, University of Oklahoma, Norman, Oklahoma, 105.

Hardisty, L., 2020, Stratigraphic Variability of Mississippian Meramec Chemofacies and Petrophysical Properties Using Machine Learning and Geostatistical Modeling, STACK Trend, Anadarko Basin, Oklahoma , M.S. thesis, University of Oklahoma, Norman, Oklahoma, 87.

Iacopini, D., R. W. H. Butler, S. Purves, N. McArdle, and N. De Freslon, 2016, Exploring the seismic expression of fault zones in 3D seismic volumes: Journal of Structural Geology, 89, 54–73, doi:10.1016/j.jsg.2016.05.005.

Infante-Paez, L., and K. J. Marfurt, 2018, In-context interpretation: Avoiding pitfalls in misidentification of igneous bodies in seismic data: Interpretation, 6, no. 4, SL29–SL42, doi: 10.1190/INT-2018-0076.1

Johnson, K. S., 1988, Geologic evolution of the Anadarko basin, in K. S. Johnson, ed., Anadarko basin Symposium: Norman, Oklahoma, Oklahoma Geological Survey Circular 90, 3–12.

Keller, G. R., R. A. Stephenson, R. D. Hatcher, M. P. Carlson, and J. H. McBride. 2007, The southern Oklahoma and Dniepr-Donets aulacogens: A comparative analysis. MEMOIRS-GEOLOGICAL SOCIETY OF AMERICA 200, 127.

Kolawole, F., C. S. Johnston, C. B. Morgan, J. C. Chang, K. J. Marfurt, D. A. Lockner, Z. Reches, and B. M. Carpenter, 2019, The susceptibility of Oklahoma's basement to seismic reactivation. Nature Geoscience 12, no. 10, 839-844.

Leavitt, A., 2018, Depositional systems of the STACK and SCOOP Mississippian units; regional understanding from logs and core, STACK play Workshop Technical Program and Core Viewing, Norman, Oklahoma.

Liao, Z., Z. Reches, K. J. Marfurt, and N. Gupta, 2013, Characterizing a fault-zone and associated fractures using lab experiments and attribute-based seismic analysis: An example from Woodford Shale, Anadarko Basin, Oklahoma: Tulsa, Oklahoma, Society of Exploration Geophysicists Technical Program Expanded Abstracts 2013, 1416–1420., doi:10.1190/segam2013-0656.1.

Liao, Z., H. Liu, Z. Jiang, K. J. Marfurt, and Z. Reches, 2017, Fault damage zone at subsurface: A case study using 3D seismic attributes and a clay model analogue for the Anadarko Basin, Oklahoma: Interpretation 5, no. 2, T143–T150, doi:10.1190/INT-2016-0033.1

Liao, Z., H. Liu, B. M. Carpenter, K. J. Marfurt, and Z. Reches, 2019, analysis of fault damage zones using three-dimensional seismic coherence in the Anadarko Basin, Oklahoma: AAPG Bulletin, 103, no. 8, 1771–1785, doi:10.1306/1219181413417207

Marsh, S.,and, A., Holland, 2016, Comprehensive fault database and interpretive fault map of Oklahoma. Oklahoma Geological Survey Open-File Report, 15.

Mazullo, S. J., and B. W. Wilhite, 2010, CHERT, TRIPOLITE, SPICULITE, CHAT –WHAT'S IN A NAME? Kansas Geological Society Bulletin, 85, no. 1.

Mazzullo, S. J., 2011, Mississippian oil reservoirs in the southern Midcontinent: new exploration concepts for a mature reservoir objective: Search and Discovery Article #10373.

Mazzullo, S. J., B. W. Wilhite, D. R. Boardman, B. T. Morris., and C. J. Godwin, 2016, Stratigraphic architecture and petroleum reservoirs in lower to Middle Mississippian strata (Kinderhookian to basal Meramecian) in subsurface central to southern Kansas and northern Oklahoma: Shale Shaker 67 no. 2, 20–49.

Miller, J. C., M. J. Pranter, and A. B. Cullen, 2019, Regional stratigraphy and organic richness of the Mississippian Meramec and associated strata, Anadarko Basin, cen- tral Oklahoma: Shale Shaker 70, 50–79.

Miller, J., 2018, Regional stratigraphy and organic richness of the Mississippian Meramec and associated strata, Anadarko basin, central Oklahoma, M.S. thesis, University of Oklahoma, Norman, Oklahoma, 154.

Miller, M., 2019, Mississippian Meramec lithologies and petrophysical property variability, STACK trend, Anadarko Basin, Oklahoma, M.S. Thesis, University of Oklahoma, Norman, Oklahoma, 60.

Mukerji, T., A. Jørstad, P. Avseth, G. Mavko, and J. R. Granli, 2001, Mapping lithofacies and pore-fluid probabilities in a North Sea reservoir: Seismic inversions and statistical rock physics. Geophysics 66, no. 4, 988-1001.

Patel, S., F. Kolawole, J. I. Walter, X. Chen, and K. Marfurt, 2021, Seismic illumination of small-offset seismogenic faults, Anadarko Basin, Oklahoma. Interpretation 9, no. 2, 1-50.

Powers, P. M., and T. H. Jordan, 2010, distribution of seismicity across strike-slip faults in California: Journal of Geophysical Research 115, no. B5, 3040–3065., doi:10.1029/2008JB006234.

Price, B., K. Haustveit, and A. Lamb, 2017, Influence of stratigraphy on barriers to fracture growth and completion optimization in the Meramec Stack Play, Anadarko Basin, Oklahoma: Unconventional Resources Technology Conference (URTEC), Article 2697585, 8.

Price, B. J., , A. C. Pollack, , A. P. Lamb, , T. C. Peryam, and, J. R Anderson, 2020, Depositional interpretation and sequence stratigraphic control on reservoir quality and distribution in the Meramecian Sooner trend Anadarko Basin, Canadian, and Kingfisher Counties (STACK) play, Anadarko Basin, Oklahoma, United States. AAPG Bulletin, 104, no. 2, 357–386

Sagy, A., Z. Reches, and I. Roman, 2001, Dynamic fracturing: Field and experimental observations: Journal of Structural Geology 23, no. 8, 1223–1239, doi:10.1016 /S0191-8141(00)00190-5.

Shah, A. K., and G. R. Keller, 2017, Geologic influence on induced seismicity: Constraints from potential field data in Oklahoma. Geophysical Research Letters 44, 152–161. https://doi.org/10.1002/2016GL07180

Simpson, M., 2019, "A structural re-evaluation of the Ardmore basin." Mid-Continent Section. Search and Discovery Article 10795, 4-6.

Sloss, L. L., 1963, Sequences in the cratonic interior of North America: Geological Society of America Bulletin 74, no. 2, 93–114.

Suriamin, F., and M. J. Pranter, in press, Variability of Mississippian lithofacies, depositional environments, diagenetic processes, and reservoir quality within a mixed siliciclastic-carbonate system, eastern Anadarko Basin, Oklahoma, USA. Interpretation: Special Issue on STACK Play, Oklahoma.

Wilson, J. E., J. E. Chester, and F. M. Chester, 2003, Microfracture analysis of fault growth and wear processes, Punchbowl Fault, San Andreas system, California: Journal of Structural Geology 25, no. 11, 1855–1873, doi:10.1016/S0191-8141(03)00036-1.

Chapter 3: Mechanical stratigraphy of Mississippian strata using machine learning and seismic-based reservoir characterization and modeling, Anadarko Basin, Oklahoma

Jerson Tellez[1], Matthew Pranter[1], [2]Carl Sondergeld, [2] Chandra Rai [2], [2]Jing Fu, [2]Heyleem Han, [2]Son Dang and [3]Chris McLain

[1]School of Geosciences, The University of Oklahoma, 100 East Boyd Street, RM 710, Norman, Oklahoma, 73019, USA

[2] Mewbourne School of Petroleum and Geological Engineering, The University of Oklahoma, 100 East Boyd Street, RM 1210, Norman, Oklahoma, 73019, USA

[3]Marathon Oil Corporation, 5555 Sam Felipe Street, Houston, Texas, 77056, USA

Preface

The stratigraphic heterogeneity of the Meramec strata relates to the sequence stratigraphic framework. Such as relationship is clearly exhibited in the abundance of lithologies related to regressive and transgressive cycles. Regressive cycles are often comprised of brittle rocks, whereas ductile rocks dominate the transgressive cycles. The characterization and three-dimensional modeling of these brittle and ductile couplets show how proximal and distal variations in composition play an essential role in the lateral distribution and vertical staking of lithologies. The production analysis of selected wells suggests that vertical stacking patterns and their lateral continuity control the cumulative production of horizontally drilled wells in the Meramec unconventional reservoirs.

This manuscript appears in Interpretation, Vol. 9, No. 2 (March 2021); p. 1-62
https://doi.org/10.1190/int-2020-0167.1

Tellez, J., *M. J. Pranter, C. Sondergeld, Rai, C., Fu, J., Han, H., and C. McLain, 2021, Mechanical stratigraphy of Mississippian strata using machine learning and seismic-based reservoir characterization and modeling, Anadarko Basin, Oklahoma. Interpretation vol:9, iss:2, 1-62.*

Abstract

The Sooner Trend in the Anadarko (Basin) in Canadian and Kingfisher counties play primarily produces oil and gas from Mississippian strata. The interval consists of interbedded argillaceous mudstones and calcareous siltstones. Such a contrast in rock composition is linked directly to the mechanical stratigraphy of the strata. Brittle (calcareous siltstones) and ductile beds (argillaceous mudstones) are related to the sequence stratigraphic framework at different scales. We have used seismic and well log data to estimate and map the geomechanical properties distribution and interpret the mechanical stratigraphy of rocks within the Mississippian strata. First, we defined the parasequences that form the main reservoir zones of the Meramecian-Mississippian strata. Once we established the stratigraphic framework, we estimated and compared rock brittleness index (BI) using two independent laboratory-based measurements from the core. The first method, the mineralogicalderived BI, uses mineralogical composition inverted from Fourier-transform infrared spectroscopy analyses, whereas the second method, the mechanical-derived BI, involves measurements of compressional and shear velocities from core plugs. We use the data from core plug velocity measurements along with well logs and an artificial neural network approach to establish relationships among the geomechanical properties, well logs, and acoustic impedance values. We then applied these relationships to generate 3D geomechanical models constrained to seismic volumes. The resulting grid distributions illustrate the stratigraphic variability of the properties at the parasequence scale. Overall, brittle strata decrease in thickness and abundance basinward as the frequency of interbedded brittle and ductile zones increases and gradually transitions into thin calcite-cemented siltstones and clay-rich mudstones. Analysis of the production performance of selected horizontal wells drilled within the Mississippian strata indicates that the proportion of

brittle and ductile rocks along the well path drilled and the drilled area vertical stacking pattern play a significant role in hydrocarbon production for these Mississippian units.

Introduction

Reservoir characterization of unconventional resources considers the rock composition, texture, thickness, maturity, pore pressure, and petrophysical and geomechanical properties, as well as the volume of hydrocarbons present. Several field-scale studies have shown that unconventional tight reservoirs are highly heterogeneous (Suarez-Rivera et al., 2009; Baytok and Pranter, 2013; Miller, 2019). A better understanding of this heterogeneity helps to accurately define landing zones in sweet spots and plan hydraulic-fracture treatment. Furthermore, it provides information to optimize the drilling process to avoid zones composed of hard and challenging rock intervals to drill along the well paths. Brittle and dense formations composed of chert or highly cemented rocks are challenging to drill because they significantly reduce the penetration rate in horizontal wells (German et al., 2015). Therefore, the estimated bit lifetime is shorter than expected and increases the expenses and drilling time for infill wells.

On the other hand, brittle rocks break naturally and produce a better response to hydraulic-fracture stimulation. Brittle rocks can produce from open fracture networks, hold injected proppant, and remain open for extended periods. Wells landed in brittle rock intervals are likely to produce more hydrocarbons when pressure, oil saturation, and other variables are favorable in unconventional shale rocks.

Rock brittleness can be expressed by the brittleness index (BI), and it is often used in rock mechanics to describe how likely rocks will break when stress is applied. This concept has

several definitions depending upon the approach used to define it, including (1) strain-stress laboratory measurements (Altindag et al., 2003), (2) rock elastic properties (mechanically derived BI [MEDBI]) (Rickman et al., 2008), and (3) mineralogical composition (mineralogically derived BI [MIDBI]) (Jarvie et al., 2007; Wang and Gale, 2009).

The definition and characterization of the geomechanical properties within the Mississippian-Meramec strata are not well documented. Several studies have defined the stratigraphy and lithology of the rocks in the northern and eastern Anadarko Basin (Rogers, 2001; Mazullo and Wilhite, 2010; Mazullo, 2011; Mazullo et al., 2016), and more recent studies have characterized the Meramec "Mississippian lime" strata in the Sooner Trend in the Anadarko (Basin) in Canadian and Kingfisher counties play of central Oklahoma in terms of stratigraphy, lithologic composition, chemofacies, petrophysical properties, and total organic carbon (Price et al., 2017; Drummond, 2018; Duarte, 2018; Hardwick, 2018; Hickman, 2018; Leavitt, 2018; Miller, 2018, 2019) (Figure 3-1). Hardwick (2018) reports the presence of marine cement in silt-dominated facies that occludes the pore space. Miller (2019) describes the effect of cementation in the variability of petrophysical properties and, consequently, in the reservoir hydrocarbon pore volume. This study found that chemical cementation was dominated by calcite and dolomite, followed by quartz and pyrite minerals. Miller (2019) also reports an inverse relationship between the clay content and chemical cementation in the rocks.

To expand the information about the geomechanical properties and mechanical stratigraphy of these Mississippian strata, this study (1) explores the mechanical stratigraphy and variability of geomechanical properties of the Meramec strata and their spatial distributions and

(2) relates the stratigraphic variability of the geomechanical properties to the sequence stratigraphic framework.

To address these topics, a combination of methods to estimate geomechanical properties from different data sources is used along with machine learning techniques, specifically, artificial neural networks (ANNs) and geostatistical seismic-constrained reservoir models to estimate and predict their spatial variation and to evaluate its implications in terms of reservoir quality and well production performance.

Geological setting

The Anadarko Basin is composed of distinct tectonic features created after three major orogenic events that took place from the Middle Devonian to Pennsylvanian time (approximately 320–390 m.y.), which are the Acadian, Antler, and proto-Ouachita events (Gutschick and Sandberg, 1983).

As a result of these events, a cratonic platform originated along the Transcontinental Arch bounded by the eastern interior, Ouachita, and Antler foreland troughs and separated into the Madison and Burlington platforms to the northwest and southeast, respectively (Beebe, 1959; Lane and De Keyser, 1980; Gutschick and Sandberg, 1983; Ball et al., 1991).

The Burlington platform was located to the east of the Transcontinental Arch and occupied the northern portion of the Anadarko Basin. Rocks deposited in this platform represent rapid, uninterrupted, and progradational carbonate sedimentation during a transgressive stage to a highstand position (Gutschick and Sandberg, 1983).

Mississippian rocks were deposited on shallow water shelves in an overall southward direction across shelf-edge, slope, and basinal environments. The top of the interval is bounded by Pennsylvanian (approximately 320 m.y.) rocks that form an angular unconformity and become a paraconformity toward the deepest part of the basin (Beebe, 1959). The base of the section unconformably overlies the Devonian rocks of the Woodford shale. Sloss (1963) defines the Mississippian interval as a second-order transgressive sequence limited at the base by a minor disconformity and by a regional unconformity at the top representing the top of the Kaskaskian sequence. Deposits within this interval were divided into four series, or ages, which comprise, from base to top, the Kinderhookian, Osagean, Meramecian, and Chesterian (Curtis and Champlin, 1959) (Figure 3-2).

The Meramecian series sediments exhibit an even distribution across the basin with a northwest–southeast depositional trend that coincides with the strike (Curtis and Champlin, 1959; Mazullo, 2009). The thickness of this series ranges between 100 and 900 ft (30–270 m), and often in northcentral Oklahoma is not thicker than 100 ft (30 m). The deposition of this rock series occurred during a marine transgression in which some of the Meramecian deposition occurred below the wave base due to local subsidence or sheltered waters. Commonly cross bedded calcarenites, calcareous sandstones, and siltstones are found within the upper Meramec (Curtis and Champlin, 1959; Price et al., 2020).

Data and methods

Data description

The data include 288 vertical wells drilled through the Meramec interval with log data (gamma ray [GR], neutron porosity [NPHI], bulk density [RhoB], deep resistivity [RILD], photoelectric effect factor [PE], and sonic [DT]). We used normalized GR logs to filter outliers of spikes within the well log data and carried out a manual inspection of other logs during the well correlation process. Likewise, we used information from 10 horizontal wells with production data and a post-stack seismic volume of 143 mi2 (370 km2). The seismic data bin size is 110 × 110 ft (33.5 × 33.5 m) with a frequency range of 10–60 Hz, and it is standard American polarity. The data also include two acoustic impedance volumes (compressional and shear) obtained from an elastic impedance inversion of a pre-stacked seismic volume. We incorporate core descriptions and routine core laboratory measurements (N = 185) from previous studies (Miller, 2019) and additional descriptions of two core wells to complete five wells (2066 ft [629 m]) located in the surrounding area.

Stratigraphic framework

Previous studies showed that the Meramec strata exhibit vertical variations that allow us to apply the sequence stratigraphy concepts for unconventional resources (Price et al., 2017, Price et al., 2020; Drummond, 2018; Miller, 2018). We complemented previous core-based studies with information of two additional cored wells (wells A and B) to identify lithofacies, interpret depositional geometries, and describe sedimentary structures to develop a sequence stratigraphic framework. To extend the observations described in the core, we

generated several dip- and strike-oriented cross sections and used the GR log signatures to define low and high-frequency cycles interpreted as parasequences. These cycles/parasequences were interpreted as high-frequency regardless of a temporal frame and are defined as three signature types: (1) increasing upward, (2) decreasing upward, or (3) serrated (no-change upward). Then, we defined key surfaces, such as flooding surfaces (FS) and regressive surfaces (RS), where GR trends changed between the GR-defined stacked intervals.

The interpreted well tops were matched to four interpreted seismic horizons: parasequence 8, 3, Osage, and Woodford and five conformable surfaces representing the top of parasequences 7, 6, 5, 4, 2, and 1 within the Meramec strata. The generated surfaces are structural maps of the top of flooding surfaces interpreted in well log data and divide the Meramec strata into eight parasequences. Furthermore, isopach maps were generated for each parasequence to visualize the stratigraphic trends and control the interpretation quality.

MIneralogical Derived Brittleness Index (MIDBI)

MIDBI uses the average volumetric composition of the minerals present in the rock to estimate the values of BI. For the Meramec strata, two methods were used to calculate the mineralogical composition to compute MIDBI. The first method, X-ray fluorescence (XRF) analysis, was run for five cored wells to obtain the elemental composition of the rocks (Han et al., 2019). This method detects major elements such as Si, Ca, Al, K, Mg, and Fe as well as traces elements (Turner ans Slatt, 2016). The second method, Fourier Transform InfraRed spectroscopy (FTIR), was run in 165 core plug samples from the five cored wells. To obtain the weighted mineral percentages of the samples (Dang et al., 2013) an inversion scheme was

applied for each dataset. This inversion predicts the weighted mineral composition of the rock with small error and standard deviation (Ballard, 2007).

To calculate the MIDBI, we refer to the equation used by Jarvie et al. (2007). This equation established a relationship between brittle and ductile minerals and was later modified by Wang and Gale (2009) equation (1) below. Additionally, we explored the relationship suggested by Jin et al. (2014) equation (2) below, including calcite and feldspar as brittle minerals in the rock. The estimation of the MIDBI shows a strong dependency on the selected equation used in the calculation.

(1) $BI_1 = \frac{\text{Quartz+Dolomite}}{\text{Quartz+Dolomite+Calcite+Clays}}$ (2) $BI_2 = \frac{\text{Quartz+Dolomite+Feldspar+Calcite}}{\text{Quartz+Dolomite+Calcite+Clays+TOC}}$

MEchanical Derived Brittleness Index (MEDBI)

We also used the MEDBI estimation defined by Rickman et al. (2008). This approach estimates BI using the geomechanical variables Young's modulus, E and Poisson's ratio, ν. To calculate these parameters, we first estimated compressional and shear velocities (Vp and Vs) (Fu, 2019 personal communication) using velocity data from ultrasonic pulse transmission measurements in the core plugs (Mohapatra et al., 2019). Next, we used equations (3) and (4) to calculate the geomechanical parameters (E and υ) and later derived the MEDBI using equation (5) (Rickman et al., 2008).

(3) $\mathrm{E} = \frac{\rho \mathrm{Vs}^2(3\mathrm{Vp}^2 - 4\mathrm{Vs}^2)}{\mathrm{Vp}^2 - \mathrm{Vs}^2}$ (4) $v = \frac{\mathrm{Vp}^2 - 2\mathrm{Vs}^2}{(\mathrm{Vp}^2 - \mathrm{Vs}^2)}$ (5) $\mathrm{BI} = \frac{1}{2}\left[\frac{\mathrm{E} - \mathrm{Emin}}{\mathrm{Emax} - \mathrm{Emin}} + \frac{v\mathrm{max} - v}{v\mathrm{max} - v\mathrm{min}}\right]$

The evaluated core plugs represented the defined lithologies (mudstone, argillaceous siltstone, argillaceous calcareous siltstone, calcareous siltstone, and silty limestone) within the Meramec wells along a transect of 38 mi (61.8 km) following the depositional trend from proximal to distal (Figure 3-3, 3-4).

Machine learning to estimate geomechanical properties ν, E and BI in wells

To estimate the geomechanical properties υ and E in wells from log data, we used a supervised Artificial Neural Networks (ANN) approach. ANN models are part of the machine learning techniques for artificial intelligence studies (Haykin, 2000). They are composed of a group of interconnected artificial neurons that work together in an organized scheme. One characteristic of an ANN is that it learns by training, therefore, ANNs allow users to bias the output data resulted from the technique. To improve the results from the network, training data is split into two parts. The first part provides the information for the actual variable training and, the second part is used to estimate the error in the network by comparing the result to the given target (5%) (Kalogirou, 2000).

Application of ANNs for classification and estimation

Two workflows using ANNs were attempted to generate three-dimensional geomechanical models and evaluate the mechanical stratigraphy of the Meramec strata. First, we attempted to estimate the geomechanical variables (E and υ) using the core plug data along with well logs in a classification approach. This method computes discrete data (classes or categories) trained with an input dataset (well logs). The output represents the highest probability of the input data belonging to a particular class or category.

To produce the required discrete data used as input, we evaluated the statistical distribution of the data and selected the percentiles P25 and P75 as end members for the upper and lower values for two classes and then, split the remaining values into three categories.

We generate discrete logs with the defined five classes for each variable (E, υ, and BI), and divided the dataset into a training set composed of 114 samples and a testing set of 23 samples. The training set used the discrete well logs to compare them to its corresponding well log signatures as part of the training process. After the relationships were established, they were used to estimate classes within non-cored intervals and wells based solely on well log responses to generated new discrete logs as output data. The log suite available for this process contains the following well logs: gamma-ray (GR), neutron porosity (NPHI), bulk density (RhoB), photoelectric effect factor (PE), deep resistivity (RILD), and sonic (DT). At least four different combinations were used in the training of the ANN 1) GR, NPHI, RhoB, RILD, PE, DT 2) GR, NPHI, RhoB, RILD, PE, 3) GR, RhoB, RILD, PE, and, 4) NPHI, PE, GR.

We evaluated the results of the trained and applied model for each well log combination using a confusion matrix. This table quantifies the prediction performance of the model. The confusion matrix compares the output classes of each variable to the actual core defined classification (Ting, 2011; Allen and Pranter, 2016). The metrics obtained from this matrix are 1) overall accuracy and 2) user's accuracy. The overall accuracy relates the summation of all true positive answers to the number of total true positives in the model. This relation helps to define how good is the whole prediction of the model. However, the overall accuracy might omit the error in estimation for each class. A more detailed quantification is given when looking at the user's accuracy which provides an estimation of the number of correctly predicted samples of

one specific class and divide it by the total amount of samples of that specific class (Janssen and Van der Wel, 1994).

The second method used to estimate the geomechanical properties was a "regression/estimation" technique. This method used the actual calculated values of geomechanical properties (E, *v*) from the core plugs as continuous variables, to predict the values of geomechanical properties in the wells without core data. Four combinations of well logs were used along with the core data to estimate the values of geomechanical properties 1) GR, NPHI, RhoB, RILD, PE, DT 2) GR, NPHI, RhoB, RILD, PE, 3) GR, RhoB, RILD, PE, and, 4) NPHI, PE, GR. We used the testing set to calculate the percent error of the estimation using the equation (6). The prediction accuracy evaluation of the ANN models allowed us to select best well log combination to predict the geomechanical properties best Poisson's ratio, Young's modulus, and brittleness index (E, v, BI) (Figure 3-8).

$$(6)\ \frac{|Actual\ Value - Estimated\ Value|}{Actual\ Value} * 100$$

Velocity model

We generated a velocity model to perform the multi-attribute analysis in-depth domain and facilitate the integration of well data in the structural interpretation. Three horizons in time (Meramec, parasequence 3, and Woodford) were used along with 894 well tops interpreted in 298 wells to build the velocity model within the study area. This model considered the intervallic velocity defined at the datum using the following relation:

(7) $$z = z_r + v_0(t - t_r)$$

Where z is the calculated depth of the point, zr, the depth at the well location, v0 the calculated velocity and (t-t_r) the difference in time.

Seismic constraints for three-dimensional modeling

The acquisition parameters of the seismic survey limit the vertical resolution of geomechanical variables from seismic volumes. The average vertical resolution of the seismic data in the section of interest ranges from 55~60ft whereas the horizontal resolution is 110ft. It makes it hard to compare and contrast the results of geomechanical generated BI from seismic and well log data. However, the volumetric distribution of seismic data provides an excellent guide for constraining the horizontal distribution of geomechanical properties.

We calculated volumes of the Lame parameters (μ and λ) that relate the rigidity and incompressibility of the rocks and allow for the fundamental parametrization of seismic waves used in seismic studies. They were derived from the acoustic and shear impedance volumes using the relations shown in (8) and (9).

(8) $\lambda\rho = (AI)^2 - 2\,(SI)^2$ (9) $\mu\rho = (SI)^2$

To create a Poisson's ratio (υ) volume, we used equation (10) that shows a relationship between Lamé parameters(lambda and mu) to obtain the variable. On the other hand, we used a linear correlation between the acoustic impedance and YM values from the calculated well logs to generate the YM volume trend (E):

(10) $\upsilon = \frac{\lambda}{(2\lambda+2\mu)}$ (11) E = (0.001943*AI) - 20

Geomechanical modeling

The parasequence structural maps defined in the stratigraphic analysis were used to build the 3D stratigraphic framework (3D grid). The grid covers an area of 143 mi^2 (370 km^2) and the grid size was defined based on 1) the bin size of the seismic volume for the horizontal size, and 2) the vertical thickness of cell size that represents the vertical variations observed in the core plugs. The grid is comprised of seven zones with thickness established using isopach maps.

To represent the spatial variability of The data derived from the ANN regression/estimation approach was modeled using a sequential-gaussian simulation (SGS) constrain to 1) 3-D lithology model, 2) upscaled well logs from geomechanical properties, 3) histograms by zone, 4) interpreted stratigraphic surfaces, 5) seismic-derived trend volumes and 5) variogram parameters by zone.

The vertical variograms for the models were estimated using a nested spherical-exponential variogram model, whereas the horizontal variability was constrained using seismic-derived volumes for v and E as trends. The volumes were generated using equations (10) and (11), respectively. We incorporate these volumes using a collocated-co-kriging approach to provide a smooth horizontal distribution of the modeled variableshe vertical variograms for the models were estimated using a nested spherical-exponential variogram model whereas the horizontal variability was constrained to seismic-derived volumes as trends. We incorporate these volumes using a collocated-co-kriging approach to provide a smooth horizontal distribution of the modeled variables.

Sequence stratigraphy and geomechanical analysis

To analyze the relationships between sequence stratigraphy and geomechanical properties in this study, we first established a sequence stratigraphic framework to identify (1) vertical facies trends, (2) cycle bounding surfaces, (3) packages of transgressive/regressive cycles, (4) stacking patterns and lower frequency sequences, and (5) mechanical units within the cycle hierarchy. To evaluate the correlation between depositional trends and geomechanical properties within the same sedimentary interval, we divided the strata into brittle versus ductile intervals based on the geomechanical properties estimated in well logs using an ANN approach. This methodology allowed us to analyze the sequence stratigraphic components and vertical multiscale cyclicity with the mechanical layering (Moretinni et al., 2005; Slatt and Abousleiman, 2011; Galvis-Portilla, 2017) to better understand the stratigraphic variations of mechanical properties such as BI, YM, and Poisson's ratio across the study area.

Production analysis

The database used for this analysis includes normalized 360-day cumulative oil production data from 10 horizontal wells drilled within the Meramec and divided by reservoir zone (Figure 3-3). We used the generated 3D model to extract the MEDBI mechanical property information along the well path for each horizontal well to analyze relationships between the MEDBI mechanical and oil production. The values and percentages of brittle and ductile rocks were quantified to observe the correlation between these variables. In addition, we used vertical profiles extracted from the model to evaluate the vertical configuration (stacking patterns) of brittle- ductile beds and possible production data relationships.

Results

Stratigraphic framework

The The Meramec strata represent a vertical succession of the second-order transgressive sequence (5–50 Ma) composed of eight higher frequency parasequences characterized by coarsening-upward deposits that represent regressive phases with small and often absent fining upward transgressive phases (e.g., Price et al., 2017; Drummond, 2018; Miller, 2018, 2019). The tops of the parasequences correspond to marine flooding surfaces. Parasequences 1–4 represent a transgressive parasequence set capped by a maximum flooding surface (MFS) at the top of parasequence 4. The subsequent parasequences 5 and 6 compose an aggradational-progradational parasequence set followed by a retrogradational set characterized by backstepping of parasequences 7 and 8. The first transgressive parasequence set shows dominantly silty limestones and calcareous lithologies associated with proximal deposits within the outer carbonate shelf. Parasequence 3 displays a thick and retrogradational- aggradational interval composed of thin interbedded siltstones and clay-rich deposits transitioning to finer grained deposits in parasequence 4 and capped by an MFS. These rocks reflect better sedimentary characteristics of a lower energy setting with intermittent flows of coarser silt size sediments associated with gravity flows as described by Duarte (2018). The second aggradational-progradational parasequence set (parasequences 5 and 6) shows an asymmetric coarsening-upward signature in GR. Siltstones dominate the parasequence set with few interbedded mudstones. The third and uppermost parasequence set (parasequences 7 and 8) is retrogradational and exhibits a fining upward signature, capped by a transgressive surface of erosion representing the top of the Meramec strata.

MIneralogical Derived Brittleness Index (MIDBI)

The MIDBI obtained from FTIR and XRF analysis is shown in Figure 3-5A for wells 1 and 4, which respectively denote proximal and distal localities. The calculated MIDBI results using equation (2) which includes calcite and feldspar as brittle minerals in the rock are often higher (blue dots) than MIDBI values estimated using the traditional Wang and Gale relationship (equation 1) (green dots). We also compare the MIDBI values estimated from XRF and FTIR derived mineralogy, using equation (1) in a cross-plot. The results show stratigraphic consistency but a poor linear correlation (41%) between the MIDBI values in wells 1 and 4 (Figure 3-5b). The larger differences observed between MIDBI estimations occur at random points, making it difficult to detect which minerals affect the estimation between the two methods. In general, the MIDBI displays a contrasting response between proximal and distal locations. The MIDBI values in the proximal locations (well 1) are underestimated, whereas the MIDBI values in the distal locations (well 4) are overestimated when compared with those of MEDBI.

MEchanical Derived Brittleness Index (MEDBI)

We derived the MEDBI for each cored plug sample (N=137) using equations (3), (4), and (5) (Rickman, 2008). Figure 3-6 shows a cross-plot of the calculated variables in well 1. The results show that low values of Poisson's ratio and high values of Young's modulus are typical of brittle rocks as suggested in previous studies by Rickman, (2008). The MEDBI values show an inverse relationship with pore pressure.

Machine learning approach – Artificial Neural Networks ANN

To predict the geomechanical properties Poisson's ratio and Young's modulus (E, and v) in wells, we used two ANN approaches 1) classification and 2) estimation/regression.

Classification approach

The division of the core plug dataset resulted in five classes or categories: 1) low, 2) medium-low, 3) medium, 4) medium-high, and 5) high (Figure 3-7). The classes are not related to lithologies or rock types because geomechanical parameters of the Meramec are also related to diagenesis and diagenetic products are not clearly manifested in distinctive well log signatures, making them difficult to associate with lithologies directly.

The accuracy of the classification predicted by each ANN model was measured using a confusion matrix. The highest accuracy for the Poisson's ratio training classification was 61% using a combination of GR, NPHI, RhoB, RILD, PE and DT well logs. However, the application of this model to the test data resulted in less than 10% of accuracy in the prediction. We found similar results in the evaluation of the trained models to classify Young's modulus and Brittleness index with overall accuracy values of 63% and 57%, respectively. The well log combination that showed the higher accuracy for Young's modulus training classification was GR, NPHI, RhoB, RILD, PE, and DT, whereas, for the BI training classification, the combination corresponds to NPHI, ResD, GR, PE, and RHOB well logs. We did not apply any of the generated ANN classification models to the whole dataset due to low accuracy for prediction.

Estimation/regression approach

For geomechanical properties based on estimation and regression, the average error obtained for Poisson's ratio was 20 % for blind test data and corresponds with the combination GR, NPHI, RhoB, RILD, PE, and DT. The estimation of Young's modulus shows the average error of 12.5%. In the testing data with the well log combination of GR, RhoB, and PE. We applied the generated ANN regression models to the entire dataset to generate E and ν synthetic well logs.

Spatial distribution of brittleness Index, Poisson's ratio and Young's modulus.

3D model

The 3-D grid covers an area of 143 mi^2 (370 km^2) with horizontal cell dimensions of 110 ft x 110 ft (33.5m x 33.5m) to preserve the horizontal resolution of the seismic. Proportional layers were used with an average cell/layer thickness of 2 ft (0.6m). The grid contains seven zones that contain parasequences 1 to 8 (Figure 3-9a). We combined parasequence 4 and 5 to one as zone 4. The final dimensions of the model are 575 x 577 x 406 cells for i, j, and k, with a total of 134,700,650 cells.

Geomechanical properties

To represent the spatial distribution of the brittleness index, Poisson's ratio, and Young's modulus, we determined variograms ranges through variography analysis of the well data. Horizontal variograms were adjusted to 4000 ft (1220 m) and 2000 ft (610 m) in the major and minor directions respectively for both properties (E, ν). The vertical variograms for the properties vary from 3 to 5 ft (0.9 to 1.5 m).

Poisson's ratio values in the model are lower in the northwestern of the study area. Poisson's ratios in zones 1, 2, 3 and 4 range from 0.2 to 0.3 across the model whereas zones 6, 7, and 8 show more contrasting and gradational values that range from 0.1 to 0.35 for the upper regressive zones (Figure 3-10).

Young's modulus values in the model decrease from northwest to southeast and change parallel to the deposition dip – direction. Vertical changes in PR are related to parasequence stacking. The progradational and aggradational parasequence sets show high E values in calcareous-siltstone and argillaceous calcareous siltstone lithologies in proximal areas whereas the retrogradational parasequence set show high variability reflecting the interbedding mudstones and siltstones along the section (Figure 3-11).

The MEDBI is predominantly high to the northwest (proximal) transitions to lower values toward the south (distal) (Figure 3-13C). Higher MEDBI values are dominant within zones 1, 2, and 6, whereas, moderate values are present in zones 3, and 5. MEDBI is variable within zones 7 and 8 (Figure 3-12). Lithology variations drive lateral changes of MEDBI mainly from northwest to southeast in the dip direction (Figures 3-13 and 3-14). Lithology variations drive lateral changes of MEDBI mainly from northwest to southeast in the direction of deposition (Figure 3-14). Proximal locations (well 10) contain intervals of high-MEDBI calcareous siltstones that transitions to low MEDBI argillaceous siltstones in distal positions (well 13) within the study area.

Stratigraphic variability of geomechanical analysis

Meramec parasequences included from base to top parasequences 1 to 8. Stratigraphically, the parasequences exhibit a cyclic pattern represented by two distinctive lithologies, calcareous siltstones, and argillaceous siltstones, contrasted according to their composition. A relative fall of the sea level produced coarser deposits that were easily cemented and tend to have a relatively brittle behavior. In contrast, relative sea-level rise results in the deposition of organic, clay-rich and ductile rocks. We relate the observed cyclicity in the strata to brittle-ductile intervals within the stratigraphic framework (Figure 3-15). To describe the mechanical behavior of the rocks we interpreted the brittle-ductile intervals using geomechanical logs and gamma-ray profiles. Overall, parasequences 1, 2 and 6 exhibit asymmetric coarsening-upward geometries that resulted in a higher proportion of brittle to ductile deposits (70:30) within each parasequence. Parasequences 3 and 5 exhibit serrated signature composed of brittle and ductile rocks (50:50) with high internal variability in the mechanical properties within the interval. Parasequences 7, and 8 show a combination of fining and coarsening upwards patterns dominated by fined-grain deposits that result in a high proportion of ductile rocks (30:70) in the upper Meramec. On a large scale, the Meramec strata exhibit one ductile interval that represents one transgressive parasequence set composed of parasequences 1 to 3. The brittle-ductile ratio of this parasequence set transitions from 50:50-to-20:80 at the maximum flooding surface. The following aggradational-progradational parasequence set is composed of a brittle interval comprised of parasequences 5 and 6 and displays a gradational upward increase of the brittle-ductile ratio from 20:80-to-60:40. The upper interval of the Meramec is composed of one transgressive and ductile parasequence set comprised of parasequences 7 and 8 and with a brittle-ductile ratio of 30:70 (Figure 3-16).

Production analysis

We extracted the modeled BI property along the well paths of ten horizontal wells within the model (Figure 3-17). Since the BI property was modeled as a continuous variable, we defined a brittle-ductile boundary for the Meramec rocks of 67% to discretize the variable. This limit was established considering the mean value of MEDBI for the parasequence 4 which contains a higher proportion of ductile rocks within the Meramec interval (Figure 3-18). Rocks with MEDBI values greater than 67% were considered brittle whereas rocks with values equal or lesser than 67% BI were considered as ductile. Figure 3-19 shows the calculated brittle and ductile percentages of rock along the paths of ten selected wells (wells 20 to 30) and Figure 3-20 shows the normalized 36-days cumulative production for the selected horizontal wells. Overall, wells drilled through more than 50 % of ductile rocks exhibit better performance in oil production compared to wells drilled through lower percentages of ductile rocks.

We extracted vertical profiles or sections from the generated model along the well trajectories. To illustrate the impact of the vertical stacking in production we selected three horizontal wells that represent, a good (well 20), intermediate (well 22) and poor (well 21) production performance cases. The three cases correspond to 130, 90 and, 31 MBO from the 360-day normalized oil cumulative data respectively.

Vertical profiles for well 20 (Figure 3-17a) show the well path landed within zone 5. The horizontal section drilled through 49% of brittle rocks and 51 % of ductile rocks. The stratigraphic configuration of the rocks shows a brittle interval in zone 5 bounded at the top and base by ductile rocks that extend parallel to the horizontal well path. This well shows a good cumulative oil production with 130 MBO. In the case of well 21 vertical profiles show the well landed within zone 3 (Figure 3-17b). The lateral section drilled through 62% of brittle and 38%

of ductile rocks. The stacking pattern configuration along the well trajectory shows a heterogeneous interval bounded at the top by brittle rocks and partially at the base by ductile rocks and resulted in a poor hydrocarbon production with 90MBO. The well 22 landed in zone 5 (Figure 3-17c) and drilled through 57% and 43% of brittle and ductile rocks respectively. The vertical sections along this well path display a brittle interval bounded at the top by interbedded brittle-ductile beds and continuous ductile rocks at the base. This well production is 90 MBO and represents our average well in the analysis.

DISCUSSION

MEDBI versus MIDBI

The estimation of the MIDBI from two different data sources, the XRF and FTIR elemental inversions indicated a good stratigraphic agreement where contrasting high and low brittleness index intervals were defined within similar depths. However, the XRF inversion scheme tends to overestimate alumina and silica oxides present mainly in clays (Nayak and Singh, 2007), whereas the FTIR data minimize this error using an inversion scheme that defines significantly more output minerals. We found that equation (2) proposed by Jin et al. (2014) overestimates the BI values. Because calcite cement content is high within the Meramec strata, the ratio of brittle-to-ductile minerals changes significantly, resulting in high MIDBI values (Figure 3-5). In contrast, equation (1) proposed by Wang and Gale (2009), results in estimations of MIDBI values that compare better to the MEDBI.

The comparison between MIDBI and MEDBI estimations at the parasequence scale shows significant differences. We attribute these differences to the diagenetic alteration of the rock fabric, more specifically calcite and quartz cementation that might affect its mechanical properties (Miller, 2019). The mineralogical composition used to calculate MIDBI does not

allow to differentiate the presence of calcite or quartz minerals as part of the framework or the matrix (grains or cement) in the rock. Therefore, the MIDBI method does not accurately reflects the cement in the rock. Based on core and thin-section observations we established that samples with high values of carbonates represent high carbonate cement content, as reported by Miller, (2019). Intervals with carbonate content higher than 25% show an average overestimation of 25% between the BI estimations, whereas intervals with less than 25% of carbonate content show less than 5% difference between the two BI estimations (MIDBI and MEDBI) in the well profile (Figure 3-18).

The effects of cement in the estimation of geomechanical properties have been described before in large-scale (Perez Altamar and Marfurt, 2014) and small-scale (Gale at al, 2007). For the Meramec strata, the carbonate cement enhances the anisotropic behavior of the rock due to the diagenetic cement that affects the rock microstructure (Martin and Davis, 1987; Vecsey et al., 2008). This anisotropy in the rocks can be quantified by comparing the ultrasonic shear velocity measurements for the slow and fast directions. For well 1, intervals with high anisotropy (differences between slow fast velocities) display a strong positive correlation with intervals that exhibit high differences between the MEDBI and MIDBI. This correlation suggests the presence of cement within these intervals and was confirmed in the thin-section descriptions.

We found the MEDBI estimations more reliable to characterize the geomechanical properties of rocks in the diagenetically altered Meramec strata. The calculated MEDBI values are the result of velocity measurements that reflect the grain arrangement, matrix, porous space, mineralogical composition and the effects of diagenetic processes in the rock.

Mechanical Stratigraphy

The Meramec strata exhibit a mixed composition of calcareous and clastic lithologies that resulted in contrasting values of geomechanical properties within the section (Figures 3-14 and 3-15). We relate the mechanical stratigraphy within the Meramec to primary factors such as depositional environment, and paleogeography, as well as secondary factors such as diagenetic processes. The vertical heterogeneity of these mixed clastic-carbonate deposits is related to relative sea-level changes (Price et al., 2017; Duarte, 2018; Leavitt, 2018; Miller, 2018; Miller, 2019). The regressive intervals of the parasequences contain coarser grains that exhibit higher cementation due to early diagenesis caused as a consequence of burial and chemical compaction resulting in significant calcite-dolomite and quartz cement (Miller 2019). In contrast, the genetically related transgressive intervals of the parasequences display clay-rich lithologies composed of pelagic sediments and fine grain sediments deposited during stages of relative high sea-level. The high-frequency deposits form asymmetric parasequence geometries (Miller, 2019) with thick brittle regressive intervals and thin genetically related ductile transgressive intervals.

We relate the horizontal variability of the geomechanical properties to the depositional environment (Figures 3-10,3-12). The Meramec strata display gradational changes in the geomechanical properties associated with changes of facies within a carbonate ramp (Curtis and Champlin, 1959; Witzke, 1990; Mazzulo and Wilhite, 2010) (Figure 3-13). The proximal locations in the study area are dominated by thick brittle calcareous siltstones and carbonates interpreted as deposited in a shallow ramp to the northwest whereas the southeast is dominated by thin interbedded ductile argillaceous mudstones and siltstones deposited in the outer ramp (Drummond, 2018; Duarte, 2018; Miller, 2018, 2019; Price et al., 2020)

Impact in hydrocarbon production

The mechanical properties in the Meramec strata show a strong relationship to the sequence stratigraphic framework. Transgressive intervals are generally characterized by fine-grained argillaceous siltstones and mudstones, whereas overlying regressive intervals are dominated by calcareous siltstones and silty limestones. This difference in lithologies has a profound effect on hydrocarbon production (storage capacity and brittleness). The diagenetic processes such as cementation affect the regressive cycles of high-order sequences resulting in high brittleness index rocks with reduced porosity whereas the transgressive cycles exhibit less diagenesis in more clay-rich lithologies with larger storage capacity but limited permeability (Miller, 2019).

The analysis of lateral sections from the selected wells shows that well trajectories drilled through higher percentages of ductile rocks exhibit up to 63% higher production than wells that contain predominantly brittle rocks along the well path (Figure 3-20). We additionally found that wells drilled in brittle zones bounded by thick lateral extensive ductile rocks reported higher hydrocarbon production. In proximal locations (northwest) wells with high oil production landed at the top of zone 5. We associate this good performance to the lateral extensive mudstones at the base of zone 4 (maximum flooding interval in parasequence 4). The higher oil production of the analyzed wells comes from well 20 drilled in a more distal position (Figure 3-3b).This well landed in a brittle interval (zone 5) bounded at the top and base by two ductile intervals (zone 4 and 6) that correspond to parasequences with thicker transgressive intervals (Figures 3-12 and 3-17).

We noticed that thining of transgressive sequences associated with marine flooding surfaces (Miller et al., 2018) toward more proximal locations (northwest) reduces the percentage

of ductile rocks between regressive cycles affecting negatively the oil cumulative production in wells drilled through a high percentage of brittle rocks (Figure 3-19 and 3-20).

Conclusions

We explored different methods to define the geomechanical properties of the Meramec strata in the study area. Specifically, for the brittleness index BI, we evaluated two main methods 1) the MEDBI and 2) the MIDBI. To calculate the best relationship for MIDBI we found equation (1) most reliable in the Meramec strata.

We found that MIDBI values are highly affected by the mineral weight percentage using the mineralogical inversion from data using X-ray diffraction (XRF) and Fourier Transform Infra-red (FTIR) techniques. The FTIR inversion resulted in a more accurate estimation of the weight percentage of minerals to calculate the MIDBI when compared to MEDBI estimated from ultrasonic velocities.

The MEDBI method provides the most reliable estimation of the brittleness index for the Meramec strata since this relationship uses the information of geomechanical properties reducing the mineralogical volume uncertainty implicit when calculating the MIDBI.

The use of regression/estimation ANN models, along with well logs and core plug data, showed better results in the estimation of Poisson's ratio and Young's Modulus (ν, E) using well logs when compared to the ANN classification model. The regression method provided an average error without bias of the lithological definition.

The mechanical properties of the Meramec strata are strongly related to the sequence stratigraphic framework of these rocks. It provides a tool to evaluate the lateral and vertical continuity of brittle and ductile rocks, as well as to define sweet spots for hydrocarbon production. Wells drilled within the Meramec strata in proximal locations and landed within

zone 5 show a high oil cumulative production likely associated with the adjacent lateral extensive ductile interval in parasequence 4 related to a maximum flooding surface. On contrast, wells with high production in distal locations landed in brittle zones bounded at the top and base for laterally continuous ductile beds associated with flooding surfaces that separate zones 5 and 7.

The vertical stacking patterns, brittle/ductile ratio drilled along the horizontal well path, and geomechanical distribution of properties play an important role to map, predict and target possible sweet spots for development wells. However, many other operational variables need to be considered and evaluated in conjunction with the stratigraphic and geomechanical models to establish a fully supported development strategy for hydrocarbon production.

Acknowledgments

This research was funded through the Reservoir Characterization and Modeling Laboratory at the University of Oklahoma, COLCIENCIAS, and the Agencia Nacional de Hidrocarburos Scholarship. We thank Marathon Oil Corporation and the Integrated Core Characterization Center for providing data. I thank Ishank Gupta, Jing Fu, Son Dang and Heyleem Han for the rock type, core plug velocity data, X-Ray diffraction and mineralogy data, and respectively. Special thanks to Chris McClain and James Packwood from Marathon Oil Corporation for their valuable support in the project. Finally, we thank Schlumberger (Petrel and Techlog) for providing software.

Figures

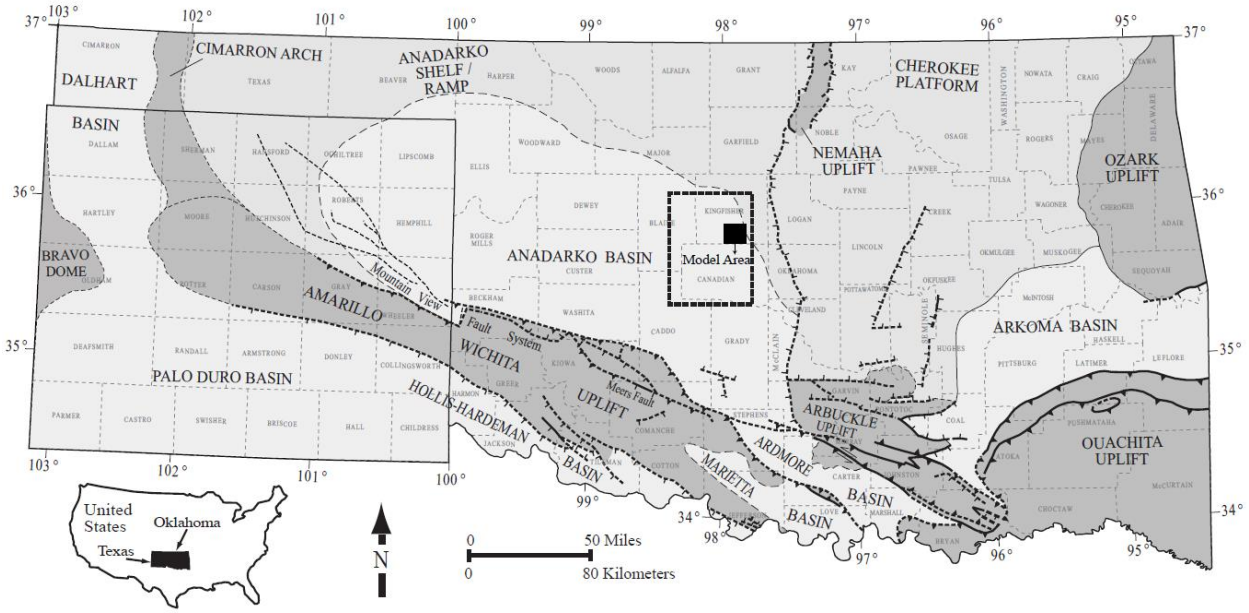

Figure 58: Map of the regional tectonic provinces of Oklahoma and the Texas Panhandle. The study area lies in the Anadarko Basin 34 (modified from Dutton, 1984; Campbell et al., 1988; McConnell et al., 1989; Johnson and Luza, 2008; LoCriccho, 2012).

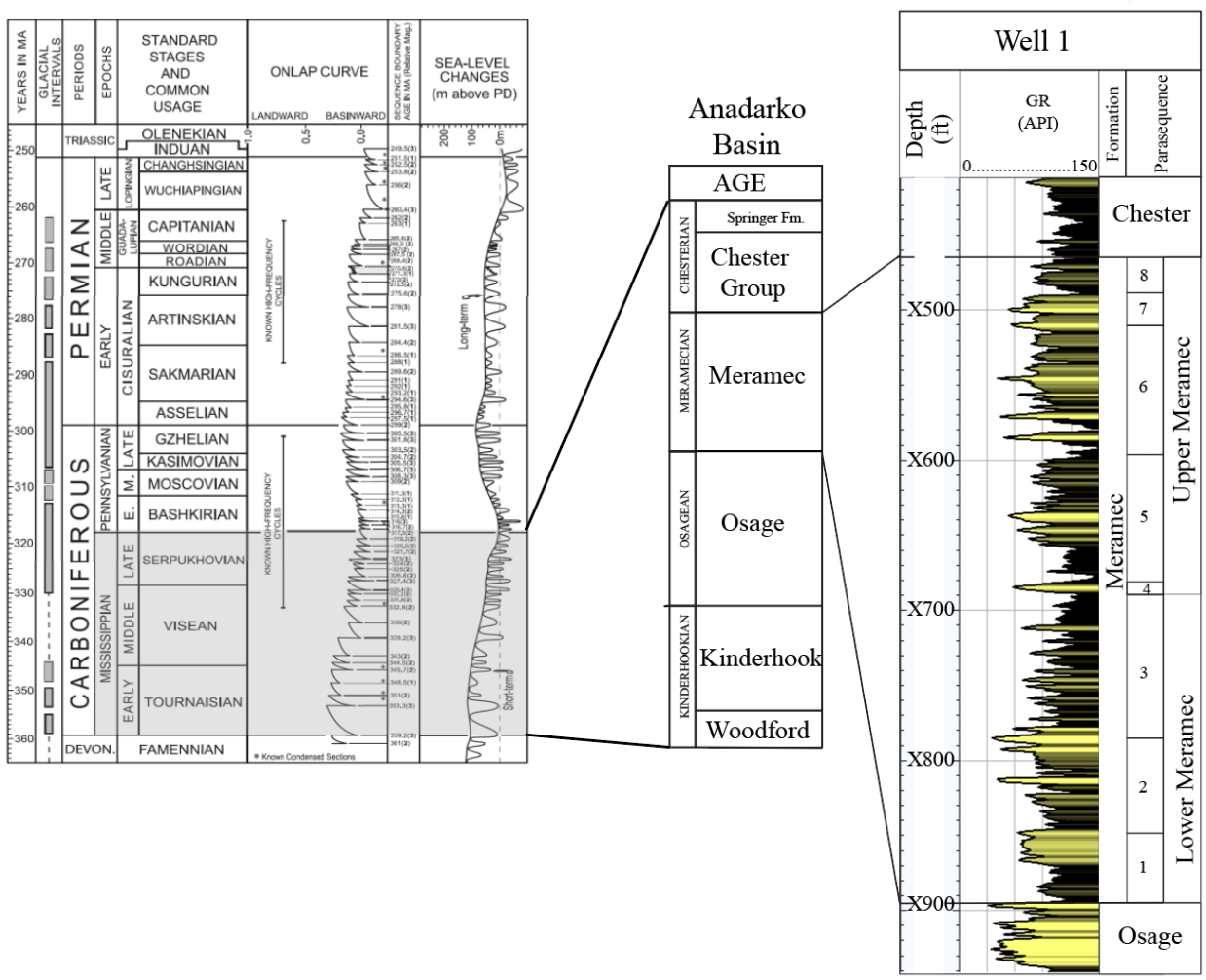

Figure 59 :Generalized stratigraphic column and type log of the Mississippian section. The type log shows the interpreted parasequences from 1 to 8 (modified from Haq and Schutter, 2008).

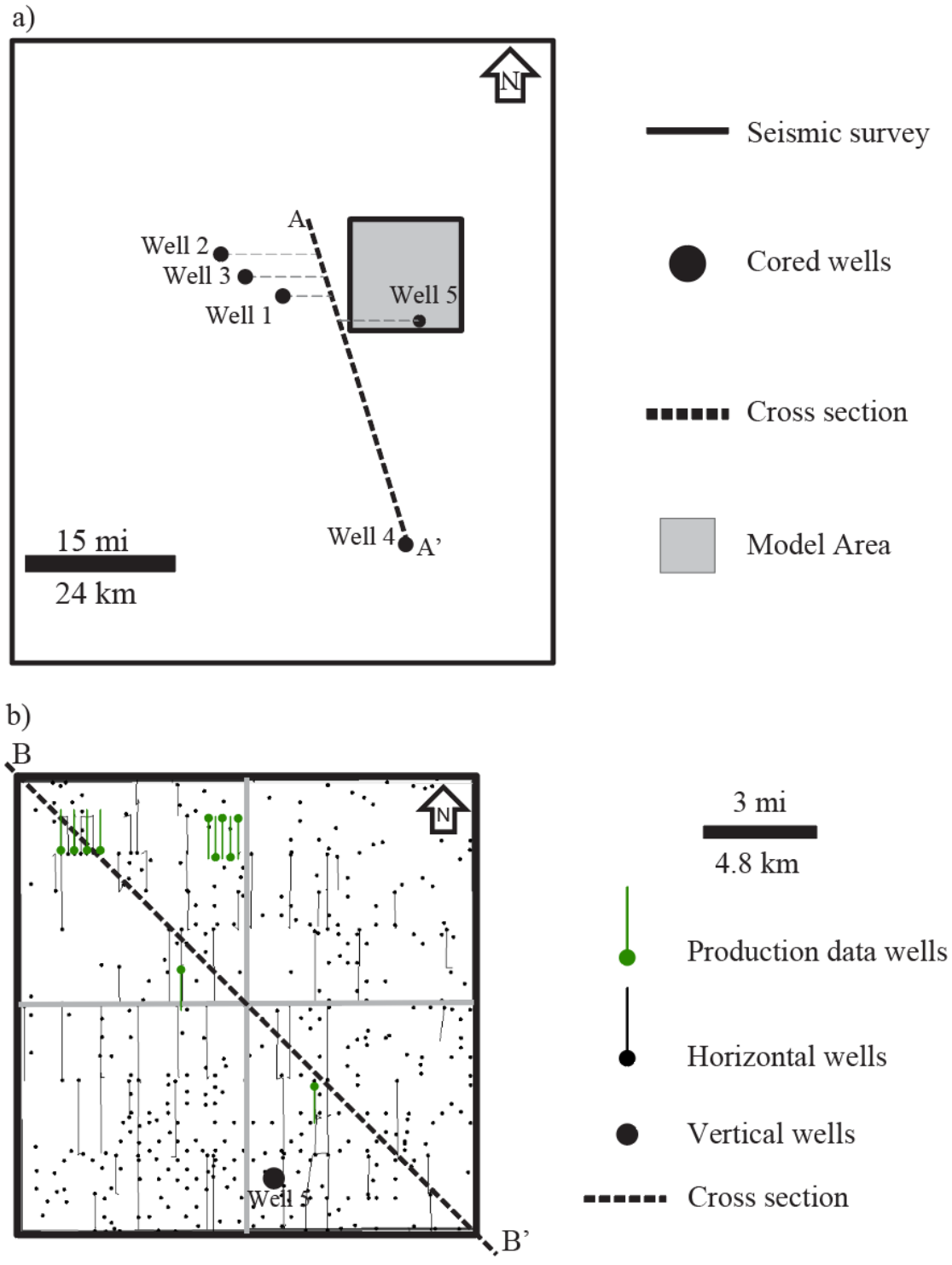

Figure 60: (a) Regional map with a cross section and the cored wells surrounding the modeled area. (b) Detailed map of the study area showing the locations of 288 wells with wireline logs (GR, NPHI, RhoB, PE, RILD, and DT), as well as five cored wells and two cross sections.

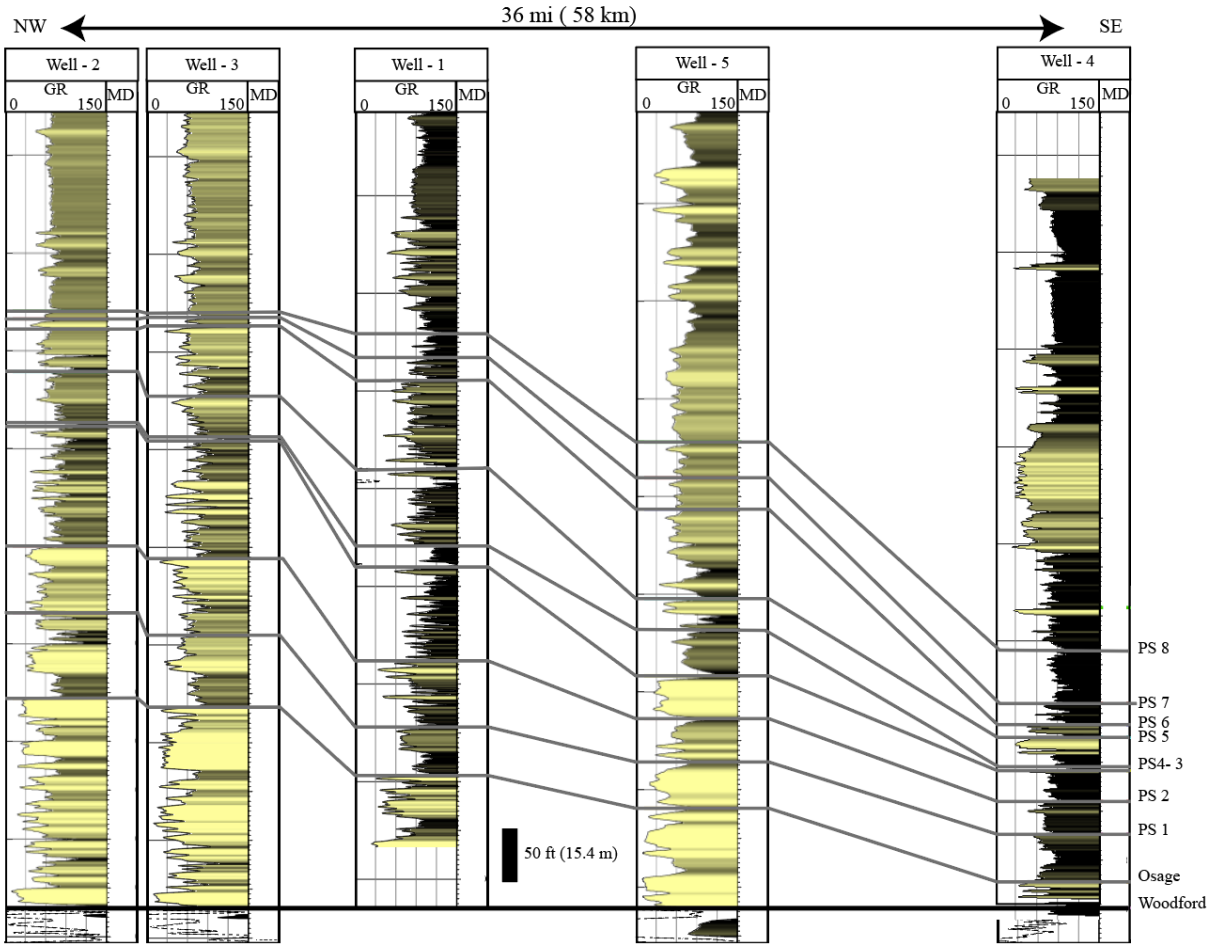

Figure 61: (A-A′) Regional cross section that includes wells with available core plug data within the study area flattened on the Woodford shale. The black lines correspond to the parasequence tops interpreted for the Mississippian Meramec. The GR track is shaded by the GR values, and it was used for stratigraphic correlations. The section is oriented northwest–southeast and shows the progradational clinoforms in the study area and the decrease in the overall thickness of the Meramec toward the southeast.

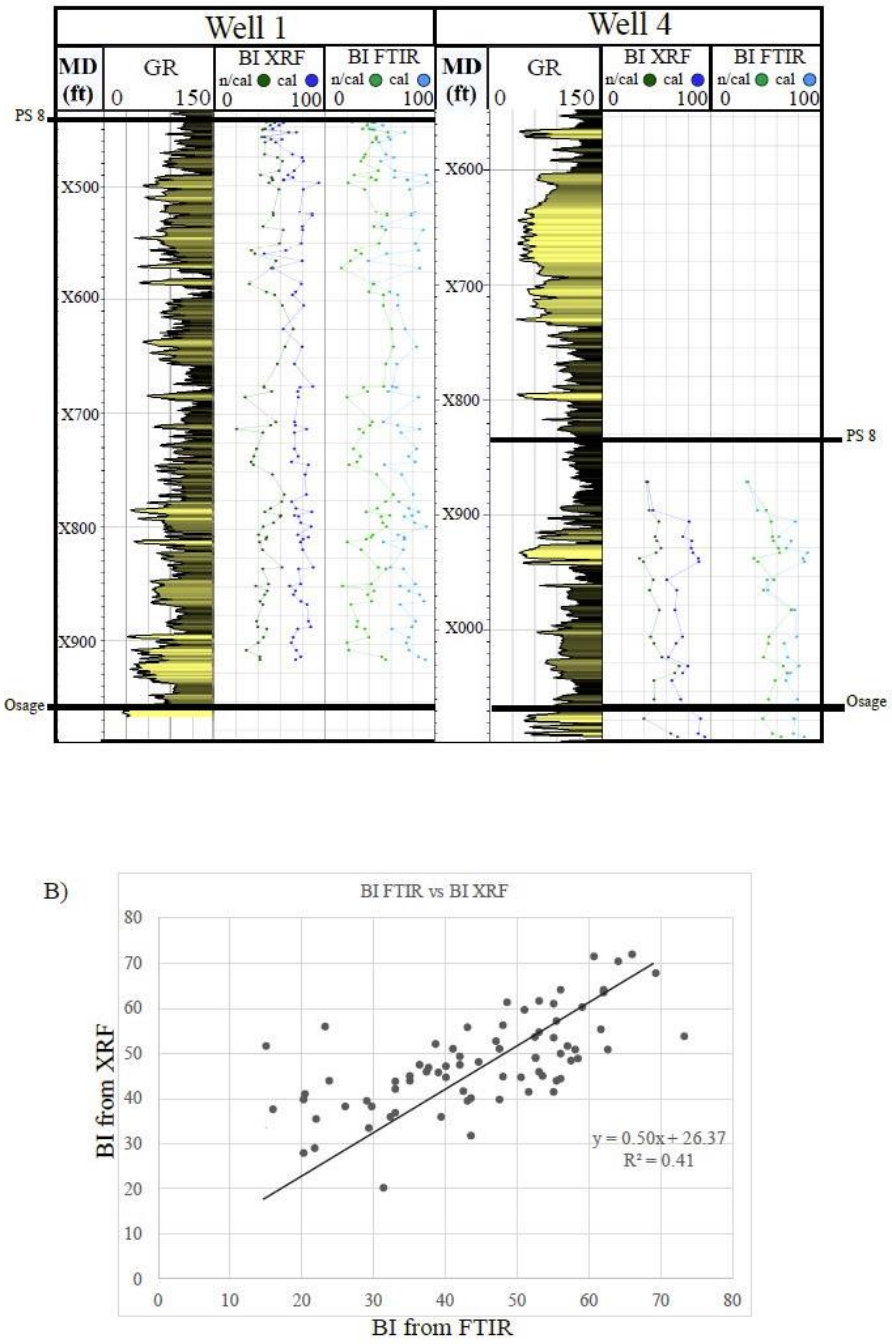

Figure 62: GR and mineralogical BI calculations for wells 1 and 4. The term PS 8 represents the top of the interval. These wells represent proximal and distal positions within the study area. The term "n\cal" in green shows the estimation of the MIDBI using equation 1, whereas "cal" shows the estimation using equation 2. MIDBI XRF tracks show the calculation using the mineralogical information from X-ray diffraction, whereas FTIR tracks represent the estimation done using the data inverted from the FTIR analysis. (b) The lower image shows the correlation between the FTIR- and XRF-generated values using the available core data and equation 1.

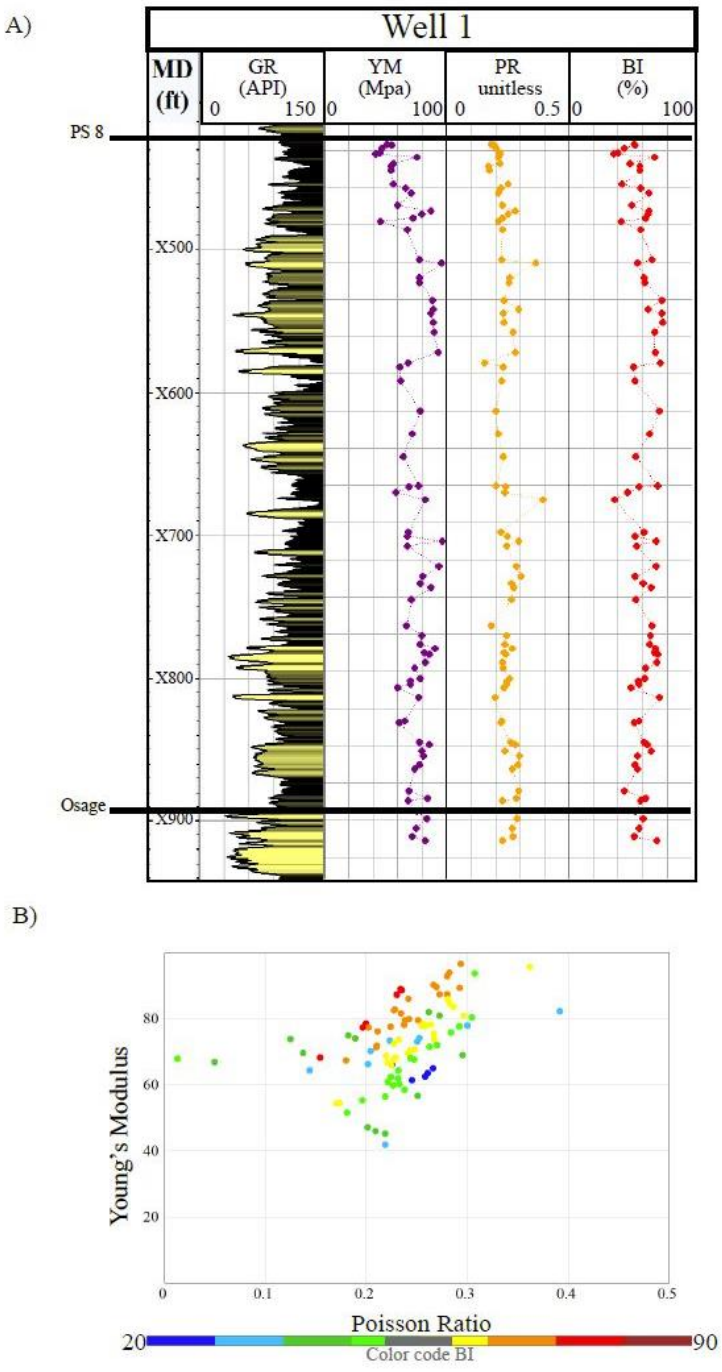

Figure 63:(a) Geomechanical properties (Poisson's ratio, YM, and mechanical BI) calculated from core plug ultrasonic velocity data for well 4 along with GR in the Meramec strata. PS 8 represents parasequence 8 or the top of the interval. (b) Crossplot of Poisson's ratio versus YM. The core data are color coded using the MEDBI mechanical values in a rainbow color scheme. In general, high values of YM and low Poisson's ratio represent brittle rocks. However, this behavior is not observed with the brittle index in this data set, similar to Rickman's et al. (2008) observations that highlighted that the shale's internal variability would affect the geomechanical properties.

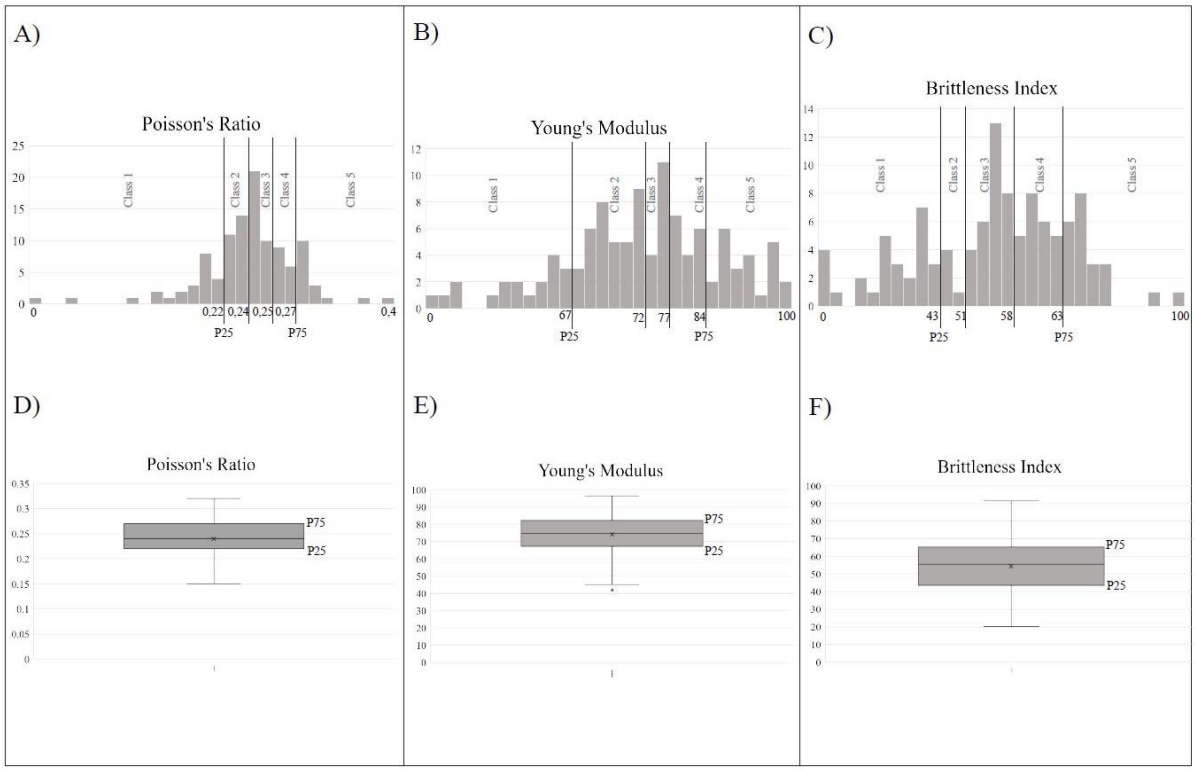

Figure 64: Histograms of geomechanical properties calculated from the core plugs data set. Percentiles P25 and P75 set the maximum and minimum limits for two classes. The other limits for each defined class are shown in the black lines. The y-axis is the fraction of samples in each range that corresponds to the mechanical property on the x-axis. The lower images show the distributions for the calculated properties in a box plot.

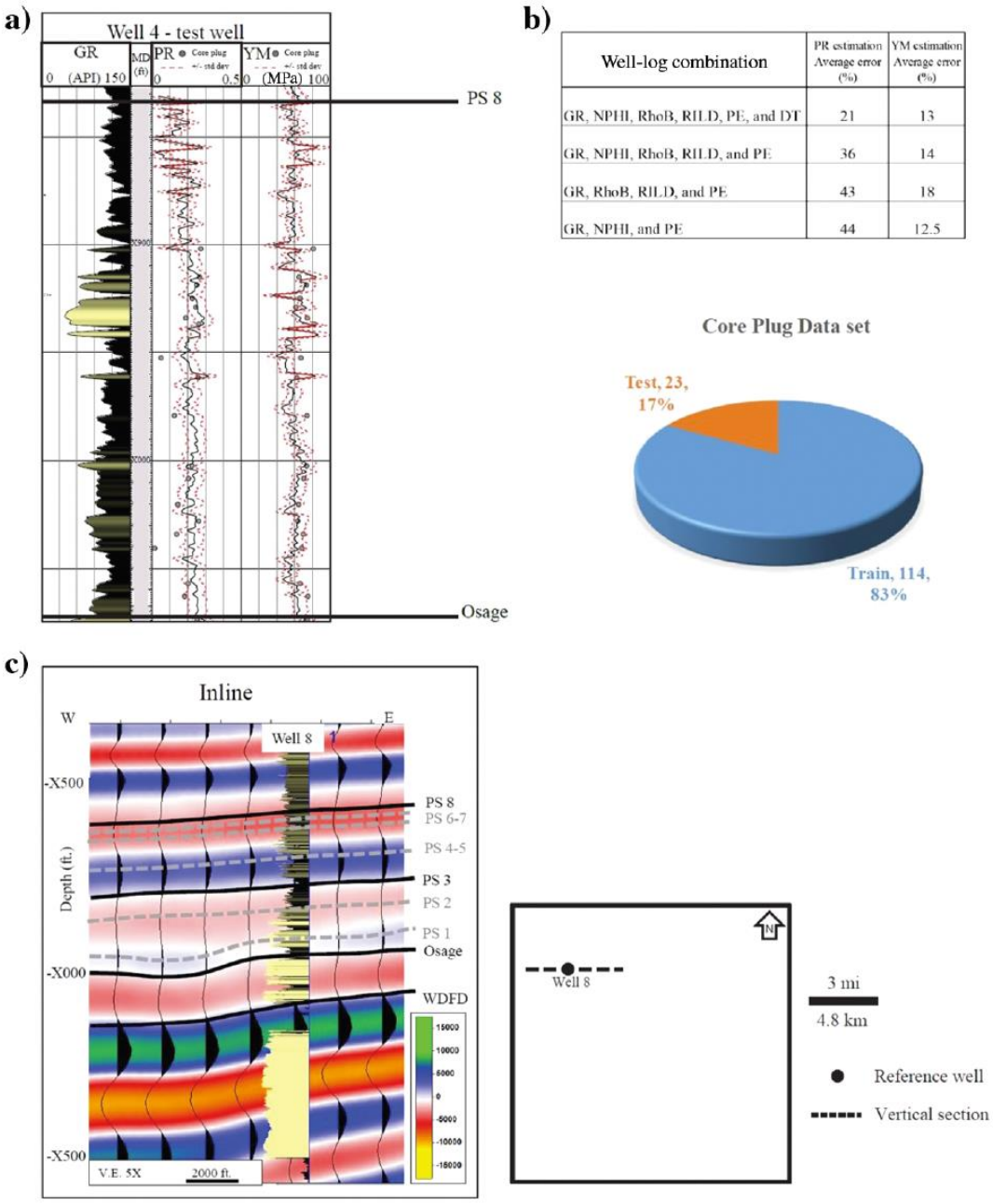

Well-log combination	PR estimation Average error (%)	YM estimation Average error (%)
GR, NPHI, RhoB, RILD, PE, and DT	21	13
GR, NPHI, RhoB, RILD, and PE	36	14
GR, RhoB, RILD, and PE	43	18
GR, NPHI, and PE	44	12.5

Figure 65: (a) The GR and geomechanical continuous logs from the estimation/regression process using well log combinations along with core plug data in a regression ANN model. For the geomechanical properties, the black line corresponds to the prediction using the ANN model. The dashed red lines correspond to an error equal to ± one standard deviation of the data set distribution. The gray dots represent the actual values of the properties calculated from the core plug data. (b) A table displays the combinations used for the estimation/regression ANN and the error associated with each ANN model with respect to the blind test. The lower image shows the distribution of the data set for training and testing of the ANN model. (c) Arbitrary seismic amplitude line along with the well showing the interpreted horizons used to build the velocity model as well as the conformable surfaces generated to build the stratigraphic framework in the model.

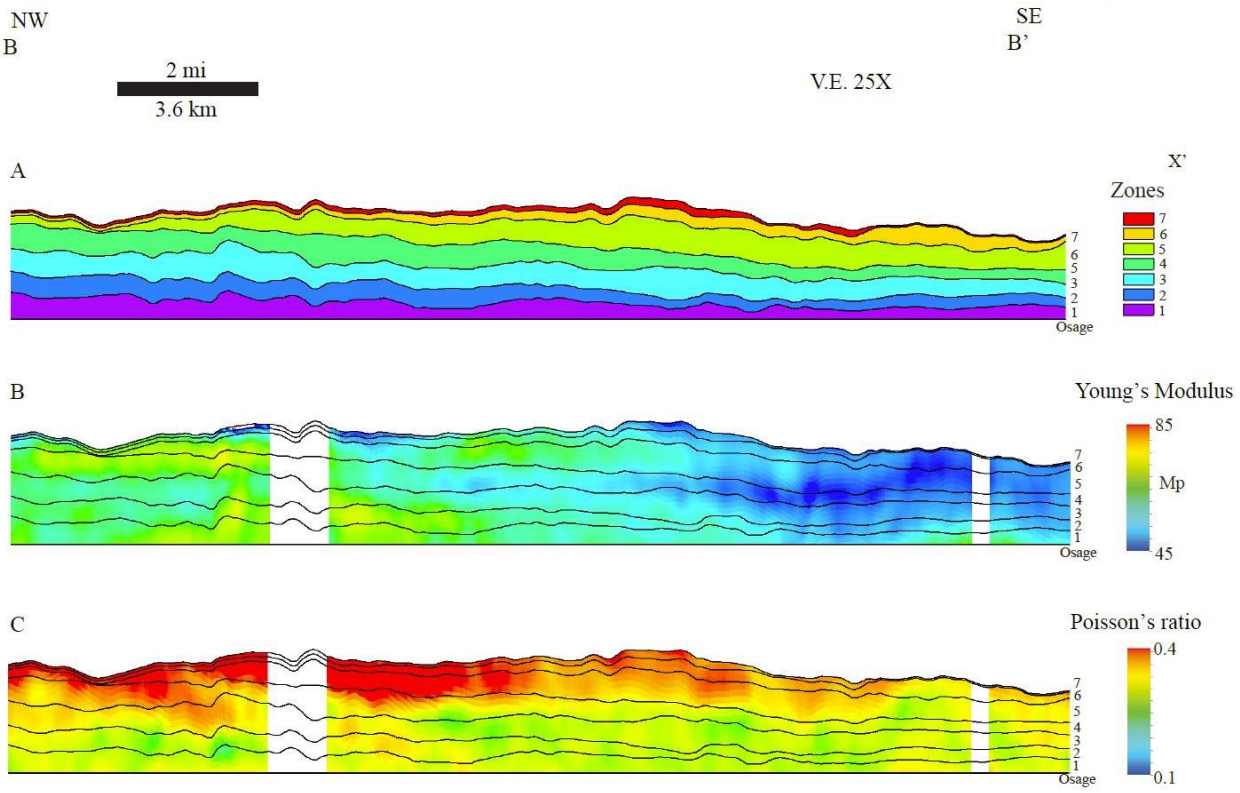

Figure 66: Northwest–southeast-oriented cross sections through the 3D model flattened on the Osage horizon. (a) The seven stratigraphic zones and the lateral variations of thickness within the parasequences within the Meramec in the study area. (b) The seismic-derived trend model used to constrain the YM property. (c) The seismic-derived trend volume used to constrain the variability of the Poisson's ratio property.

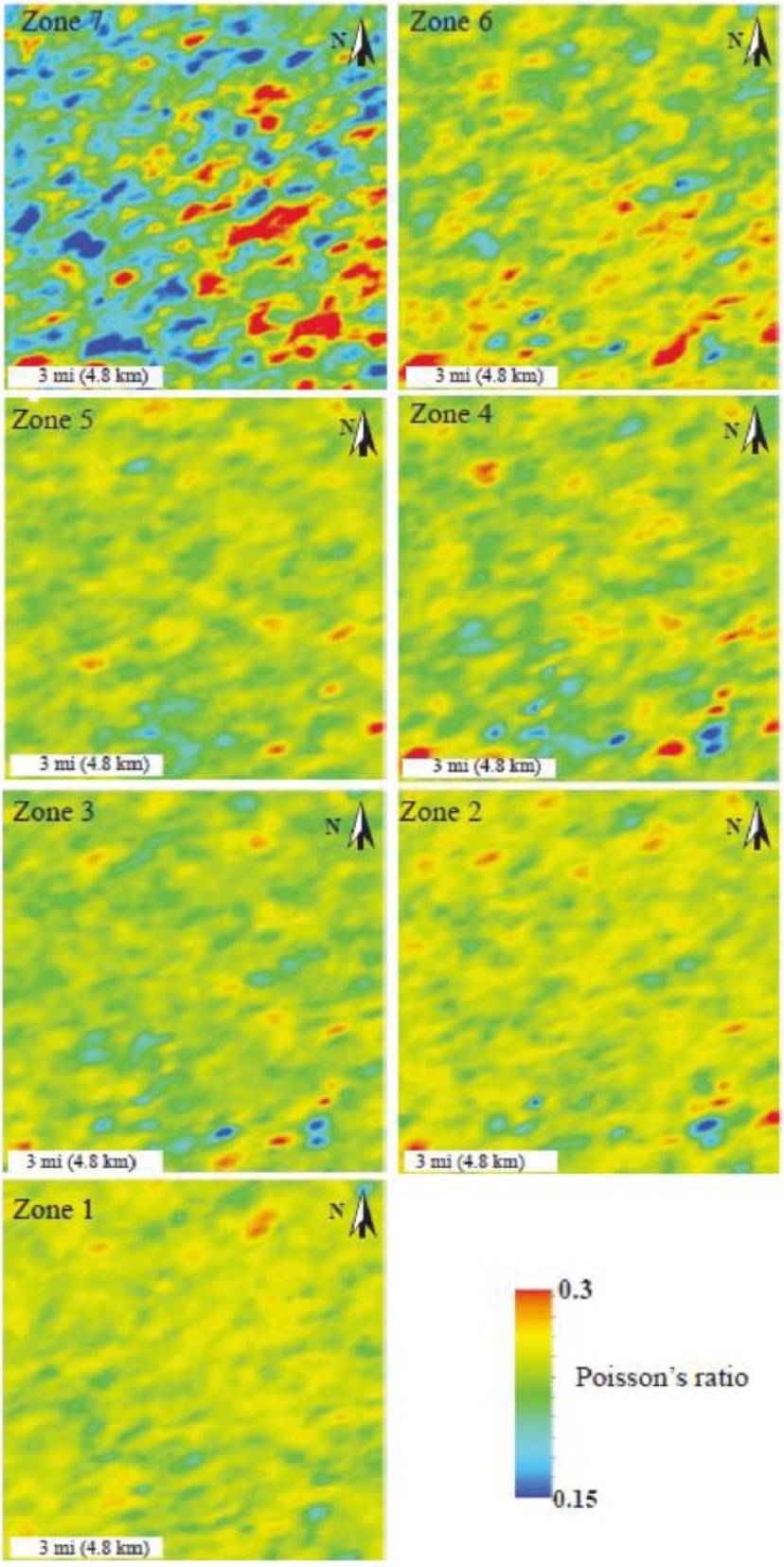

Figure 67: Average maps of Poisson's ratio for the Meramec zones. Zones 1–5 show a relatively homogeneous distribution of the Poisson's ratio, whereas an upward increase in Poisson's ratio and heterogeneity is observed in zones 6 and 7, possibly related to the increase in clay content toward the top of the Meramec strata.

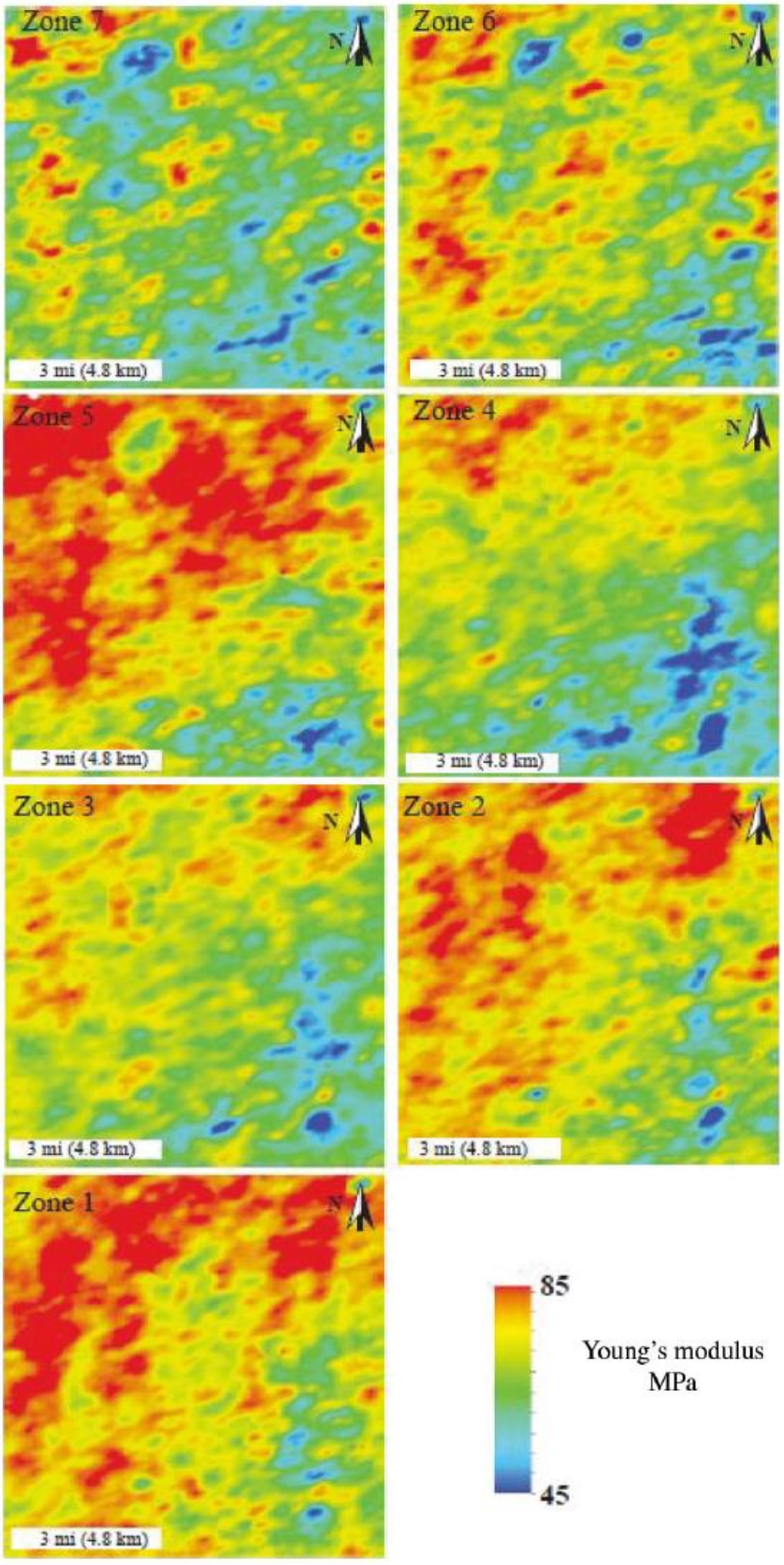

Figure 68:Average maps for YM for the Meramec. Zones 1–3 show high values of the YM toward the proximal northwest locations. Zone 4 shows a decrease in the property values related
to the increase in the clay percentage close to an MFS. Zone 5 shows high values of YM in the northwest, decreasing gradually upward in zones 6 and 7.

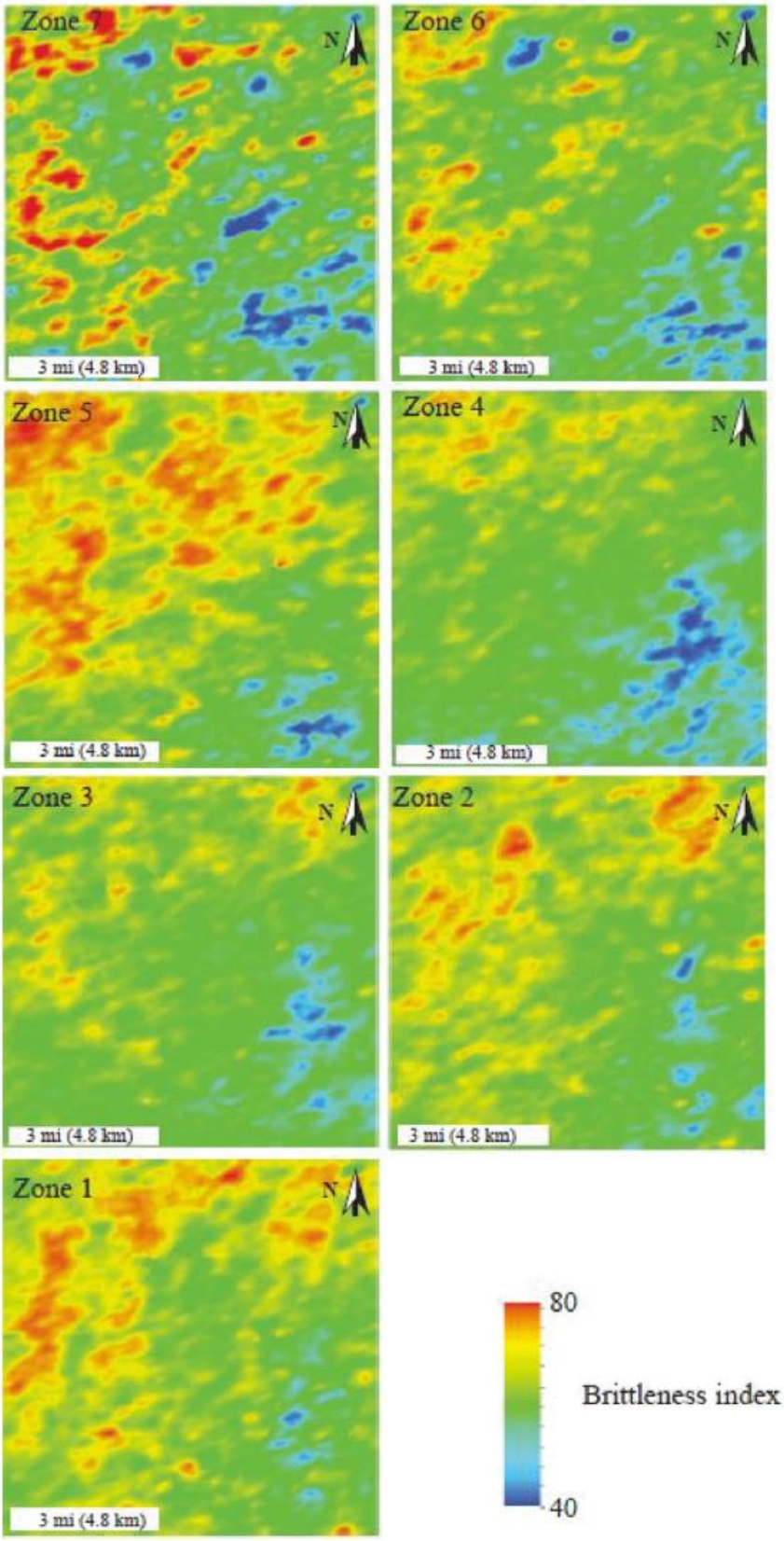

Figure 69: Average maps for the BI (MEDBI) for the lower Meramec. Zones 1–3 show high MEDBI values gradually decreasing upward consistent with the stratigraphic framework cyclicity. Zone 5 displays an increase in MEDBI values toward the northwest, followed by a gradual decrease in MEDBI and an increase in heterogeneity in zones 6 and 7.

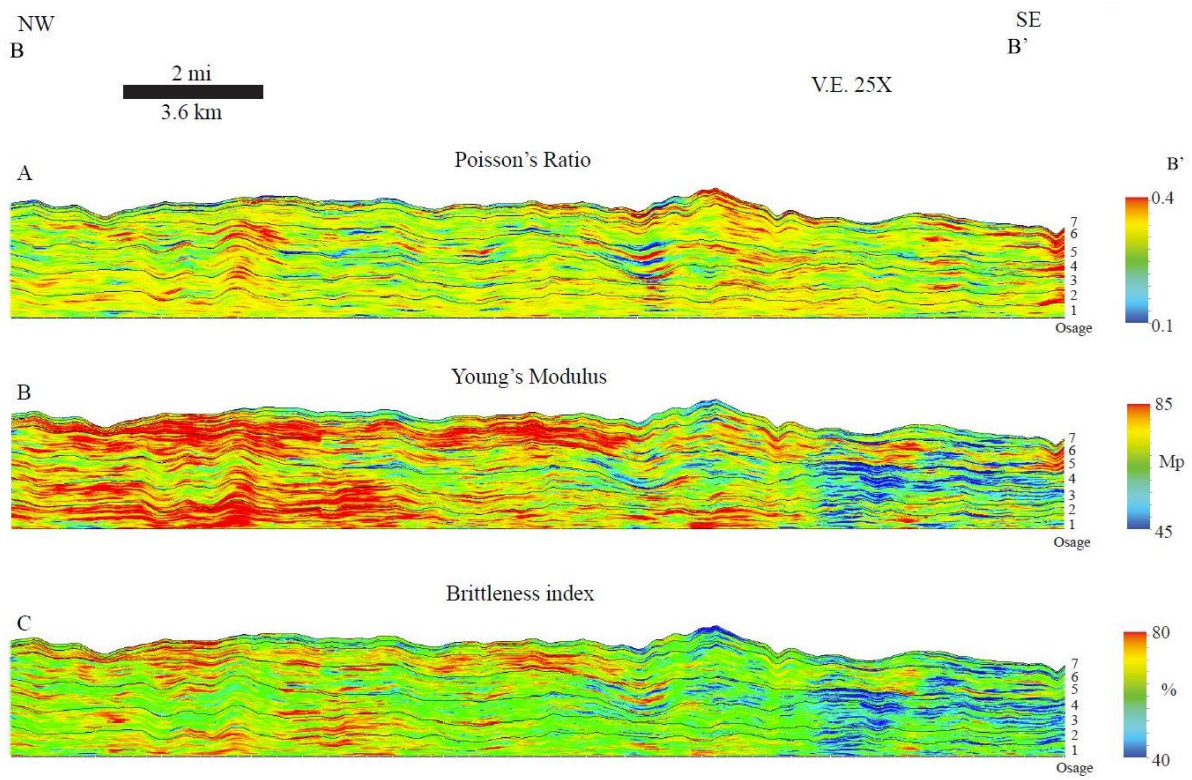

Figure 70:Northwest–southeast-oriented cross section through the 3D model flattened on the Osage horizon. (a) The spatial distribution of Poisson's ratio within the study area. This property shows an increase in Poisson's ratio toward the top of each zone. (b) The spatial distribution of YM within the study area. An overall decrease in YM is observed from the proximal to the distal locations within the modeled area. (c) The resulting model of spatial distribution calculated from the Poisson's ratio and YM grids. The model reflects the vertical and horizontal variability of the Meramec strata. In distal locations, zones 1–4 show low values of MEDBI, whereas zones 5–7 display slightly higher values of MEDBI. These variations agree with the transgressive-regressive-transgressive parasequences sets from the sequence stratigraphic analysis.

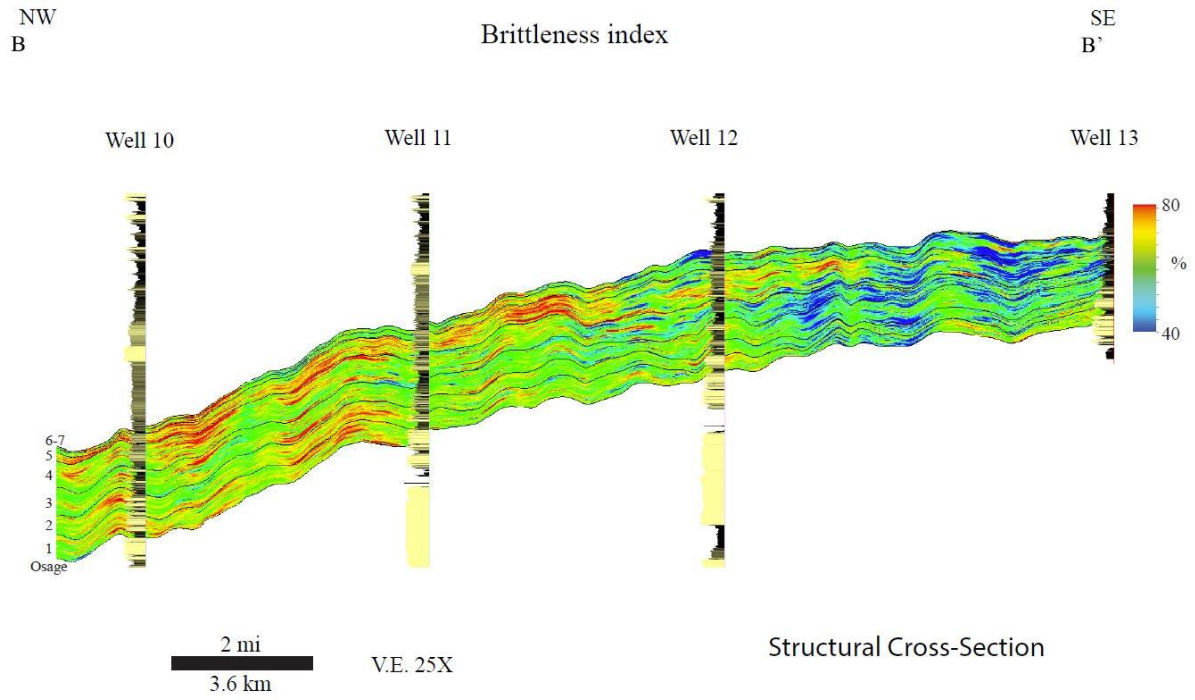

Figure 71:Northwest–southeast-oriented structural cross section through the MEDBI 3D model along with four wells with the GR profile. The Meramec strata show high values of MEDBI to the northwest, where coarser grain-size rocks (sandstones and siltstones) dominate (well 10). MEDBI values gradually change to the southeast, where fine-grain rocks deposited as part of an outer carbonate platform dominate (well 13).

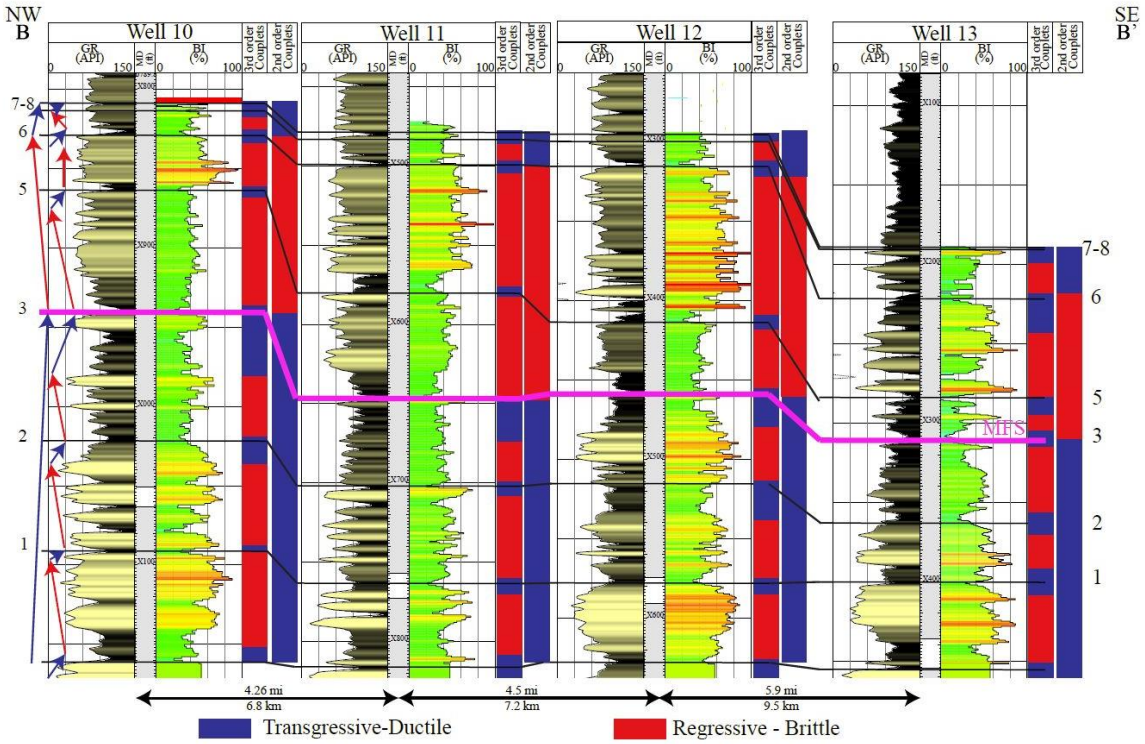

Figure 72: Cross section displaying the mechanical stratigraphic framework of the Meramec strata along the study area from proximal northwest to distal southeast. The Meramec strata display a single transgressive-regressive cycle bounded by a minor disconformity and a major unconformity at the second-order scale. Several high-order sequences superimpose the second-order sequence and are separated by flooding surfaces (fs). Blue arrows: increasing-upward GR. Red arrows: decreasing-upward GR. The pink line represents an MFS. The blue and red squares represent a transgressive and regressive interval of the couplets, respectively. Two scales of ductile-brittle couplets. (sequence = second order and parasequence = higher order).

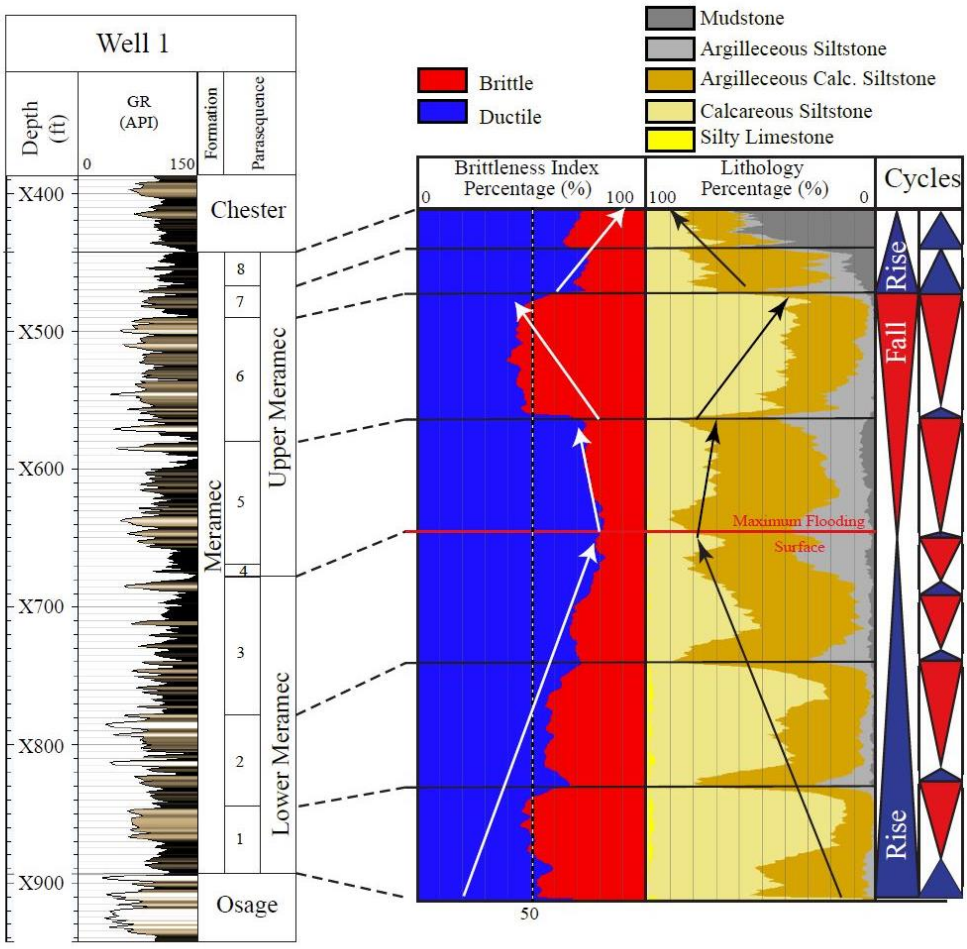

Figure 73: A summary with the type well for the study area along with the lithology and BI vertical proportion curves with the interpreted higher order cycles. These curves represent the rock percentages along the stratigraphic section (modified from Price et al., 2017).

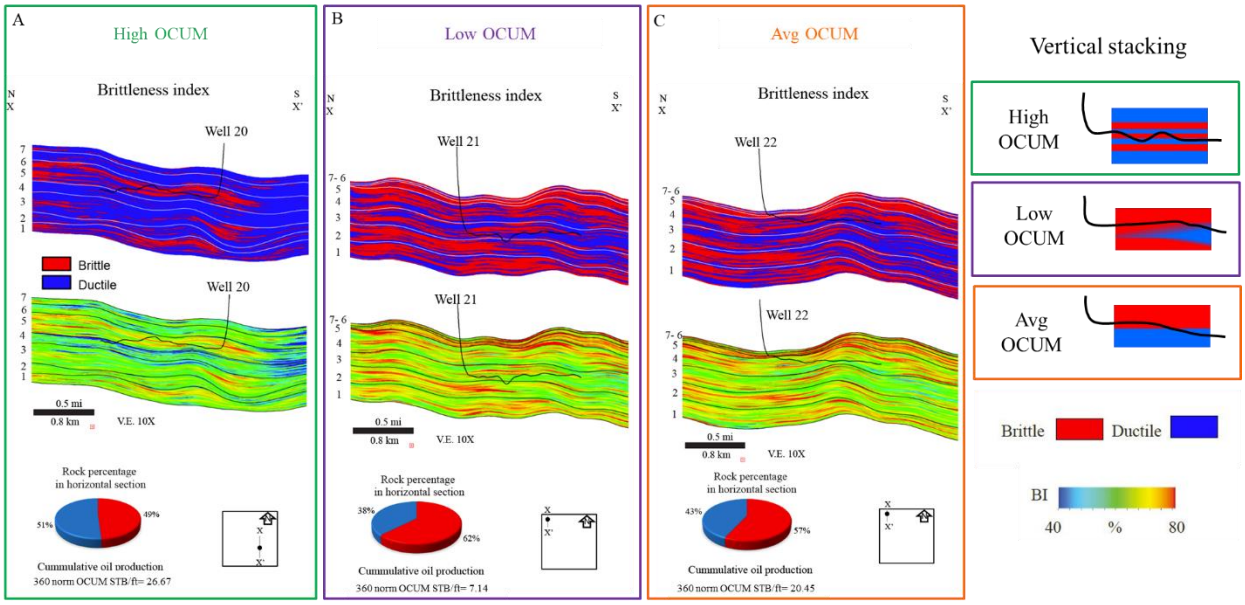

Figure 74: Vertical profiles of the discrete and continuous BI models along the well paths of (a) well 20, (b) well 21, and (c) well 22. For the discrete model, the blue and red colors represent the ductile and brittle zones, respectively. Below the continuous BI model along the same vertical section. Warm colors show high values of MEDBI, whereas cold colors show lower values of MEDBI. A pie chart displays the distribution of rocks drilled along the trajectory of the wells.75

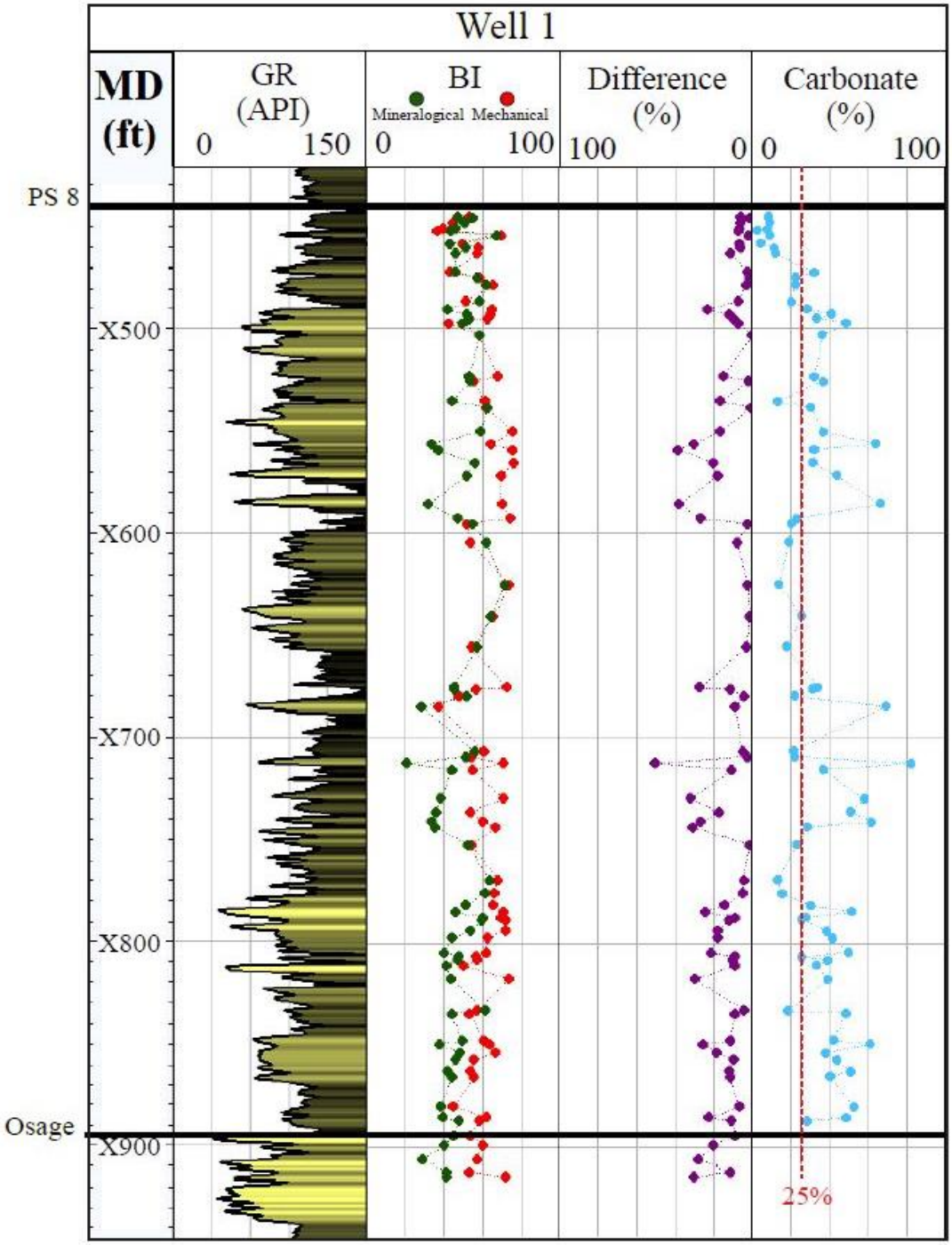

Figure 76:The GR profile for well 1 along with the estimations of mineralogical MIDBI (green) and the mechanical MEDBI (red) from core plugs. The third track shows the absolute value of the difference between the estimations of mineralogical and mechanical MEDBI in percentage (purple). The fourth track shows the weight percentage of carbonate minerals in the samples (light blue).

Well	Brittle		Ductile		OCUM
	ft	%	ft	%	STB/ft
Well 20	2567	51	2678	49	26.67
Well 21	2921	62	1760	38	7.14
Well 22	2655	57	2011	43	20.45
Well 23	1763	35	3201	65	21.60
Well 24	2403	51	2274	49	7.42
Well 25	2789	62	1696	38	8.30
Well 26	3558	71	1433	29	24.11
Well 27	1762	36	3128	64	26.31
Well 28	1638	37	2748	63	21.66
Well 29	2123	47	2334	53	8.03

Figure 77: Percentage of brittle and ductile rocks drilled by 10 wells within the study area. The lateral length and cumulative oil production were normalized for comparison.

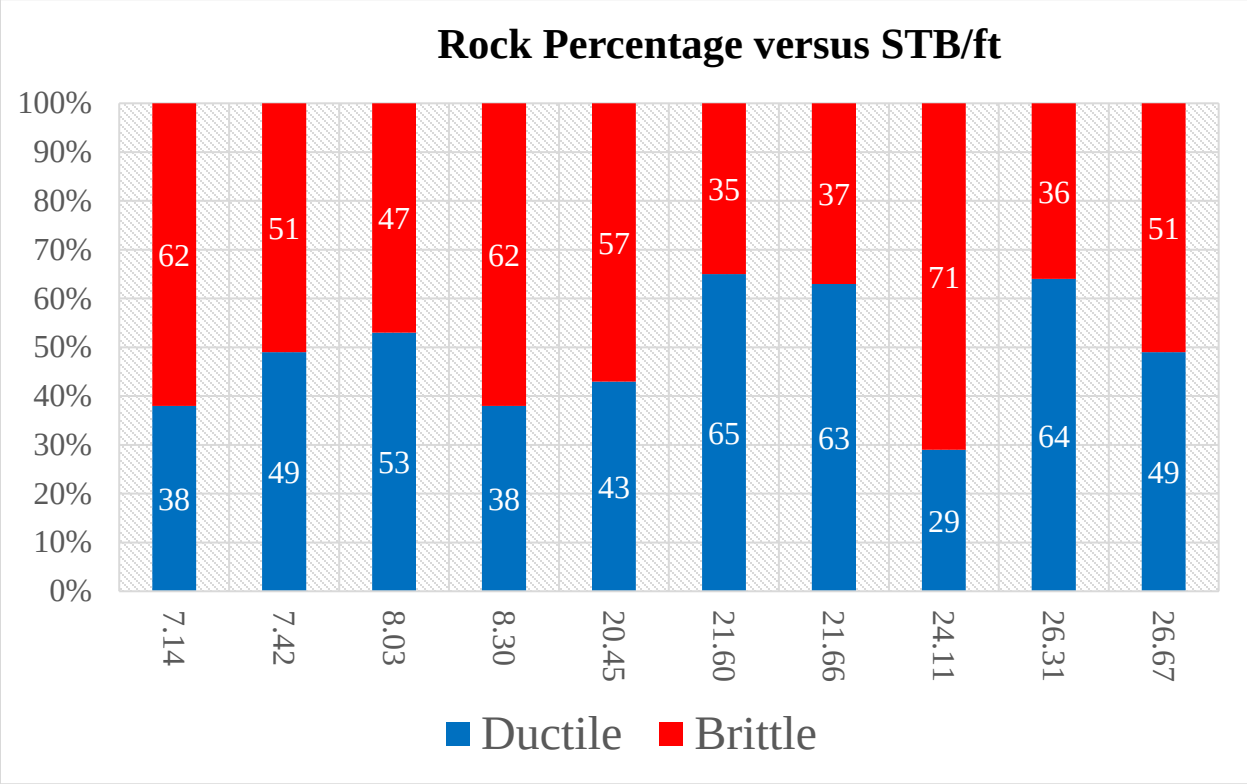

Figure 78: Stacked column diagram that shows the percentage of brittle (red) and ductile (blue) rocks along the lateral section of 10 analyzed wells and 360 days of normalized oil production.

References

Allen, D. B., and M. J. Pranter, 2016, Geologically constrained electrofacies classification of fluvial deposits: An example from the Cretaceous Mesaverde group, Uinta and Piceance Basins: AAPG Bulletin, 100, 1775– 1801, doi: 10.1306/05131614229.

Altindag, R., 2003, Correlation of specific energy with rock brittleness concepts on rock cutting: Journal of the Southern African Institute of Mining and Metallurgy, 103, 163–171.

Ball, M. M., M. E. Henry, and S. E. Frezon, 1991, Petroleum geology of the Anadarko Basin region, province (115), Kansas, Oklahoma, and Texas: Department of the Interior U.S. Geological Survey 36.

Ballard, B. D., 2007, Quantitative mineralogy of reservoir rocks using Fourier transform infrared spectroscopy: SPE.

Baytok, S., and M. J. Pranter, 2013, Fault and fracture distribution within a tight-gas sandstone reservoir: Mesaverde Group, Mamm Creek Field, Piceance Basin, Colorado, USA: Petroleum Geoscience, 19, 203–222, doi: 10.1144/petgeo2011-093.

Beebe, B. W., 1959, Characteristics of Mississippian production in the northwestern Anadarko Basin: Tulsa Geological Society Digest, 27, 190–205.

Campbell, J. A., C. J. Mankin, A. B. Schwarzkopf, and J. J. Raymer, 1988, Habitat of petroleum in Permian rocks of the midcontinent region, in W. A. Morgan and J. A. Babcock, eds., Permian rocks of the midcontinent: Midcontinent Society of Economic Paleontologists and Mineralogists Special Publication 1, 13–35.

Curtis, D. M., and S. C. Champlin, 1959, Depositional environments of Mississippian limestones of Oklahoma: Tulsa Geological Society Digest, 27, 90–103.

Dang, S., 2013, Study of Kerogen maturity using transmission Fourier transform infrared spectroscopy (FTIR): Presented at the Annual Technical Conference and Exhibition, SPE.

Drummond, K., 2018, Regional stratigraphy and proximal to distal variation of lithology and porosity within a mixed carbonate-siliciclastic system, Meramec and Osage series (Mississippian), central Oklahoma: M.S. thesis, University of Oklahoma.

Duarte, D., 2018, Rock characterization and stratigraphy of the Mississippian strata, Meramec/Sycamore merge play, central Oklahoma: M.S. thesis, University of Oklahoma, Norman, Oklahoma, 80.

Dutton, S. P., 1984, Fan-delta granite wash of the Texas Panhandle: Oklahoma City Geological Society Short Course 144.

Gale, J. F., R. M. Reed, and J. Holder, 2007, Natural fractures in the Barnett Shale and their importance for hydraulic fracture treatments: AAPG Bulletin, 91, 603–622, doi: 10.1306/11010606061.

Galvis-Portilla, H., 2017, Detailed lithostratigraphic characterization and sequence stratigraphy of a complete Woodford Shale outcrop section in southern Oklahoma: M.S. thesis, University of Oklahoma.

German, V., M. Pak, M. Azar, and S. Bits, 2015, Conical diamond element bit sets new performance benchmarks drilling extremely hard carbonate/Chert Formations, Perm Region Russia: SPE.

Gutschick, R. C., and C. A. Sandberg, 1983, Mississippian continental margins of the conterminous United States, in D. J. Stanley and G. T. Moore, eds., The shelfbreak: Critical interface on continental margins: SEPM Special Publication 33, 79–96.

Han, H., S. Dang, J. Acosta, J. Fu, C. Sondergeld, and C. Rai, 2019, X-ray fluorescence and laser induced breakdown spectroscopy for advanced rock elemental analysis: Unconventional Resources Technology Conference (URTEC), Article 1072.

Haq, B. U., and S. R. Schutter, 2008, A chronology of Paleozoic sea-level changes: Science, 322, 64–68, doi: 10 .1126/science.1161648.

Hardwick, J., 2018, Reservoir quality evaluation of the Meramec and Upper Osage units in the Anadarko Basin: M.S. thesis, University of Oklahoma.

Haykin, S., 2000, Neural networks: A guided tour, Nonlinear Biomedical Signal Processing, vol. 1, 53–68.

Hickman, G., 2018, Parasequence scale stratigraphic variability of lithology and porosity of Mississippian Meramec reservoirs and the relationships to production characteristics, STACK trend, Oklahoma: M.S. thesis, University of Oklahoma.

Jannsen, L. F., and F. M. Van der Wel, 1994, Accuracy assessment of satellite derived land-cover data: A review: Photogrammetric Engineering and Remote Sensing, 60, 419–426.

Jarvie, D. M., R. J. Hill, T. E. Ruble, and R. M. Pollastro, 2007, Unconventional shale-gas systems: The Mississippian Barnett Shale of North-Central Texas as one model for thermogenic shale-gas assessment: AAPG Bulletin, 91, 475–499, doi: 10.1306/12190606068.

Jin, X., S. N. Shah, J. C. Roegiers, and B. Zhang, 2014, Fracability evaluation in shale reservoirs—An integrated petrophysics and geomechanics approach: Presented at the Hydraulic Fracturing Technology Conference, SPE.

Johnson, K. S., and K. V. Luza, 2008, Earth sciences and mineral resources of Oklahoma: Oklahoma Geological Survey Educational Publication 9.

Kalogirou, S. A., 2000, Applications of artificial neural-networks for energy systems: Applied Energy, 67, 17–35, doi: 10.1016/S0306-2619(00)00005-2.

Lane, H. R., and T. L. De Keyser, 1980, Paleogeography of the late Early Mississippian (Tournaisian 3) in the central and southwestern United States, in T. D. Fouch and E. R. Magathan, eds., Paleozoic paleogeography of the West-Central United States: Rocky Mountain Symposium, Rocky Mountain Section SEPM (Society for Sedimentary Geology), Vol. 1, 149–162.

Leavitt, A., 2018, Depositional systems of the STACK and SCOOP Mississippian units; regional understanding from logs and core: STACK Play Workshop Technical Program and Core Viewing.

LoCricchio, E., 2012, Granite Wash play overview, Anadarko Basin: Stratigraphic framework and controls on Pennsylvanian Granite Wash production, Anadarko Basin, Texas and Oklahoma: Presented at the AAPG Annual Convention and Exhibition, AAPG.

Martin, M. A., and T. L. Davis, 1987, Shear-wave birefringence: A new tool for evaluating fractured reservoirs: The Leading Edge, 6, 22–28, doi: 10.1190/1 .1439333.

Mazzullo, S. J., B. W. Wilhite, and W. Woolsey, 2009, Rhythmic carbonate versus spiculite deposition in Mississippian hydrocarbon reservoirs in the Midcontinent USA: Causative factors and resulting reservoir petrophysical attributes, AAPG Search and Discovery #10209.

Mazullo, S. J., 2011, Mississippian oil reservoirs in the southern Midcontinent: New exploration concepts for a mature reservoir objective: Search and Discovery Article 10373.

Mazullo, S. J., and B. W. Wilhite, 2010, Chert, tripolite, spiculite, chat — What's in a name?: Kansas Geological Society Bulletin, 85, 21–25.

Mazullo, S. J., B. W. Wilhite, D. R. Boardman, B. T. Morris, and C. J. Godwin, 2016, Stratigraphic architecture and petroleum reservoirs in lower to Middle Mississippian strata (Kinderhookian to basal Meramecian) in subsurface central to southern Kansas and northern Oklahoma: Shale Shaker, 67, 20–49.

McConnell, D. A., M. J. Goydas, G. N. Smith, and J. P. Chitwood, 1989, Morphology of the frontal fault zone, southwest Oklahoma: Implications for deformation and deposition in

the Wichita uplift and Anadarko Basin: Geology, 18, 634–637, doi: 10.1130/0091-7613(1990) 018<0634:MOTFFZ>2.3.CO;2.

Miller, J., 2018, Regional stratigraphy and organic richness of the Mississippian Meramec and associated strata, Anadarko Basin, central Oklahoma: M.S. thesis, University of Oklahoma.

Miller, M., 2019, Mississippian Meramec lithologies and petrophysical property variability, STACK trend, Anadarko Basin, Oklahoma: M.S. thesis, University of Oklahoma.

Mohapatra, A., C. Rai, C. H. Sondergeld, and T. Richards, 2019, Laboratory study of ultrasonic velocity variations during CO2 flooding in Tuscaloosa Sandstone: SPE.

Morettini, E., A. Thompson, G. Eberli, K. Rawnsley, R. Roeterdink, W. Asyee, P. Christman, A. Cortis, K. Foster, V. Hitchings, and W. Kolkman, 2005, Combining highresolution sequence stratigraphy and mechanical stratigraphy for improved reservoir characterization in the Fahud field of Oman: Geoarabia, 10, 17–44.

Nayak, P. S., and B. K. Singh, 2007, Instrumental characterization of clay by XRF, XRD and FTIR: Bulletin of Materials Science, 30, 235–238.

Perez Altamar, R., and K. Marfurt, 2014, Mineralogy-based brittleness prediction from surface seismic data: Application to the Barnett Shale: Interpretation, 2, no. 4, T255–T271, doi: 10.1190/INT-2013-0161.1.

Price, B., K. Haustveit, and A. Lamb, 2017, Influence of stratigraphy on barriers to fracture growth and completion optimization in the Meramec Stack Play, Anadarko Basin, Oklahoma: Unconventional Resources Technology Conference (URTEC), Article 2697585.

Price, B. J., A. C. Pollack, A. P. Lamb, T. C. Peryam, and J. R. Anderson, 2020, Depositional interpretation and sequence stratigraphic control on reservoir quality and distribution in the Meramecian Sooner trend Anadarko Basin, Canadian, and Kingfisher Counties (STACK) play, Anadarko Basin, Oklahoma, United States: AAPG Bulletin, 104, no. (2), 357–386.

Rickman, R., M. J. Mullen, J. E. Petre, W. V. Grieser, and D. Kundert, 2008, A practical use of shale petrophysics for stimulation design optimization: All shale plays are not clones of the Barnett Shale: SPE.

Rogers, S. M., 2001, Deposition and diagenesis of Mississippian chat reservoirs, north-central Oklahoma: AAPG Bulletin, 85, no. 1, 115–129.

Slatt, R. M., and Y. Abousleiman, 2011, Merging sequence stratigraphy and geomechanics for unconventional gas shales: The Leading Edge, 30, 274–282, doi: 10.1190/1 .3567258.

Sloss, L. L., 1963, Sequences in the cratonic interior of North America: Geological Society of America Bulletin, 74, 93– 114, doi: 10.1130/0016-7606(1963)74[93:SITCIO]2.0.CO;2.

Suárez-Rivera, R., C. Deenadayalu, and Y. K. Yang, 2009, SS: Unlocking the unconventional oil and gas reservoirs: The effect of laminated heterogeneity in wellbore stability and completion of tight gas shale reservoirs: Offshore Technology Conference

Ting, K. M., 2011, Confusion matrix, in C. Sammut and G. I. Webb, eds., Encyclopedia of machine learning, 1st ed: Springer.

Turner, B. W., and R. M. Slatt, 2016, Assessing bottom water anoxia within the Late Devonian Woodford Shale in the Arkoma Basin, southern Oklahoma: Marine and Petroleum Geology, 78, 536–546, doi: 10.1016/j.marpetgeo.2016.10.009.

Vecsey, L., J. Plomerová, and V. Babuska, 2008, Shearwave splitting measurements — Problems and solutions: Tectonophysics, 462, 178–196, doi: 10.1016/j .tecto.2008.01.021.

Wang, F. P., and J. F. W. Gale, 2009, Screening criteria for shale-gas systems: GCAGS Transactions, 59, 779–793.

Witzke, B. J., 1990, Palaeoclimatic constraints for Palaeozoic palaeolatitudes of Laurentia and Euramerica. Geological Society, London, Memoirs, 12, v.1, 57-73.

General conclusions

I started this dissertation with a chapter that explains the importance of data integration and the use of new techniques to improve reservoir characterization. The subsequent chapters showed multiple workflows that integrate data from outcrops, measured sections, and thin sections to datasets derived from multiple sources such as core, well logs, and 3D seismic data. The integration of new data in chapter one was done by collecting information from Unmanned Aerial Systems (UAS) that provided a quick, efficient, and reliable technique to characterize qualitatively and quantitatively large outcrops in a relatively short time. The statistical measurements collected from this study are valuable for subsurface modeling of fluvial deposit analogs to the Burro Canyon Formation. The study also establishes a regional sequence stratigraphic framework for the fluvial system.

Chapters 2 and 3 present different workflows that involve integration of seismic and well data through supervised machine learning techniques. The methods are complemented with an analysis that allowed me to relate geological characteristics to hydrocarbon production results.

Chapter 2 shows that lithology and rock type proportions do not directly control the production performance of wells drilled within the Meramec strata. However, the spatial distribution of prospective rocks is strongly related to the sequence stratigraphic framework in proximal and distal locations within the Anadarko Basin. Analysis of production and distance from interpreted faults showed a negative correlation suggesting that wells located nearby damage zones are likely to have a high cumulative oil production. Additionally, I illustrated a workflow to characterize damage zone based on seismic attributes (variance) to generate permeability modifiers for reservoir modeling.

Chapter 3 showed a methodology to estimate and build reservoir models of geomechanical properties to evaluate the impact of mechanical stratigraphy in hydrocarbon production. The analysis suggests that the sequence stratigraphic framework of the Meramec strata plays an important role in the vertical and horizontal distribution of brittle and ductile rocks. However, the percentage of brittle or ductile rocks does not suggest a clear relationship with the production. Results indicate that the vertical stacking and lateral continuity of brittle and ductile rocks are potentially related to cumulative hydrocarbon production in the Meramec unconventional reservoirs.

Despite data integration, it is essential to highlight that for analysis of the Meramec reservoirs (or unconventional siliciclastic reservoirs in general), many other operational parameters make it challenging to predict and estimate relationships between geological characteristics and hydrocarbon production. The number of fracture stages, proppant volume, well path direction, reservoir pressure, and parent-child well interference, among other operational factors, significantly impact well performance. Therefore, a multidisciplinary approach to guarantee the best geological, dynamic, and operational conditions to drill optimal development wells within the Meramec reservoirs is necessary.

An appropriate reservoir characterization should aim to reduce uncertainty and de-risk development wells. Reservoir modeling is the result of data integration from multiscale sources. Realizations of these models are used to assess and quantify uncertainty. Furthermore, a multiscale study combined with probabilistic methods and new technologies provides an excellent approach to better characterize the structural and stratigraphic configuration of tight unconventional reservoirs for energy applications.